UNIVERSITÉ DU QUÉBEC

THÈSE PRÉSENTÉE À L'UNIVERSITÉ DU QUÉBEC À CHICOUTIMI COMME EXIGENCE PARTIELLE DU DOCTORAT EN INGÉNIERIE

PAR
HAMID BANITALEBI DEHKORDI

STUDY OF THE INFLUENCE OF ICE ACCRETION ON THE AERODYNAMIC COEFFICIENTS OF LATTICE TOWER ELEMENTS

ÉTUDE DE L'INFLUENCE DE L'ACCRÉTION DE GLACE SUR LES COEFFICIENTS AÉRODYNAMIQUES DES PYLÔNES DES LIGNES DE TRANSPORT DE COURANT ÉLECTRIQUE

May 2014

ABSTRACT

In cold regions, overhead line cables and their supporting structures are usually fully exposed to atmospheric icing. In addition, rising temperatures due to climate changes are expected to increase the risks associated with extreme weather events which in turn could possibly increase the frequency and severity of storms such as winter blizzards and ice storms.

Atmospheric icing is one of the major problems in cold climate regions, which can cause serious damage to transmission line structures, such as overhead transmission networks. Towers or pylons, usually steel lattice structures, represent an important part of the cost of transmission lines.

Ice deposits on exposed structures can be the source of several mechanical problems. On transmission line towers in particular, the loads due to heavy ice accretion, coupled with wind-on-ice loads, may lead to aerodynamic effects and cause structural damages, or failure and even cascading collapse of towers.

The present investigation is mainly focused on the study of aerodynamic characteristics of angle member icing. The objective is to understand the influence of ice accretion on drag, lift and moment in respect to different ice profiles. In most of the previous experimental studies of ice effects on aerodynamic characteristics, aerodynamic bodies such as airfoils and wings were modeled, whereas in this research, the ice effects on bluff bodies is studied.

Experimental models that explicitly consider different glaze ice profiles by including the thermo-physical properties of ice during accretion are proposed. Drag, lift and moment coefficient of those angle member reproduced using cement molded glaze ice profiles are thus measured in a wind tunnel.

The models serve as a basis to study various criteria of atmospheric glaze ice effects in terms of aerodynamic coefficient and, aerodynamic forces. Various tower section geometries with glaze ice profiles can also be readily investigated using these models. Several aerodynamic scenarios of an angle member are simulated in order to investigate how variables including ice thickness, liquid water content (LWC), droplet size distribution (DSD) and Reynolds number affect the drag, lift and moment coefficients of an iced angle member subjected to air velocity.

Ice morphology of an angle member for different aerodynamic angles and different model orientations are also explored in order to study the flow characteristics effects on ice accretion.

RÉSUMÉ

Dans les régions froides, les câbles des lignes de transport et leurs structures sont généralement exposés au givrage atmosphérique. En outre, l'élévation des températures en raison des changements climatiques devraient accroître les risques associés aux phénomènes météorologiques extrêmes, qui à leur tour pourraient éventuellement augmenter la fréquence et la gravité des tempêtes telles que les tempêtes de neige hivernales et les tempêtes de verglas.

Dans les régions au climat froid, le givrage atmosphérique est un des problèmes majeurs qui peut causer de graves dommages aux structures des lignes aériennes de transport de l'énergie électrique. Les pylônes, dont les structures sont normalement composées de treillis métalliques, représentent une part importante du coût des lignes de transport.

Les dépôts de glace sur les structures exposées peuvent être la source de plusieurs problèmes mécaniques. Plus spécifiquement sur les pylônes des lignes électriques, les charges occasionnées par une épaisse couche de glace, couplées avec celles créées par le vent, peuvent entraîner des charges aérodynamiques excessives et causer des dommages structuraux, des bris ou même un effondrement en cascade des pylônes.

Cette recherche a principalement porté sur l'étude des caractéristiques aérodynamiques des cornières sous l'effet du givrage. L'objectif était de comprendre l'influence de différents profils de glace sur la traînée, la portance et le moment aérodynamique. Dans la plupart des études expérimentales précédentes sur les effets de la glace sur les caractéristiques aérodynamiques, des corps profilés tels des ailes d'avion ont été modélisés alors que dans cette recherche, ce sont les effets de la glace sur des corps non profilés qui ont été étudiés.

Des modèles expérimentaux tenant explicitement compte de différents profils de glace, tout en incluant les propriétés thermo-physiques de la glace durant l'accrétion, ont été proposés. Les coefficients de traînée, de portance et le moment des profils de glace reproduits à l'aide de ciment moulé sur une cornière ont été mesurés en soufflerie.

Les modèles développés peuvent servir de base pour l'étude des effets de la glace atmosphérique, tels les coefficients aérodynamiques et les forces aérodynamiques. Différentes géométries de section de pylônes avec des profils de glace peuvent également être plus facilement étudiées à l'aide de ces modèles. Plusieurs scénarios aérodynamiques sont simulés afin d'étudier comment des variables, tels que l'épaisseur de la glace, la teneur en eau liquide, la taille des gouttelettes et le nombre de Reynolds, affectent les coefficients de traînée, la portance et le moment d'une cornière givrée soumise à un écoulement d'air.

La morphologie de la glace accumulée sur une cornière, pour différents angles d'attaque aérodynamiques et différentes orientations de la cornière, est également explorée afin d'étudier l'effet des paramètres du vent sur une accrétion de glace.

TABLE OF CONTENTS

ABSTRACT i
RÉSUMÉ iii
TABLE OF CONTENTS v
ACKNOWLEDGMENT ix
LIST OF FIGURES: xi
LIST OF TABLES: xiv

CHAPTER 1
INTRODUCTION

1-1-Problem definition 1
1-2-Research Objectives 5
1-3-Originality and contributions to knowledge 6
1-4-Methodology 7
1-4-1-Wind tunnel calibration 7
1-4-2-Natural Icing Event Measurements 8
1-4-3- Natural Icing Simulation 9
1-4-4-Aerodynamic measurements 10
1-4-5-An introduction to the use of the Particle Image Velocimetry (PIV) method 10
1-5-Thesis organization 11

CHAPTER 2
LITERATURE REVIEW

Introduction 13
2-1- Atmospheric icing 14
2-1-1- Types of ice accretion 14
2-1-2- Accretions on transmission line towers 18
2-1-3- Ice morphology 20
2-2- Ice-related loads on transmission line towers 22
2-2-1- Ice shedding 22
2-2-2- Galloping 23
2-2-3- Aeolian vibration 23
2-2-4- Aerodynamic forces 24
2-3- Interaction between ice effects and wind load 24
2-3-1- Aerodynamic forces 26
2-3-2- Flow field measurements 29
2-3-3- Blockage effects 39
2-4- The effect of DSD and LWC on aerodynamic coefficients 41
Conclusion 43

CHAPTER 3
EXPERIMENTAL FACILITIES, TEST MODELS AND TEST PROCEDURES

Introduction 45
3-1- Experimental Facilities 46
3-1-1- CIGELE Atmospheric Icing Research Wind Tunnel (CAIRWT) 46

3-1-1-1- Construction of CAIRWT 47
3-1-1-2-General Layout of CAIRWT 48
3-1-1-3-CAIRWT's Main Systems 49
3-1-1-3-1-Fan system 49
3-1-1-3-2-Refrigeration system 50
3-1-1-3-3-Nozzle spray-bar system 51
3-1-1-4-Control Panel 52
3-1-1-4-1-Water Transfer System 53
3-1-1-4-2-Air Transfer System 53
3-1-1-4-3-Nozzle Heating System 53
3-1-1-4-4-Air Heating System 54
3-1-1-5-Physical parameters of the aerosol cloud produced in the wind tunnel 54
3-1-1-5-1-Temperature 55
3-1-1-5-2-Velocity 55
3-1-1-5-3-Relative and Absolute Humidity 55
3-1-1-5-4-Liquid Water Content (LWC) 56
3-1-1-5-5-Droplet Size Distribution (DSD) 56
3-1-1-6-CAIRWT related equipment 57
3-1-1-6-1-Integrated System for Icing Studies by Droplets Measurement Technologies 57
3-1-1-6-2-Particle Image Velocimetry (PIV) 57
3-1-2- Low speed aerodynamic tunnel 59
3-1-2-1- General layout 59
3-1-2-2- Tunnel parameters 59
3-1-2-3- Tunnel related equipment (External balance) 59
3-2- Test models 60
3-2-1-Wind effects on ice accretion 60
3-2-2- DSD and LWC effects on ice accretion and drag coefficient 62
3-2-3- Aerodynamic models 62
3-3- Test procedures and selecting experimental conditions 66
3-3-1- Wind effects on ice accretions 66
3-3-2- DSD and LWC effects on ice accretion and drag coefficient 67
3-3-3- Aerodynamic measurements 68
Conclusion 72

CHAPTER 4

ICE SIMULATION AND WIND EFFECTS ON AN ANGLE MEMBER ICING

Introduction 73
4-1-Ice simulation 74
4-1-1-Glaze ice 74
4-1-2- Rime ice 77
4-2-Wind effects on horizontal angle member icing in the test section 79
4-2-1-Sign convention and definition of the variables 80
4-2-2-Angle of attack 80
4-2-3-Side slip angle (Yaw angle) 89

4-2-4-Rolling angle 92
4-2-5-Estimation of Drag Coefficients of Ice-Covered Angle Bars for different angles of attack 94
4-3-Wind effects on vertical angle member icing in the test section 96
4-3-1- Sign convention and definition of the variables 96
4-3-2- Angle of attack 97
4-3-3-Sideslip angle (Yaw angle) 99
4-3-4-Rolling angle 100
Conclusion 102
CHAPTER 5
THE EFFECT OF DSD AND LWC ON ICE ACCRETION AND DRAG COEFFICIENTS
Introduction 104
5-1- Sign convention and definition of the variables 105
5-2-DSD and LWC measurements 106
5-2-1-Streamwise and Vertical Variations of Median Volume Diameter (MVD) and LWC of the droplets 106
5-3-Ice Accretion Measurements on Tower-Leg Model 113
5-3-1-Streamwise and Vertical Variations of Ice Accretion on Angle Bar 113
5-3-2-Calculation of Drag Coefficients of Ice-Covered Angle Bars 124
Conclusion 127
CHAPTER 6
INTERACTION OF WIND WITH A CEMENT ICE PROFILE ON AN ANGLE MEMBER
Introduction 129
6-1-Sign convention and definition of the variables 130
6-2-Reynolds number effects 131
6-3-Ice thickness effects 138
6-4-Considering different ice profiles 146
6-5-Different angle member profiles 149
6-6-Droplet effects 153
6-7-Effects of projected area 157
6-8-Drag from standard 162
6-9-Aerodynamic Forces 167
6-9-1- Drag Force per unit length 167
6-9-2- Lift Force per unit length 169
Conclusion 170
CHAPTER 7
AN INTRODUCTION OF USING PIV TECHNIQUE TO STUDY THE EFFECTS OF ICE SHAPE ON THE VORTEX SHEDDING OF A CYLINDER
Introduction 173
7-1-Test models 174
7-2-Test procedure 175
7-3-Experimental Results 177
Conclusion 182

CHAPTER 8
CONCLUSIONS AND RECOMMENDATIONS

8-1-Conclusions 184
8-2-Recommendations for future study 187

APPENDIX

APPENDIX A: CAIRWT Layout 189
APPENDIX B: CAIRWT Calibration Results 196
APPENDIX C: Test Conditions and Results Raw Data 216

REFERENCES

References 237

ACKNOWLEDGMENT

This research was carried out within the framework of the NSERC / Hydro-Québec Industrial Chair on Atmospheric Icing of Power Network Equipment (CIGELE) and the Canada Research Chair on Atmospheric Icing Engineering of Power Network (INGIVRE) at the University of Québec at Chicoutimi (UQAC). The author would like to thank all the sponsors of the CIGELE / INGIVRE for their financial support.

I would like to thank all who gave me the possibility to complete this research. The author also gratefully acknowledges his best appreciation of Professor Masoud Farzaneh, his patience, guidance, encouragement and support of my research work. It was great to have the privilege to work with him and learn from his expertise in the past four years.

My special thanks to my co-director Dr. Pierre Van Dyke for his gentle instructions, many technical discussions and suggestions throughout this project and of course reading and editing my thesis.

Special thanks to Professor Frederic Legeron of the University of Sherbrooke for providing access to the Aerodynamic low speed wind tunnel. I am also grateful to Mr. Simon Prud'homme, Ph.D. student of the Civil engineering department of Sherbrooke University who helped me with the aerodynamic investigations of this research and performed the aerodynamic tests at Sherbrooke University's wind tunnel.

I would also like to thank Dr. Laszlo Kollar, University of Huddersfield, England, for his guidance, encouragement and technical help during this research.

I would also like to thank the research colleagues, professionals and technicians in CIGELE, for their support and help. These people include Pierre Camirand, Xavier Bouchard, Claude D'amours and Denis Masson among many others. I am thankful for the time they have taken with me. I am grateful to Mrs. Yvette Boulay for her precious efforts and editorial help.

I am pleased to have participated in the Ph.D. program offered by the University of Quebec in Chicoutimi, where I had the chance to develop my skills and find lengthy friendships.

I also want to acknowledge my parents who were always my greatest source of inspiration. Finally, I want to express my deepest thanks and appreciation to my wife, Ladan, for her patience, confidence, and moral support during my studies.

LIST OF FIGURES:

Figure 2-1: Ice accretion types (adapted from [31]) 17
Figure 2-2: Atmospheric ice accretions on transmission line towers 19
Figure 2-3: Examples of a) aerodynamic body and b) bluff bodies 25
Figure 2-4: Drag coefficient versus solidity ratio of tested tower models 27
Figure 2-5: Comparison between the pressure distributions of a flat plate (C_D = 2) and of a circular cylinder for $Re < 10^5$ (C_D = 1.2) [48] 30
Figure 2-6: Drag coefficients of various cylindrical shapes as a function of Re [48] 33
Figure 3-1: CIGELE Atmospheric Icing Research Wind Tunnel 48
Figure 3-2: Layout of a Closed Single-Return Wind Tunnel 49
Figure 3-3: CAIRWT`s Control Panel 52
Figure 3-4: Control Panel Systems 53
Figure 3-5: Support used for horizontal ice simulation 61
Figure 3-6: Support used for vertical ice simulation 61
Figure 3-7: Cement moulded ice profile for sample number1 to 7 from Table 3-3 65
Figure 3-8: Positioning of the 3 Pitot tubes 69
Figure 3-9: The distance between the rig and ice profile 70
Figure 4-1: Glaze ice with icicles, a) Petite-Rivière Saint-François, b) Wind tunnel ice simulation on angle member 75
Figure 4-2: Glaze ice, a) Mont Bélair, b) Wind tunnel ice simulation on a rotating cylinder 76
Figure 4-3: Glaze ice, a) Mont Bélair, b) Wind tunnel ice simulation on an angle member 77
Figure 4-4: Rime ice, a) Mont Bélair, b) Wind tunnel ice simulation on an angle member 78
Figure 4-5: Rime ice, a) Mont Bélair, b) Wind tunnel ice simulation on an angle member 79
Figure 4-6: Sign convention and definition for icing experiments 80
Figure 4-7: A51xL9 ice accretion for a-b) α=0°, c-d) α=180° 81
Figure 4-8: A51xL9 ice accretion for a) α=54°, b) α=234° 82
Figure 4-9: A51xL9 ice accretion for a) α=144°, b) α=324° 83
Figure 4-10: A51xL9-2 ice accretion profile for α>180° 84
Figure 4-11: A51xL9-2 ice accretion profile for α=270° to α=360° 86
Figure 4-12: A51xL9-1 (a and b) and A51xL9-2 (c and d) ice profiles for α=0° and α=180° 87
Figure 4-13: A51xL9-2 ice structure for α=360°, α=342° and α=306° 88
Figure 4-14: The normalized ice mass per unit length for A51xL9-1 and A51xL9-2 89
Figure 4-15: A51xL9-2 ice profiles for different sideslip angles 90
Figure 4-16: A51xL9-2 ice structure for β=0°, β=25° and β=65° 91
Figure 4-17: Normalized ice mass per unit length of A51xL9-1 and A51xL9-2 for different sideslip angles 91
Figure 4-18: Ice profiles of A51xL9-2 for different rolling angles 92
Figure 4-19: Accreted ice top view of A51xL9-1 for different rolling angles 93
Figure 4-20: Normalized ice mass per unit length of A51xL9-1 and A51xL9-2 for different rolling 94
Figure 4-21: Drag estimation based on standard ISO12494 for A51xL9-1 and A51xL9-2 . 96

Figure 4-22: Sign convention and definition for icing experiments 97
Figure 4-23: A51xL4 ice mass per unit length for different angles of attack 98
Figure 4-24: A51xL4 ice accretion for three different angles of attack 99
Figure 4-25: A51xL4 ice accretion for a) β=6°, b) A51xL4 upper side, c) A51xL4 lower side 100
Figure 4-26: A51xL4 ice mass per unit length for different rolling angles 101
Figure 4-27: A51xL4 ice accretion profiles for different rolling angles 102
Figure 5-1: Sign convention and reference point 105
Figure 5-2: MVD variations along the streamwise direction at y = –0.07 m 108
Figure 5-3: LWC variations along the streamwise direction at *y* = –0.07m 110
Figure 5-4: MVD variations along the vertical direction at x = 0.5 m 111
Figure 5-5: LWC variations along the vertical direction at x = 0.5 m 113
Figure 5-6: Mass per unit length, P_w=300 kPa, P_a= 300 kPa and V_a= 25 m/s 115
Figure 5-7: Side view of the iced horizontal angle bar, P_w=300 kPa, P_a= 300 kPa 116
Figure 5-8: Front view of the iced horizontal angle bar, P_w=300 kPa, P_a= 300 kPa 117
Figure 5-9: Top view of the iced horizontal angle bar, P_w=300 kPa, P_a= 300 kPa 118
Figure 5-10: Mass per unit length P_w=300 kPa, P_a= 200 kPa and V_a= 12 m/s 119
Figure 5-11: Side view of the iced horizontal angle bar, P_w=300 kPa, P_a= 200 kPa 120
Figure 5-12: Front view of the iced horizontal angle bar, P_w=300 kPa, P_a= 200 kPa 121
Figure 5-13: Top view of the iced horizontal angle bar, P_w=300 kPa, P_a= 200 kPa 121
Figure 5-14 Mass per unit length for V_a = 25 m/s and V_a = 12 m/s 122
Figure 5-15: Accreted vertical angle bar, V_a = 25 m/s 123
Figure 5-16: Accreted vertical angle bar, V_a = 12 m/s 124
Figure 6-1: Sign convention and definition of variables 131
Figure 6-2: Aerodynamic coefficients of S25-G1 with respect to Reynolds number 133
Figure 6-3: Aerodynamic coefficients of S51-G3 with respect to Reynolds number 134
Figure 6-4: Aerodynamic coefficients of S51-G5 with respect to Reynolds number 135
Figure 6-5: Aerodynamic coefficients of S51-G6 with respect to Reynolds number 136
Figure 6-6: Aerodynamic coefficients of S51-G7 with respect to Reynolds number 137
Figure 6-7: Ice thickness effects on aerodynamic coefficients for S25-G1 and S25-G2 139
Figure 6-8: Ice thickness effects on C_D^n and C_{D0}^p for S25-G1 and S25-G2 141
Figure 6-9: Ice thickness effects on aerodynamic coefficients for S51-G3 and S51-G4 143
Figure 6-10: Ice thickness effects on C_D^n and C_{D0}^p for S51-G3 and S51-G4 145
Figure 6-11: Aerodynamic coefficients for different ice profiles, Air velocity: 5 m/s 147
Figure 6-12: Ice thickness in the wind direction, t, of different ice profiles for α=0° 148
Figure 6-13: C_D^n and C_{D0}^p for different ice profiles 149
Figure 6-14: Aerodynamic coefficients for two different angle member profile: S25-G2 and S51-G5 151
Figure 6-15: C_D^n and C_{D0}^p for two different angle member profile: S25-G2 and S51-G5 152
Figure 6-16: Aerodynamic coefficient for two different DSDs. S51-G3 and S51-G5 154
Figure 6-17: Droplet effects on C_D^n and C_{D0}^p 156
Figure 6-18: Aerodynamic coefficients of S51-G3 for two projected areas 158

Figure 6-19: Aerodynamic coefficients of S51-G5 for two projected areas.....159
Figure 6-20: Aerodynamic coefficients of S51-G6 for two projected areas.....160
Figure 6-21: Aerodynamic coefficients of S51-G7 for two projected areas.....161
Figure 6-22: Drag force formulation for different angle of attacks. Adopted from ISO 12494 163
Figure 6-23: Drag coefficient from ISO12494 for a windward direction.....165
Figure 6-24: Normalized drag coefficient obtained from ISO12494 and experimental tests for S51-G3, G5, G6 and G7.....166
Figure 6-25: Drag force of different ice profiles compare to bare member for V ≈ 5 m/s.168
Figure 6-26: Drag force of different ice profile compare to bare member for V ≈ 10 m/s 168
Figure 6-27: Lift force of different ice profile compare to bare member for V ≈ 5 m/s 169
Figure 6-28: Lift force of different ice profile compare to bare member for V ≈ 10 m/s ..170
Figure 7-1: Accretion cylinders with a) bare profile, and b) profile with ice accretion shape 174
Figure 7-2: Flow field around a) a bare profile, and b) an ice accretion shape profile; air velocity: 10m/s.....178
Figure 7-3: Vorticity contour for bare profile, air velocity: 10m/s.....179
Figure 7-4: Vorticity contour for ice accretion profile, air velocity: 10m/s 180
Figure 7-5: Average velocity field vectors for bare profile, air velocity: 10m/s 181
Figure 7-6: Average velocity field vectors for ice accretion profile, air velocity: 10m/s...182

LIST OF TABLES:

Table 2-1 Types and characteristics of ice accretion (adapted from [27], [28], [29]) 15
Table 2-2: Recommended equations for calculating drag coefficient 28
Table 3-1: Laser machine information 59
Table 3-2: Angle member dimensions for icing simulation 62
Table 3-3: Angle member specifications with related thermo physical parameters 63
Table 3-4 Thermo physical parameters of ice simulation 66
Table 3-5: Air velocity and angle of attack for aerodynamic models 69
Table 3-6: Models length with and without ice 71
Table 4-1: Thermo physical parameters for different glaze ice accretions with icicles 75
Table 4-2: Thermo physical parameters for different glaze ice accretions 76
Table 4-3: Thermo physical parameters for different rime ice accretions 78
Table 4-4: Average ice mass per unit length for A51xL9 82
Table 5-1: Thermo-physical parameters for icing conditions 114
Table 5-2: Drag coefficient variation for iced angle bar in vertical position (lower LWC and higher velocity) 126
Table 5-3: Drag coefficient variation for iced angle bar in vertical position (higher LWC and lower air velocity) 126
Table 6-1: Calculated drag coefficients based on ISO12494 162
Table 6-2: Calculated drag coefficient for different icing conditions presented by different MVDs 166
Table 7-1: Test parameters of PIV investigations 177
Table 7-2: Ice accretion parameters 177
Table 7-3: Velocity measurement values 177

CHAPTER 1

INTRODUCTION

CHAPTER 1

INTRODUCTION

1-1-Problem definition

Atmospheric icing is one of the major problems in cold climate regions, which can cause serious damage to structures, such as overhead transmission networks. For example, the January 1998 ice storm that hit Eastern Canada, downed hundreds of km of transmission lines, collapsed hundreds of pylons and broke several thousands of transmission and distribution wooden poles [1].

Towers or pylons, usually steel lattice structures, represent an important part of the cost of transmission lines. They are used to support overhead conductors on transmission

lines and as such, may be subjected to major stresses. In Nordic countries, the combination of wind and ice on conductors as well as towers may correspond to the towers' critical load. Economic aspects dictate us to build lines that will sustain these loads and, at the same time, avoid any over strengthening to keep the construction cost as low as possible. This goal may be reached only with a better understanding of the phenomenon.

In recent years, there have been considerable research efforts in the study of ice and wet-snow accretion on overhead transmission lines [2], [3]. The main objectives are to collect ice load and wind-on-ice load data, to better understand the effect of various complex forms of ice and wet-snow accretion, to develop and validate icing models and to introduce probabilistic design load approaches [3].

Spray icing often forms in cold environments as a result of the collection of an aerosol of water or brine by a structure. Aviation icing, icing of electrical transmission towers, lines and insulators as well as marine icing are some well-known examples. It is important to take the type of ice in consideration because under specific conditions, different ice shapes appear with profiles that depend intrinsically on aero-thermal conditions.

The accreted ice will modify tower's shape and also affect the air flow over the whole tower. Accordingly, the type of ice accretion and meteorological and climatic information as well as the location where the test have been conducted are important. In 1994, some tests were conducted at Mt. Valin natural icing test site. This test site allowed the

observation of about fifteen significant icing events, with about 60% of icing events corresponding to soft rime accretion and about 40% to freezing rain, hard rime or wet snow [4].

Contrarily to Druez et al. [4], Sundin and Makkonen observed that the main type of ice on tower was in-cloud icing while freezing precipitation was less frequent and also lower in magnitude [5].

Vargas and Tsao presented a photographic investigation of ice growth on swept wings in an icing research tunnel. They observed roughness elements, icing feathers, initial scallop and complete scallop in glaze icing conditions [6]. They conducted an experiment in natural icing conditions using an icing research aircraft for different sweep angles to compare the mechanism of ice deposit separated by air inclusion called *lobster tail* or *scallop* icing formation with results which were collected from tunnel investigation [7]. Presteau et al. showed that the results from a 3D numerical model for a scallop ice shape were in good agreement with experimental tests for a plain cylinder [8].

Ice growth often occurs in cold environments coincident with the entrapment of a portion of the impinging liquid by the growing ice matrix. This type of ice accretion is said to be spongy. Dendritic ice crystal growth into supercooled liquid at the icing surface entraps a portion of the liquid into the advancing ice matrix [9].

Maeno showed that the length of an icicle increases by the downward growth of thin dendritic crystals into the supercooled pendant water drop at the tip as well as the diameter

and that it increases also by the freezing of a water film flowing down along the icicle wall [10]. Makkonen proposed a model of icicle growth. It was demonstrated that the growth of an icicle is a complicated process which is very sensitive to atmospheric conditions and water flux. The shape and weight of icicles predicted by the model agree well with laboratory data [11].

In areas where ice accretion on towers is possible, the different explained ice profiles resulting from added weight and changing profile shape beside wind effects become an important parameter on increased aerodynamic forces. Kollar and Farzaneh studied the effects of various wind velocity angles and cylindrical icing object axes experimentally. The mass, shape and profile of ice accretion were calculated as a function of cylinder inclination [12]. For aerodynamic structures, it was shown that the effects of the angle of attack variation on atmospheric ice accretion near the blade tip are less severe, both in terms of local ice mass and relative ice thickness [13]. The effect of airfoil angle of attack on the drag coefficient of different ice profiles was studied by Rejado et al. [14]. For power network facilities, the aerodynamic studies focus on bluff body characteristics.

Bayar investigated the drag coefficient of latticed towers. He studied the effect of solidity ratio (area of members / total enclosed area) on drag coefficient by using different models [15]. Prud'homme et al. studied the effects of wind forces on angle members. They studied the variation of drag and lift coefficients for different angle members [16]. Besides experimental researches, some analytical techniques were used to determine drag coefficient on bluff bodies [17], [18], [19].

In order to study the effects of ice on aerodynamic characteristics of transmission towers the present investigation is mainly focused on the study of aerodynamic characteristics of angle member icing. In the first step, the ice was simulated on an angle member based on photographic data of power network icing. After validating the ice simulations, glaze ice accretion was selected for the next steps of the research. Then, the ice shape and ice mass per unit length were studied for different wind directions and model orientations in the icing wind tunnel.

Then, some ice profiles were chosen to be reproduced by cement in a multi-steps casting process in order to obtain aerodynamic measurements in the aerodynamic wind tunnel. The two dimensional aerodynamic characteristics, drag coefficient and lift coefficient and subsequently drag force and lift force were measured by using an external balance for different angles of attack and different velocities.

The main goal of this study is to experimentally investigate the effects of different ice profiles on two-dimensional aerodynamic characteristics.

1-2-Research Objectives

This research aims at evaluating the influence of ice accretion on the aerodynamic coefficients of lattice structures specifically transmission lines' structures. The main objectives of the present study are:

- Wind tunnel investigation using an angle member to compare the ice simulation

results with those obtained from natural icing.

- Wind tunnel investigation to obtain the ice quantity, ice profile and area of accreted ice considering the effects of:

✓ Wind velocities

✓ Wind directions

✓ Model orientations

- Study the variations of aerodynamic characteristics on a model with ice-shaped profiles for different wind velocities.
- Study the variations of aerodynamic characteristics on a model with ice-shaped profile for different wind angles of attack.

1-3-Originality and contributions to knowledge

In most previous studies of aerodynamic coefficients of bodies with ice [14], [20], [21], [22], the aerodynamic bodies such as aerodynamic airfoils and wind turbines blades were modeled as well as different models of electrical cables numerically and experimentally. There are some standards such as: ISO 12494 and IEC which give the aerodynamic properties of specific shapes and profiles. However specified assumptions should be considered to apply these standards which decrease the approximation precision. Actual observations of natural ice accretions on tower leg are scarce, and anyhow the modeling of combination of ice and wind effects on electrical towers cannot be passed up, especially when these effects cause serious damages on power networks.

To the best of our knowledge there is no experience done on the experimental modeling of aerodynamic characteristics of tower component which is an angle member considering different ice profiles and wind effects. Considering this new modeling approach of ice effects on aerodynamic characteristics of an angle member, it is possible to expand this model for larger models subjected to icing and provide a powerful data sheet for several practical industrial applications.

1-4-Methodology

This research is carried out mainly in two stages:

1) Wind tunnel icing simulations using natural icing parameters of icing events on a tower leg.

2) Wind tunnel aerodynamic simulations using reduced-scale laboratory experiments of cement molded ice profiles of an angle member.

1-4-1-Wind tunnel calibration

In the first step, because of some modifications on tunnel construction, tests must be done to calibrate the wind tunnel. The ice uniformity, LWC map and DSD are some parameters which should be specified exactly for different conditions and also to give avail to future experiments. The tests are conducted in two main parts;

- Air velocity and turbulence distribution in the nozzle area and test section to draw

velocity profile in x and y direction and to specify boundary condition effects.

- LWC, DSD and draw LWC map to check ice uniformity.

1-4-2-Natural Icing Event Measurements

Concerning ice accretion measurement, the glaze ice is more stable because of density and formation during the storms. So, the best way is to measure glaze accretions after freezing rain occurrences on transmission lines. The density of glaze ice is very high, about 0.9 g/m^3. As icing events are random and generally rare, and on site study impractical because of access and securities issues, a more practical way is to use pictures from ice storms. Such pictures were available from the Hydro-Québec archives with corresponding information about icing conditions. To validate this work, the following steps were undertaken:

- Find suitable pictures to distinguish the ice profile of a tower, and data like air velocity, air temperature and LWC
- Obtain wind velocity during the ice accretion and other required parameters from standard.
- Describe the types of accretion

In this study, the types of ice accretion, such as glaze ice and rime ice, are considered as being the main parameter. The LWC, temperature and air velocity during ice accretion are secondary parameters since their value will determine the resulting type of ice accretion.

1-4-3- Natural Icing Simulation

Different iced angle member simulations have been investigated and the influence of different parameters: ice shape and ice type have been considered as well. To consider these effects, the following steps were undertaken:

- Accumulate ice on the scaled physical models of the tower leg in different orientations; the models are mounted on a strut with 3 dimensional movements in order to change the orientation of samples easily.
- For the effect of wind azimuth, Bayar et al. showed the effect of wind direction by rotating the sample at constant intervals [15]. Because of the three dimensional nature of the wind, the sample should be rotated in different angles to observe the angle of attack of the wind on the model and study this effect on the aerodynamic coefficient. During the installation of the model inside the tunnel, the ratio of the frontal area of the model to the stream cross sectional area is effectively small. This ratio reflects the relative size of the model and the test section. An effect of this ratio being finite is that the surface stresses are larger than for the corresponding free-air condition. This effect is represented by considering the blockage to produce an effective change in oncoming flow speed or dynamic pressure [23].

Outdoors, the flow around towers is turbulent but it is laminar in CAIRWT because of the entrance region of flow and position of the test section [24]. So the experiments will be conducted based on laminar flow assumption. There are different techniques to create

turbulence in such tunnels but it is difficult to create turbulence in the tunnel with the same scale as in nature.

- Considering the effect of DSD and LWC, first, the variations of DSD and LWC in vertical and stream-wise directions are studied. Then, variations of ice accretion on an angle bar in the same direction as the flow will be shown to determine the aerodynamic forces on a tower leg as a function of ice accretion. The ice accretion experiments were carried out under two conditions with different LWCs and air velocities. The drag coefficient was calculated with different masses and ice shapes for the angle bar as determined by the experiments.

1-4-4-Aerodynamic measurements

In order to study the effects of the wind force on an angle member with ice profile, seven different cement molded ice profiles which were installed on the angle members were used. Detailed aerodynamic tests in the wind tunnel, over a practical range of wind speeds and angle of attacks were done. The effects of Re number, ice thickness, droplet sizes, angle member size and different ice profiles shape on aerodynamic coefficients are presented for windward and leeward orientations. Then the obtained results are compared with the results obtained from standard.

1-4-5-An introduction to the use of the Particle Image Velocimetry (PIV) method

PIV is a measurement technique with many applications. It provides accurate velocity

measurements in such flows. The physical principles behind this technique rely upon the illumination and capture of seeding particles that trace out the flow field. On the basis of Gregorio et al. [25] investigations, an ice shape is considered for measurements. The shape is derived from measurements performed in CAIRWT. The velocity measurements, which were obtained in the wake of the samples as far as possible downstream, were used in the analytical expression. The following step were undertaken:

- Measure flow field around a simple model (cylinder) and a casted model to consider the effect of ice accretion on separation point and flow field.

1-5-Thesis organization

This introduction chapter has presented the motivation for this research: the increasing need of reliable aerodynamic coefficients and measurement methods aimed at preventing transmission line towers from getting damaged following severe atmospheric icing events. So, the necessity of this study dealing with a narrow section of the problem i.e. the effects of ice in combination with a wind load on transmission line towers by experimental modeling. The objectives and the original contributions of this research along with the methodology have also been presented. The thesis is composed of seven more chapters outlined next.

The salient features of a comprehensive literature survey related to the aerodynamic problems associated with atmospheric icing of transmission lines, flow field measurements and recent numerical model developments of the aerodynamic measurements are

summarized in Chapter 2. Experimental facilities, test models and test procedures of a typical test sequence are introduced in Chapter 3. The process of casting of ice profiles and the use of cement profiles instead of ice profiles is also presented in this chapter. Ice simulation and consideration of the effects of model orientations and wind azimuth on an angle member icing are presented in Chapter 4. Considering the effects of DSD and LWC on ice accretion and drag coefficients is presented in Chapter 5. The aerodynamic models applied to measurements of reduced-scale tower leg and the effects of several variables including ice thickness, Reynolds number, ice profiles, droplet sizes and angle member profiles are discussed in Chapter 6. Chapter 7 introduces alternative flow measurement approaches and discusses the obtained results.

In addition, thematic conclusions are given at the end of each chapter if relevant, while the general conclusions and recommendations for aerodynamic model improvements and future studies are presented in Chapter 8. Key references are also provided.

Appendix A provides a summary of the main instrument of this study which is an icing wind tunnel. In Appendix B, the calibration results which were done for the icing wind tunnel after reconstruction are presented. In Appendix C, Test Conditions and Results Raw Data are presented.

CHAPTER 2

LITERATURE REVIEW

CHAPTER 2

LITERATURE REVIEW

Introduction

This chapter presents a brief overview of atmospheric icing such as types of ice accretion, accretions on transmission line towers and ice morphology. Then, it focuses on ice-related loads on transmission line towers like ice shedding, galloping, aeollian vibration and aerodynamic forces. As well, it includes a review of the recent research on the interaction between ice effects and wind load, how aerodynamic forces act, the flow field charactristics and the blockage effects. Finally, it alsoincludes a literature review about the effect of droplet size distribution and liquid water content on aerodynamic coefficients.

2-1- Atmospheric icing

Atmospheric icing is a complex phenomenon that results either from precipitation icing such as freezing rain and wet snow accretion or from in-cloud icing [26]. The occurrence, severity, and type of atmospheric icing depend largely on temperature, wind speed, LWC, and water droplet size. It may take place at ambient air temperatures between -10°C and 0°C, or sometimes, at lower temperatures under particular conditions.

In-cloud icing occurs when suspended, supercooled droplets freeze immediately upon impact on an object exposed to the airflow. The occurrence and severity of this type of atmospheric icing strongly depend on the location of the exposed object and on the topography of the surroundings.

Precipitation icing can take the form of freezing precipitation and frozen precipitation. Freezing precipitation occurs when any form of precipitation (freezing rain, freezing drizzle, or freezing fog) freezes upon impact on or contact with an exposed object. Frozen precipitation is any form of precipitation that reaches the ground in frozen form such as snow, snow pellets, snow grains, ice crystals, ice pellets, and hail [26].

2-1-1- Types of ice accretion

Icing events on structures are phenomena relevant to the weather. Many meteorological parameters are significant in relation to icing build up. Essentially five types of ice accretion may deposit on structures, as defined in Table 2-1, that are basically

classified by their density as glaze, rime (soft and hard), wet snow, dry snow, and hoar frost [27].

Table 2-1 Types and characteristics of ice accretion (adapted from [27], [28], [29])

Type	Description	Density (kg/m^3)
Glaze	Hard, almost bubble-free, clear homogenous ice with a density close to that of pure ice. Very strong adhesion	700-900
Hard rime	Rather hard, white or translucent homogenous ice with inclusions of air bubbles. Strong adhesion.	300-700
Soft rime	White or opaque ice with a loosely bonded structure ("feather-like" or "cauliflower-like"). Can be removed by hand	150-300
Wet snow	Opaque ice with a crystal size much smaller than that of glaze ice. When the temperature is close to zero it may have high LWC and slip off easily. If the temperature drops after the accretion, it may have very strong adhesion	100-850
Dry snow	Very light pack of regular snow. Very easy to remove	50-100
Hoar frost	Crystal structure (needle-like, scale-like). Low adhesion	< 100

Glaze ice forms when water is collected from the impingement of supercooled water droplets on exposed objects [30]. In other words, it forms on exposed objects by the freezing of a film of supercooled water (i.e. water still in the liquid phase but at sub-zero temperatures) which is deposited by rain, drizzle, or fog. A large droplet size, slight super cooling, and slow dissipation of heat of fusion favor the formation of glaze which is the most probable at temperatures between 0°C and -3°C [28]. It produces the densest form of

atmospheric icing and on overhead power lines in particular, very large ice loads are reached within hours [29].

Sometimes during glaze ice accretion, unfrozen surface liquid that does not freeze at some location must be shed, either as a result of gravity or wind stress. When there is a source of water at the root (top) of the icicle, a liquid film forms on the icicle surface and flows towards the tip due to gravity or wind drag. Water spreads effectively on an icicle surface, so that a liquid water film tends to cover the entire icicle surface unless the flux of water is extremely small of the order of 0.01 m^3/s or less. Icicles are formed also during freezing precipitation, because air temperatures are typically near freezing temperature [3].

Rime ice forms when the freezing of small, supercooled water droplets reach on the surface of the exposed object at air temperatures typically below -5°C. The small droplet size, slow accretion, high degree of super cooling, and rapid dissipation of heat of fusion favor the formation of rime [29]. Rime density varies depending on the size of droplets and the freezing time (Figure 2-1). When the droplets possess small momentum and freeze quasi-instantly on impact, air pockets are created between the frozen droplets and a soft rime deposit is produced. When the droplets possess greater momentum, or the freezing time is greater, the frozen droplets pack closer together in a dense structure and create a hard rime deposit [26]. Rime ice can also form from glaze ice but in small amount when there is ice feather shape appear on surface [6-7].

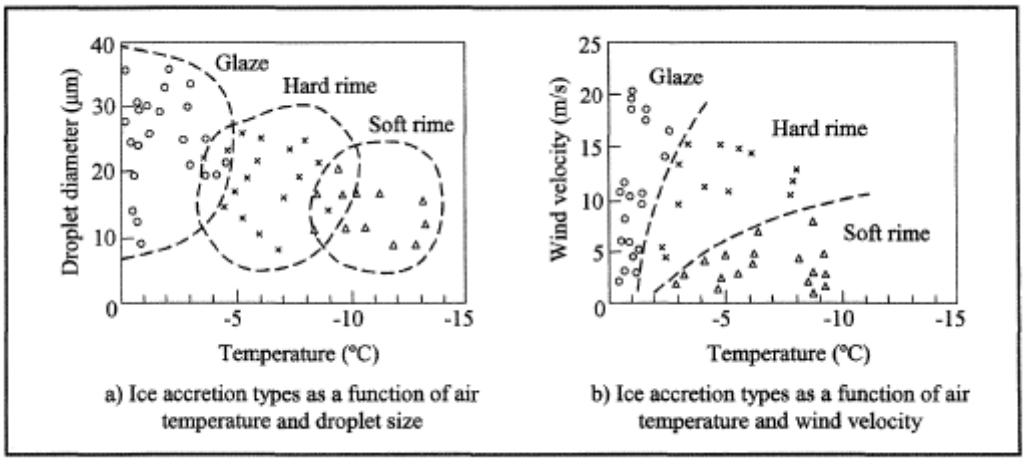

Figure 2-1: Ice accretion types (adapted from [31])

Wet snow flakes commonly occur as ice crystals suspended in a LWC matrix at temperatures just above the freezing point (0.5-2°C) and is a mixture of ice, LWC and air [32], [33]. The very wet snow is defined when free water entirely fills the air space in the snow. Snow flakes are more likely capable of causing wet snow accretion at LWC between 15 and 40% in mass (i.e. percentage of the mass of LWC per the total mass of wet snow) [28], [32]. The density range of wet snow deposits depends on the wind force that compresses the snow on the surface of accretion. It may have strong adhesion with the exposed objects, and like glaze ice, it can lead to very high loads within hours on overhead conductors.

Dry snow flakes may also accumulate on objects to form a dry snow accretion at temperatures significantly below freezing point under very low wind speed conditions [28].

Hoar frost forms when the vapor in the air with a dew-point below freezing

condensates [29]. It causes very thin and porous layers of ice usually on the windward side of objects and is therefore not critical when the ice is regarded as a gravity load as these deposits have low density. However, large hoar frost deposits on overhead conductors may result in significant wind loads.

2-1-2- Accretions on transmission line towers

As discussed in the previous section, ice can deposit on transmission line towers and conductors in different forms and densities. The types of atmospheric ice accretions that are significant for our purpose are, rime, large deposits of lightweight rime ice, and dense glaze ice. In this section, examples of these types of atmospheric ice accretions on transmission line towers are illustrated. Figure 2-2 presents examples of glaze and rime accumulations on electrical towers, respectively.

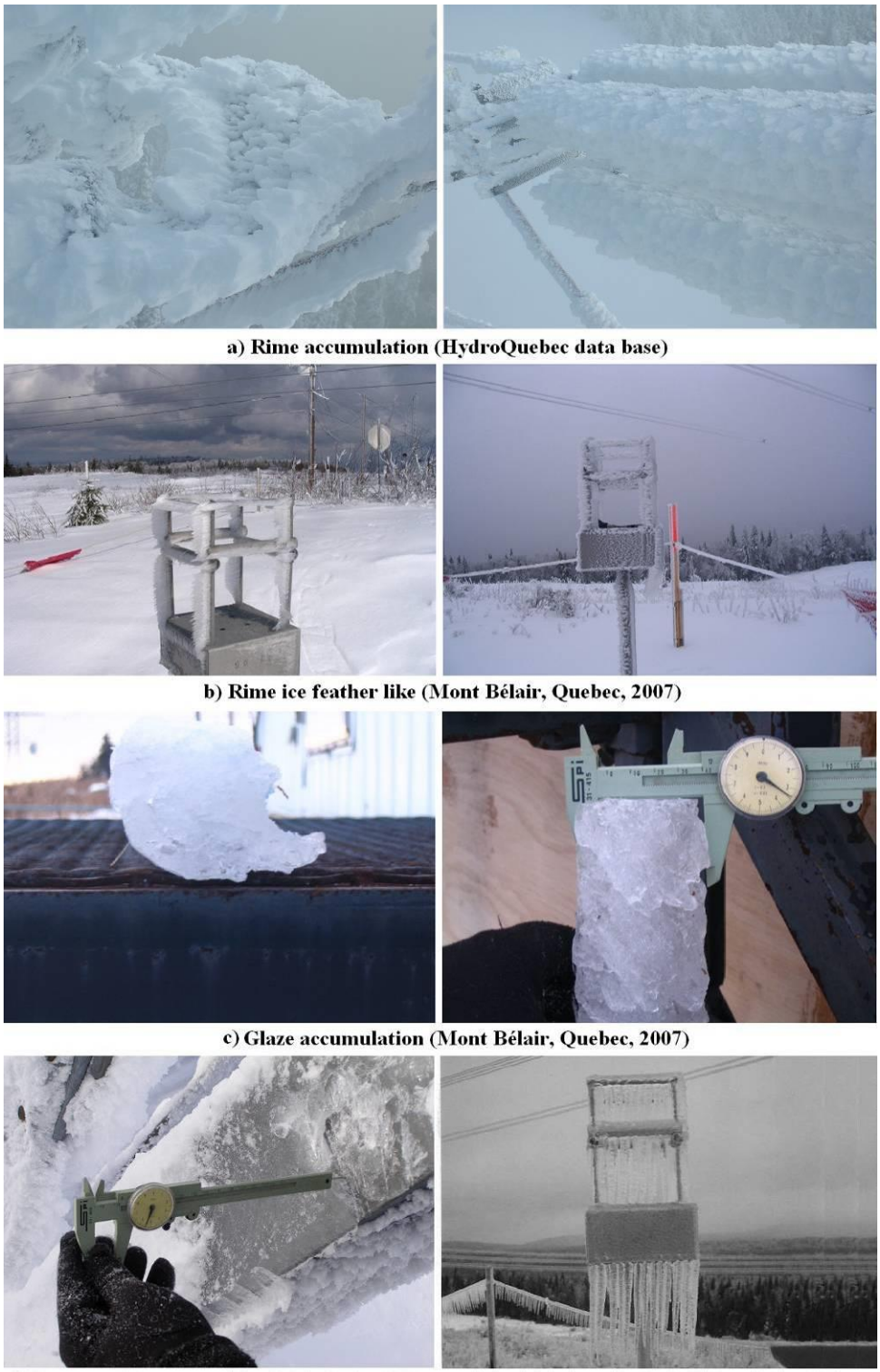

Figure 2-2: Atmospheric ice accretions on transmission line towers

2-1-3- Ice morphology

It is important to take the type of ice into consideration because under specific conditions, different ice shapes may appear depending on icing object geometry parameters and aero-thermal conditions. Close-up photographic data were taken on an aluminum NACA 0012 swept wing tip airfoil [6], [34]. Two types of photographic data were obtained: time sequence close-up photographic data during the run and close-up photographic data of the ice accretion at the end of each run. Icing runs were conducted for short ice accretion times from 10 to 180 s. The movies confirmed that at glaze icing conditions in the attachment line area icing feathers develop from roughness elements. The close-up photographic data at the end of each run showed that roughness elements change into a pointed shape with an upstream facet and join on the side with other elements having the same change to form ridges with pointed shape.

The ice accretion formation on swept wing tip in natural icing conditions showed that at 45° and 30° sweep angles the ice accretions were complete scallops made of feathers with a preferred direction of growth [7], [35]. The presence of large feathers or the top of large feathers along the attachment line area agrees with tunnel observations at similar low LWC icing conditions [36]. Vargas et al. [7] observed the same ice elements of formation that have been obtained in tunnel experiments. They observed that the presence of the attachment line and glaze ice feathers zone have brought different classifications of ice accretions as no-scallop, incomplete scallop or complete scallop [7].

Several tests have been performed using a bare cylinder for several sweep angles, velocity, temperature, MVD and LWC to simulate 3D scallop ice by Presteau et al. [8]. Firstly, a reference model was developed for 3D scallop ice simulation. Then, a full 3D numerical scallop ice formation was built which consists of injecting supercooled droplets through a 2D window. A classical way to provide all physical parameters for the model is to use a 3D Navier-Stokes. Ice shape simulated with this new microphysical model is finally compared to the experimental ice shape database. It showed that a 3D numerical model results for scallop ice shape were in good agreement with experimental test for a plain cylinder.

Ice growth often occurs in cold environments coincident with the entrapment of a portion of the impinging liquid by the growing ice matrix. This type of ice accretion is said to be spongy. Dendritic ice crystal growth into supercooled liquid at the icing surface entraps a portion of the liquid into the advancing ice matrix [9].

Maeno shows that the length of an icicle increases by the downward growth of thin dendritic crystals into the supercooled water droplets when water dropped at the tip. The diameter increased also by the freezing of a water film flowing down along the icicle wall [10]. Makkonen proposed a model of icicle growth. It was demonstrated that the growth of an icicle is a complicated process and very sensitive to the atmospheric conditions and water flux. The shape and weight of icicles predicted by the model agree well with laboratory data [11].

2-2- Ice-related loads on transmission line towers

Ice accretions on transmission line structures can be the source of several mechanical and electrical problems. In this study, only the ice-related mechanical problems are emphasized. The gravity loads due to heavy ice accretion on overhead lines, coupled with wind on ice loads, may lead to structural damages, or failure and even cascading collapse of towers. Ice shedding from cables, wind-induced cable motions such as galloping associated with aerodynamically unstable ice profiles and severe Aeolian vibrations of ice-covered cables as well as interaction between ice profiles and wind load on transmission line towers are among the most severe loads acting on transmission lines structures.

2-2-1- Ice shedding

Ice shedding is the physical phenomenon which is classified as a type of ice mass reduction. The ice mass reduction can be caused by three physical mechanisms: ice melting, ice sublimation and mechanical ice breaking. Ice shedding, or the sudden dropping off of atmospheric ice, is created by mechanical breaking or its combination with the two other mechanisms. In other words, it is responsible for large imbalance forces and moments on supports, impact forces, overloads, vibrations, and in the case of electrical conductors, short-circuits causing flashover [37] when electrical clearances become insufficient. In extreme situations, the increased cable tensions may result in broken insulator assemblies, or short circuits may cause cable breakages that may in turn lead to longitudinal cascading failure of the line [38], [39].

Damage can occur to structural elements (antennas, etc.) when ice from higher parts fall and hit lower elements in the structure. The height of falling ice is an important factor when evaluating risks of damage, because a greater height means greater dynamic forces from the ice. A method of avoiding or reducing damage from falling ice is the use of shielding structures [40].

2-2-2- Galloping

Galloping of ice-coated conductors is a low frequency, high amplitude, wind induced vibration associated with the effect of atmospheric ice deposits on the conductors. This phenomenon occurs when the aerodynamic lift on the conductor can be modulated by the periodic motion of the conductor in such a way that the variations in lift act to augment or at least sustain that periodic motion. Ice galloping on overhead lines is associated with aerodynamically unstable ice profiles [41], [42]. In addition, the change in cross-sectional shape due to the accreted ice causes dynamic effects.

2-2-3- Aeolian vibration

Severe Aeolian vibrations of the enlarged-diameter, ice-covered conductor may also lead to fatigue failures of conductor strands at suspension clamps and serious damages on electrical structures. In opposition to galloping, Aeolian vibration is defined as high frequency and low amplitude wind-induced vibration of both single and bundled conductors. The primary cause of this type of conductor vibration is the alternate shedding of wind-induced vortices from the top and bottom sides of the conductor that creates an

alternating pressure unbalance which causes the conductor to move up and down at right angle to the direction of air flow [43]. Aeolian vibrations usually occur when a steady, low-velocity crosswind (below 7 m/s) acts upon a bare or uniformly iced conductor surface.

Since the power imparted by the wind to the conductor is proportional to the conductor diameter at the fourth power [34], ice accretion may lead to a dramatic increase of aeolian vibration severity.

Also, fully iced mast or tower sections can introduce vortex shedding, resulting in cross wind vibrations.

2-2-4- Aerodynamic forces

The interaction between ice effects and wind load around a physical structure can cause beneficial or destructive effects on the physical structure itself. The geometry of the physical iced structure and the characteristics of the oncoming flow help determine the nature of the flow field. It has not yet been shown conclusively which circumstances might lead to dramatic variations in different flow field characteristics such as aerodynamic coefficients [44], [45], vortex street structure, geometric wake parameters [46], [47], Reynolds number (Re) and Strouhal number (St).

2-3- Interaction between ice effects and wind load

The bodies are classified as aerodynamic and bluff bodies with respect to the features of the flow field that they produce when they are immersed in a cross-stream or through

fluid Figure 2-3. Aerodynamic bodies are characterized by boundary layers completely attached over their whole surface, which leave behind them thin and generally steady wakes containing vortices [48]. The aerodynamic forces acting on these bodies may be evaluated through the simplified potential flow – boundary layer procedure [20], [49], [50].

Conversely, bluff bodies are characterized by a separation of boundary layer from its surface, and wakes having significant lateral dimensions and normally unsteady velocity fields [48]. For these bodies no simplified mathematical treatment is usually possible, and the forces acting on them may be evaluated either from the solution of the complete Navier-Stokes equations [17], [18], [51] or from the results of experiments [15], [16], [46], [52], [53]. It is well known that structures such as electrical towers are bluff bodies.

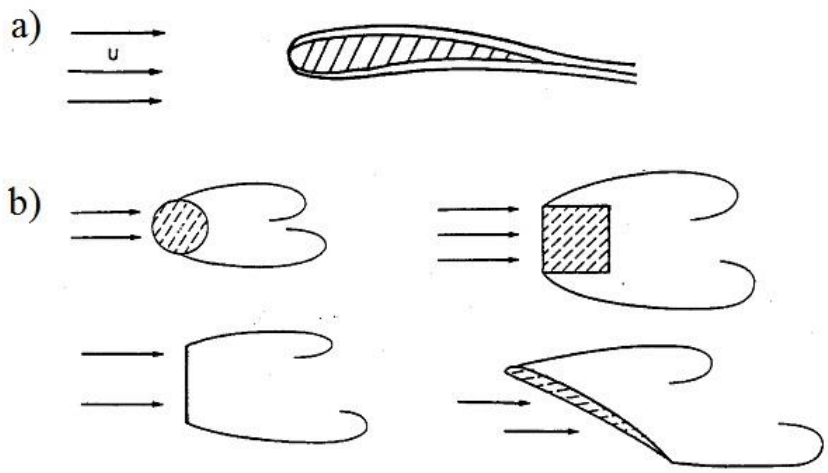

Figure 2-3: Examples of a) aerodynamic body and b) bluff bodies

2-3-1- Aerodynamic forces

The most important force components are drag and lift. The component of the aerodynamic force in the upstream flow direction (or in the direction of motion of the body if it is moving in still fluid) is drag and the component of the aerodynamic force in the direction perpendicular to flow direction is lift. One striking difference between aerodynamic and bluff bodies is that the former have drag coefficients that are at least one order of magnitude smaller than the latter. This is due to the remarkable increase in pressure drag deriving from the boundary layer separation.

There is a vast experimental research on icing effects on aerodynamic body such as aircraft airfoils [14], [21], [22], [54], [55] and turbine blades [13] as well as numerical investigations [20], [50] which is out of scope of this research. However there is less investigations on icing effects on bluff body.

The simplest part of electrical line towers is an angle member. Prud'homme et al. [16] studied the aerodynamic forces on single and shielded angle members in lattice structures. They measured drag coefficients between 2 and 2.4 for different angle member profiles without shielding effect. They indicated that there is no significant effect with regards to the Reynolds number, the edges' shape and the thickness ratio on drag and lift coefficient. It was shown that the turbulence generally reduces slightly the drag coefficient.

The force coefficients are different for truss elements compared to simple element because of the shielding effects. Bayar et al. [15] determined appropriate drag coefficients

for square self-supported latticed towers. They constructed and tested two models. The critical maximum drag coefficients corresponding to their solidity ratios, Φ, are plotted on Figure 2-4 for the towers with heel angle attached to the leg member and without them. The actual relationships between drag coefficients and solidity ratios are also plotted.

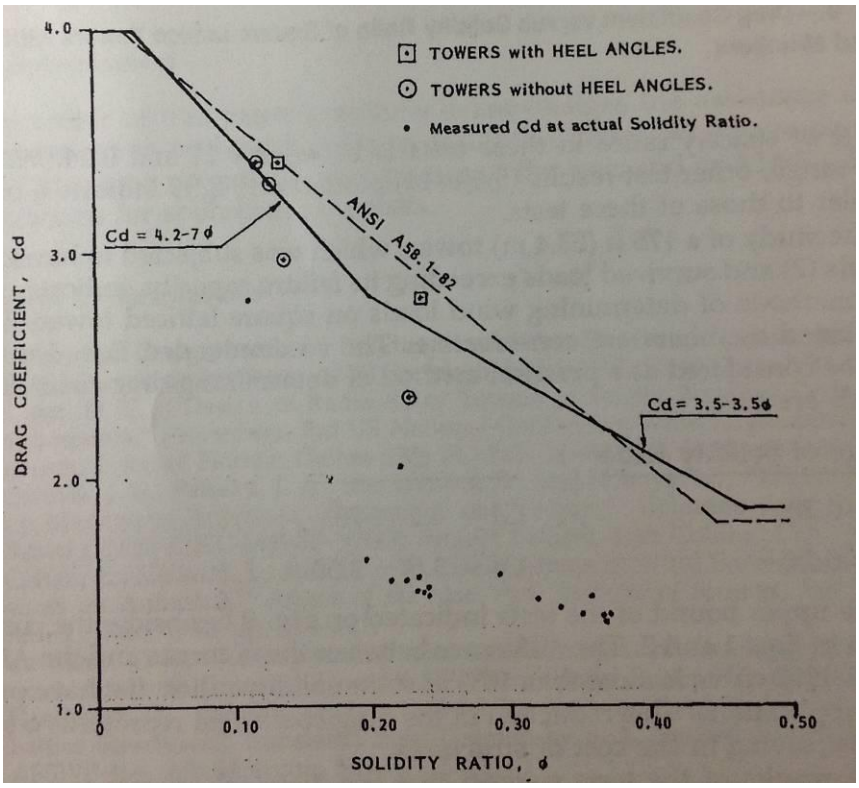

Figure 2-4: Drag coefficient versus solidity ratio of tested tower models

They recommended equations (1) and (2) (in Table 2-2) as a practical method of determining drag coefficients:

Table 2-2: Recommended equations for calculating drag coefficient

Range of Solidity Ratio (Φ)	C_d	
0.11-0.20	$C_d=4.2-7.0\times\Phi$	(1)
0.20-0.24	$C_d=3.5-3.5\times\Phi$	(2)

Likewise the results of Prud'homme et al. [16] for simple angle member have also shown that the tower sections drag were independent of the Reynolds number.

Some structures consist of circular cross section members which are bluff bodies. Basu [52] obtained the aerodynamic forces of circular cross section structures. He studied the roughness effect on the magnitude of the coefficients in low-turbulence flows as well as the influence of turbulence and three-dimensional effects. Basu [52] obtained C_D =1.17 for sub-critical regime around circular cylinder for different relative roughness which confirms that C_D is reasonably independent of Re in sub-critical regime above about 10^4 [56], [57]. He showed that for super-critical and post-critical flow regimes C_D has an exponential function when relative roughness increased.

The lattice structures together with tensioned steel conductors are sensitive to various wind drag and lift caused by icing. Wind action on iced structures may be calculated based on the same principles as the action on an ice-free structure. However, the dimensions of the structural members and their drag coefficients are both subject to changes.

Nigol and Buchan [45] generated natural ice shapes over a range of practical conductor galloping situations in order to test these shapes under static and dynamic

conditions in the wind tunnel. They presented the lift and drag coefficients for ice on windward and leeward sides of the conductor. It was shown that it is not possible to generalize the lift characteristics in terms of ice shape. Ice deposits of similar shape produce completely different lift curves as minor variations in surface texture seem to have large effects.

Examination of the drag coefficients show that they are relatively constant with respect to the angle of attack as expected for samples having a relatively constant projected area. A notable feature is that the drag data shows a consistent shift to lower values with increasing turbulence. While examination of the moment coefficients shows that the moment normally changes its sign for windward and leeward orientations of ice.

2-3-2- Flow field measurements

The flow field around bluff bodies is completely different compare to aerodynamic bodies, because separation prevents the occurrence of the recompression in the rear part of the body [48], so that the values of the pressure in this region are considerably smaller than those acting in the front part (and corresponds normally to negative pressure coefficients). This gives rise to a significant value of the pressure drag, which is normally much higher than the friction drag [48].

The pressure drag may be divided in two contributions, respectively given by the fore-body, i.e. the front part of the body with attached boundary layer, and by the so called after-body or base region, i.e. the portion of the body surface lying inside the separated

wake. Depending on the shape of the fore-body, the first contribution may be large or small, as can be seen by comparing the qualitative pressure distributions around a flat plate and a circular cylinder (see Figure 2-5). The second contribution, on the other hand, is determined by the value of the suctions (pressures act always towards the body surface, but the term suction is often used when the difference is negative) acting on the base, which are primarily connected with the velocity outside the boundary layer at the separation point, V_s. Indeed, particularly in the case of after-bodies with limited longitudinal extent, the pressures on the base are almost constant and equal to the pressure in the outer flow at the separation point [48].

In terms of pressure coefficient, by using Bernoulli's equation, the higher is the velocity outside the boundary layer at the separation points; the lower is the base pressure, and the higher the base drag.

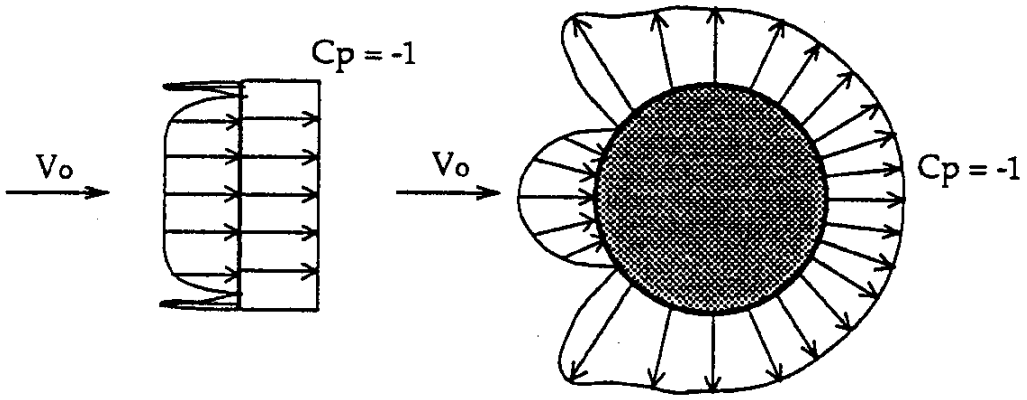

Figure 2-5: Comparison between the pressure distributions of a flat plate (C_D = 2) and of a circular cylinder for $Re < 10^5$ (C_D = 1.2) [48]

Particularly important is the dependence of the drag coefficient of a bluff body on the Reynolds number [15], [16], [52]. As can be seen from Figure 2-6, while for bodies with sharp corners this dependence is negligible, it becomes more and more significant with the rounding of the body, with the appearance of a sudden decrease of the drag coefficient [48]. This behavior is connected with the phenomenon of transition of the boundary layer to the turbulent state. Therefore, for bluff bodies without sharp corners, a critical value of the Reynolds number exists which corresponds to transition taking place before the laminar separation, so that the separation points move downstream, a narrower wake forms, a higher pressure recompression before separation takes place, and a consequent significant decrease of the drag coefficient is observed. Obviously, all parameters that may influence the boundary layer transition (as the incoming turbulence level [15], [58], [59] and the surface roughness of the body [44] have a significant influence on the C_D-Re curve, and produce a variation of the critical Reynolds number.

Yeung [46] has made an attempt to formulate a relationship involving Strouhal number, pressure drag, and separation pressure for flow around a two-dimensional bluff section of various shapes in a confined environment such as a wind tunnel. He obtained the relation between Strouhal number ,Sc_d, and separation-pressure parameter, k, which is applicable to a variety of two dimensional sections. For the flat-plate and the wedge modified Strouhal number was around 0.15. However, this value for a rectangular prism increases from 0.092 to 0.138 and it is as high as 0.185 for a circular cylinder at sub-critical Reynolds numbers. The variations indicate that the size and shape of the aft body may significantly influence the vortex formation region. Therefore, the similarity in the wake

structure of different bluff-bodies, as originally proposed by Roshko [60] may require careful consideration.

It was shown that the different values in drag of different bodies may be related to differences in the energy content in their wakes [61], [62]. This type of reasoning, although obvious to a certain extent, is actually extremely fruitful not only to justify different values of drag, but also to give a rationale for any design action aimed at obtaining a drag reduction of a body.

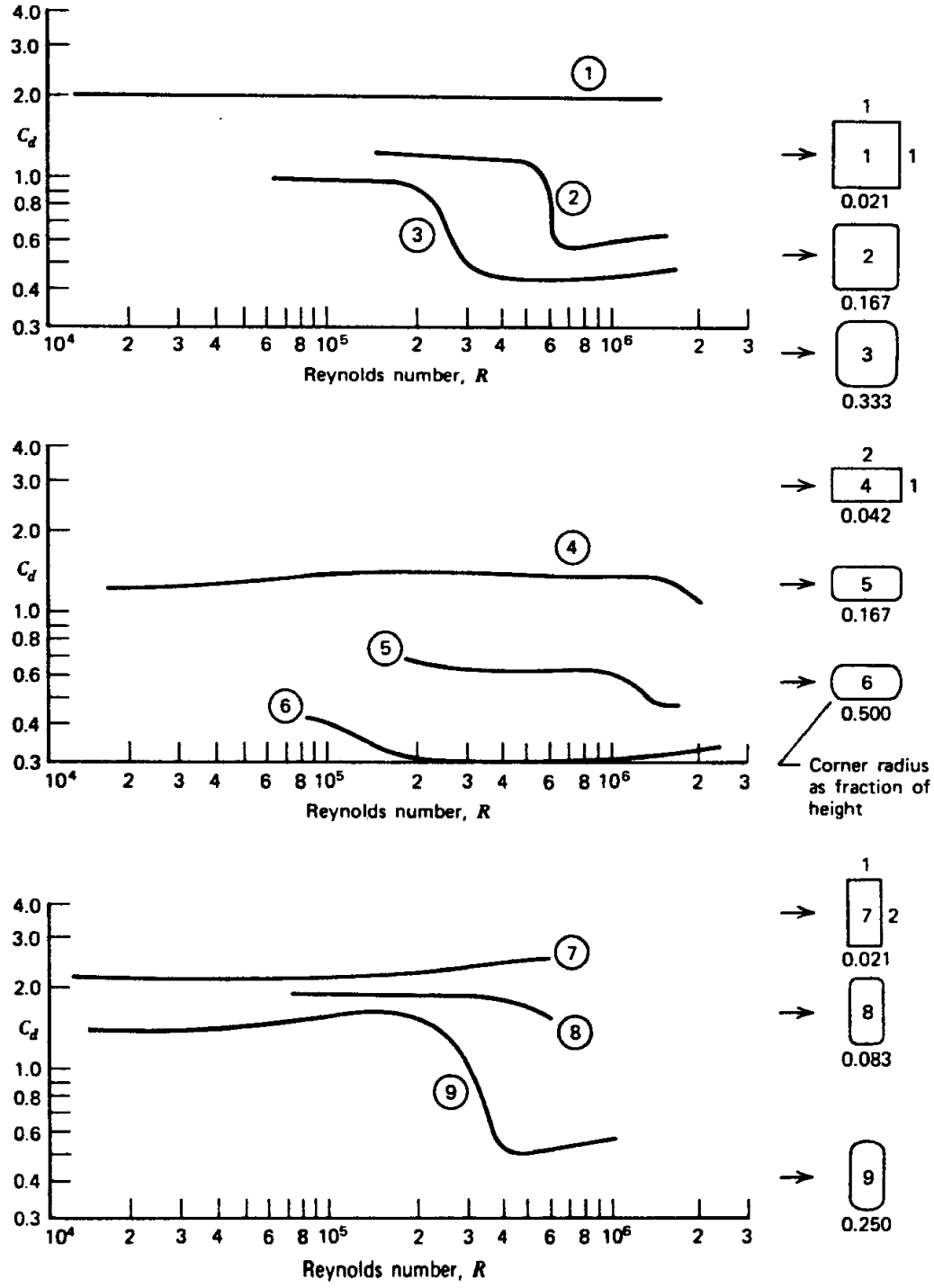

Figure 2-6: Drag coefficients of various cylindrical shapes as a function of Re [48]

It has already been mentioned that value of the drag coefficient of an aerodynamic body is 15 to 20 times smaller than for a bluff body. It may be explained by extremely thin wake produced by aerodynamic bodies which causes to rise to very small perturbation energy [61], [62]. The opposite is true for typical two-dimensional bluff bodies which shows a highly-energetic wake, characterized by the presence of a double row of alternate concentrated vortices (known as Karman vortex street) [63]. A detailed review on the phenomenon of vortex shedding, on the consequent induced forces, and on the effects of the variation of geometry and of various fluid dynamic parameters may be found in [64]. The main point that will be made here is that a strict connection exists between the amount of perturbation energy and the organization of the vortices present in the wake. Indeed, the drag of a bluff body is an increasing function of the degree of concentration in space of the vortices shed in its wake, and of the distance between the regions where the positive and negative vortices are contained. Further details on drag reduction may be found in [48].

Flow fields and wake regions of lattice structures are sensitive to icing. Wind action on iced structures may be simulated based on some simple models [44], [45] or some numerical models. However, experimental simulations of bluff body icing are a way to have better understanding of the phenomena. Zdero and Turan [44] investigated the influence of ice accumulation on the flow field around electrical power cables of various geometries to examine the effect of these factors on the near wake flow field.

They showed that heavy ice formation produces across-sectional geometry that is more ‘‘wing shaped’’ than the lightly iced model at the same angle of attack. The results

revealed that heavily iced models versus lightly iced model may be more likely to experience relative increases in vortex shedding frequency and Strouhal number when Re >15,000 for certain angles of attack. They showed that, rises in Strouhal number and the accompanying drop in drag [65] and rise in lift [66] force may make heavily iced models more susceptible to the onset of movement normal to the free stream. It was also shown that multiple vortex shedding frequencies can compete for dominance when heavy ice accumulation occurs.

The numerical simulations have a difficulty in validating their prediction results such as flow separation angle, recirculation length, and turbulence statistics; this implies that there are strong demands for reliable experimental data. Particle imaging velocimetry (PIV) is one of the experimental techniques available to measure flow velocity and flow direction at one instant in time within a large area of the flow field. The physical principles behind this technique rely upon the illumination and capture of seeding particles that follow the streamlines of the flow. For that purpose, PIV utilizes the light scattered by small particles in the flow, which are illuminated by two short laser pulses. The first explicit recognition of the importance of particle images was made in two short, contemporaneous papers by Pickering and Halliwell [67] and Adrian [68]. They called it Particle Image Velocimetry (PIV) to distinguish this method from other laser techniques. One of the primary uses of PIV technique is flow field visualisation around aerodynamic and bluff bodies. Additionally, 2-D PIV provides accurate velocity measurements in such flows.

There is a vast of investigations on flow characteristics around bluff bodies, especially circular cylinders. Ouali et al. [69] investigated interaction between the near wake and the cross – sectional variation for a circular cylinder in uniform flow. A camshaft and a set of cams were used to effect cylinder's diameter change. The ratio of rotating motion and the free stream velocity defines a forcing Strouhal number where when the Reynolds number was set on 80000, the forcing Strouhal number was 0.02. They calculated St number for different conditions. They obtained vortices distribution and then used it to calculate drag by applying the following equation which was presented by Shiels and Leonard [70]:

$$Drag = -\rho \frac{d}{dt}\left(\iint_A ywdA \right) \tag{2-1}$$

where the area A represents the entire flow field, w is the vortex structures which are shed from the body contain significant components of both signs of vorticity, ρ is the air density and y is distance between center and surface of the cylinder.

They showed that drag is correspondingly decreased due to positive vortices diffusions from the cylinder's surface into the negative vortices of the shear layer (vortices move from high energy level to low energy level). The result confirms the one obtained by Lin et al. [71] for different ranges of Reynolds number between 1000< Re <10000. They showed that also Large-scale Karman vortex formation in conjunction with patterns of small-scale Kelvin-Helmholtz vertical structures; allow physical interpretation of the vortex formation length.

Jang and Lee [58] did the same study for a sphere at a sub-critical Reynolds number. They obtained the velocity fields, detailed vertical structure in the recirculation region such as recirculation vortices, reversed velocity zone and out-of-plane vortices distribution for Reynolds number equals to 11000. They measured many instantaneous velocity fields of recirculation region where ensemble averaged to get the mean velocity fields. The vortices were calculated using the following equation:

$$w_x = \left(\partial V_z / \partial y - \partial V_y / \partial Z \right) \tag{2-2}$$

where V_Z and V_y are velocity distributions in y and z directions.

They showed that the vortical structure of sphere near-wake had a wavy flow structure and the onset of shear-layer instability.

Fujisawa et al. [72] applied a PIV technique to evaluate the pressure field and the fluid forces on a circular cylinder with and without rotational oscillation. They used instantaneous velocity data measured by this technique to solve pressure Poisson equation numerically. They applied this technique to obtain the drag force on a circular cylinder for Reynolds number 2000. They found that the drag force on a circular cylinder is magnified at low-frequency oscillation and reduced at high-frequency oscillation. They also showed that the drag coefficient at high-frequency oscillation is reduced by 30% with respect to the stationary cylinder, while the fluctuating lift is slightly increased due to the generation of synchronized vortex shedding at high-frequency oscillation.

The PIV technique will be more applicable when the model geometry is more complicated and categorized in bluff body geometry. Lim and Lee [62] experimentally studied the flow structure around a circular cylinder with U-grooved surfaces. They measured the drag force and turbulence statistics of wake (mean velocity, turbulence intensity and Reynolds shear stress) behind each cylinder for Reynolds numbers based on the cylinder diameter (D = 60 mm) in the range $Re_D = 8\times 10^3$-1.4×10^5. They concluded that for the case of smooth cylinder, large-scale vortices formed behind the cylinder maintain round shape and do not spread out noticeably in the near wake. However, for the case of U-grooved cylinder, the vortices are largely distorted and spread out significantly as they go downstream. They showed that the longitudinal grooves seem to shift the location of spanwise vortices toward the cylinder, reducing the vortex formation region, compared with the smooth cylinder. The longitudinal grooves have been used as an effective flow control device for drag reduction and heat transfer enhancement [73].

There is the possibility to consider a shape of ice profile on different geometries for flow characteristics measurements and consequently aerodynamic calculations. De Georgio et al. [74] did an investigation on airfoil with ice accretions to study the performance degradation. The considered model was a NACA 0012 airfoil section with 100 mm-chord and 300 mm length span. They considered four different configurations of the airfoil model; bare airfoil, profile with glaze, rime and mixed ice accretions. The Reynolds number was 200000 based on chord dimension. The instantaneous and mean velocity fields, longitudinal turbulence level were measured and then aerodynamic coefficients were calculated. The results showed remarkable aerodynamic characteristics decay due to the

simulated ice formation: glaze configuration showed worst performances with inversion of the lift-incidence curve and a dramatic increase of the drag coefficient. PIV measurements showed large regions of separated flow even at low incidence and for moderate amount of ice (mixed shape): in fact, due to the low chord Reynolds number, no flow reattachment occurs downstream the separation.

It was tried to carry out an experimental study to investigate the effect of ice accretion on the flow characteristics of a circular cylinder. They studied the variations of flow characteristics such as velocity field and turbulence intensity for two different ice profiles; bare profile, and profile with ice accretion shapes. The velocity field and turbulence statistics of the wake behind each cylinder were measured for Reynolds numbers based on a 38-mm cylinder diameter in the range of 2×10^5 -1.2×10^6. The experimental results showed large regions of separated flow even at low incidence and for moderate amounts of ice. They showed that the calculated shedding frequency was 48.68 Hz based on using Strouhal relationship [43] which agrees well with the observed period of vortex shedding of about 0.02 s.

2-3-3- Blockage effects

It is quite important to estimate the wind tunnel blockage effect on the test data, and correct them properly. Maskell first examined the blockage effect on drag coefficient of flat plate normal to wind, and proposed a correction method introducing the model of bluff-body wake [75]. His theory is based on the correction of the dynamic pressure increment

around the model. The theory is well supported by experiment and leads to the correction formula:

$$\Delta q/q = cC_D S/C \qquad (2\text{-}3)$$

Where Δq is the effective increase in dynamic pressure due to constraint, and c is a blockage factor dependent on the magnitude of the base-pressure coefficient. The factor c is shown to range between values a little greater than 2.5 for axisymmetric flow to a little less than unity for two-dimensional flow. But the variation from 2.5 is found to be small for aspect ratios in the range of 1 to 10.

Cowdrey [76] and Sykes [77] examined the applicability of Maskell's theory to rectangular sections. They found a slight difference in the blockage factor that they obtained. The relation between blockage factor and depth to height ratio was made by Awbi [78]. Utsunomiya et al. [79] and Noda et al. [80] applied Maskell's and Awbi's methods to correct drag coefficient of their models. They studied the blockage effects on aerostatic forces such as base pressure coefficient and drag force coefficient for the cube, the rectangular cylinder, and two rectangular parallel cylinders. Takeda and Kato [81] applied Maskell's theory to different types of truss girder (porous body) and hexagonal sections which are frequently used as a bridge girder. They used an expression of blockage factor through the new definition of drag coefficient by model outlined area.

As already mentioned all the empirical techniques and semi-empirical methods are used to adjust the pressure and drag coefficients for blockage effects. The difficulty with

the empirical methods is their lack of “universality” that originates from a set of data obtained in given wind tunnel and usually with one level of turbulence. The semi-empirical correction methods are often developed on similitude hypotheses or invariance that restricts their domain of validity. Laneville and Trepanier [82] tried to correlate the available experimental results and to formulate a general empirical correction technique that can adjust most available data by taking into account the effect of the free stream turbulence intensity. Their formulation takes into account the effects of the solid blockage (The ratio of the frontal area of an article to the stream cross-sectional area. In wind tunnel tests, this ratio reflects the relative size of the test article and the test section), S/C, the aspect ratio (The length of an article to its depth), L/D, the after-body length (The height of an article to its depth), H/D, and the intensity of turbulence; I. the validity of their procedure is restricted to solid blockage less than 15%. Application of empirical methods [78] gave a good correlation for different sets of data for smooth flow.

2-4- The effect of DSD and LWC on aerodynamic coefficients

Meteorological parameters such as LWC and DSD are decisive factors in determining the various types of atmospheric ice accretion and consequently their aerodynamic coefficients. One of the important differences between natural aerosol clouds and its experimental models is their dimensions in relation to a size of the icing structures that are exposed to those clouds. The dimensions of the supercooled aerosol clouds are greater in all directions under natural icing conditions [55], [83], [84] whereas the same order of magnitude is observed for the same factors when simulating ice accretion in wind tunnel.

Therefore, knowing the zone of the uniformity of the artificial aerosol clouds is essential in order to predict the local LWC and DSD. Although the dimensions of zone of uniformity of natural aerosol clouds are not achievable in experimental modeling, it is possible to obtain LWC and DSD having approximately the same level as what is found in natural aerosol clouds. Different combinations of these characteristics produce different types of natural icing phenomena. The LWC is in the range of a few tenth of g/m^3 under in-cloud icing conditions; however, values between 1 and 10 g/m^3 were also observed under other ambient conditions such as freezing drizzle or freezing rain [83], [84], [85], [86], [87]. The DSD falls in the range of a few μm to about 50 μm under in-cloud icing conditions, whereas it takes significantly greater values under freezing drizzle (in the range of 100 μm) and freezing rain (from the range of 100 μm to several mm) conditions [84], [85], [87].

The LWC and DSD vary inside the aerosol cloud. These variations are more significant when the air velocity is low and when the cloud droplets are large. The main reason of these variations is related to gravity and inertia forces acting on supercooled droplets. These forces alter the trajectories of particles that contribute to the ice accretion [88], [89]. Thus, they have an influence on the ice mass and ice shape, resulting in varying aerodynamic coefficients on the tower.

The effects of LWC and DSD on the aerodynamics of a body have been studied for decades. Large-droplet ice accretion on aircraft wings is important to aircraft industry since its effects are crucial on aerodynamics. Bragg [90] studied these effects on drag coefficient, lift coefficient and pitching moment that vary during aircraft control. The results showed

that a ridge of ice aft of the boot can lead to large losses in lift, increase in drag and changes in the pitching moments. He continued this study with Lee [22] to simulate the effects of large-droplet ice shapes on airfoil aerodynamics experimentally. They investigated the influence of simulated supercooled large-droplet ice accretion on a modified NACA 23012 airfoil. They realized that when the simulated ice was placed at critical chordwise locations, separation bubbles formed downstream of the simulated ice shape, and there was a dramatic reduction in the maximum lift coefficient which was then as low as 0.27.

Vargas et al. [7] and Vargas [35] studied and simulated different formations of ice accretions on swept wings in natural icing conditions for different LWCs.

Conclusion

A complete review on the interaction between ice effects and wind load was presented. Literature review of new research on aerodynamic measurement of bluff body was also presented. The definition of aerodynamic and bluff body, flow field characteristics and their measurement techniques were summarized. From this review, the following can be concluded:

Glaze ice because of the density and ice mass has a significant effect on aerodynamic coefficient of electrical towers

Calculating aerodynamic coefficient of bluff body shape without having experimental work is very difficult and sometimes it is impossible.

The input parameters for icing simulation was considered based on information provided by Hydro Quebec from previous ice storms.

It was observed that using external balance is essential to measure aerodynamic coefficient experimentally.

The input parameters for aerodynamic measurements were considered based on available data from Hydro Quebec to cover all possibilities.

CHAPTER 3

EXPERIMENTAL FACILITIES, TEST MODELS AND TEST PROCEDURES

CHAPTER 3

EXPERIMENTAL FACILITIES, TEST MODELS AND TEST PROCEDURES

Introduction

In order to achieve our objective, i.e. the aerodynamic measurements, the following steps were taken: 1) natural icing simulation to optimize input parameters of icing simulation, and 2) aerodynamic measurement of angle member with different ice profiles which were produced based on optimized parameters of previous step. This chapter deals with the most important techniques that have been used in this work to measure the interaction forces between ice effects and wind load. To simulate natural icing conditions a low speed wind tunnel was used. The new casting process which was designed for this

research to reproduce ice profiles by cement was explained. The low speed aerodynamic wind tunnel and external balance were used to measure aerodynamic coefficient. Besides those instruments the laser techniques was applied to measure cloud characteristics as well as flow field characteristics in order to study their effects on the drag coefficient.

3-1- Experimental Facilities

3-1-1- CIGELE Atmospheric Icing Research Wind Tunnel (CAIRWT)

The complexities inherent to the study of atmospheric icing phenomena occurring in the atmospheric boundary layer and involving ice accretion on structures make it a difficult task to solve. The absence of a final unified theory for understanding the mechanisms, which trigger and halt the various types of ice accretion, as well as the impossibility of following its complete development in nature make laboratory investigations of this phenomenon more productive than field observations. Such experimental modeling of atmospheric icing in a wind tunnel or in a climatic room is an integral part of examining the phenomenon that includes field measurements, theoretical and experimental modeling. Experimental modeling of these hazardous weather conditions involves maintaining the aggregate of meteorological parameters forming these conditions within as wide a range as possible in order to be as representative of all the types of atmospheric icing possible. These parameters under consideration comprise air speed, air temperature, air humidity, air pressure, LWC and DSD of the aerosol cloud.

The cold aerosol cloud is simulated by injecting water droplets into the cold air circulating in a tunnel where each meteorological parameter is maintained according to the modeled natural conditions. The wider the range of ambient conditions that can be maintained in the tunnel, the wider the range of hazardous weather conditions that may be investigated, and, consequently, the greater the number of types of atmospheric icing phenomena which may be experimentally modeled in tunnel or climatic room facilities.

The CAIRWT is designed and built to simulate atmospheric icing of overhead transmission lines as it occurs within a moving super cooled aerosol cloud with air velocities typical under icing conditions within the atmospheric boundary layer. This chapter provides an overview of the tunnel facility that is capable of covering a wide spectrum of atmospheric icing conditions and the related equipment used during this study.

3-1-1-1- Construction of CAIRWT

The CAIRWT is a closed-loop (air-recirculated) low-speed icing wind tunnel with a total length of about 30m (Figure 3-1). The construction consists of a number of consecutively connected segments of different shapes and cross-sections, forming a closed circuit for the recirculation of air inside it.

Figure 3-1: CIGELE Atmospheric Icing Research Wind Tunnel

Most of the segments are made of aluminum and covered on the outside by insulating material. The cross-section of each segment of the tunnel gradually narrows, widens or remains constant according to the functions performed by that segment in a circular air flow.

3-1-1-2-General Layout of CAIRWT

The general layout of CAIRWT is based on construction economy and tunnel efficiency. A thorough discussion of design issues, starting with the test section, is provided

in what follows. The common configuration includes the elements shown in Figure 3-2. More information about different elements is available in Appendix A.

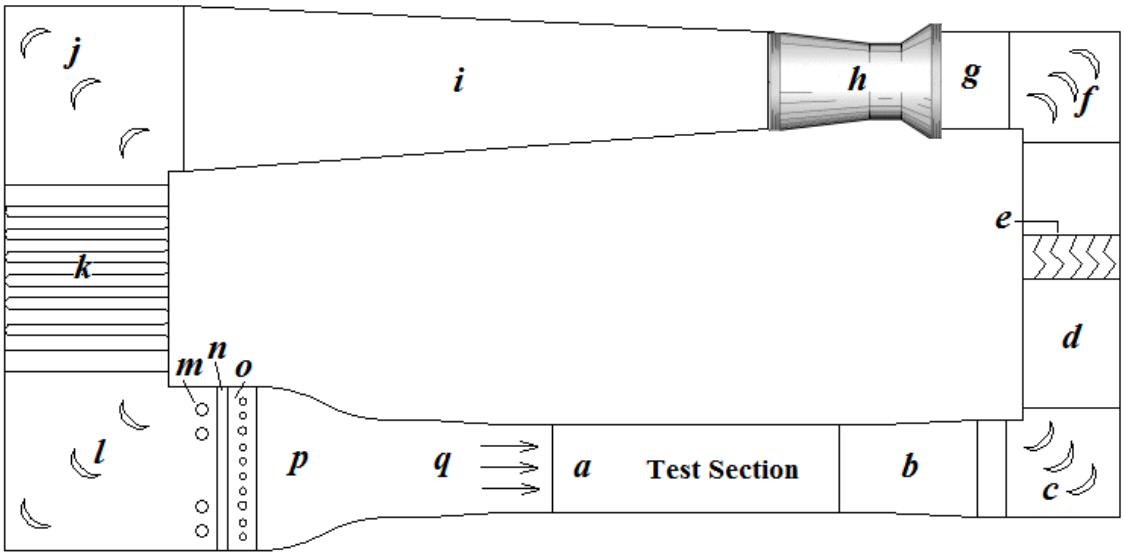

Figure 3-2: Layout of a Closed Single-Return Wind Tunnel

3-1-1-3-CAIRWT's Main Systems

3-1-1-3-1-Fan system

The air inside the tunnel is driven by a fan connected to a three-phase 45-kW motor. The frequency of the motor may be set from 5 to 60Hz using the Automation & Control software (Tech Link Version 1.7) which is provided by Minarik Corporation. This frequency range makes it possible to change air speeds from 2 to 29m/s. The air speed – fan frequency calibration graph is presented in Appendix B.

3-1-1-3-2-Refrigeration system

The desired ambient temperature in the icing wind tunnel may be set by a remote temperature control system (Honeywell T 775A) with ±0.5°C accuracy. The nominal lower limit of the temperature is -30°C The control device is connected to an RTD-type (Resistance Thermocouple Detector) temperature probe which is positioned inside the tunnel between the heating elements (Figure 3-2 Section m) and the honeycomb (Figure 3-2 Section n) (near the honeycomb). This location for the temperature probe was chosen after carrying out a specially designed series of experiments, in which the performance quality of the RTD probe and its reaction to sudden changes in ambient temperature were checked by parallel monitoring of the same parameter in the test section of the tunnel.

The coolant material in the refrigerating system is Ammonia (NH_3) which is circulated by a 75HP rotary compressor equipped with a condenser, an evaporator, a water pump and a ventilator. This system is part of a three series attached compressor monitored by an ammonia electronic valve control device to assist and maintain the suitable temperature required for every chamber in action. The contact of the circulated moving air with the evaporator leads to an air temperature drop inside the unit. The temperature, which is sensed by the RTD, is read in the tunnel by a PLC (Programming Logic Control) system and is maintained at the desired temperature with a precision of ±0.5°C. This is an automated system which controls the operation of the coolant gas compressor in order to set up the desired air temperature. The speed of the air flowing inside the tunnel has a significant effect on the time required to reach the desired air temperature and on the

amplitude of air temperature oscillations inside the tunnel. These minimal oscillations in temperature are unavoidable throughout the experiments, as a result of the capacity of the system to regain the desired temperature after addition of the coolant to the cooler or heat exchanger. The ice accretion on the blade changes the velocity after a certain time during the experiment therefore increasing the temperature and decreasing the fan velocity in the tunnel. The higher speed reduces the set-up time and decreases the amplitude of the oscillations of air temperature [91].

3-1-1-3-3-Nozzle spray-bar system

The technique used in CAIRWT to simulate atmospheric icing processes is to inject water at room temperature into a cold air stream through the nozzles located at the trailing edge of the horizontal spray bar which is designed in the shape of a NACA 0012 airfoil. The spray bar is located just downstream of the honeycomb, 4.4m upstream of the middle of the test section, where the icing structure being analyzed is usually placed. The water and air are supplied to the nozzles on the spray bar through independent water and air supply lines. This makes it possible to maintain specific conditions for each nozzle separately, without mutual influence between the lines. The water line is linked to a reservoir of regular domestic tap water and passes through a filter, while the air supplied by a compressor using ambient air passes through a dehumidifier at room temperature. Water atomized in nozzles by high-pressure air is pulled by the air wake from the trailing edge of the spray bar into the flowing cooled air stream. As a result, an aerosol cloud of the desired DSD is formed.

3-1-1-4-Control Panel

In order to produce the aerosol cloud with the desired characteristics, it is necessary to control the dynamic parameters in both water and air lines of the fluid transfer system. The control panel for monitoring and modifying the dynamic parameters in both lines is presented in Figure 3-3. The panel makes it possible to control the water flow rate and the water and air pressures in the three lines independently.

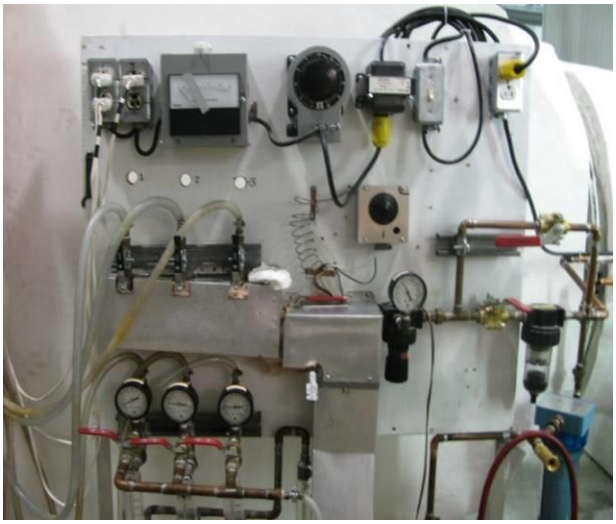

Figure 3-3: CAIRWT`s Control Panel

The CAIRWT's Control panel has been divided into two systems. Each of them is further divided into two subsystems, (Figure 3-4).

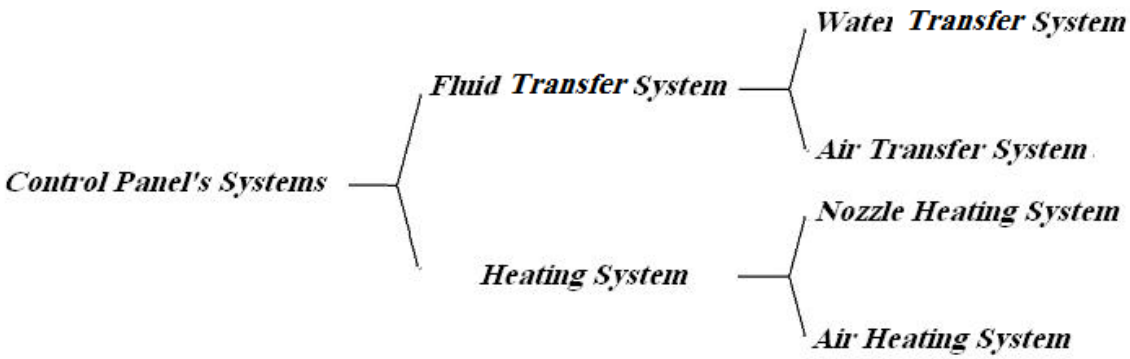

Figure 3-4: Control Panel Systems

3-1-1-4-1-Water Transfer System

Each system of fluid transfer is composed of many instruments in the lines to control flow, pressure and other parameters that are related to the fluid. The water transfer system supplies water to the nozzles to produce water droplets in the wind tunnel.

3-1-1-4-2-Air Transfer System

The air transfer system supplies air to the nozzles. There is a water collector in the air line to remove water from the air line. The air humidity must be kept very low to prevent freezing in the air lines leading to the nozzles.

3-1-1-4-3-Nozzle Heating System

The nozzle heating system is used to heat the nozzles in order to avoid frozen water particles to block the nozzle opening. This system is composed of four wall plug-in connections, an ON/OFF Switch, an AC Ampere meter and a 110V rheostat switch. Three

wall plug-in connections are used to connect electrical current between the control panel and heating elements fixed around each nozzle, while the fourth one is the by-pass connection.

3-1-1-4-4-Air Heating System

The air heating system is used for heating air in the nozzle air line which helps prevent freezing in the nozzles. This system is composed of a wall plug-in connection and a thermo-control knob. The wall plug-in connection connects the current to the heating element, and the thermo-control knob is used to adjust the heating level. Normally, the knob should be set between 1 and 1.5 on its scale to avoid overheating. For high air pressures, too warm air may cause the blow up of tubes in nozzle air lines.

The air will be warm enough 10 to 15 minutes after switching on the air heating system. It can be checked by touching the surface of the cover of the heating element which is an insulated box made of aluminum.

3-1-1-5-Physical parameters of the aerosol cloud produced in the wind tunnel

The characteristics of the aerosol cloud are decisive factors affecting the type, mass and shape of ice accumulation. The most important parameters characterizing the aerosol cloud are temperature, velocity, humidity, LWC and DSD.

3-1-1-5-1-Temperature

The air temperature in CAIRWT is adjusted via the specific control panel which has been designed for this purpose. The lower limit at which the air temperature may be cooled down is -30°C. The screen on the control panel displays the temperature measured before the spray bar section. The air temperature in the test section may be measured by thermocouples and it is expected to be 1-2°C warmer than the temperature before the spray bar section.

3-1-1-5-2-Velocity

The air velocity under icing conditions in nature varies between 0 and 40m/s [92], while it can be increased up to 29m/s in the test section of the CAIRWT. The air velocity and turbulence calibrations are available in Appendix B.

3-1-1-5-3-Relative and Absolute Humidity

Humidity expresses the amount of water vapour in air. Relative humidity is defined as the ratio of the partial pressure of water vapour in a mixture of air and water vapour to the saturated vapour pressure of water at a specified temperature. Absolute humidity is the quantity of water in a unit volume of air. Relative humidity and absolute humidity are measured in CAIRWT by a “Smart” humidity transmitter by Vaisala which is installed near the end of the test section.

3-1-1-5-4-Liquid Water Content (LWC)

The LWC expresses the mass of liquid water per unit volume of air. The LWC of the aerosol cloud produced in CAIRWT is a function of the nozzle air and water line pressures, air speed and, within a certain range of the temperature, the flow rate of water supplied to the nozzles. The LWC in the middle of the test section of CAIRWT in the horizontal configuration was previously determined as a function of these parameters [89]. The LWC calibration data for the new vertical configuration are in Appendix B. The LWC in the geometrical center of the middle of the test section of CAIRWT using Type A nozzles may vary between 0.2 and 8g/m^3, an interval covering the major part of the range characterizing atmospheric icing processes.

3-1-1-5-5-Droplet Size Distribution (DSD)

One of the important parameters in the characterization of a spray is the DSD. It shows the variation of diameter of spherical droplets in the flow. An instructive picture of DSD may be obtained by plotting a histogram of DSD. There are different techniques to measure this parameter. A representative diameter i.e. MVD, is often used to describe DSD in a cloud. The MVD is defined as the diameter in which half of the volume of water is contained in droplets with a smaller diameter. The MVD calibration data are presented in Appendix B. The MVD in the geometrical center of the middle of the test section of CAIRWT using Type A nozzles which may vary between 10 and 100μm.

3-1-1-6-CAIRWT related equipment

3-1-1-6-1-Integrated System for Icing Studies by Droplets Measurement Technologies

An integrated system for icing studies was manufactured by Droplet Measurement Technologies, which is applicable for LWC and DSD measurements. This instrument has two probes, the Cloud Imaging Probe (CIP) and the Cloud Droplet Probe (CDP). The CIP is a combination probe incorporating several basic measuring instruments to characterize cloud parameters. The CIP measures particles ranging in size from 25μm to 1550μm. This combination probe also includes a hot-wire LWC sensor, an air temperature sensor and a Pitot tube air speed sensor. The measured data are displayed by the particle analysis and collection system (PACS) which has an intuitive graphical user interface at the host computer and provides powerful control of the measured parameters while simultaneously displaying real-time size distributions and derived parameters. Various other parameters that can be calculated include the average drop diameter, mass weighted diameter, mode distributed diameter, standard deviation and LWC.

3-1-1-6-2-Particle Image Velocimetry (PIV)

Two-dimensional (2-D) PIV is a measurement technique with many applications. One of the primary uses is flow field visualization. Additionally, 2-D PIV provides accurate velocity measurements in such flows. The physical principles behind this technique rely upon the illumination and capture of seeding particles that follow the streamlines of the flow. By capturing images in close succession and by using correlation techniques, it is

possible to analyze the displacement of the seeding particles; hence describing the motion of these particles in the flow field. To illuminate the seeding particles, a high intensity and frequency laser is used. This laser produces a light sheet which illuminates the seeding particles within a finite volume. A CCD (Charge-Coupled Device) camera is used to capture the position of the seeding particles at different instances. Commercial software, Dynamic Studio V2.2, is used to analyse and visualise the flow field electronically. The phases involved in the entire experimental procedure can be summarized as follows: calibration, measurement, and analysis. The system used for PIV in CAIRWT is provided by Dantec Dynamics.

The laser produces a high intensity green light sheet. In order to visualise the flow field using this light sheet, a green filter is used on the CCD camera to ensure that optical wave lengths in excess of approximately 532nm are allowed to pass through. The lens and filters for this camera are from Nikon. This enables a large portion of background noise caused by other light sources for instance, to be minimized. The laser light sheet is created by combining infrared light from two cavities using a beam combiner and passing the bundle through a harmonic generator. Table 3-1 shows the model and serial number information of Laser machine. More detailed information about these techniques and introduction to the Dynamic Studio software are available in [93].

Table 3-1: Laser machine information

Device	Company	Model	Serial Number
Laser	Litron Laser	LDY302-PIV	LM0638
Camera	Dantec Dynamics	X3MP-G-4	13-0508-0512

3-1-2- Low speed aerodynamic tunnel

3-1-2-1- General layout

All the aerodynamic tests were conducted in the Université de Sherbrooke's main wind tunnel. The tunnel is a return circuit and closed test section type. The testing section is 1.83 m (6 feet) wide by 1.83 m tall (6 feet) and allows wind velocity ranging from 1.2 to 32 m/s.

3-1-2-2- Tunnel parameters

The mean wind speed was measured by Pitot tubes and their individual manometers. The air temperature was measured by a thermocouple which was installed downstream of the tunnel after the specimen. The air pressure was measured by reading barometer.

3-1-2-3- Tunnel related equipment (External balance)

The system used to measure wind forces is 3 degrees of freedom (DoF) dynamic force balance [94]. This balance allows dynamic and static testing of sectional models. Each DoF are uncoupled using air bearings for the translation ones and conventional ball

bearings for the rotation along the model's axis. The force at every attachment point, 8 for each DoF, is measured using a FUTEK load cells, model LCM300. The displacements of the sectional model, when needed, is measured with 6 laser displacement sensors (Sunx, model LM10). The acquisition system used is a DaqLab2000 from IOtech.

3-2- Test models

3-2-1-Wind effects on ice accretion

Two angle members were used as icing objects. Table 3-2 shows their dimensions. They were fixed in the middle of the test section. To change the angle of attack, α, and side slip angle, β, the endpoints of the angle member were fixed to a special support installed in the test section from the top. The support can then rotate around the horizontal axis passing through the midpoint of the test section wall perpendicular to the stream-wise direction as well as the vertical axis passing through the midpoint of the support, Figure 3-5. To vary the rolling angle, γ, of the angle member, another support was used in order to be able to change angles around the stream-wise direction. To alter α for the model in the vertical direction, the angle member was fixed directly from two sides at the top and bottom of the test section while for the β and γ, a special support with a spherical joint was used where it was mounted from the top of the test section Figure 3-6. In all cases, special care was taken in order to keep the midpoint of the angle member at the tunnel center line.

Figure 3-5: Support used for horizontal ice simulation

Figure 3-6: Support used for vertical ice simulation

Table 3-2: Angle member dimensions for icing simulation

Specimen	Section	Material	**L**ength (mm)	Width-**b** (mm)	**T**hickness (mm)
A51x**L**9	L51x3.2	**A**luminum	920	50.8	3.175
A51x**L**4	L51x3.2	**A**luminum	460	50.8	3.175

3-2-2- DSD and LWC effects on ice accretion and drag coefficient

The same angle bars with the same specifications fabricated from AL 6061-T6 were used for experimental tests.

3-2-3- Aerodynamic models

To study the effects of wind force on an angle member, seven different glaze ice profiles were developed. Table 3-3 gives the information of the thermo physical parameters which were used to create primary ice shapes.

Table 3-3: Angle member specifications with related thermo physical parameters

Specimen	Section	Material	LWC(g/m^3)	Ice Type	Air velocity = V_a(m/s)	Ice accretion time = time(min)	Air temperature = T_a(°C)
S25-**G**1	L25x3.2	**S**teel	0.9	**G**laze	20	15	-5
S25-**G**2	L25x3.2	**S**teel	0.9	**G**laze	20	30	-5
S51-**G**3	L51x3.2	**S**teel	3.3	**G**laze	20	30	-5
S51-**G**4	L51x3.2	**S**teel	3.3	**G**laze	20	45	-5
S51-**G**5	L51x3.2	**S**teel	2.9	**G**laze	20	30	-5
S51-**G**6	L51x3.2	**S**teel	0.9	**G**laze	10	30	-5
S51-**G**7	L51x3.2	**S**teel	0.9	**G**laze	20	30	-5

The ice profiles were reproduced with cement. The main purpose of generating realistic ice shapes was to make new cement ice models which could be used in wind tunnel in different scales. The cement replicas of the original iced angle members for wind tunnel studies were made by a triple moulding process in which a first negative mould was obtained by potting the original ice-covered samples with the length of between 25cm to 45cm in low-temperature polyurethane-based isolating foam. This compound cures at -5°C in a few hours. The original ice model melted in a few hours and the negative foam mould was filled with cement. The cement cures at room temperature in a few hours. The cement-moulded model was easily removed by slitting the foam mould.

The second negative mould was obtained by potting the cement-moulded ice profile samples in RTV rubber. This compound cures in a few hours, and then cement moulded

was easily removed by slitting the rubber mould. The empty mould was then used to cast the final cement replica of the original iced angle members by pouring in cement. When the mould of the ice sample was ready, the last step of the procedure was to cast the mould in cement a minimum of four times (based on the ice profile which was used in the first step after ice accumulation) or more, to get the same cement profiles of ice for different ice accretions. These profiles were installed on the angle members by using polyurethane construction adhesive.

The reason to apply this triple moulding process is the different size of the chosen ice specimens and wind tunnel test section. As mentioned before the ice specimen length was between 25cm to 45cm. The wind tunnel section used to measure the aerodynamic coefficients of the ice shapes was four times larger than the test section of the wind tunnel used to generate ice accretion. Accordingly, not only the ice profiles should be reproduced but also, they should be repeated based on the original dimensions of the ice specimens to cover the whole angle member for the aerodynamic tunnel test section. Figure 3-7 shows the cement molded ice profiles for ice samples related to Table 3-2.

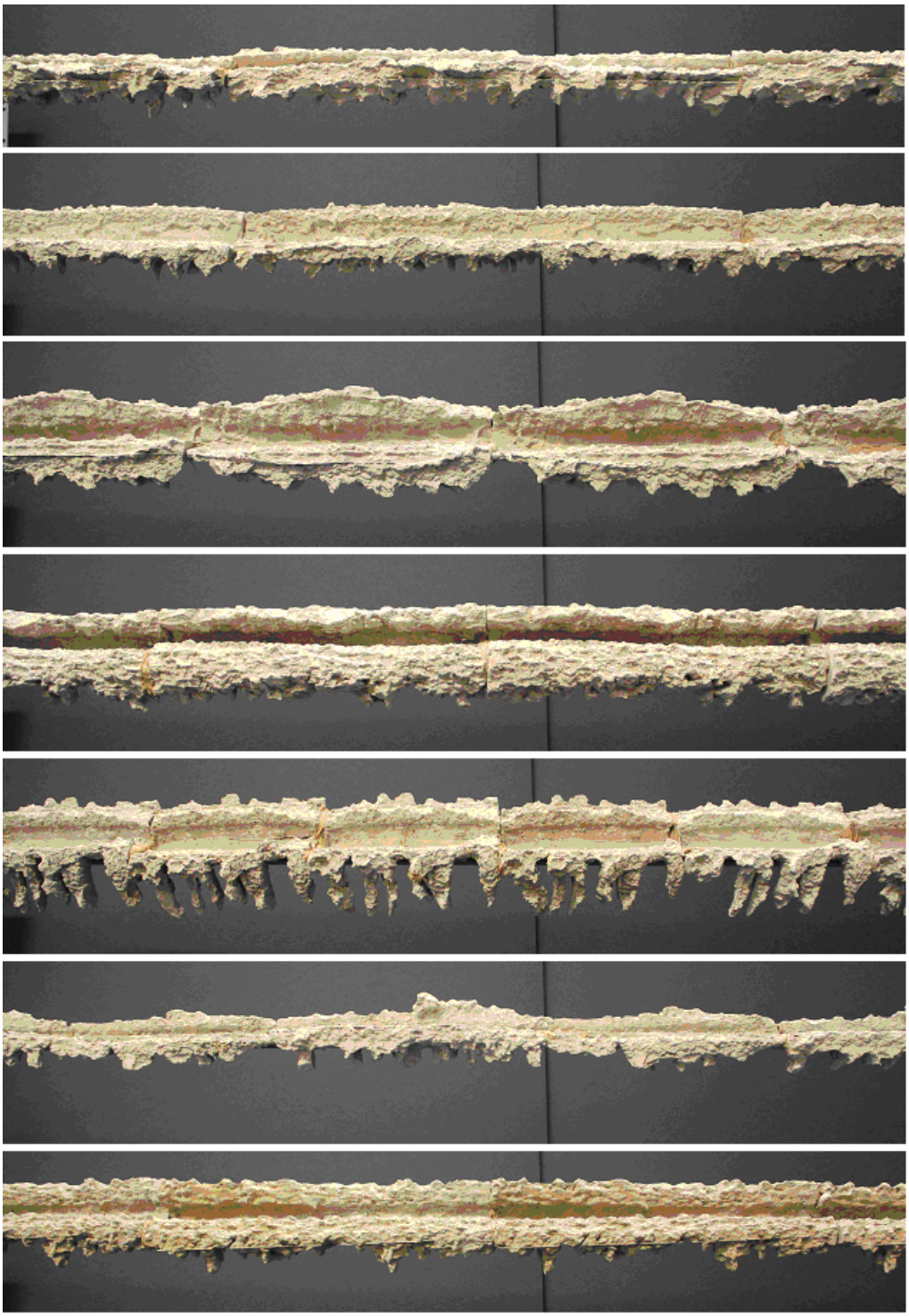

Figure 3-7: Cement moulded ice profile for sample number1 to 7 from Table 3-3

3-3- Test procedures and selecting experimental conditions

3-3-1- Wind effects on ice accretions

Table 3-4 shows thermo-physical parameters: air velocity, V_a, air temperature, T_a, water pressure, P_w and air pressure, P_a, which were set for icing simulations.

Table 3-4 Thermo physical parameters of ice simulation

Specimen	V_a(m/s)	T_a(°C)	P_w(kPa)	P_a(kPa)	LWC(g/cm^3)	Time duration (min)
A51xL9-1	10	-5	120	160	0.9	30
A51xL9-2	25	-5	300	300	2.9	45
A51xL4	10	-5	120	160	0.9	30

For the ice simulation mass of ice accretion per unit length of angle members, ice shape, and profile of ice accretion were collected for each test. The mass of ice accretion per unit length, ice shape, and profile of ice accretion were collected after each experiment, using the collection method presented in Kollar and Farzaneh [12]. Ice shapes were recorded by taking photos of their front and top views. In order to measure ice mass, the tower-leg model was taken off its supports and set into a specially designed support for further examination outside the tunnel. A thin preheated aluminum cutter was used to cut ice specimens at right angle before measuring their mass and length. Samples with different lengths were taken from different parts of the angle bar. After cutting the ice accretion, additional photos were taken to record ice profiles.

3-3-2- DSD and LWC effects on ice accretion and drag coefficient

For DSD and LWC measurements, the integrated system described in section 3-1-1-6-1 was used in different vertical and streamwise positions in the tunnel test section for different free-stream velocities and initial DSDs (DSD at nozzle outlet). Throughout the tests, the temperature was set at 15°C and the duration of each measurement was 30s. The measurements were done for four air velocities: V_a= 5, 10, 20, and 28m/s. The DSD was adjusted by the pressure in the nozzle water and air lines. The water pressure, P_w, was set at 450kPa, and the air pressure, P_a, was varied from 180 to 620kPa. Therefore aerosol clouds were produced with varying DSD and LWC so that they simulated different icing conditions including in-cloud icing and freezing drizzle. The upper limit for air pressure was determined by the condition that the nozzle could produce spray. Further increase of air pressure above 620kPa with unchanging water pressure would block the water in the nozzle mixing chamber so that spray was not produced. These measurements were repeated for three vertical positions with 0.07m increments and four horizontal positions with 0.5m increments. The adopted coordinate system was as follows:

- The origin was at the center point of the test section.
- The x-axis coincided with the tunnel longitudinal center line and it was oriented in the direction of the free-stream velocity. Its zero was aligned with the position of the angle bars to be tested.
- The y-axis was vertical and oriented upward.

Thus, measurements were made at the following positions: x = -1, -0.5, 0, +0.5m; y = -0.07, 0, +0.07m.

For ice accretion measurements, the A51xL9 was mounted in the test section horizontally in three vertical positions y = -0.07, 0, +0.07m and in three streamwise positions, x = -0.5, 0, +0.5m for the ice accumulation tests. The 0.46m angle bar was used vertically in the same three streamwise positions. The air velocity was set at 12 and 25 m/s, and two different combinations of water and air pressure were applied: P_w=300 kPa, P_a=300, 200 kPa. The temperature was -5°C and the duration of each test was 30 minutes.

The mass of ice accretion per unit length of angle members, ice shape, and profile of ice accretion were collected for each tests using the collection method presented in section 3-2-1.

3-3-3- Aerodynamic measurements

For aerodynamic measurements, the tunnel air temperature was measured by a thermocouple which was mounted downstream of the force measurement system inside the test section. The air pressure was read from a barometer. The air temperature and air pressure were used to calculate air density. The mean wind speed was measured simultaneously at three different points using three Pitot tubes and their individual manometers. The first was installed a few meters upstream the specimen and the two others, above and underneath the specimen's leading edge, midway to the walls (Figure 3-8).

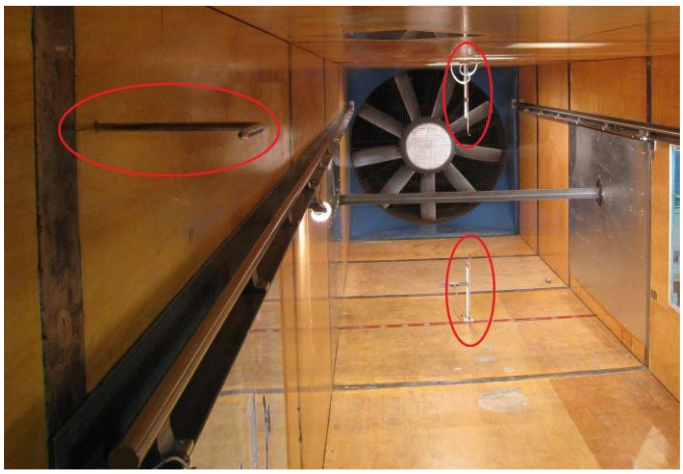

Figure 3-8: Positioning of the 3 Pitot tubes

For all measurements, force time histories of 30 seconds at a sampling rate of 100 Hz were recorded. Table 3-5 shows the adjusted air velocity and angle of attack for different samples.

Table 3-5: Air velocity and angle of attack for aerodynamic models

Specimen	S25-G1	S25-G2	S51-G3	S51-G4	S51-G5	S51-G6	S51-G7
Air Velocity (m/s)	5-10-20	5-10-20	5-10-20	5-10-20	5-10-20	5-10-20	5-10-15
Angle of attack (°)	0<α<360	-20<α<20	0<α<360	-20<α<20	0<α<360	0<α<360	0<α<360

Figure 3-9 shows that it was difficult to mount ice profiles on all of the angle member length. The interference between mounting slots on the rigs for mounting and dismounting caused to put a little space from the ends.

Figure 3-9: The distance between the rig and ice profile

$$C_D = \frac{F_D}{1/2\,\rho V^2} \tag{3-1}$$

Based on the designed external balance, the components for each aerodynamic force should be considered based on its direction. It is necessary to consider the correction based on the part of the angle member without ice profile. Table 3-6 shows the length of each model with ice and without ice.

Table 3-6: Models length with and without ice

Models	Length with ice (m)	Length without ice (m)	Length without ice (%)
S25-G1	1.6610	0.1454	8
S25-G2	1.6610	0.1454	8
S51-G3	1.4896	0.3104	17
S51-G4	1.4686	0.3394	19
S51-G5	1.2420	0.5644	31
S51-G6	1.2440	0.5624	31
S51-G7	1.4606	0.3434	19

So, F_D is a net drag force on an angle member which is component of lift coefficient in the direction of X, component of drag coefficient in the X direction and the correction for the part of the angle member without ice profiles (both extremities):

$$F_D = F_{Dmeasured}\cos\alpha + F_{Lmeasured}\sin\alpha - F_{Dcorrection} \quad (3\text{-}2)$$

Where α is angle of attack, F_D and F_L are measured with the external balance. For $F_{Dcorrection}$ the formulation below was used:

$$F_{Dcorrection} = 0.5\rho V^2 (Projected\ Area\ without\ ice) \times C_D \quad (3\text{-}3)$$

Where C_D is the drag coefficient from the experiment without ice profile for the same angle of attack [16]. The same procedure was done for lift coefficient:

$$C_L = \frac{F_L}{1/2\,\rho V^2} \quad (3\text{-}4)$$

$$F_L = F_{Dmeasured} \sin\alpha + F_{Lmeasured} \cos\alpha - F_{Lcorrection} \quad (3\text{-}5)s$$

applied by the formula below:

$$\rho = \frac{p_a}{RT} \quad (3\text{-}7)$$

The moment Coefficient was normalized based on the dimension of the angle member with iced profile.

$$C_M = \frac{T}{1/2\,\rho V^2 b^2 l} \quad (3\text{-}8)$$

T was measured by the external balance, b is the angle member width and l is the angle member length with ice.

Conclusion

For the ice simulation experiments the available icing wind tunnel at CIGELE was used while for aerodynamic experiments the low speed aerodynamic tunnel available at Sherbrooke University was used. For all cloud characteristics measurements and flow field measurements the laser technique was applied by using a cloud analyzer probe and PIV machine. Regarding the use of angle member models for ice simulation tests, the AL6061 material was used while for aerodynamic measurements the iron alloy material was applied.

CHAPTER 4

ICE SIMULATION AND WIND EFFECTS ON AN ANGLE MEMBER ICING

CHAPTER 4

ICE SIMULATION AND WIND EFFECTS ON AN ANGLE MEMBER ICING

Introduction

Most atmospheric icing models of bluff body consider an icing object placed in an air flow carrying super-cooled droplets. Such a geometrical arrangement involves the possibility of simplifying the model to a 2D representation. This simplification is advantageous for immediate freezing under extremely cold conditions. However, when the axis of the icing object is placed at an angle with the air velocity, then 3D models are essential for reliable simulation.

In this chapter, firstly, a vast number of ice simulations will be presented and compared with some available photographic results from the Hydro Quebec icing data base.

In order to study the wind effects on bluff body, the process was as follows: firstly, the focus was placed on the horizontal angle member icing for two icing conditions and three aerodynamic angles. Then, the angle member was mounted vertically for ice simulation under one icing condition for three aerodynamic angles. All aerodynamic angles definition explained in section 3-2-1. The normalized ice mass per unit length was calculated for each aerodynamic angle.

4-1-Ice simulation

In the first step, we compared some atmospheric icing results from wind tunnel simulation tests with some icing phenomena photos from the Hydro-Quebec data base. Ice shapes were recorded by taking photos of their front and top views.

4-1-1-Glaze ice

The first type of ice accretion simulated in the icing tunnel was glaze ice with icicles. Glaze ice forms when water is collected from the impingement of super cooled water droplets. Icicles are formed from the unfrozen surface liquid that does not freeze at some location. It must be shed, either as a result of gravity or wind stress [32]. Table 4-1 shows the thermo physical parameters for different glaze ice accretions. For all the tests, the glaze ice with icicles was observed. Figure 4-1 shows the glaze ice with finger icicles (test number 1) compared with the accreted ice in “Petite-Rivière Saint-François” in November 2003. It is observed that the vertical growth rate of the icicles is much higher than the

horizontal growth rate, so it is the vertical dimension of the tip of the icicle that is growing fast compared to the thickness.

Table 4-1: Thermo physical parameters for different glaze ice accretions with icicles

Test Number	V_a (m/s)	T_a (°C)	P_a (kPa)	P_w (kPa)	LWC (g/m^3)	Time duration (min)	Ice definition
1	10	-5	320	200	1	45	Glaze with icicles
2	10	-5	100	200	1.8	30	Glaze with icicles
3	10	-5	300	300	3.3	15	Glaze with icicles

Figure 4-1 shows icicles formed when inertia forces were small, with a dominant drag and droplets that followed closely the stream air lines.

Figure 4-1: Glaze ice with icicles, a) Petite-Rivière Saint-François, b) Wind tunnel ice simulation on angle member

On the other hand, for large droplets, inertia forces were dominant and droplets tended to hit the angle member. Table 4-2 shows different ice simulations made to obtain glaze ice profiles. The ice simulations were done on a cylinder and an angle member to validate the obtained photos from Hydro Québec data base. Figure 4-2 shows the accreted ice in Mont Belair compared to the results obtained on a cylinder (Table 4-2, test number 2). It is almost impossible to obtain the same ice shape because of the complicated process of ice accretion.

Table 4-2: Thermo physical parameters for different glaze ice accretions

Test Number	V_a (m/s)	T_a (°C)	P_a (kPa)	P_w (kPa)	LWC (g/m^3)	Time duration (min)	Ice definition
1	20	-5	300	300	3.3	30	Glaze ice
2	10	-5	160	120	0.9	150	Glaze ice
3	10	-5	160	120	0.9	30	Glaze ice

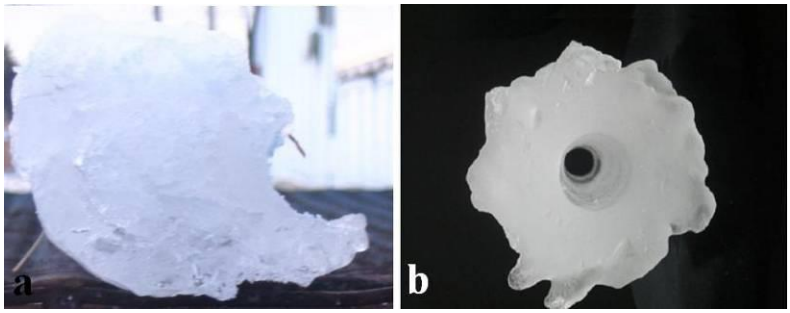

Figure 4-2: Glaze ice, a) Mont Bélair, b) Wind tunnel ice simulation on a rotating cylinder

The same results were obtained with ice simulation on an angle member. Figure 4-3 shows the ice sample obtained from Mont Bélair compared to accreted ice on an angle member (Table 4-2, test number 1).

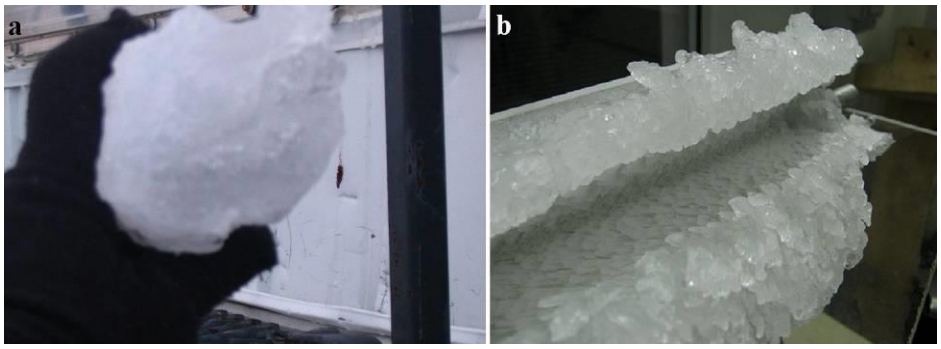

Figure 4-3: Glaze ice, a) Mont Bélair, b) Wind tunnel ice simulation on an angle member

4-1-2- Rime ice

The second type of ice which was simulated was rime ice. Rime ice occurs when super cooled water droplets that travel along with the wind flow in low temperature come into contact with a physical body [33].

Table 4-3 shows different ice simulation parameters to obtain rime ice. The air velocity, air temperature and LWC were changed to obtain rime ice on an angle member. Figure 4-4a shows the ice accreted on Mont Bélair compared to ice simulated in a wind tunnel (Table 4-3, test number 5). As shown in both photos, tightly packed ice feathers were observed. It is obvious that the direction of the feathers growth is different in Figure

4-4 a and b because the preferred direction of growth is perpendicular to the external streamlines. The ice prepared on the angle member was very brittle and removed easily from the surface of angle member.

Table 4-3: Thermo physical parameters for different rime ice accretions

Test Number	V_a (m/s)	T_a (°C)	P_a (kPa)	P_w (kPa)	LWC (g/m^3)	Time duration (min)	Ice definition
1	10	-10	300	200	1	40	Rime ice
2	10	-10	300	250	1.85	15	Rime ice
3	5	-30	325	400	7.8	30	Rime ice
4	20	-15	160	120	0.9	60	Rime ice
5	10	-15	160	120	0.9	10	Rime ice

Figure 4-4: Rime ice, a) Mont Bélair, b) Wind tunnel ice simulation on an angle member

Figure 4-5 shows rime ice simulation (Table 4-3, test number 4) compared to accreted ice on Mont Belair. It has been shown that the ice on both photos is quite white and brittle. It seems that individual droplets accrete parallel to the streamlines but on a

global scale the ice grows perpendicular to the streamlines, since strongest gradients are around the angle member's corner.

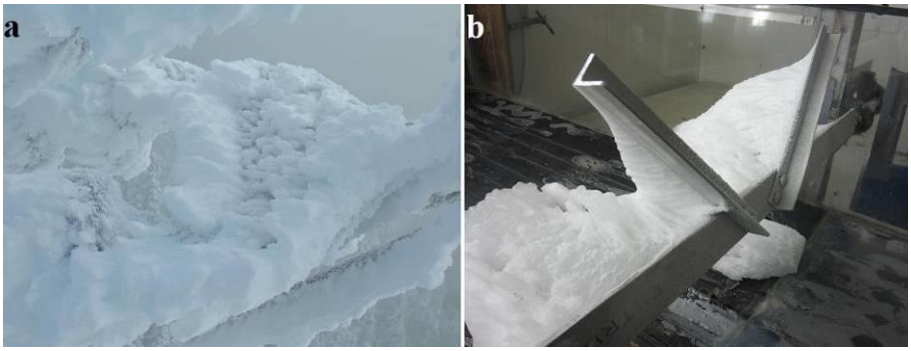

Figure 4-5: Rime ice, a) Mont Bélair, b) Wind tunnel ice simulation on an angle member

According to the ice simulations done in the tunnel, it was observed that rime ice is brittle and melts very fast outside of the test section. Therefore, it was difficult to obtain an ice profile shape for different ice simulations and do measurements. It was also noticed that it is very difficult to get the whole shape of rime ice from the angle member to cast with cement. Glaze ice accretion was chosen for the next step of this research.

4-2-Wind effects on horizontal angle member icing in the test section

The effects of wind velocity and wind direction were studied. The ice profile shape and ice mass per unit length were obtained for horizontal angle member. As it was explained, two different sets of thermo-physical parameters were chosen for this research which resulted in two different LWCs (Table 3-3).

4-2-1-Sign convention and definition of the variables

Figure 4-6 presents the sign convention used and defines the aerodynamic angles and terminology, in order to simplify the reading.

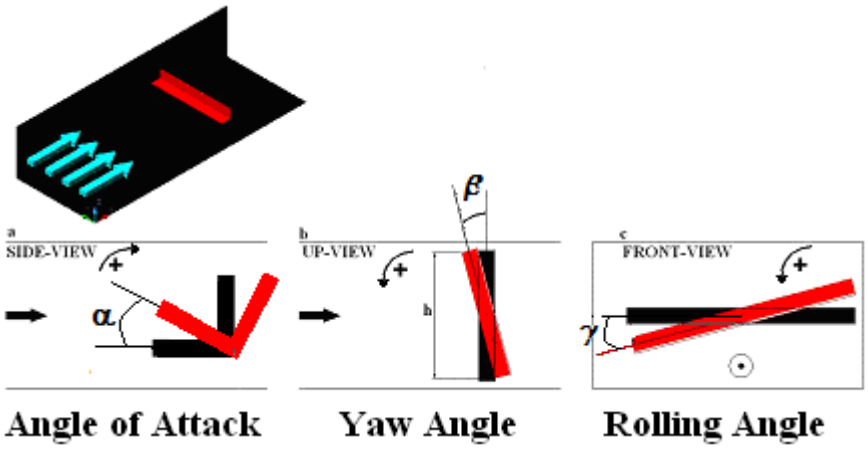

Figure 4-6: Sign convention and definition for icing experiments

4-2-2-Angle of attack

The ice mass per unit length for α=180° is 42% greater than α=0°. As it is obvious from Figure 4-7a-c, the projected height for both angles is the same, around 50.8mm, but the accreted ice mass is higher for α=180°. It may be explained by considering the effects of the flat plate, Figure 4-7a, on changing the direction of flow stream lines. It seems that the droplets velocity is reduced to zero in front of the flat plate which means there is a stagnation line in this part and that is where the ice starts to accumulate. The droplets which

direction was changed by the flat plate in the upper side started to accumulate on the vertical plate Figure 4-7b.

The ice profile shape for α=180° is shown in Figure 4-7c. The stagnation icing is observed on the vertical plate. Because of the flow pattern around the vertical plate [49], the droplets start to freeze from the stagnation line and continue on both sides. It may be explained by the fact that the ice surface height is the size of the boundary layer on the vertical surface. The same results were observed for the cylinder [95] and the airfoil [6].

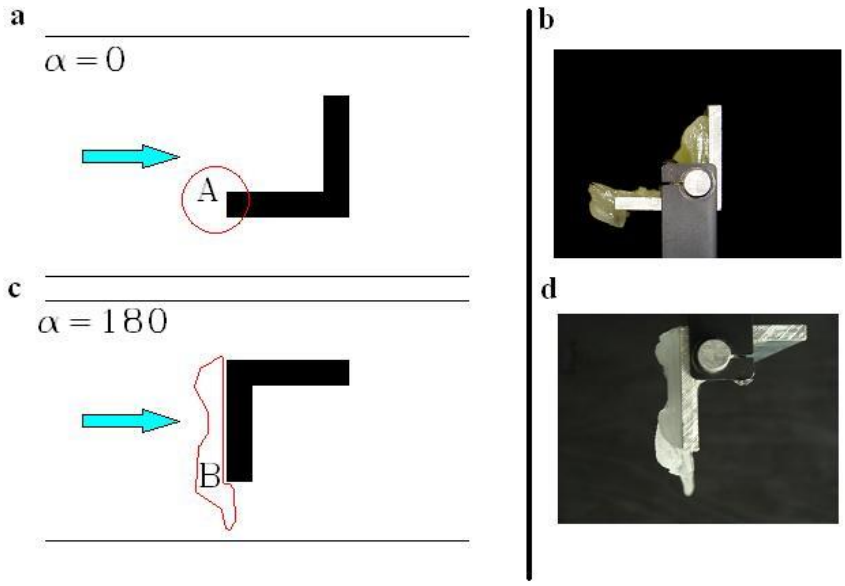

Figure 4-7: A51xL9 ice accretion for a-b) α=0°, c-d) α=180°

The same results were observed for α=90° and α=270°. The ice mass per unit length for α=90° was less than α=270° where the projected height was the same for both angles (Table 4-4).

Table 4-4: Average ice mass per unit length for A51xL9

Angle of attack(deg)	M/L(g/cm)	Projected height(mm)
0	3.4162	50.8
90	5.5625	50.8
180	4.8491	50.8
270	2.3798	50.8

The ice mass per unit length for α= 54°, 234° was calculated around 4g/cm. There is not much difference between average ice mass per unit length. Figure 4-8 present the ice profiles. As shown, the gravity effect causes the ice profiles to accumulate towards the bottom of the angle member for both angles.

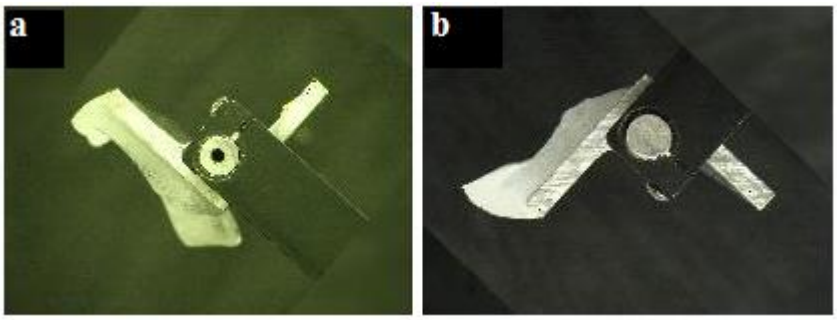

Figure 4-8: A51xL9 ice accretion for a) α=54°, b) α=234°

Figure 4-9a and b shows ice profiles for two angles α=144°, 324° respectively. The ice mass per unit length was calculated 5.906g/cm for 144° and 3.609g/cm for 324° where the exposed height was 41.1mm. Figure 4-9a shows that the corner changed the streamline directions towards the surfaces of the angle members. It seems that some streamlines reach

to zero velocity in the corner. The corner effect caused the droplets to start to accumulate on the end of the angle members' surfaces where some other droplets reached this part and froze. Figure 4-9b shows that the outside corner just changed the streamline directions to the angle member upper and lower surfaces where other droplets also reached directly to the surface and caused ice to start accumulating there. As well, a stagnation line is to be noticed on the corner.

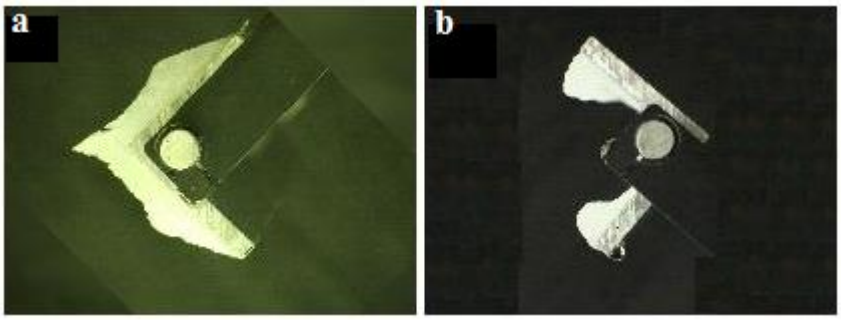

Figure 4-9: A51xL9 ice accretion for a) α=144°, b) α=324°

Figure 4-10 shows A51xL9-2 ice accretion for the angles greater than 180. As it has been shown, by increasing the angle of attack, the effects of vertical surface increased. It seems that the position of the stagnation line moves toward the middle of the vertical surface of the angle member.

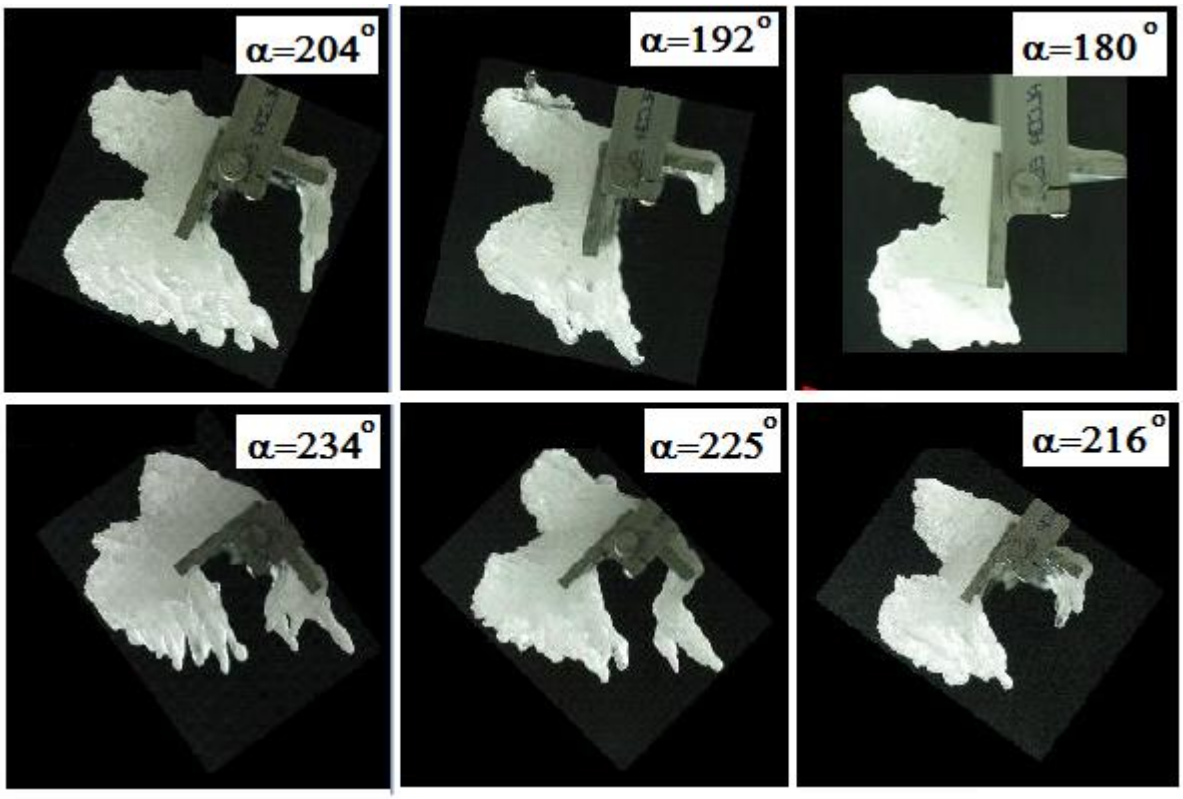

Figure 4-10: A51xL9-2 ice accretion profile for α>180°

Figure 4-11 shows A51xL9-2 ice profiles for angles of attack 270° to 360°. As it has been shown, with increasing angle of attack, the distance between accreted ices on horizontal and vertical surfaces decreased. In other words, when the angle of attack increased, the corner effects increased and flow stream lines reflected from both sides of the angle member. It was shown previously [49], that the corner effects cause to create a wake region. It was expected that after stream lines reflection from angle member surfaces, wake regions were created on both sides. So in these regions, the rotation flow causes the super cooled droplets to be trapped there and then they start to freeze.

It is also noticeable that the velocity was zero on the angle member where the vertical and horizontal surfaces connect. This area is well-known as a stagnation line. It was shown that for $\alpha=360°$, the separation distance between two parts of ice is maxima while this distance decreases by increasing both the angle of attack and the corner effects. Figure 4-11 shows that these effects are reduced after $\alpha=324°$ until $\alpha=270°$. At $\alpha=270°$, the horizontal surface causes the flow streamlines to deviate while on the surface there will be a stagnation line, likewise $\alpha=360°$, where the droplets velocity is zero and they start to freeze.

From all angles, it is obvious that accreted ice tends to the bottom of the angle member, which is mentioned as being part of the effects of gravity mechanism on droplet trajectories.

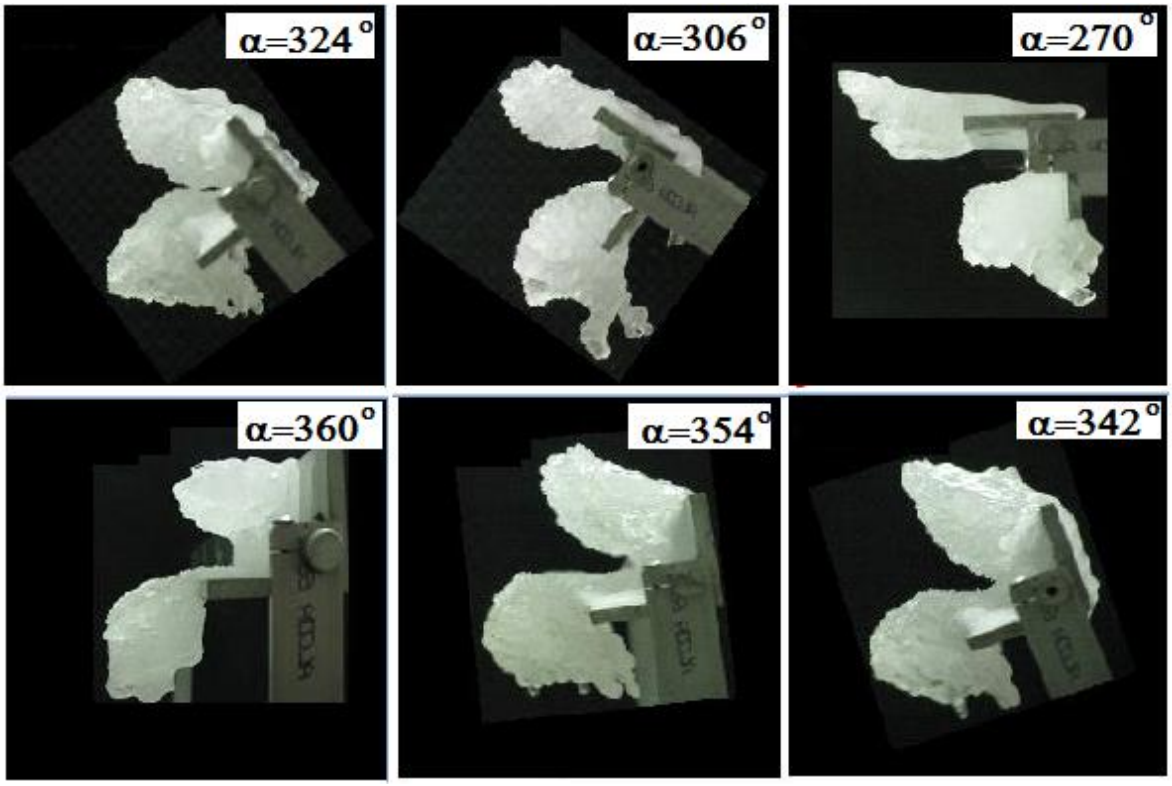

Figure 4-11: A51xL9-2 ice accretion profile for α=270° to α=360°

A comparison between A51xL9-1 and A51xL9-2 (Figure 4-12) for angles of attack α=0° and α=180° shows that because of the flow pattern around the vertical plate [49], droplets start to freeze from the stagnation line and continue on both sides. This may be explained by the fact that the ice surface height is the size of the boundary layer on the vertical surface. The same results were observed for the cylinder [95] and the airfoil [6].

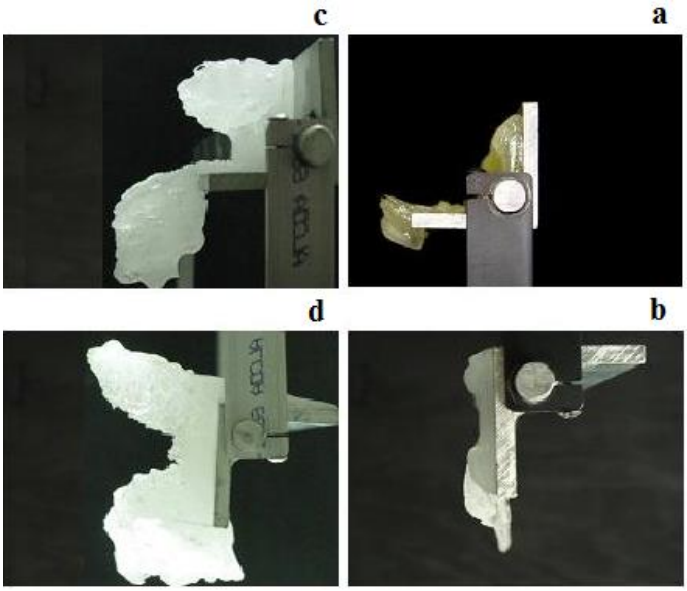

Figure 4-12: A51xL9-1 (a and b) and A51xL9-2 (c and d) ice profiles for α=0° and α=180°

Figure 4-13 shows the A51xL9-2 accumulated ice front view for different angles of attack. The tightly packed glaze ice was observed for different angles. There were some small icicles under the horizontal surface of the angle member which are explained by the gravity mechanism on super cooled water droplets. It seems that the direction of the formation of the icicles was affected by the wind direction on the angle member.

Figure 4-13: A51xL9-2 ice structure for α=360°, α=342° and α=306°

Figure 4-14 shows the normalized ice mass per unit length for A51xL9-1 and A51xL9-2. The ice mass per unit length was normalized by using equation below:

$$IM_N = \frac{(IM_{\max} - IM_C)}{(IM_{\max} - IM_{\min})} \quad (4\text{-}1)$$

Where IM_N is ice mass per unit length, IM_{max} and IM_{min} are maximum and minimum obtained ice masses obtained per unit length for different aerodynamic angles and IM_C is the ice mass obtained per unit length for each aerodynamic angle.

It seems that two normalized curves behave in the same manner, by increasing the angle of attack, but the rate of changing is different for each graph. One of the reasons to have the same manner for two different icing situations is the corner effect on ice accretion.

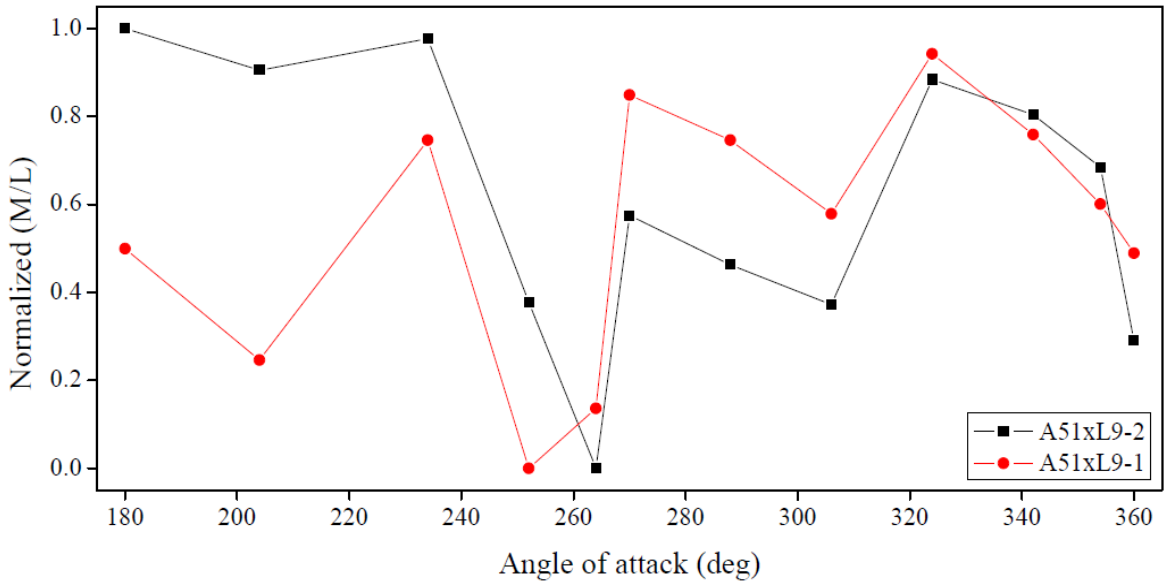

Figure 4-14: The normalized ice mass per unit length for A51xL9-1 and A51xL9-2

4-2-3-Side slip angle (Yaw angle)

The A51xL9-2 icing for different sideslip angles is shown in Figure 4-15. It was observed that by increasing sideslip angle, the accreted ice on the upper surface was changed based on the direction of accretion which is perpendicular to the direction of streamlines flow while in lower surface, the ice profile changes to a scallop shape. The scallop shape may be formed because, by changing sideslip angle, there is no variation on the stagnation line, and in bigger angles, the direction of droplet trajectories changed and the ice accumulated more in the front than in the back.

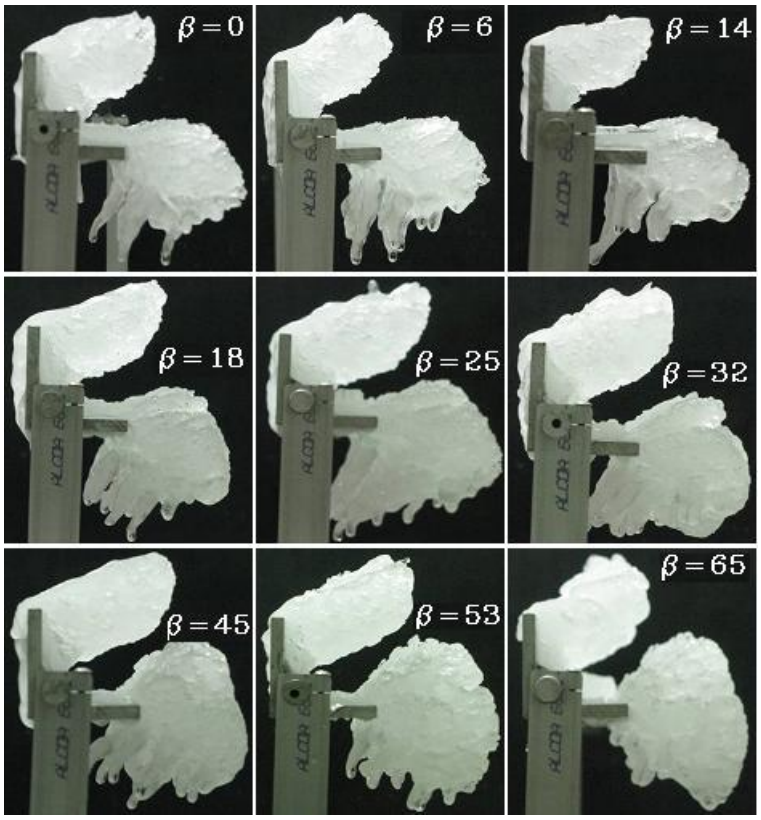

Figure 4-15: A51xL9-2 ice profiles for different sideslip angles

Figure 4-16 shows the accreted ice on A51xL9-2 for β=0°, β=25° and β=65°. When the sideslip angle increased, the tightly packed glaze ice changed to glaze ice feather forms. The feathers are icing structures that are narrow at their initiation point on the surface and wider at their top [6]. As mentioned before, the feather formation is due to the preferred direction of growth, which is perpendicular to the streamline. Accordingly, their thickness in the flow direction is less than their width in the direction perpendicular to the flow.

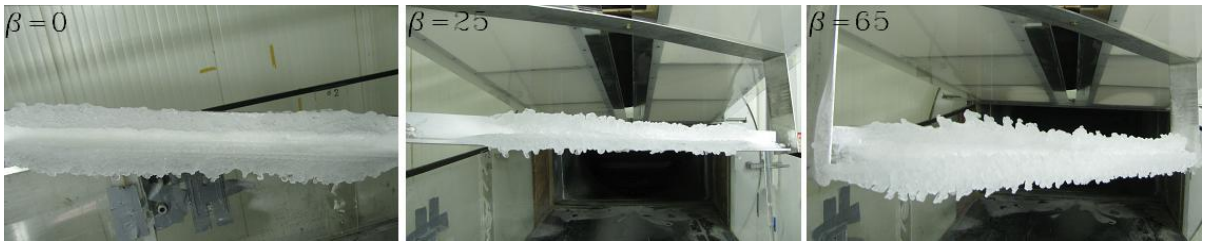

Figure 4-16: A51xL9-2 ice structure for β=0°, β=25° and β=65°

The normalized ice mass per unit length for A51xL9-1 and A51xL9-2 is shown in Figure 4-17. These graphs show that the ice mass variation for different sideslip angles for both models is similar while their slope is different.

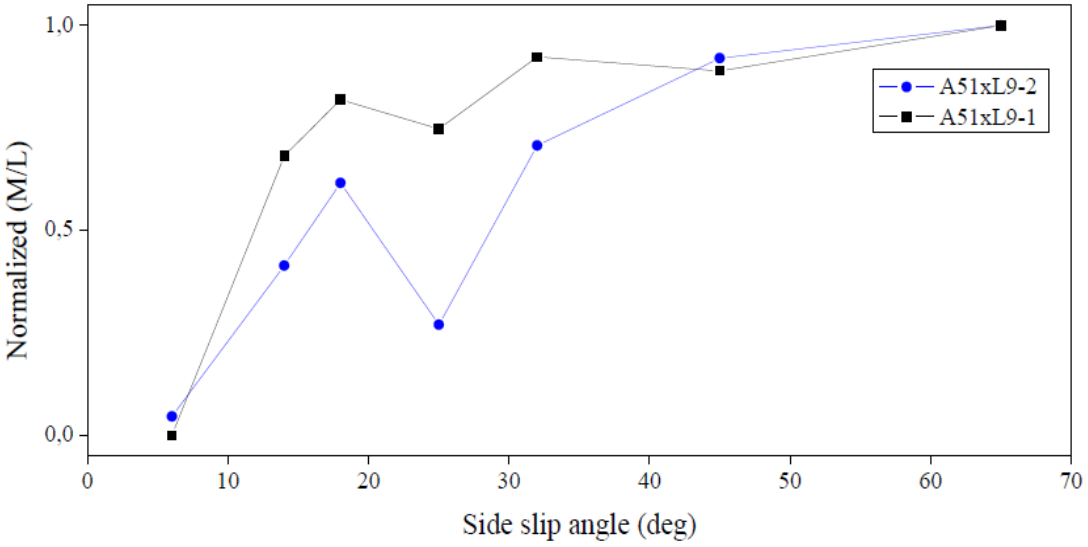

Figure 4-17: Normalized ice mass per unit length of A51xL9-1 and A51xL9-2 for different sideslip angles

4-2-4-Rolling angle

For this study, the rolling angle was set at γ=0°, γ=10°and γ=26°. The limiting values were determined by geometrical constraints. Figure 4-18 shows ice profiles for A51xL9-2. The ice was completely non-uniform on the angle member because of the gravity effects. Many droplets reached the angle surface slide on the surface, and then froze.

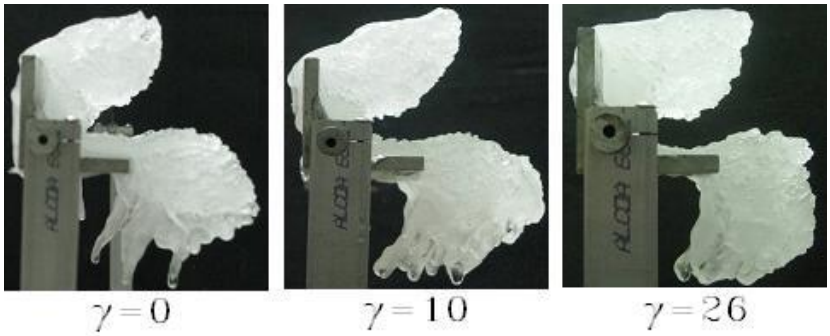

Figure 4-18: Ice profiles of A51xL9-2 for different rolling angles

The same mechanism was observed for A51xL9-1, Figure 4-19 shows the ice accretion for angles γ=10°, γ=18°and γ=26°. It seems that the maximum ice thickness started to move towards the lower side. It was difficult to distinguish any specific pattern of ice for A51xL9-1 and A51xL9-2 because the gravity effect caused droplets to move down and they become trapped between other frozen droplets.

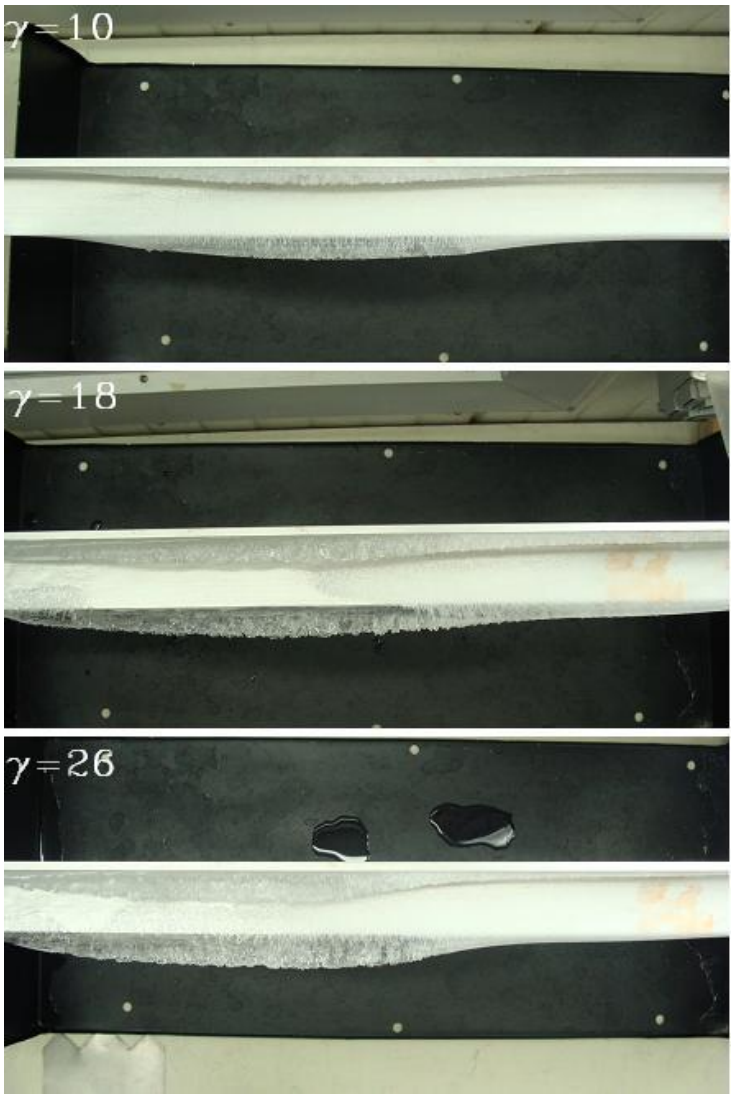

Figure 4-19: Accreted ice top view of A51xL9-1 for different rolling angles

The normalized ice mass per unit length for different angle members is shown in Figure 4-20. Both plots show that the effect of gravity becomes relatively important when increasing rolling angle. According to the two plots, it is obvious that the droplets tend to go more toward the lower side of the angle member. This may be explained by the effect of

gravity at high temperature when droplets do not have enough time to freeze immediately as they reach the angle bar surfaces.

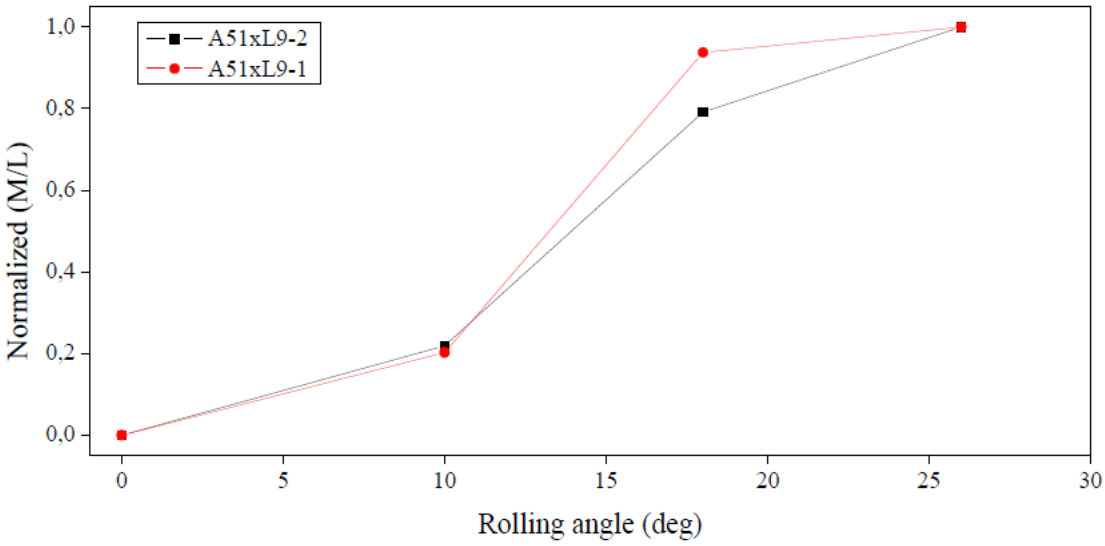

Figure 4-20: Normalized ice mass per unit length of A51xL9-1 and A51xL9-2 for different rolling

4-2-5-Estimation of Drag Coefficients of Ice-Covered Angle Bars for different angles of attack

An important practical question is to determine how the aerodynamic forces on a tower leg vary due to ice accretion. In particular, the drag coefficient is calculated for the angle member with different mass and shape of ice accretion as obtained in the experiments described in the previous section. The calculation procedure is based on the standard ISO12494 [40]. The calculation of drag coefficients for non-aerodynamic geometries, such

as an angle member, is difficult. The calculation requires several input parameters such as ice type, ice thickness, and drag coefficient of angle member without ice.

In order to calculate drag coefficients of ice-covered angle bars, the type of ice must firstly be specified; the glaze ice was the type chosen for these experiments. Considering this point and the thickness of the angle bar, which was less than 0.3 m, the corresponding tables from the standard ISO12494 were selected. Then, the thickness of ice on the angle bar measured from previous experiments was applied in order to specify the category of glaze deposits (ICGx). The drag coefficient for the angle bar without ice (C_0) was available in [3]. Once these data were known, tabulated data from the same standard provided the drag coefficient of the ice-covered angle bar.

The drag coefficient for A51xL9-1 and A51xL9-2 are presented in Figure 4-21. It is shown that the drag coefficient was reduced for greater LWC and higher velocity (A51xL9-2). In other words, the drag coefficient decreased by increasing ice accretion on the angle member. When accumulated ice increased on the angle surfaces, the projected area increased. From Equation 4-2 when the projected area is increased, the drag coefficient decreases. Where F_d is drag force, ρ is air density and v is wind velocity.

$$C_d = \frac{2F_d}{\rho A v^2} \tag{4-2}$$

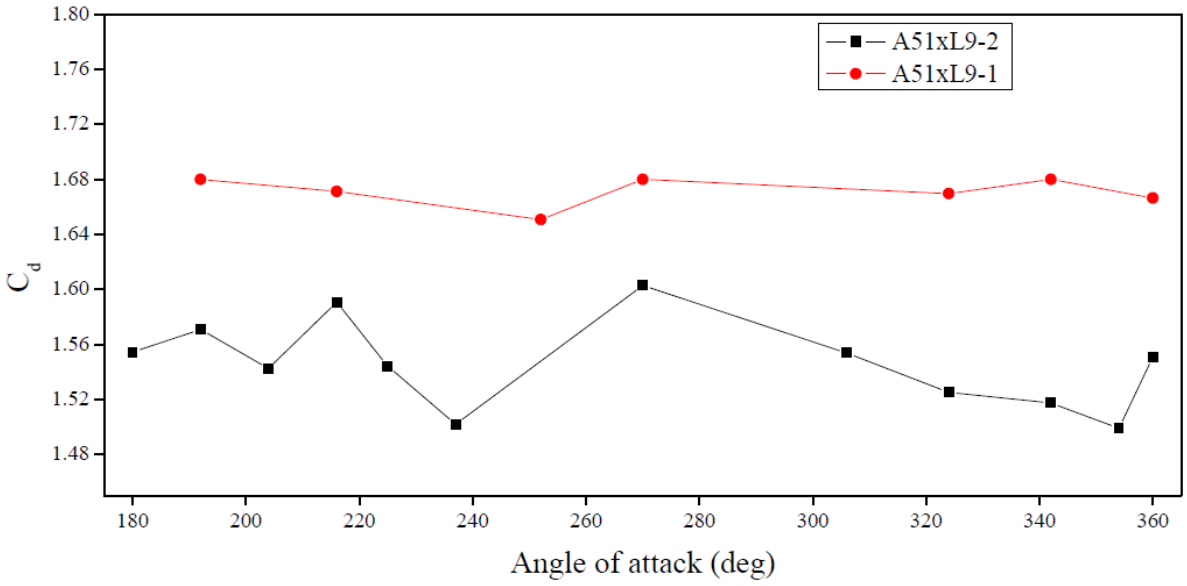

Figure 4-21: Drag estimation based on standard ISO12494 for A51xL9-1 and A51xL9-2

4-3-Wind effects on vertical angle member icing in the test section

4-3-1- Sign convention and definition of the variables

Figure 4-22 presents the sign convention used and defines the aerodynamic angles applied on the vertical angle member, in order to follow the results easily.

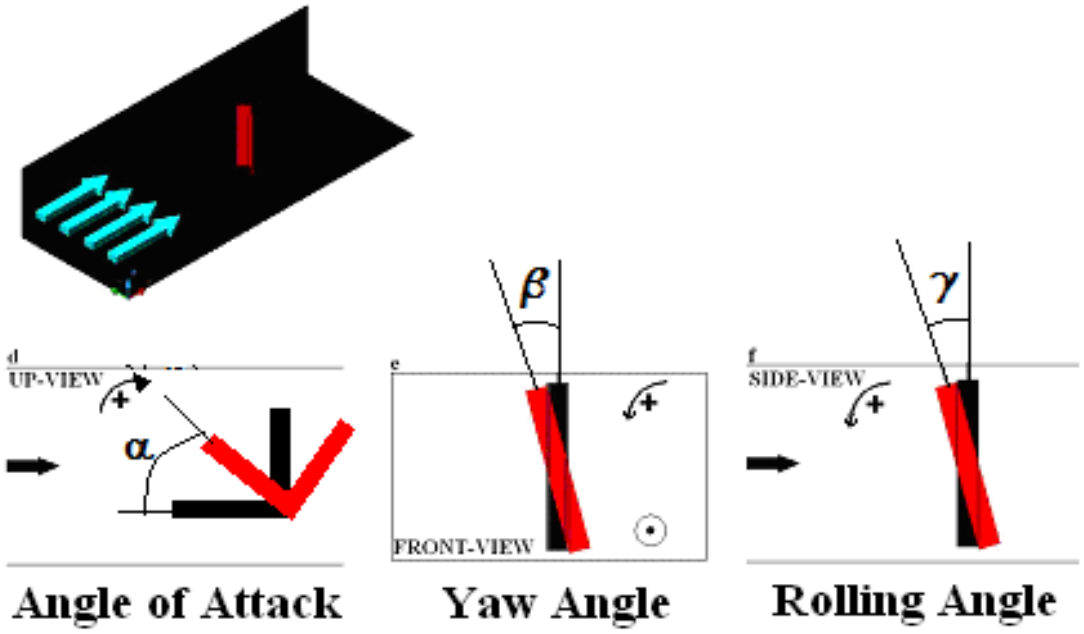

Figure 4-22: Sign convention and definition for icing experiments

4-3-2- Angle of attack

Figure 4-23 shows the ice mass per unit length for the angle member mounted vertically. The maximum projected area of the angle member is in α=135° and α=315°. This means that more droplets can freeze on angle member surfaces but for α=135°, the corner changes the stream lines direction and less ice accumulates on the surfaces of the angle member (Figure 4-23). Another significant effect on the ice accretion for a vertical angle member is gravity. Figure 4-24 shows the accreted ice for different angles of attack. The ice morphology changes on angle member surfaces. It may be explained by two mechanisms: droplet drag force and droplet gravity force. More droplets tend towards the

bottom of the angle member because droplet gravity effects are more dominant than droplet drag effects.

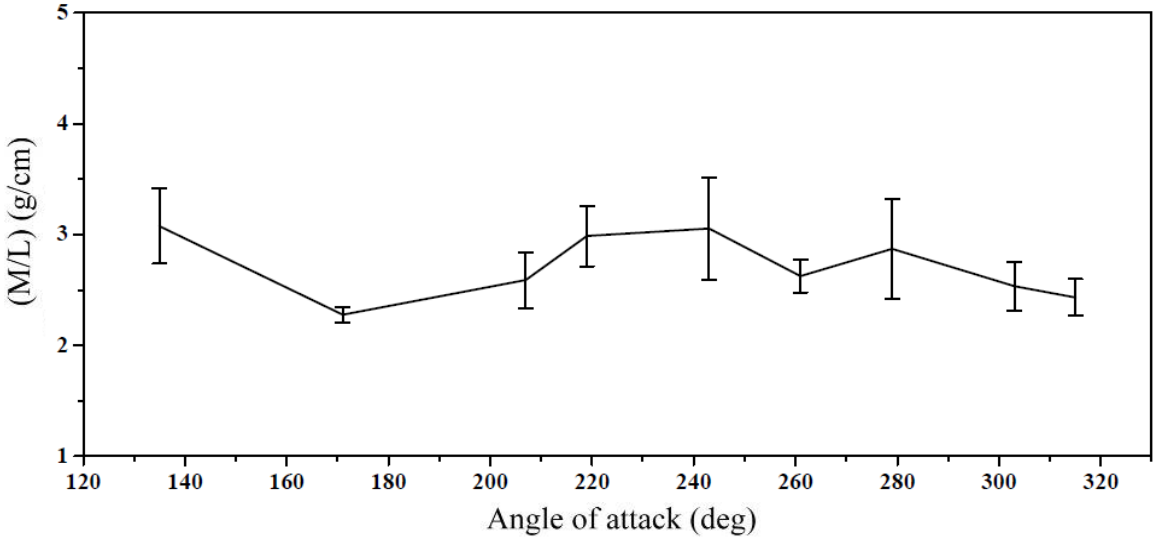

Figure 4-23: A51xL4 ice mass per unit length for different angles of attack

Figure 4-24 shows that very small curved ice structures named roughness elements by Vargas started to grow on the surface. They increased rapidly towards the bottom of the angle member because more droplets were caught between the roughness elements and froze.

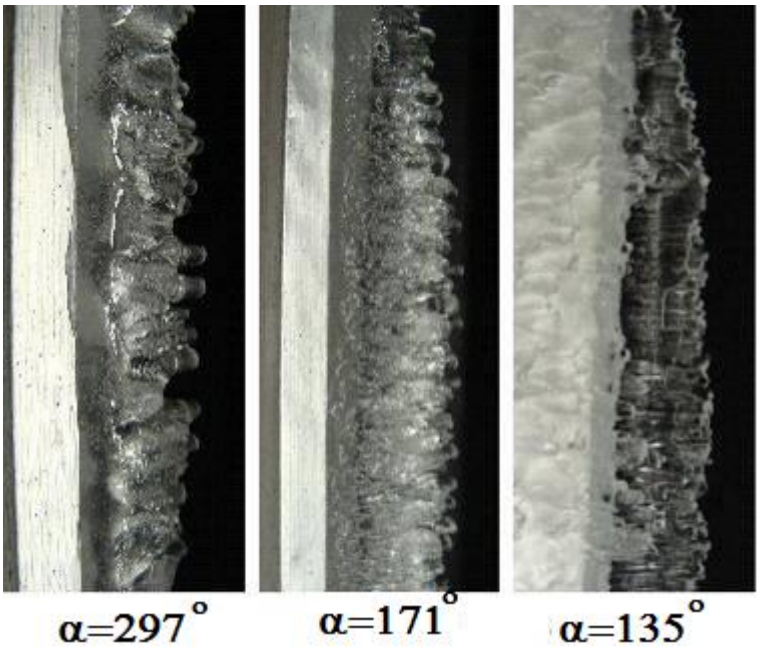

Figure 4-24: A51xL4 ice accretion for three different angles of attack

4-3-3-Sideslip angle (Yaw angle)

Figure 4-25 shows accreted ice on a vertical angle member for β=6°. As shown, roughness elements were formed at the beginning of the ice accretion process. The gravity effects on the droplet trajectory caused more droplets to move towards the bottom of the angle member. As a result, more droplets were trapped between roughnesses elements while towards the top of the angle member, the roughness elements developed into glaze ice feathers when they reached a given height. Figure 4-25b shows tightly packed feathers. For all other sideslip angles, the same results were obtained.

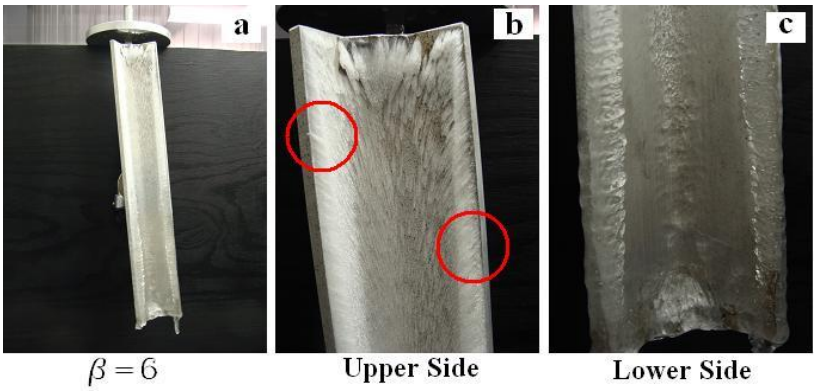

Figure 4-25: A51xL4 ice accretion for a) β=6°, b) A51xL4 upper side, c) A51xL4 lower side

4-3-4-Rolling angle

The ice mass per unit length of the angle member which was mounted vertically in the tunnel has a maximum at γ=-6°. It seems that when the angle member rotates in two directions around a lateral axis, the ice mass decreases slightly (Figure 4-26). It may be explained by the effect of the projected area. When the angle member rotates around a lateral axis, its projected area decreases and fewer droplets can reach angle member surfaces.

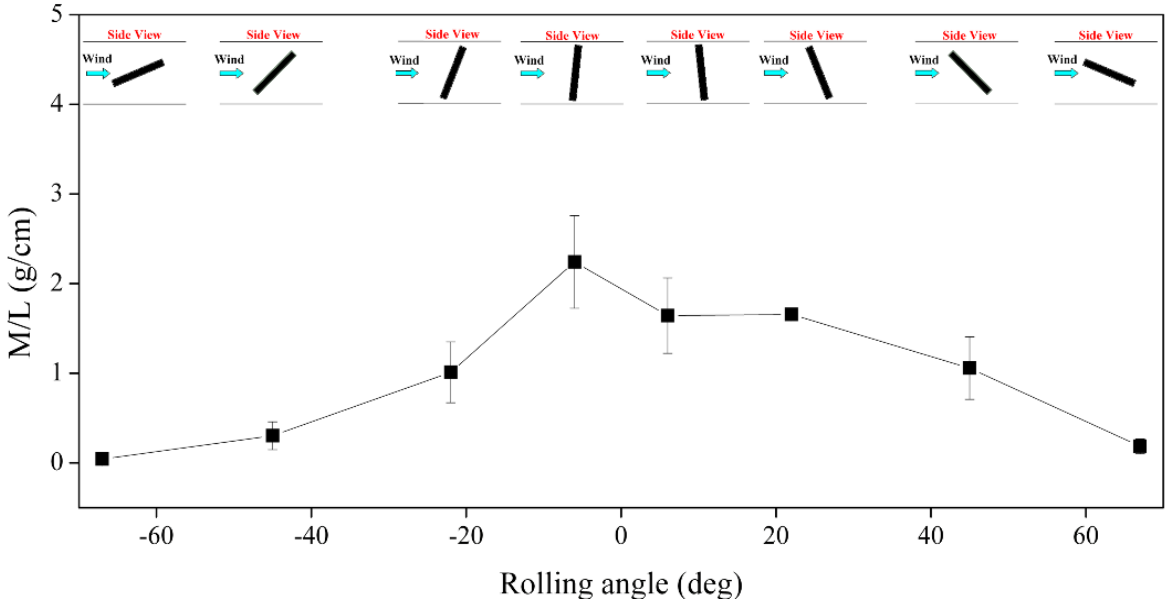

Figure 4-26: A51xL4 ice mass per unit length for different rolling angles

Figure 4-27 shows the ice morphologies for positive rolling angles. At γ=67°, the ice accreted on the edge of the angle member. A side view of ice accretion shows tightly packed feathers on the edges. By decreasing γ to 45°, the ice is covered with glaze ice feathers with a preferred direction of growth that is perpendicular to the streamlines. Then the feathers reach a specific height and join each other, creating a scallop shape [6]. For other angles, tightly packed feathers were simply observed after ice accretion.

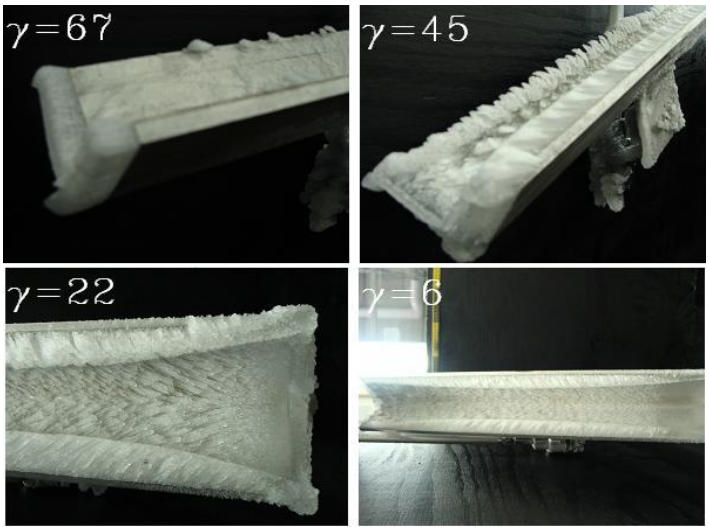

Figure 4-27: A51xL4 ice accretion profiles for different rolling angles

Conclusion

It is difficult to obtain the same ice structure in icing simulation compared to atmospheric icing. The ice simulations showed approximately the same tunnel icing simulation for glaze and rime ice. The rime ice structure was very brittle compared to glaze ice and it was difficult to get rime ice shape and do more measurements. So, the glaze ice was chosen for the next experiments of this study with two different sets of thermo physical parameters.

The stagnation line and corner effects on ice accretion were mentioned for A51xL9-1 and A51xL9-2 ice profiles for different angles of attack. It was shown that the droplets started to freeze from the stagnation line and continued on both sides. For different angles of attack, the tightly packed glaze ice was observed for A51xL9-2. While the ice

morphology for different sideslip angles show that when the sideslip angle increased, the tightly packed glaze ice changed to glaze ice feathers form.

The normalized ice mass per unit length graphs for A51xL9-1 and A51xL9-2 behaved in the same manner by increasing the angle of attack, sideslip and rolling angle but the rate of changing was different for each graph.

The drag coefficient was reduced for greater LWC and higher velocity (A51xL9-2). In other words, the drag coefficient decreased by increasing ice accretion on the angle member for different angles of attack.

For the sideslip angle of a vertical angle member, the gravity effects on droplet trajectory caused more droplets to move towards the bottom of the angle member and more droplets to be trapped between roughness elements while towards the top of the angle member, the roughness elements developed into glaze ice feathers when they reached a given height.

CHAPTER 5

THE EFFECT OF DSD AND LWC ON ICE ACCRETION AND DRAG COEFFICIENTS

CHAPTER 5

THE EFFECT OF DSD AND LWC ON ICE ACCRETION AND DRAG COEFFICIENTS

Introduction

Spray icing often forms in cold environments as a result of the collection of an aerosol of water or brine by a structure. LWC and DSD vary inside the aerosol cloud for different icing conditions. These variations are more significant when air velocity is low and cloud droplets are large. The main reason of these variations is related to gravity and inertia forces acting on super cooled droplets. These forces alter the trajectories of particles that contribute to ice accretion [26], [27] and thus, they have an influence on the ice mass and shape, resulting in varying aerodynamic coefficients on the tower.

This chapter contains two main parts. First, the variations of DSD and LWC in vertical and streamwise directions will be presented. Then, variations of ice accretion on an angle bar in the same direction as the flow will be shown to determine the aerodynamic forces on a tower leg as a function of ice accretion. After that, the ice accretion experiments were carried out under two conditions with different LWCs and air velocities. The drag coefficient was calculated with different masses and ice shapes for the angle bar as determined by the experiments.

5-1- Sign convention and definition of the variables

Figure 5-1 presents the sign convention used and defines the reference point, in order to simplify the reading.

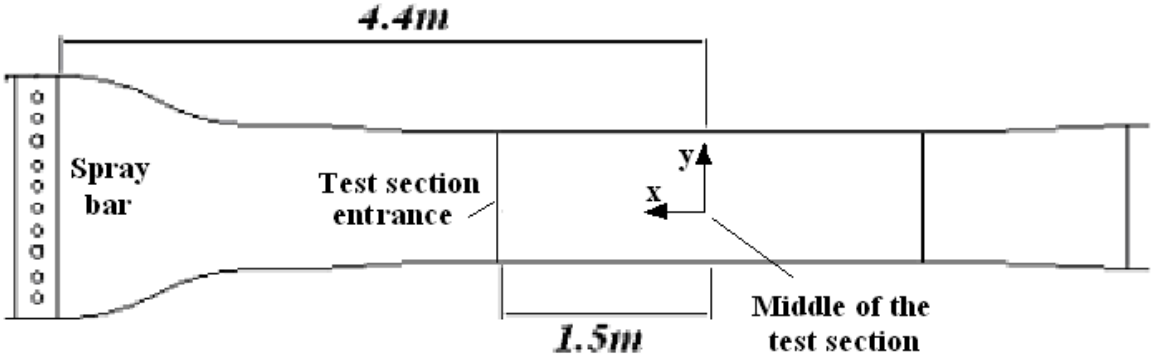

Figure 5-1: Sign convention and reference point

5-2-DSD and LWC measurements

5-2-1-Streamwise and Vertical Variations of Median Volume Diameter (MVD) and LWC of the droplets

The effects of air velocity and nozzle pressures on DSD in the produced spray and on the LWC in the cloud in the middle of the test section of a low-speed horizontal wind tunnel were studied by Kollar and Farzaneh [89] and by Kollar et al. [96], respectively. The streamwise and vertical variations of these characteristics in the test section were discussed in Kollar and Farzaneh [97] for two specific icing conditions. The following discussion focuses on the streamwise and vertical variations of MVD and LWC for different air velocities and nozzle pressures.

The experiments were carried out in 4 streamwise and 3 vertical positions, and for 4 air velocities. Furthermore, 6 different nozzle air pressures were applied between 180 and 620kPa, when the nozzle water pressure was kept constant. In order to reduce the number of figures, variations along the streamwise directions are presented in one vertical position only, and variations along the vertical direction are shown in one streamwise position only. The MVD and LWC are drawn in the figures of this section as functions of differential pressure, $dp = P_w - P_a$, which is a key parameter in determining DSD and LWC [89]. An additional parameter, either the streamwise or the vertical position, is varied in each figure.

Figure 5-2 presents the MVD variations along the streamwise direction at y = –0.07 m. The MVD is approximately constant for the lowest differential pressures. It then

increases until reaching a maximum which is followed by a decreasing tendency. The value of the differential pressure, where the increasing tendency begins, increases with air velocity (from about –100 kPa for 5 m/s to about +50 kPa for 28 m/s). The maximum also appears for a higher differential pressure when the air velocity is higher: it is around 100-150 kPa for 5 m/s, around 200 kPa for 10 m/s, and out of the diagram for 20 and 28 m/s (above 300 kPa). The gravity effect is more significant than the drag effect for low air velocity. Hence, the MVD at a specific height decreases along the streamwise direction because larger droplets go toward the bottom of the test section. When velocity increases, the drag effect becomes more significant than the gravity effect for clouds including small droplets only, and droplet separation according to their size occurs only for clouds with the larger droplets. Correspondingly, the curves presenting MVDs at different streamwise positions become distinguishable for aerosol clouds with MVD of 20 μm when air velocity is the lowest (5 m/s), whereas this limit increases to about 50μm when air velocity is the highest (28 m/s). Similar tendencies were observed at the vertical position y = 0 m with smaller differences between MVDs at different streamwise positions. These differences vanish nearly completely at y = +0.07 m, because this position is close to the top of the cloud where droplets are small even at the streamwise position of x = –1 m.

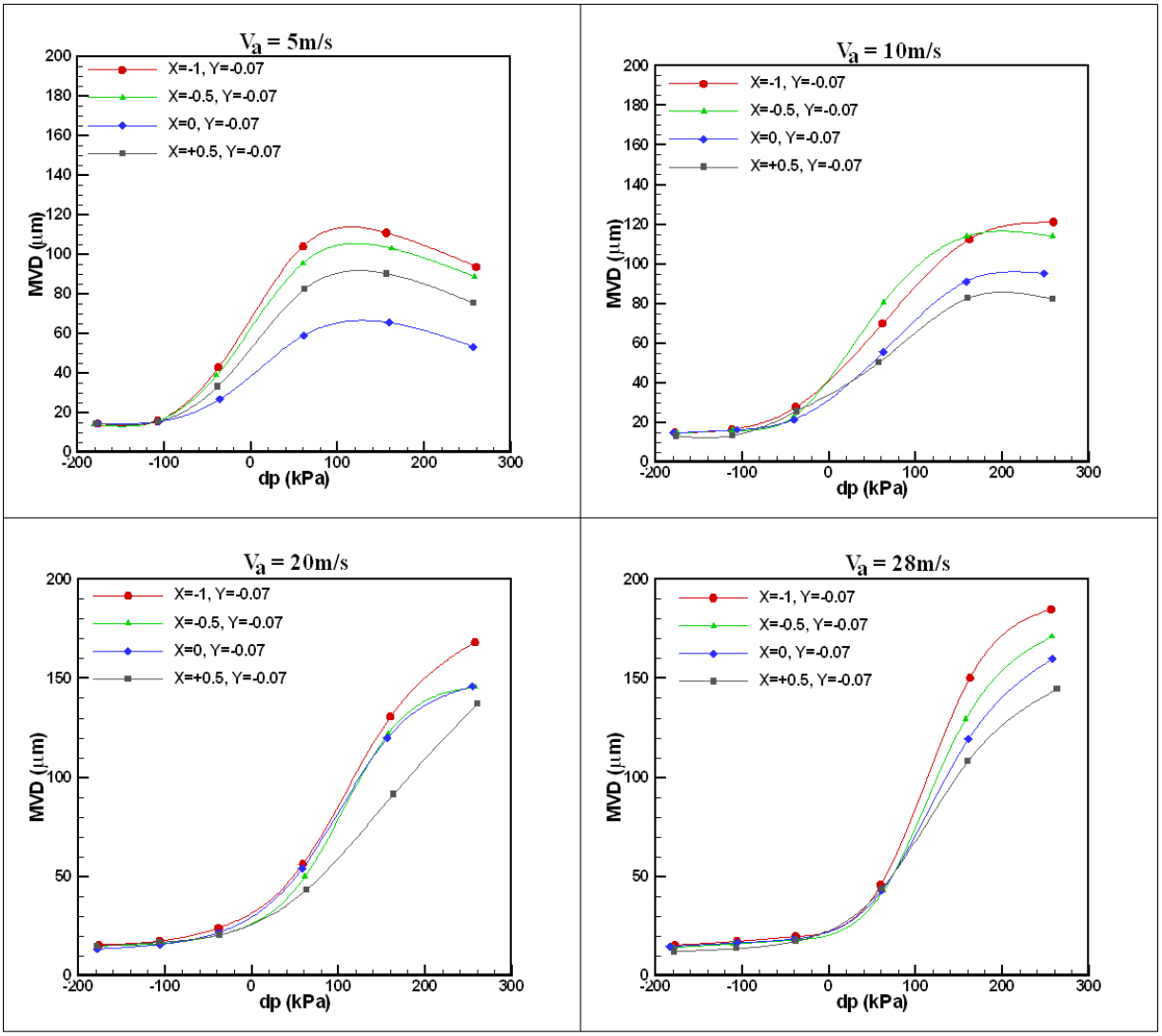

Figure 5-2: MVD variations along the streamwise direction at y = –0.07 m

LWC increases with the differential pressure, even for smaller differential pressures, until reaching a maximum which is then followed by a decreasing tendency (Figure 5-3). Similarly to the MVD, a maximum for LWC also occurs at a higher differential pressure when the air velocity is higher. LWC at the height of y = –0.07 m decreases in the

streamwise direction at 5m/s; this tendency is the same at 10m/s, but the curves obtained for different streamwise positions appear closer to each other; and LWC becomes constant along the streamwise direction when air velocity approaches 20 m/s. LWC does not change significantly in the streamwise direction at 20 m/s, but it is greater for downstream positions for some differential pressures; and the tendency is reversed completely at 28 m/s, i.e. the LWC at the height of y = –0.07 m increases in the streamwise direction. This behavior may be explained by the fact that when air velocity is high, the cloud is not much extended vertically at the beginning of the test section, but more and more droplets reach the vertical position of y = –0.07 m as they move forward in the test section. This explanation is also confirmed by the fact that a similar reverse tendency was not observed at y = 0 m. Most of the cloud was around mid-height at the beginning of the test section for all the air velocities considered, so that LWC at this height did not increase in the streamwise direction. The LWC was significantly lower at the height of y = +0.07 m, and variation in the streamwise direction was small. However, it is more difficult to evaluate the tendency, because this position is very close to the boundary of the cloud.

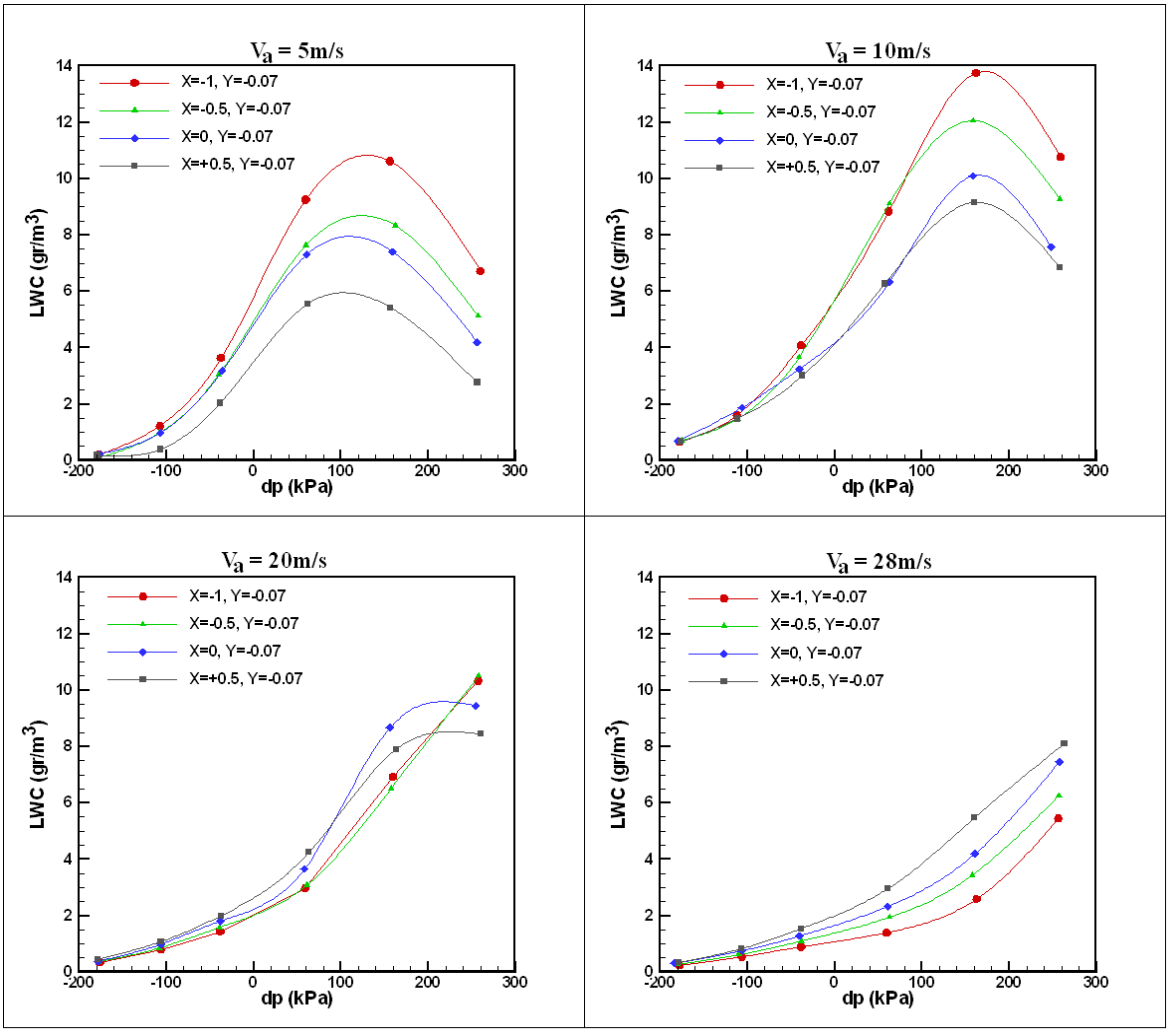

Figure 5-3: LWC variations along the streamwise direction at *y* = –0.07m

Figure 5-4 presents the variation of MVD in the vertical direction at the streamwise position of x = 0.5 m. MVD increases from top to bottom for high enough differential pressures, i.e. when clouds with MVD of at least 20 μm are produced, for air velocity of 5 m/s. For higher air velocities, MVD was similar or even greater at mid-height (y = 0 m) than at the vertical position of y = –0.07 m for clouds with MVDs up to about 80μm. Then,

when the cloud included larger droplets, the greatest MVD value was measured close to the bottom of the cloud (at y = –0.07 m). Larger droplets tend to move toward the bottom of the tunnel during their flow in the test section. However, when the droplets are not large enough (≤80 μm) and the air velocity is high enough (≥10 m/s), then numerous large droplets are still found close to mid-height at the streamwise position of x=0.5 m.

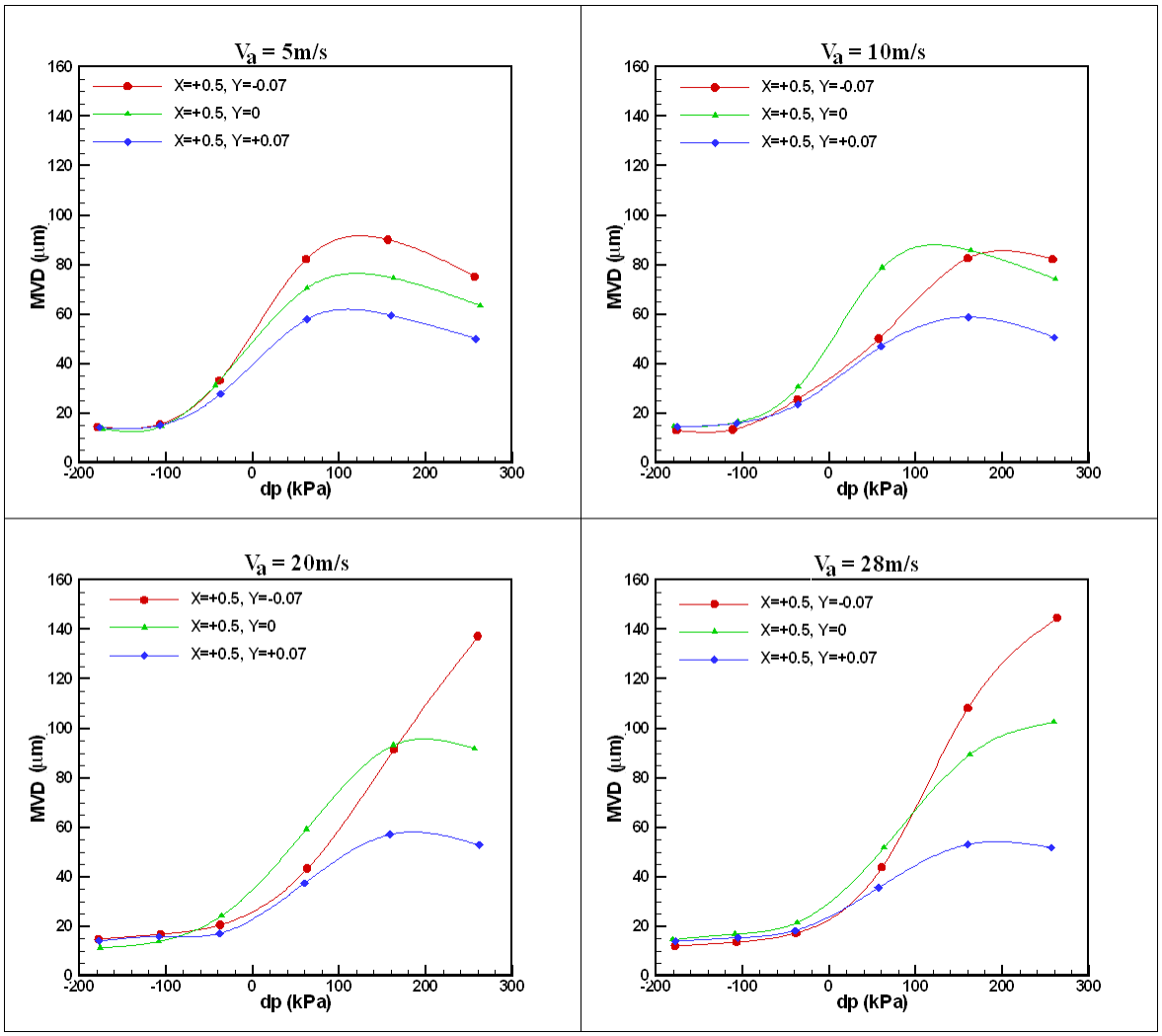

Figure 5-4: MVD variations along the vertical direction at x = 0.5 m

LWC also increases in the vertical direction toward the bottom for low air velocities and if the MVD of the cloud is large enough, the LWC increases too for higher air velocities. When the differential pressure is small, and consequently droplets are not too big (MVD $\leq$80 μm), the LWC at the vertical position y = 0 cm is equal or greater than at y = –0.07 m at the streamwise position x = 0.5 m, as shown in Figure 5-5. This is due to the same process that explained the same tendency for MVD in the previous paragraph. Upstream from this position, i.e. for x = –1 , –0.5 , and 0 m where the aerosol cloud is less expanded, for the higher air velocities considered (20 and 28 m/s), and for clouds without large droplets, LWC is significantly greater at mid-height (y = 0 m) than at the bottom of the cloud (y = –0.07 m). The all cases considered, the smallest LWC value is at the top of the cloud (y = +0.07 m).

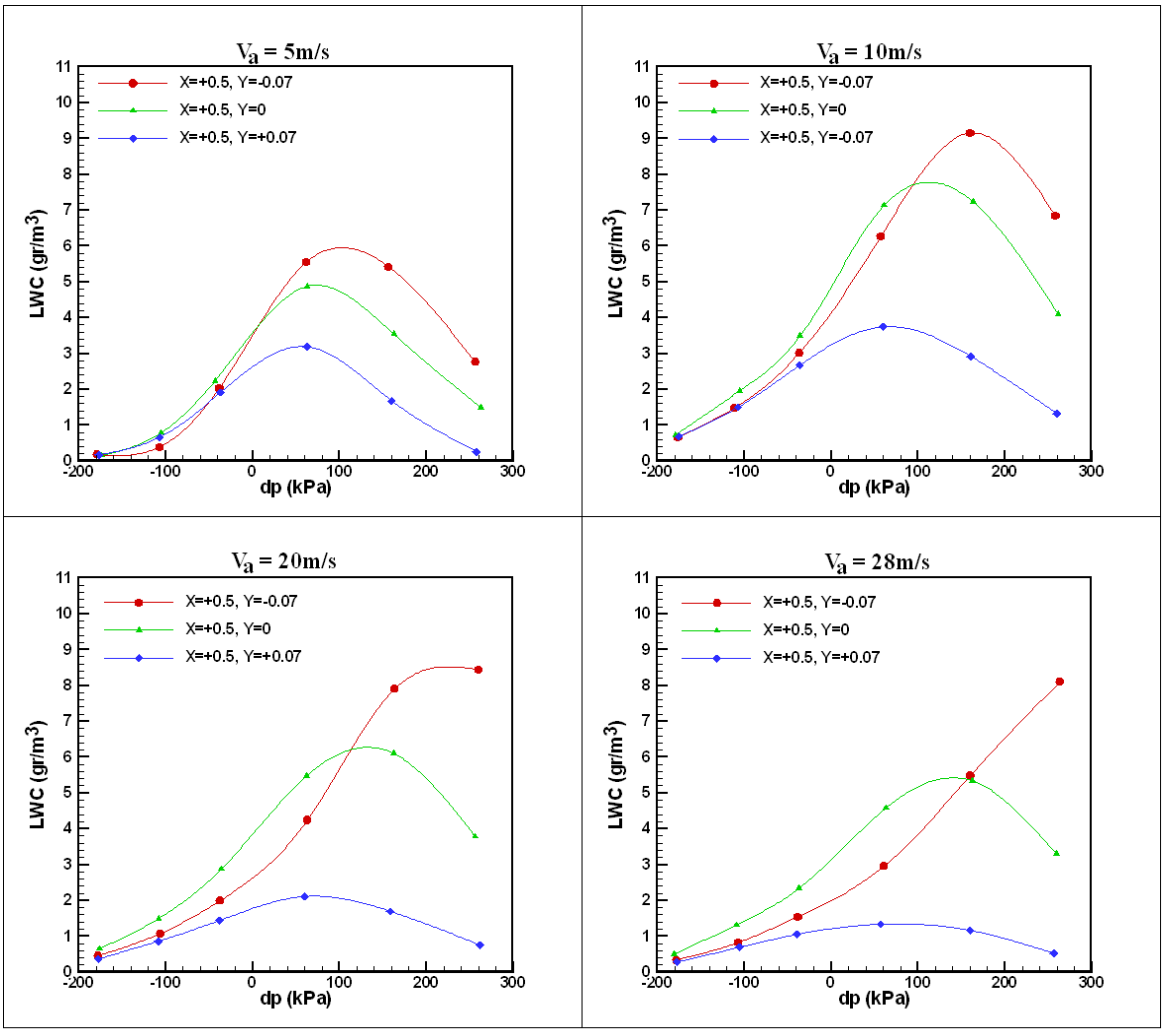

Figure 5-5: LWC variations along the vertical direction at x = 0.5 m

5-3-Ice Accretion Measurements on Tower-Leg Model

5-3-1-Streamwise and Vertical Variations of Ice Accretion on Angle Bar

The previous section discussed the streamwise and vertical variations of MVD and LWC for different air velocities and nozzle pressures. The present section mainly focuses

on studying variations of ice accretion on an angle bar in streamwise and vertical directions under two types of icing conditions, as summarized in Table 5-1. In order to reduce the number of figures, variations along the streamwise and vertical directions under the same condition and from the same view are presented in one figure.

Table 5-1: Thermo-physical parameters for icing conditions

Icing Conditions	Temperature (°C)	Velocity (m/s)	Air pressure (kPa)	Water Pressure (kPa)	LWC (center of test section) (g/m^3)	MVD (center of test section) (μm)
I	-5	25	300	300	2.8	39
II	-5	12	200	300	5.8	84

The variation of the ice mass per unit length is shown in Figure 5-6 for three vertical positions: y = +0.07, 0, and -0.07 m. The ice mass in the middle of the angle bar increases in the streamwise direction below mid-height (y = -0.07 m), which is a consequence of increasing LWC in the same direction at this height for the higher velocities considered, as can be seen in Figure 5-3.

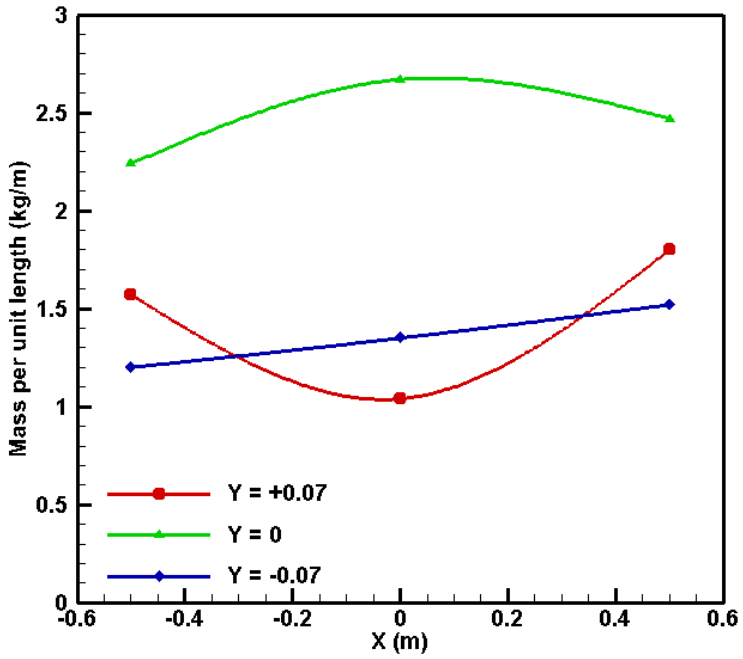

Figure 5-6: Mass per unit length, P_w=300 kPa, P_a= 300 kPa and V_a= 25 m/s

The ice profiles on the angle bar for y = -0.07 m also show that the number of impinging droplets increases downstream in the test section (Figure 5-7). Ice accretion at the position y = +0.07 m does not show an increasing or decreasing tendency, which may be consequential to the fact that this position is close to the cloud boundary that may oscillate at an interval of a few cm. Thus, LWC can considerably change even in a short vertical interval and it may also vary in time in the same vertical position [97], which makes the tendencies difficult to measure. As the cloud is less expanded in the vertical direction for high velocities, the highest ice masses were measured at mid-height (y = 0 m), which corresponds to the highest LWCs at mid-height (Figure 5-5).

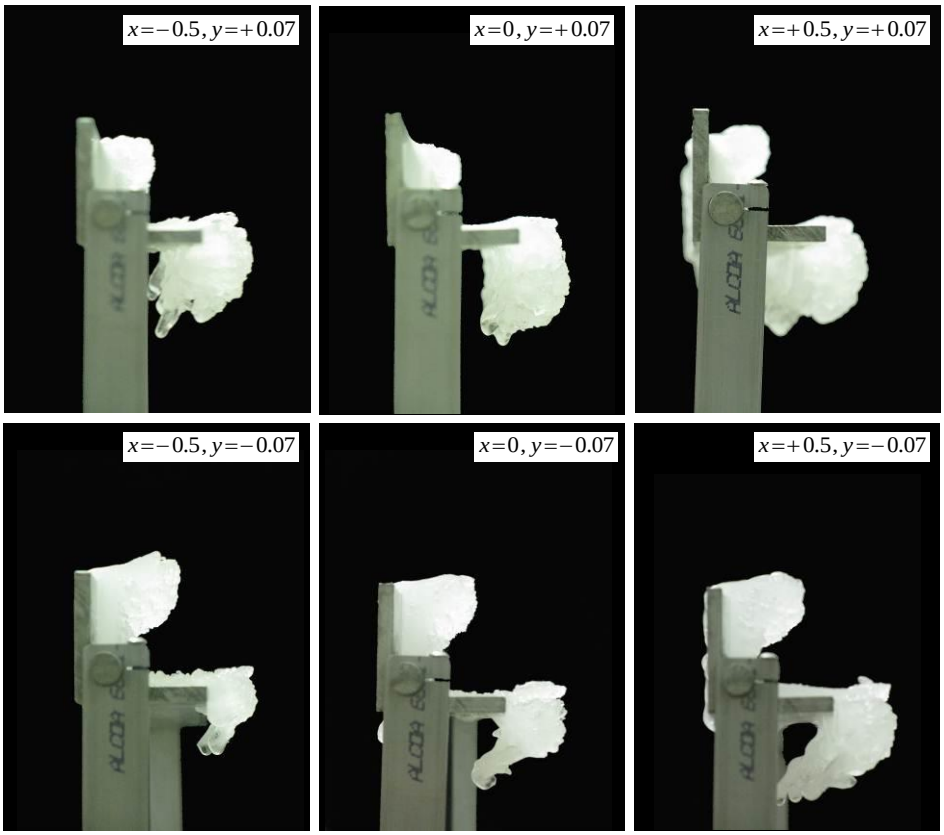

Figure 5-7: Side view of the iced horizontal angle bar, P_w=300 kPa, P_a= 300 kPa

According to the front views shown in Figure 5-8, the amount of accreted ice for x = 0, y = +0.07 is lower in the middle of the angle bar and it increases slowly towards its sides. This non-uniformity is probably due to the cloud boundary as discussed in the previous paragraph. Correspondingly, the accreted ice becomes more uniform toward the bottom of the test section.

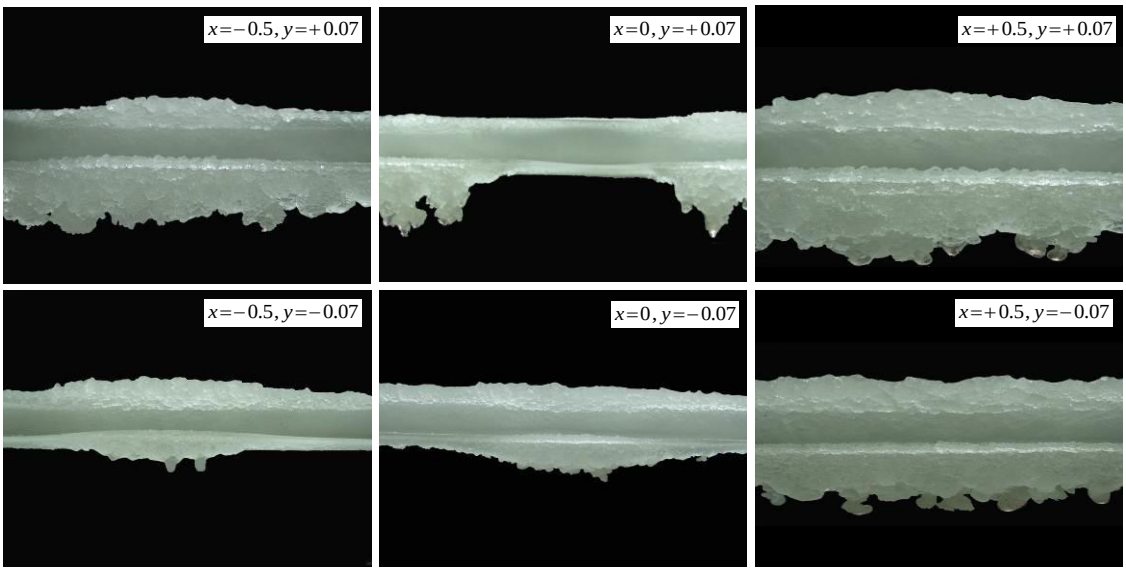

Figure 5-8: Front view of the iced horizontal angle bar, P_w=300 kPa, P_a= 300 kPa

The top views in Figure 5-9 also show that the ice accretion is more uniform for y = -0.07 m than for y = +0.07 m. However, there is a curved shape in all positions corresponding to the transverse distribution of LWC in the test section (see Chapter 4).

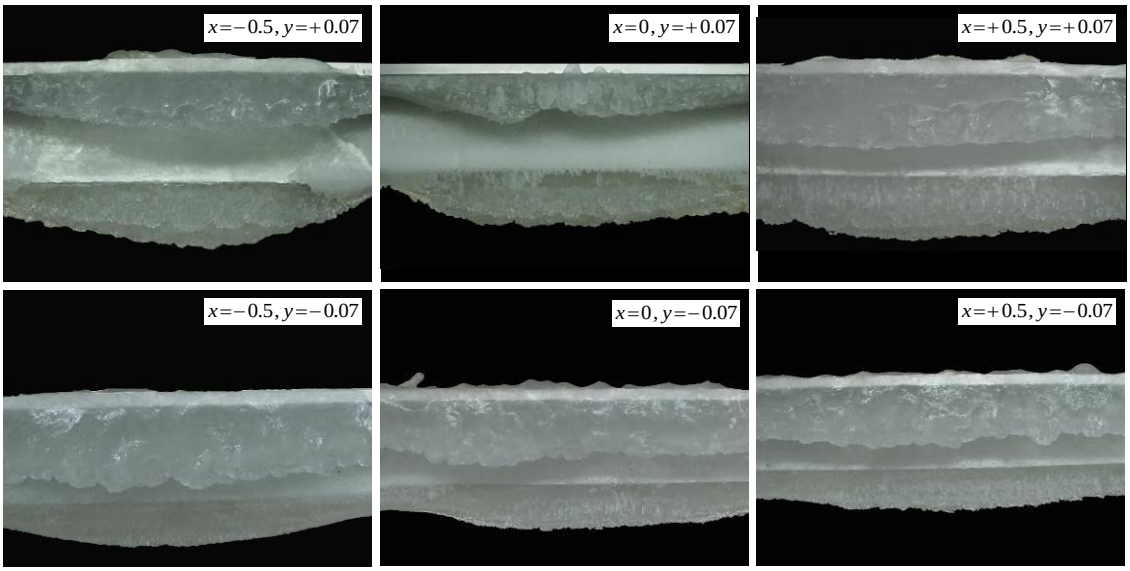

Figure 5-9: Top view of the iced horizontal angle bar, P_w=300 kPa, P_a= 300 kPa

For the condition with lower velocity, the variation in the ice mass per unit length is shown in Figure 5-10 for two vertical positions: y = +0.07 m and -0.07 m. The tendency of LWC to increase in the streamwise direction for high velocities at y = -0.07 m changes to a decreasing tendency for low velocities as seen in Figure 5-3. Correspondingly, the mass per unit length of accretion decreases in the streamwise direction. Similar to the case with higher velocity, a clear tendency cannot be seen at y = +0.07 m. However, the accretion maximum moves from mid-height toward the bottom of the tunnel. More and more droplets tend to move towards the bottom of the test section, because the effect of gravity on droplet trajectories becomes more significant than that of inertia.

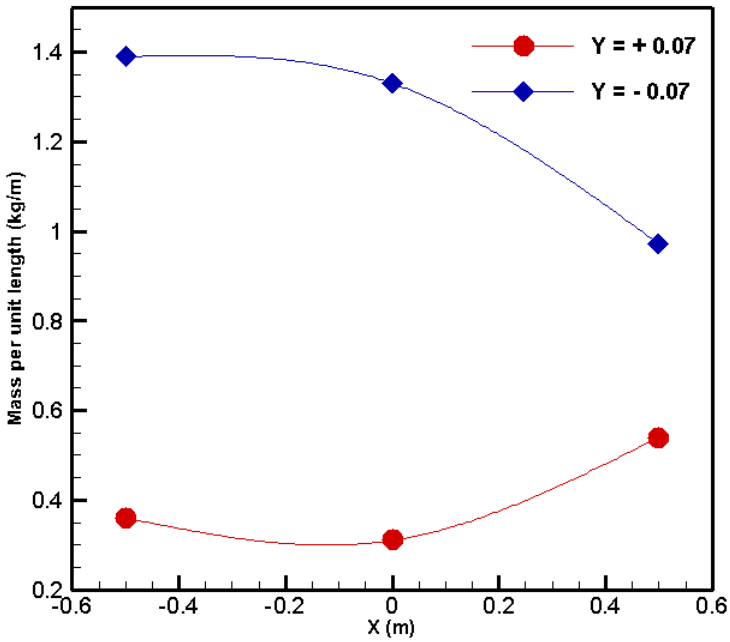

Figure 5-10: Mass per unit length P_w=300 kPa, P_a= 200 kPa and V_a= 12 m/s

According to Figure 5-11, the streamwise variation of accreted ice for the lower velocity at y = +0.07 m is similar to the one for the higher velocity (Figure 5-8), and has a minimum value in the middle of the test section. It means that the tendency of the mass per unit length is the same at y = +0.07 m for the two velocities, V_a= 12 m/s and V_a= 25 m/s. However for y = -0.07 m, the mass per unit length has an increasing tendency for V_a= 25 m/s, and a decreasing tendency for V_a= 12 m/s.

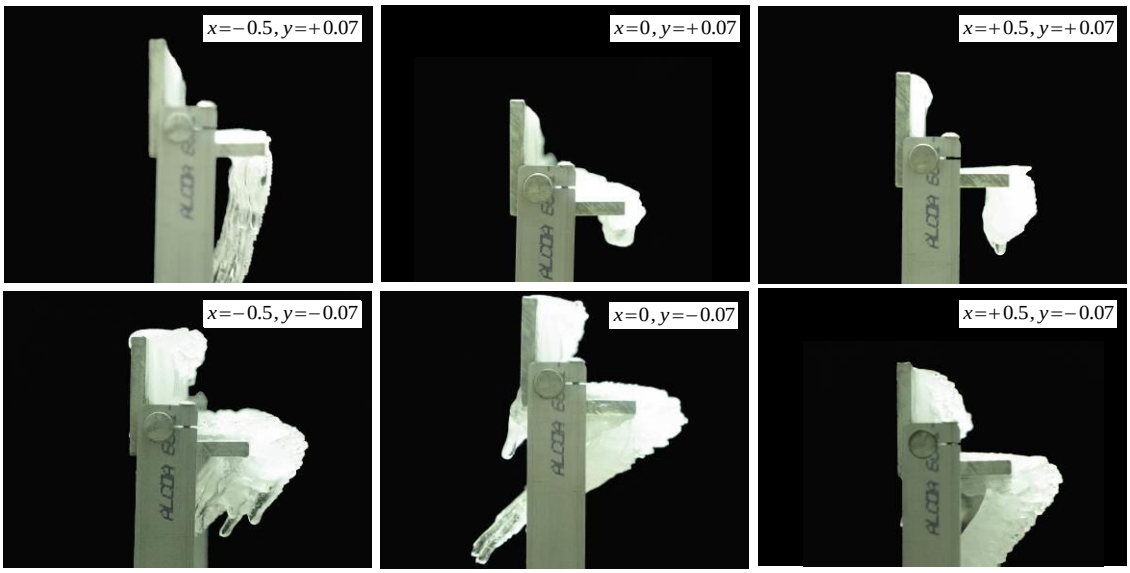

Figure 5-11: Side view of the iced horizontal angle bar, P_w=300 kPa, P_a= 200 kPa

Icicles in Figures 5-11 and 5-12 also show that the cloud extends toward the bottom. Icicles grow rapidly at y = - 0.07 m whereas those close to the top boundary of the cloud (i.e. at y = +0.07 m) are significantly shorter (except for few icicles at x = -0.5 m position). Also, it is obvious from the top views (Figures 5-9 and 5-13) that the accreted ice is more uniform for V_a= 12 m/s than for V_a= 25 m/s.

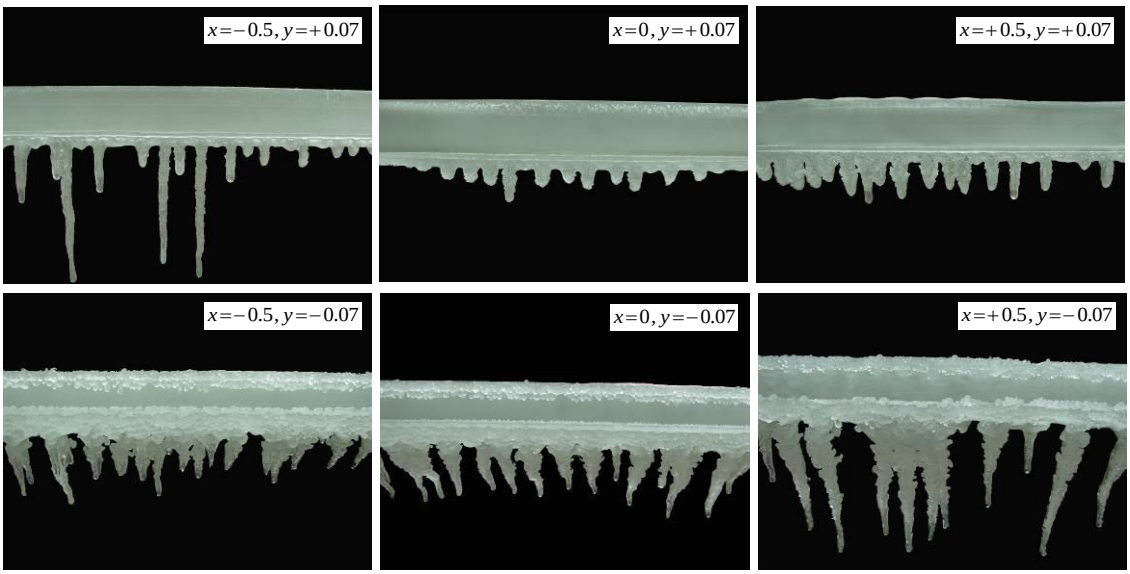

Figure 5-12: Front view of the iced horizontal angle bar, P_w=300 kPa, P_a= 200 kPa

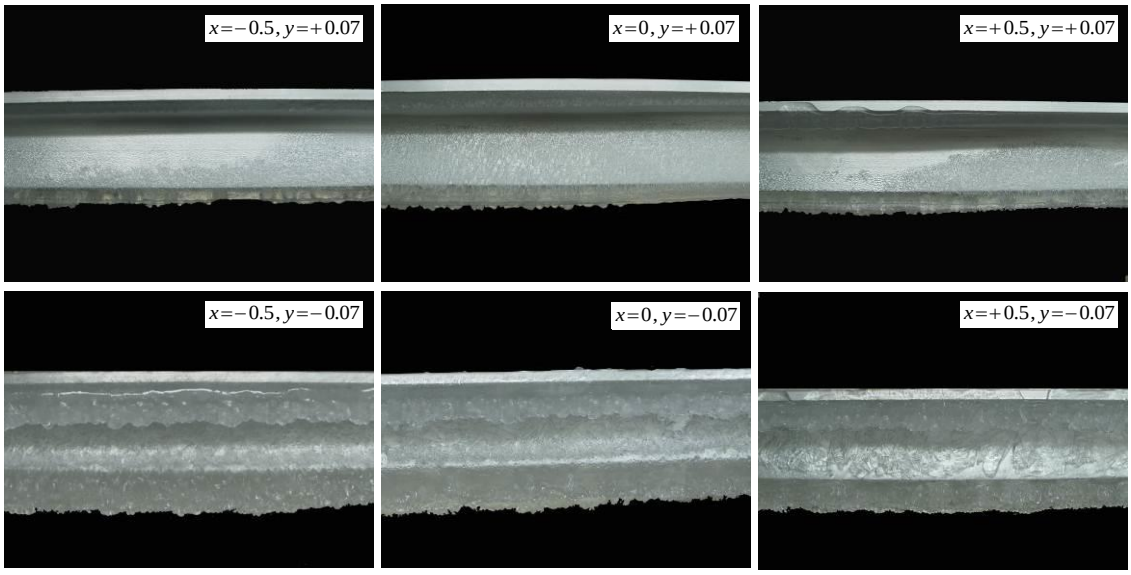

Figure 5-13: Top view of the iced horizontal angle bar, P_w=300 kPa, P_a= 200 kPa

Results of ice accretion tests on vertical angle bars are summarized in Figures 5-14 and 5-16. These results provide a more detailed view of the vertical variation of ice mass, and they also make possible the comparison of clouds in their entire vertical dimension.

Figure 5-14 compares the ice mass per unit length for the two velocities considered. The variation of ice mass per unit length in the streamwise direction for the higher air velocity (25 m/s) is not more than the measurement error (the difference between the ice masses is approximately 4% at the x = -0.5 m and x = +0.5 m positions). However, the ice mass decreases considerably in the streamwise direction (about 40% between the same positions) for the lower air velocity (12 m/s). The ice shapes in Figures 5-15 and 5-16 explain these tendencies.

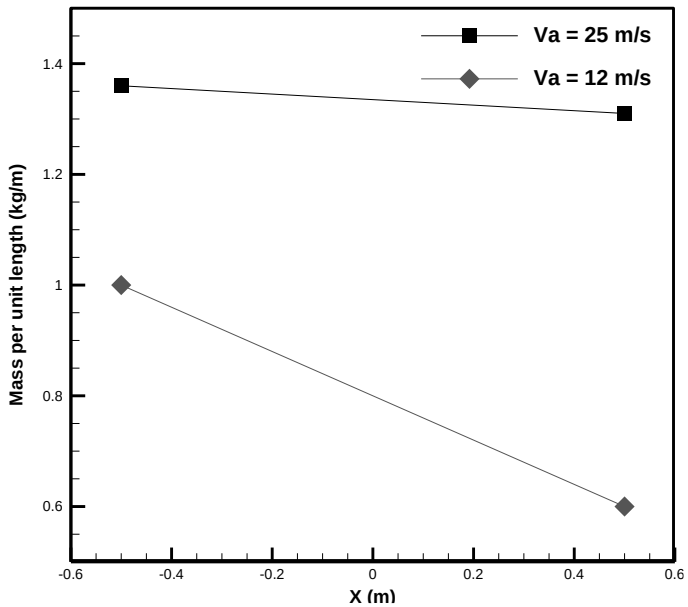

Figure 5-14 Mass per unit length for V_a = 25 m/s and V_a = 12 m/s

Figure 5-15 shows that for high velocities, the ice accretion has a maximum in the middle of the angle bar and that it decreases quickly upward and downward with no accretion on the top and bottom. The entire cloud is in the middle part for both streamwise positions. It seems that the thickness of the accreted ice is a bit higher at the lower side of the angle bar (right hand side in Figure 5-15), which is confirmed by the front view. However, the ice accretion then vanishes quickly from the bottom of the angle bar.

A comparison between Figure 5-15 and Figure 5-16 shows that for the lower velocity there is no maximum in the accretion shape as for the higher velocity, but that the amount of accreted ice increases toward the bottom, the accretion extending up to the bottom of the angle bar. Thus, the effect of gravity is more considerable for V_a = 12 m/s.

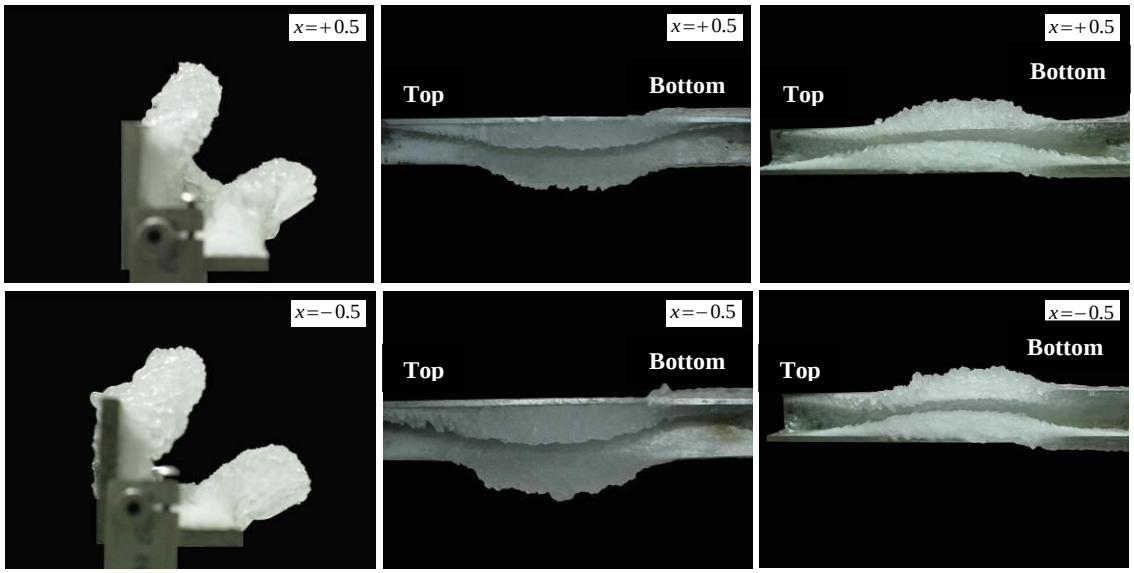

Figure 5-15: Accreted vertical angle bar, V_a = 25 m/s

An additional observation from Figure 5-14 is that the accreted ice per unit length for V_a = 25 m/s is higher than for V_a = 12 m/s which is in agreement with the results of experiments with horizontal angle bars (cf. Figures 5-6 and 5-10). The effects of three important factors on ice shape during ice accretion was observed: (i) effects of gravity force for low droplet velocity, (ii) effects of distance between the spray bar with nozzles and the angle bar, (iii) effects of temperature on immediate freezing of impinging droplets influencing the shape of ice on the surface of the angle bar.

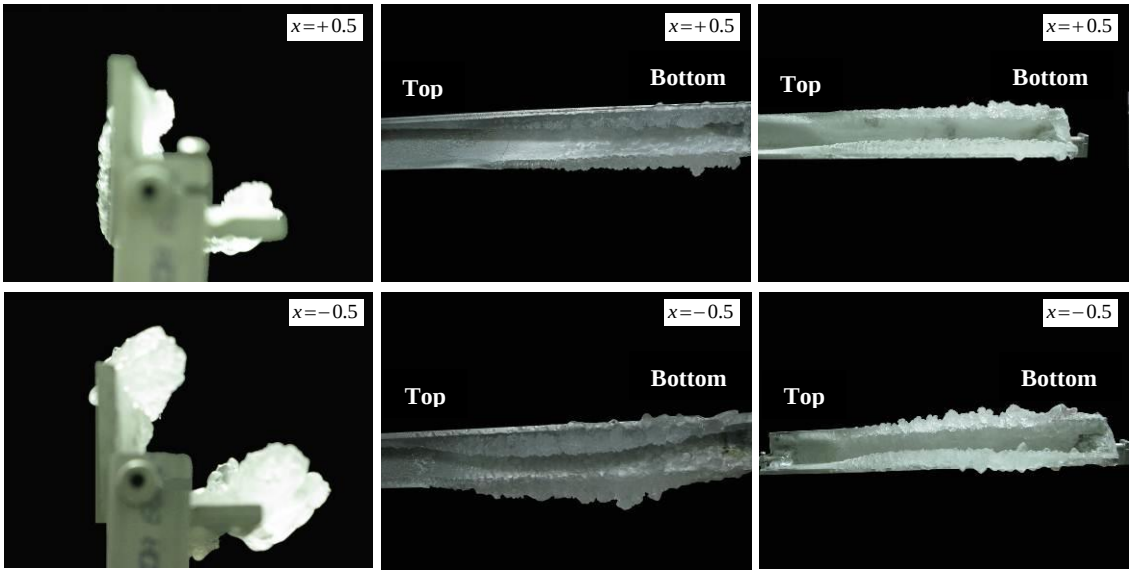

Figure 5-16: Accreted vertical angle bar, V_a = 12 m/s

5-3-2-Calculation of Drag Coefficients of Ice-Covered Angle Bars

An important practical question is to determine how the aerodynamic forces on a tower leg vary due to ice accretion. In particular, the drag coefficient is calculated for the

angle bar with different mass and shape of ice accretion, as obtained in the experiments described in the previous section. The calculation procedure is based on the standard ISO12494 [40]. The calculation of drag coefficients for non-aerodynamic geometries such as an angle bar is difficult. It requires several input parameters such as ice type, ice thickness, and drag coefficient of angle bar without ice.

In order to calculate drag coefficients of ice-covered angle bars, first, the type of ice must be specified, it was glaze for these experiments. Considering this and the thickness of the angle bar which was less than 0.3m, the corresponding tables from the standard ISO12494 were selected. Then, with the help of pictures of the experimentally accumulated ice on the angle bar, the category of glaze deposits (ICGx) was obtained from the above mentioned standard based on thickness of ice. The drag coefficient for the angle bar without ice (C_0) was available in Hoerner [98]. Once these data were known, tabulated data from the same standard provided the drag coefficient of the ice-covered angle bar.

The drag coefficient for the lower LWC and higher air velocity was calculated to be about 1.63 for the y = +0.07 m and x = -0.5, 0, +0.5 m position whereas it was calculated to 1.59 for the y = -0.07 m and x= -0.5, 0, +0.5 m position. In other words, the drag coefficient was found to vary vertically, but to be independent from the streamwise position (see Table 5-2).

Table 5-2: Drag coefficient variation for iced angle bar in vertical position (lower LWC and higher velocity)

LWC (g/m^3)	V_a (m/s)	C_0 *	C_i **	y (m)
2.8	25	1.75	1.63	+ 0.07
2.8	25	1.75	1.59	-0.07

* C_0: drag coefficient without ice

** Ci: drag coefficient with ice

The drag coefficient for an angle bar with higher LWC and lower air velocity was calculated to be about 1.75 for y = +0.07 m and x = -0.5, 0, +0.5 m which was the same as the drag coefficient for the angle bar without ice. It was observed that the ice thickness was less than 10mm at this vertical position. The drag coefficient for the y = -0.07 m and x = -0.5, 0, +0.5 m position was calculated to be about 1.61. The results show that for the lower velocity, the ice effects for y = -0.07 m are more important than for y = +0.07 m, as shown in Table 5-3.

Table 5-3: Drag coefficient variation for iced angle bar in vertical position (higher LWC and lower air velocity)

LWC (g/m^3)	V_a (m/s)	C_0	C_i	y (m)
5.8	12	1.75	1.75	+ 0.07
5.8	12	1.75	1.61	-0.07

For the vertical angle bar, it was complicated to calculate the drag coefficient. For Standard ISO12494, one of the assumptions is that the ice accumulated on the model is uniform. For a vertical angle bar, however, the effect of gravity changes the shape of the ice along the bar. Therefore, the recommendation for estimating drag coefficient of such non-uniformly iced angle bars, or tower legs, is to divide the angle bar into smaller pieces for which ice thickness may be assumed constant, and to determine the drag coefficient as a function of the position along the bar. Instead of this procedure, since experiments were also carried out on horizontal angle bars at different vertical positions, these tests were used here to obtain an approximation as to how the drag coefficient varies vertically.

Conclusion

It was found that the gravity effect on droplet trajectories is more significant than the drag effect for low air velocity, which can be observed on the variation of MVD and LWC in both streamwise and vertical directions because the larger droplets tend to go toward the bottom of the test section. When the velocity increases, the drag effect becomes more significant than the gravity effect for clouds including small droplets only, and droplet separation according to their size occurs only for clouds with larger droplets.

The larger droplets move toward the bottom of the tunnel during their flow in the test section. However, when the droplets are not large enough (less than about 80 μm) and the air velocity is high enough (greater than 10 m/s), then numerous large droplets are still present close to mid-height even at the streamwise position of x=0.5 m leading to the

greatest MVD and LWC at mid-height. The LWC increases in the vertical direction toward the bottom for low air velocities and then, if the MVD of the cloud is large enough, also for higher air velocities. Results of ice accretion measurements on the angle bar reflect the observation that ice tends to accumulate mostly in positions where LWC is higher.

The effect of accreted ice has also been observed on the drag coefficient. The drag coefficient of the horizontal angle bar may change by 5-10 % due to ice accretion. For the vertical angle bar, it was complicated to calculate drag coefficient. For Standard ISO12494, one of the assumptions is that the ice accumulated on the model is uniform. For a vertical angle bar however, the gravity effect changes the shape of the ice along the bar. Therefore, to estimate the drag coefficient of such non-uniformly iced angle bars, or tower legs, one should divide the angle bar into smaller pieces for which ice thickness is assumed constant, and determine the drag coefficient as a function of position along the bar.

CHAPTER 6

INTERACTION OF WIND WITH A CEMENT ICE PROFILE ON AN ANGLE MEMBER

CHAPTER 6

INTERACTION OF WIND WITH A CEMENT ICE PROFILE ON AN ANGLE MEMBER

Introduction

The formation of accreted ice may lead to aerodynamic instabilities of bearing members of structures such as communication lines, power transmissions lines and antenna systems. Such formations are caused by the interaction of the wind with the ice-covered structural members. As explained in Chapter 5, the investigation of different types of ice formed on structural members provided the opportunity to choose seven types of glaze ice accretion models which were explained in detail in Section 3-2-3 and in Figure 3-5.

In this chapter, the results of detailed aerodynamic tests in the wind tunnel over a practical range of wind speed and angle of attack will be presented. Firstly, the effects of Reynolds number, ice thickness, DSD, angle member size, and ice profile shape on aerodynamic coefficients will be described for each angle member. Then, the obtained results will be compared with the results provided in standard ISO12494.

6-1-Sign convention and definition of the variables

Figure 6-1 presents the sign convention used and the definition of aerodynamic coefficients, in order to follow the results easily.

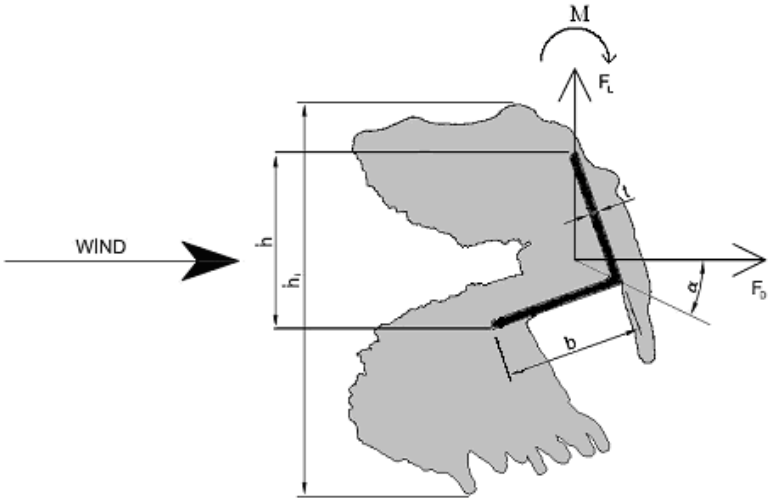

$$\textit{Projected with ice height}: \quad C_D^P = \frac{F_D}{1/2\,\rho U^2 h_i l} \qquad C_L^P = \frac{F_L}{1/2\,\rho U^2 h_i l}$$

$$\textit{Projected with angle height}: \quad C_{Do}^P = \frac{F_D}{1/2\,\rho U^2 h l} \qquad C_{Lo}^P = \frac{F_L}{1/2\,\rho U^2 h l}$$

$$\textit{Normalized height}: \quad C_D^n = \frac{F_D}{1/2\,\rho U^2 b l} \qquad C_L^n = \frac{F_L}{1/2\,\rho U^2 b l} \qquad C_M^n = \frac{M}{1/2\,\rho U^2 b^2}$$

$l = \textit{angle member length} \qquad \rho = \textit{air density} \qquad U = \textit{wind velocity}$

Figure 6-1: Sign convention and definition of variables

6-2-Reynolds number effects

Figures 6-2 to 6-6 show the results on four samples of iced angle members for three wind speeds of around 5, 10 and 20 m/s, resulting in Reynolds numbers between 1.66×10^4 - 17.3×10^4 based on the projected ice width. Results indicate that there are no significant effects regarding the Reynolds number variations. The same results were obtained for other samples based on different wind speeds. It was shown that for the same angle member without an ice profile, the aerodynamic coefficients were not influenced by Reynolds

number [16]. It was observed for S51-G7 in high velocities the angle member starts to vibrate. The vibration showed its effects on moment coefficient, Figure 6-5.

It has been shown that by increasing the ice quantity on upper section of the angle member the drag variations are greater than for smaller ice profiles. It can be seen for S51-G3 the drag coefficient reaches 2 and for smaller ice profiles; S51-G6 it reaches 1.7 while for S51-G5, S51-G7 and S25-G1, the drag coefficient does exceed 1.5. Same observation is seen for lift and moment coefficient for S51-G3 and S51-G6 because of the bigger ice profiles on the upper side the lift coefficient exceeds 1 while for other ice profiles it remains below 1.1. It may be explained by the effects of the upper ice profile on velocity field and consequently velocity variations caused the pressure changes which leads to drag and lift variations.

It seems that for S51-G6 when the icicles stand over the angle member for higher angle of attack, they affect the flow and pressure in vertical direction compare to smaller angle of attack. As it is shown the lift variations is increased to the range of -1.2 to 1.2 for $\alpha \geq 200°$ while it varies between -0.8 and 1.0 for $\alpha \leq 200°$.

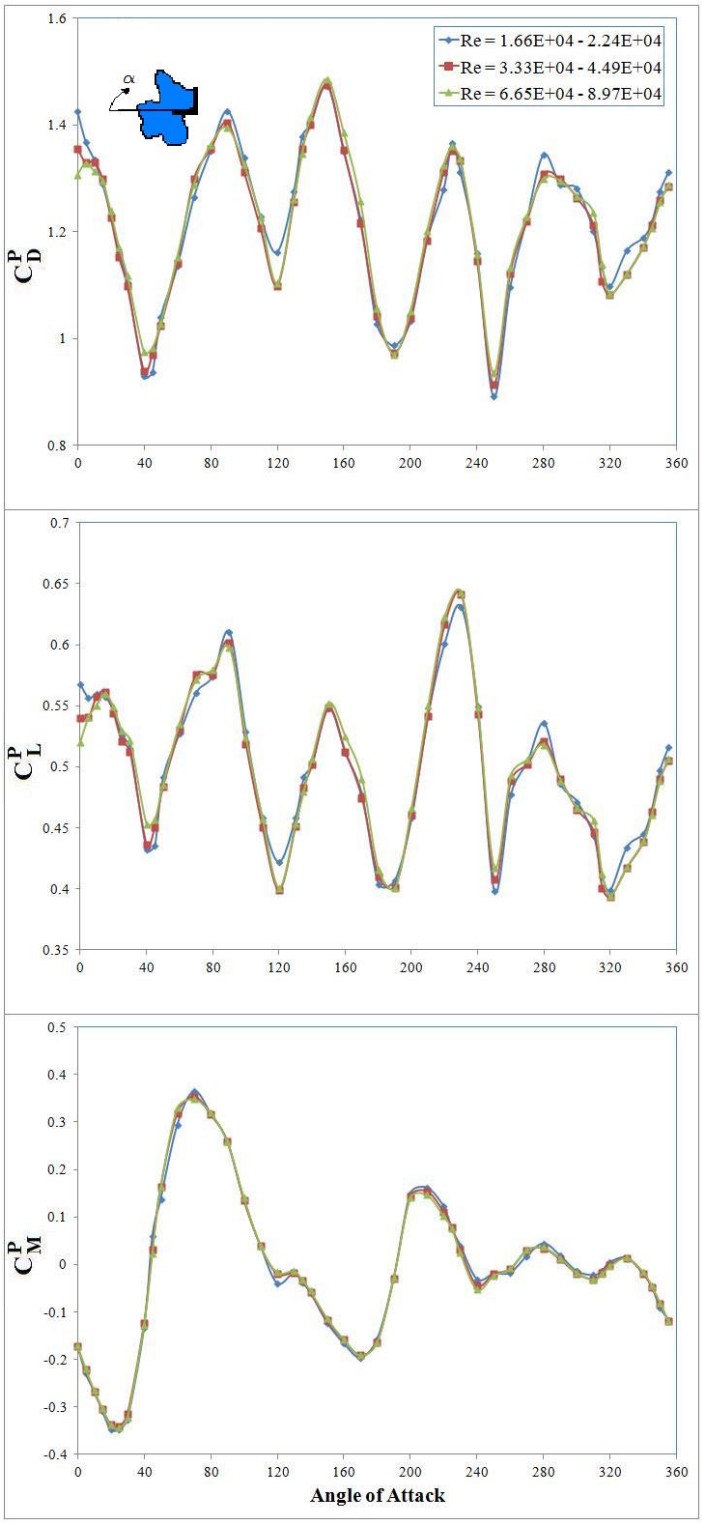

Figure 6-2: Aerodynamic coefficients of S25-G1 with respect to Reynolds number

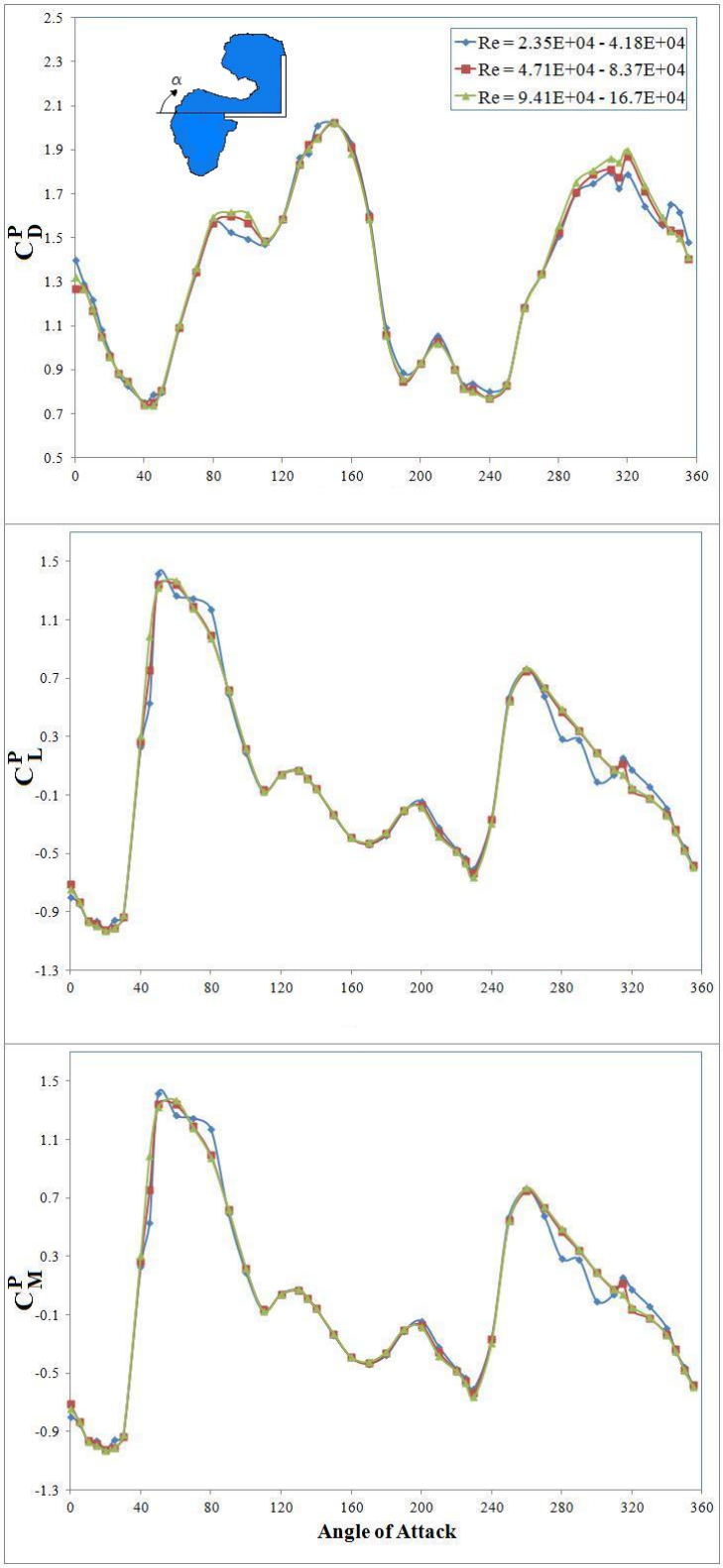

Figure 6-3: Aerodynamic coefficients of S51-G3 with respect to Reynolds number

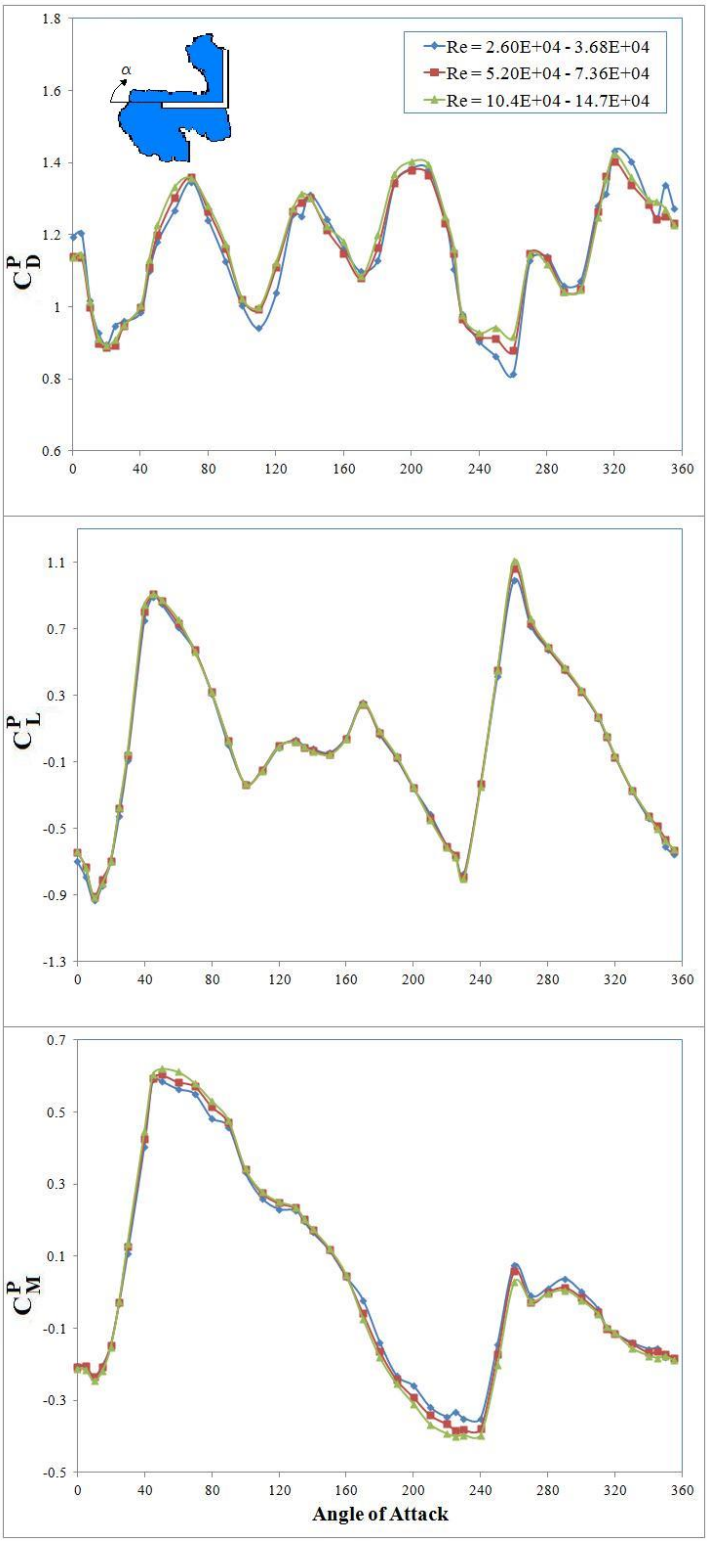

Figure 6-4: Aerodynamic coefficients of S51-G5 with respect to Reynolds number

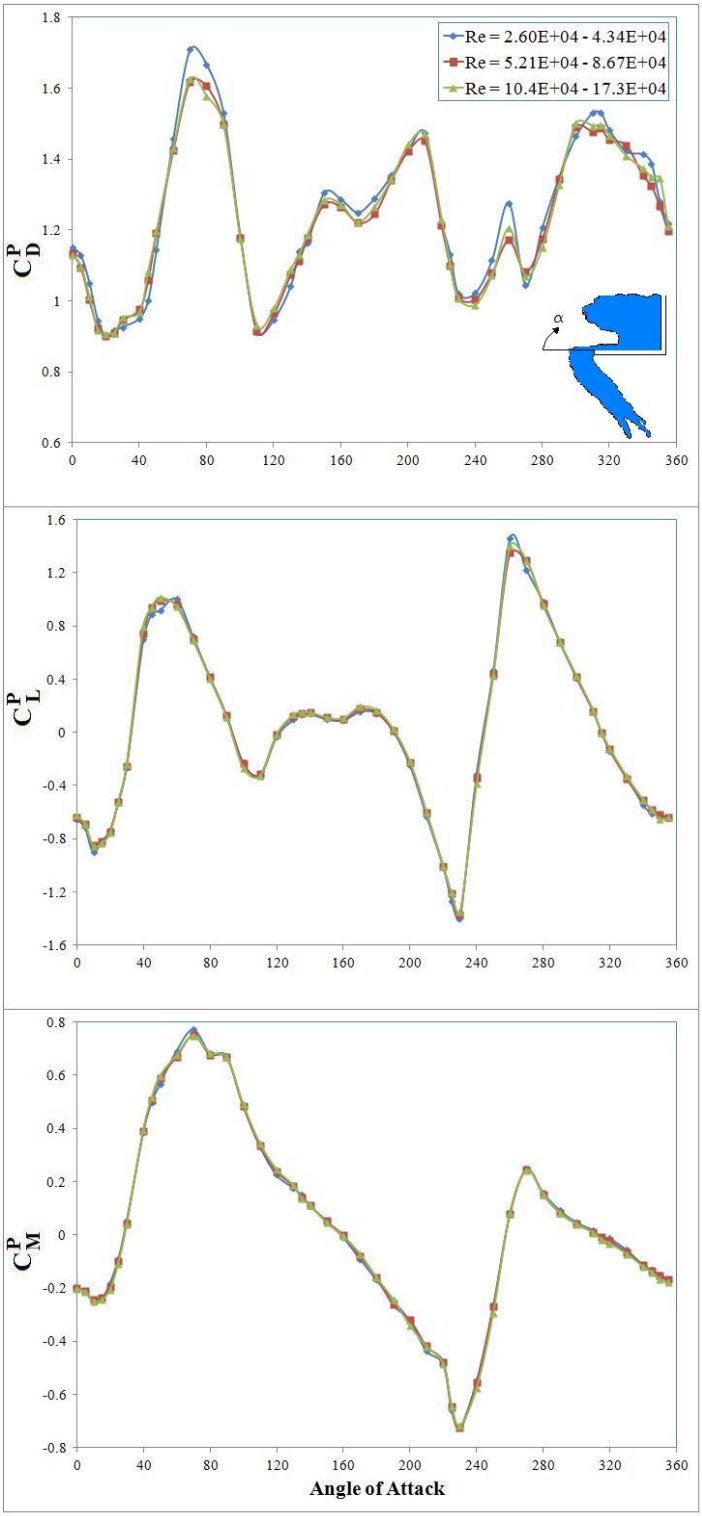

Figure 6-5: Aerodynamic coefficients of S51-G6 with respect to Reynolds number

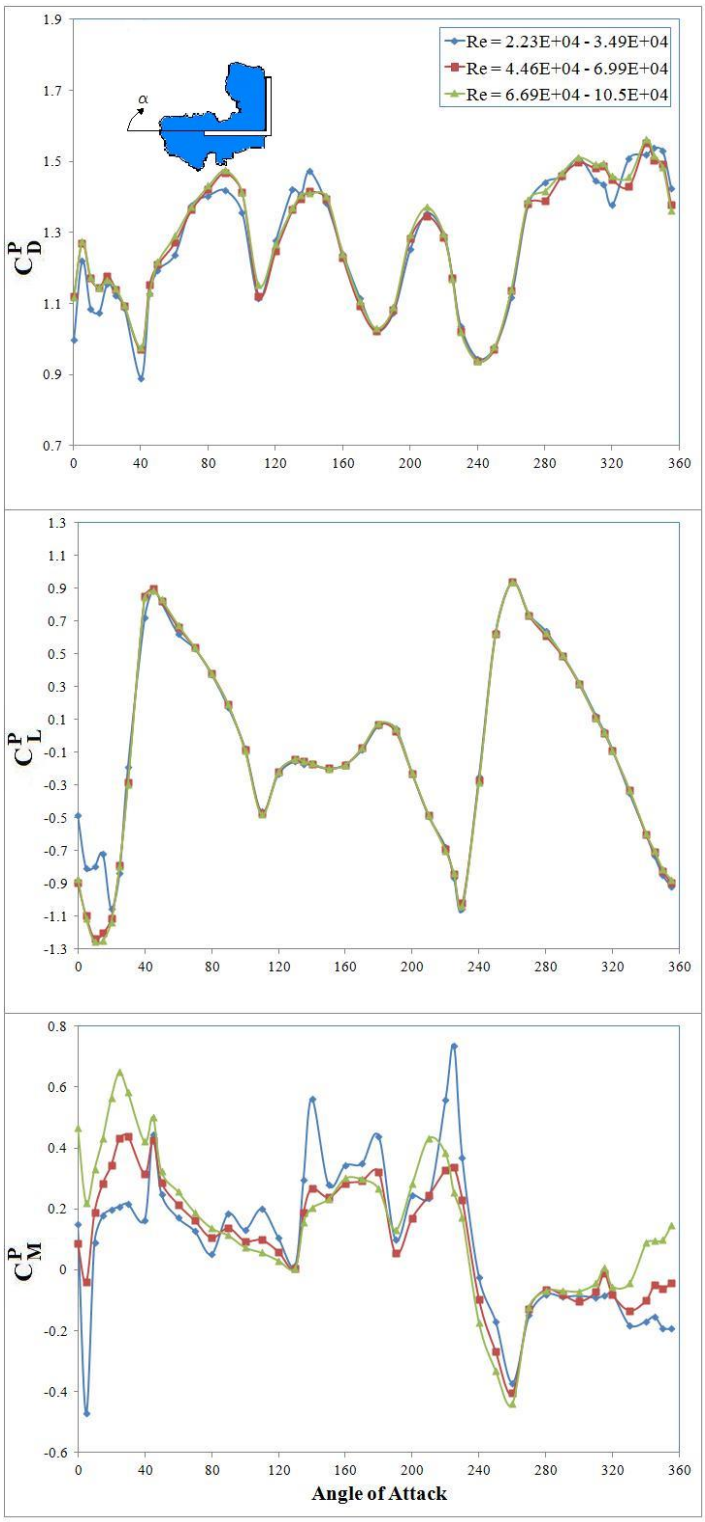

Figure 6-6: Aerodynamic coefficients of S51-G7 with respect to Reynolds number

6-3-Ice thickness effects

Figure 6-7 shows that the drag coefficient decreases when ice thickness increases in the same icing conditions for all the Reynolds numbers. In order to have the uniform ice thickness, the circular cylinder with the same projected area was used to get the equivalent ice thickness. The same result was obtained for lift coefficient. The lift coefficient shifts to negative values when the ice thickness increased on the angle member. Contrary to drag and lift coefficients, the moment coefficient increased.

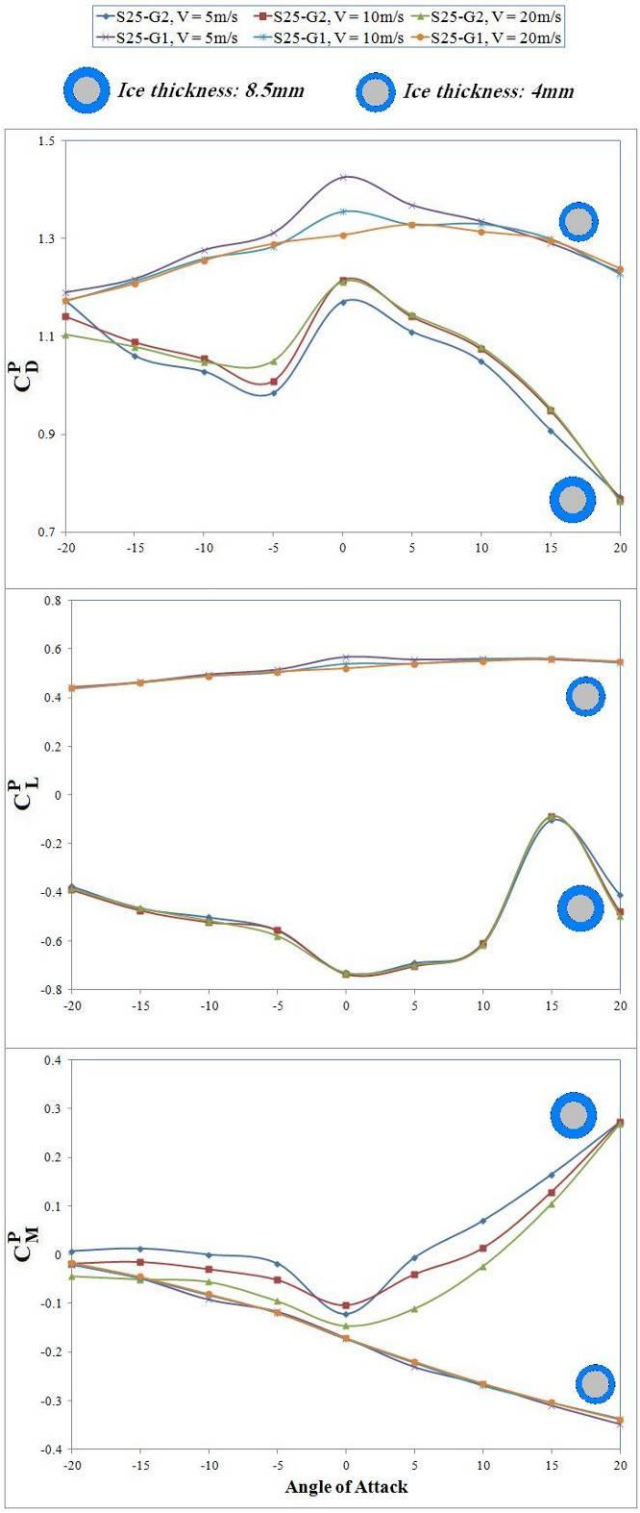

Figure 6-7: Ice thickness effects on aerodynamic coefficients for S25-G1 and S25-G2

Figure 6-8 shows drag coefficient for 8.5 mm and 4 mm ice thickness for S25-G2 and S25-G1. The drag values for C_D^n is higher than C_{D0}^p for negative angles of attack where the exposed area is greater for the former compare to the latter.

It is observed that there is a maximum at α=0° for both C_{D0}^p and C_D^n. This is because of the situation of the angle member for α=0°. The drag form (pressure drag) arises because of increasing of cross-section of an angle member; however the friction drag reduces to lower values because of decreasing on exposed area.

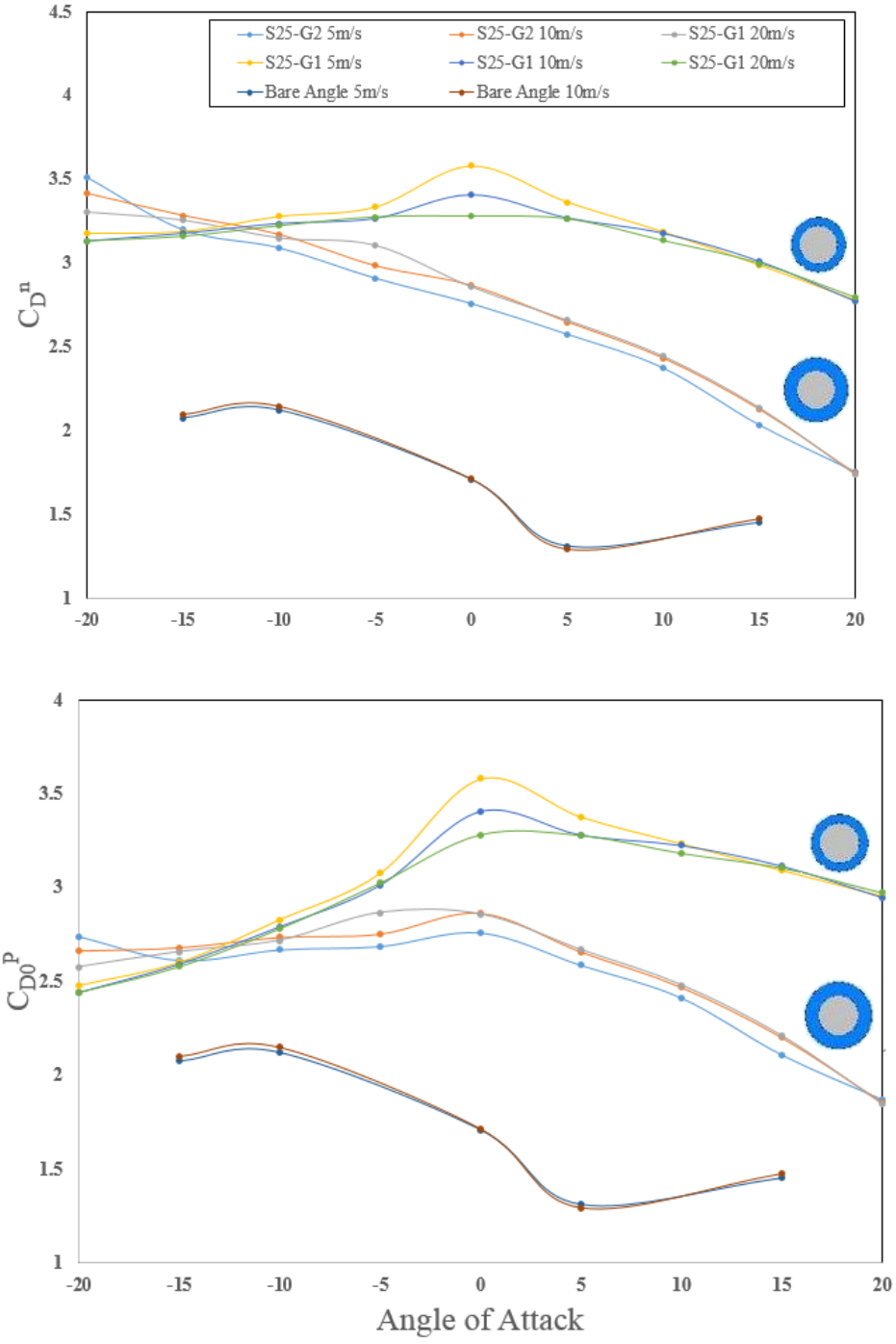

Figure 6-8: Ice thickness effects on C_D^n and C_{D0}^p for S25-G1 and S25-G2

Figure 6-9 shows the aerodynamic coefficient for S51-G3 and S51-G4 models. It is shown that the drag coefficient decreases when ice thickness increases for the same icing conditions and for all the Reynolds numbers. This result was expected based on observations on S25-G1 and S25-G2. As it is shown, the drag variations for S51-G4 is greater than for S25-G2 in respect to increasing ice thickness which means that a higher projected area cause a lower drag coefficient without considering flow field variations caused by accreted ice inside the angle member.

Contrary to drag coefficient, the lift coefficient was increased by increasing ice thickness. It means that, by increasing ice thickness, there is a higher lift coefficient for S51-G4 compared to S25-G2. In other words, the vertical force on S25-G2 is from top to bottom while it changes from bottom to top for S51-G4. The negative lift coefficient may be explained by the instabilities that ice profile causes and change flow field around the angle members.

The same results were obtained for moment coefficient that is similar to that observed for S25-G2 in respect to ice thickness variations.

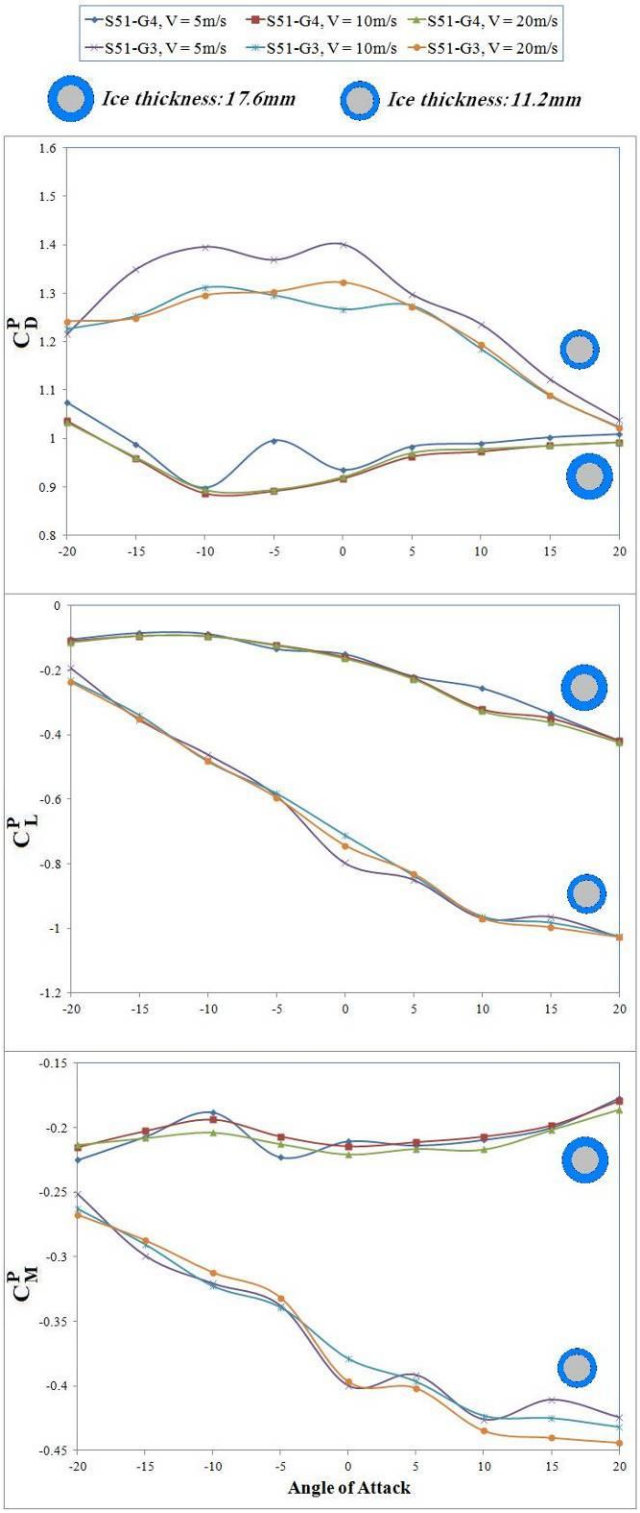

Figure 6-9: Ice thickness effects on aerodynamic coefficients for S51-G3 and S51-G4

Figure 6-10 shows drag coefficient for 17.6 mm and 11.2 mm ice thickness for S51-G4 and S51-G3. C_d^n has opposite manner for higher thickness compare to lower thickness. The same observation is noticed for C_{D0}^P while the values of the drag for C_{D0}^P is smaller than C_d^n for both thicknesses.

The drag coefficient of the bare angle member has been brought to give and idea about drag variations of bare member. It is shown that the drag values of the bare member are smaller than C_d^n and C_{D0}^P.

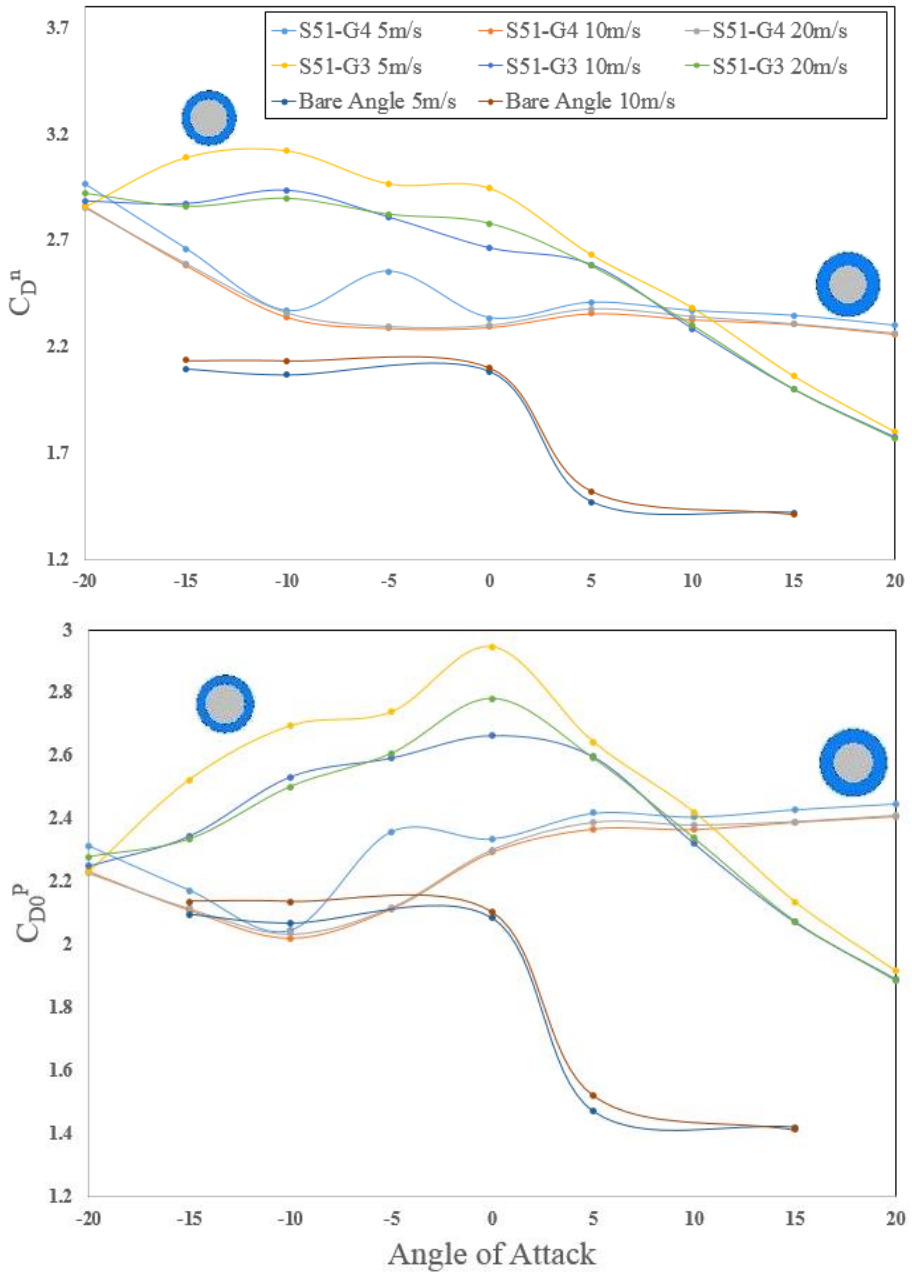

Figure 6-10: Ice thickness effects on C_D^n and C_{D0}^p for S51-G3 and S51-G4

6-4-Considering different ice profiles

Figure 6-11 shows aerodynamic coefficients for different ice profiles compared to a bare profile for air velocity of 5 m/s. The drag coefficient for the ice profiles is reduced compared to a bare profile. In other words, when the ice profiles are in the same angles of attack, different ice thickness will be exposed in flow direction. In what follows, a new parameter, *t*, will be defined as ice thickness in the direction of the wind in order to explain drag variations. Figure 6-12 shows this parameter on different ice profiles. As it is shown in Figure 6-12, S51-G6 has minimum *t*, so the projected area caused with this thickness for different angle of attacks is approximately reduced and C_D increases, while for S51-G5 there is maximum *t*, so the related projected area increases approximately and C_D decreases. Moreover a comparison between C_D^P values with C_D^n and C_{D0}^p values show that the effects of exposed area of ice caused a dramatic reduction in drag values.

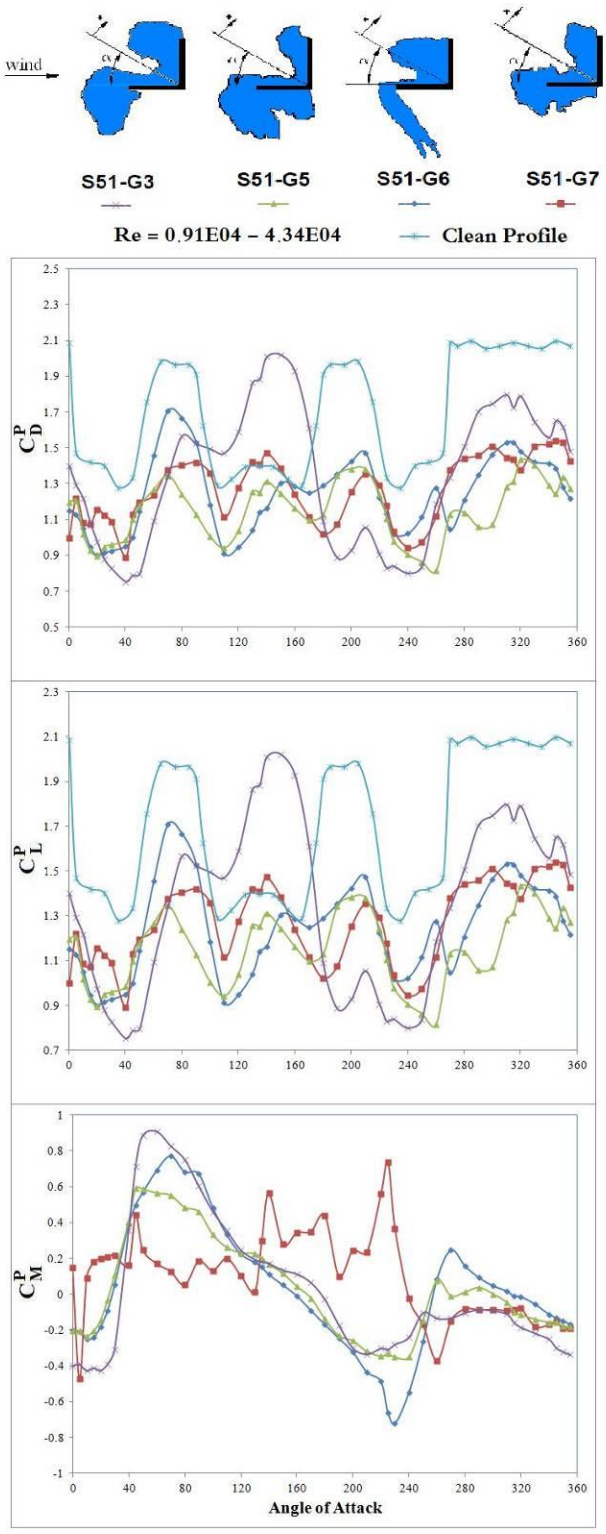

Figure 6-11: Aerodynamic coefficients for different ice profiles, Air velocity: 5 m/s

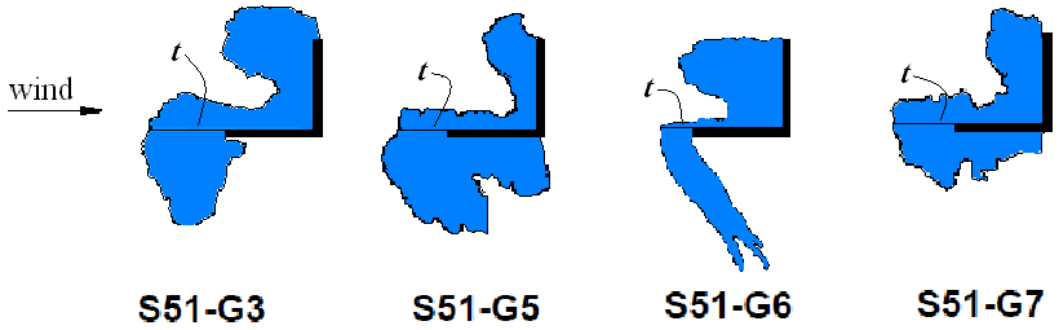

Figure 6-12: Ice thickness in the wind direction, t, of different ice profiles for α=0°

Figure 6-13 shows the drag variations of C_{D0}^{p} and C_{D}^{n} for four different ice profiles, Figure 6-12. It seems that C_{D0}^{p} and C_{D}^{n} compare to C_{D}^{p} have approximately the same variation range. It is shown that C_{D0}^{p} and C_{D}^{n} have same darg values for α= 0°, 90°, 180° and 270°. Because the exposed area of the angle member (L × l) and normal area (b × L) are the same.

It is observed that the drag variation is stronger for both S51-G3 and S51-G6 for some angles of attack. It seems that more ice on upper surface of those models compare to S51-G5 and S51-G7 causes strong variation.

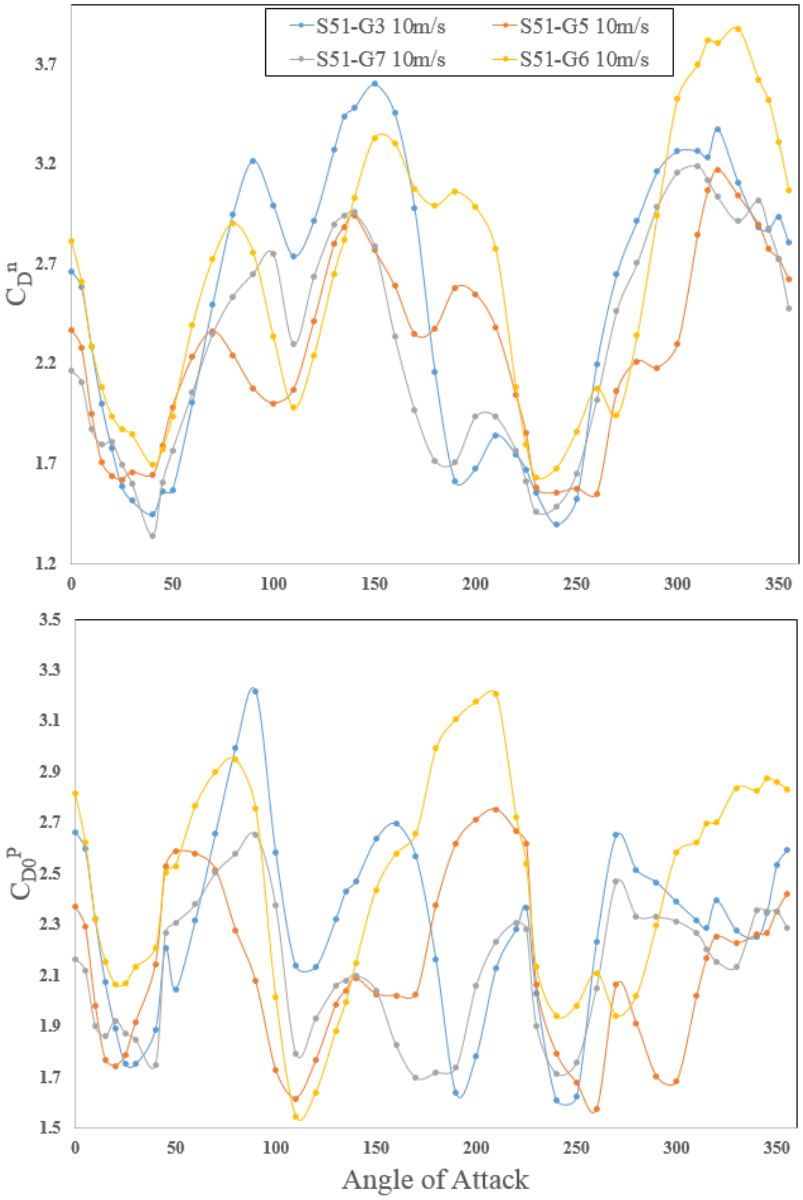

Figure 6-13: C_D^n and C_{D0}^P for different ice profiles

6-5-Different angle member profiles

Figure 6-14 shows aerodynamic coefficients for two different profile dimensions with same icing condition; S25-G2 and S51-G5, and for three different velocities: 5 m/s, 10 m/s

and 20 m/s. As it was observed before, the smaller angle member has smaller drag coefficient because there is less ice accumulated on the member. For both drag and lift curves by increasing angle of attack, they start to decrease. For the moment coefficient for both angle member profiles, it start to decrease by increasing angle of attack until $\alpha = 0°$ and then by increasing α, it slightly increases.

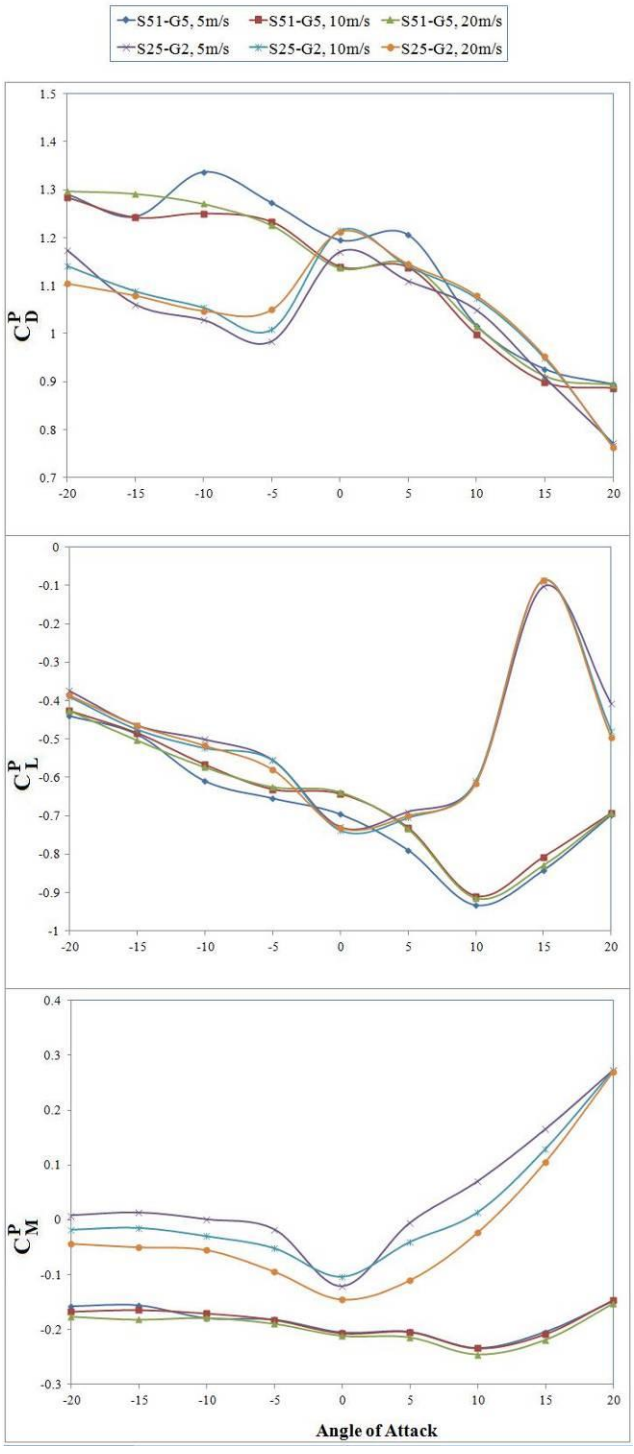

Figure 6-14: Aerodynamic coefficients for two different angle member profile: S25-G2 and S51-G5

Figure 6-15 shows C_D^n and C_{D0}^p for angle member profile S25-G2 and S51-G5. It is obvious that the variation of C_{D0}^p for S51-G5 is stronger than S25-G2 unlike C_D^n. In both coefficients the drag variations of larger member is less than smaller member. However this variation is decreasing continuously for C_D^n

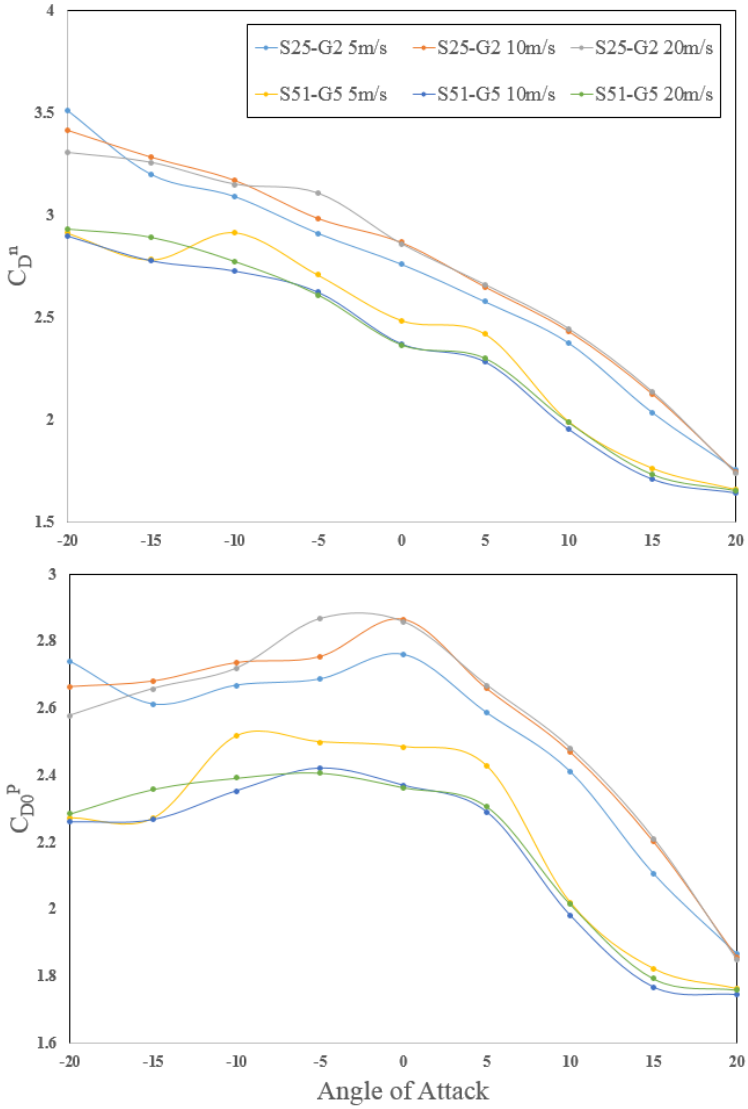

Figure 6-15: C_D^n and C_{D0}^p for two different angle member profile: S25-G2 and S51-G5

6-6-Droplet effects

Figure 6-16 indicates the effects of DSD on aerodynamic coefficients for air velocity of 5 m/s, 10 m/s and 20 m/s. S51-G3 was accreted on an angle member that was exposed to an aerosol cloud with smaller droplets, which are represented by the MVD = 47.26μm, while S51-G5 was obtained after exposure to a cloud with larger droplets, MVD = 54.96μm. It seems that for these two different DSDs, there is a similar tendency for drag, lift and moment coefficients; however, the aerodynamic coefficients are reduced in some ranges of angle of attacks for the cloud with larger DSD.

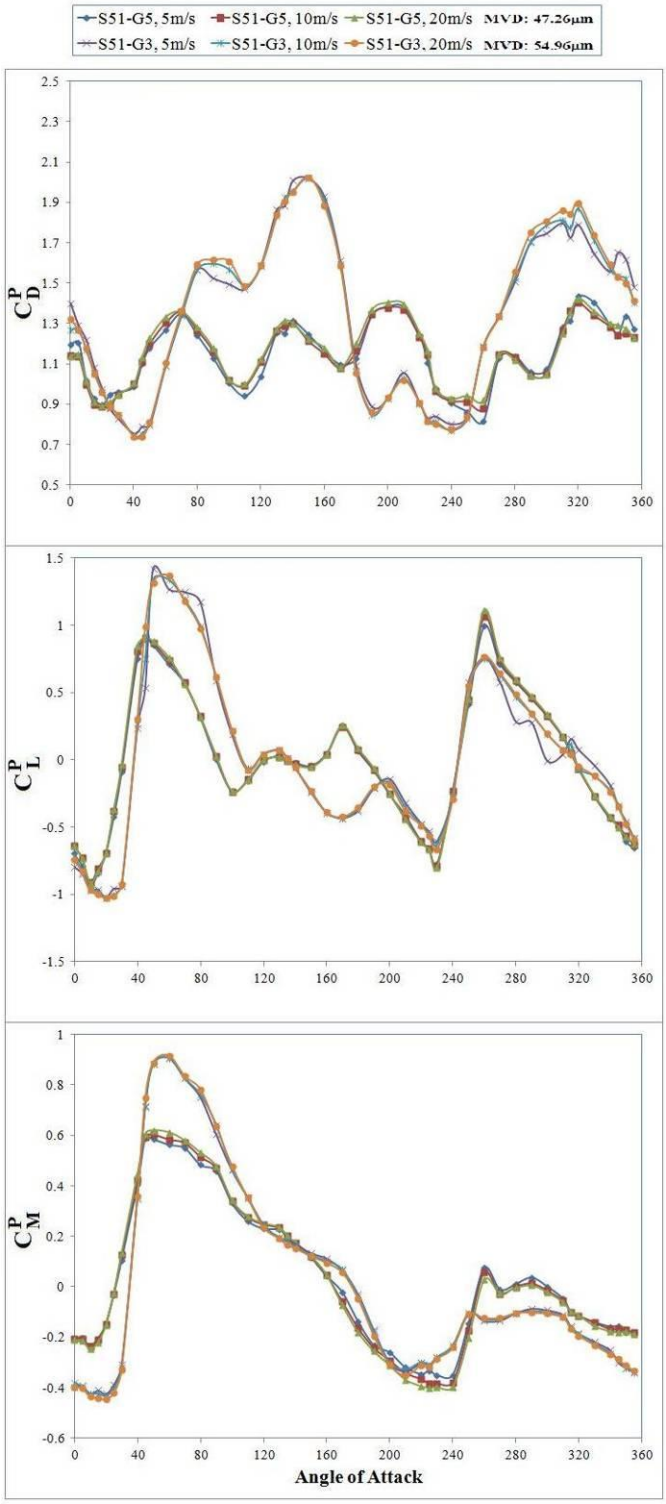

Figure 6-16: Aerodynamic coefficient for two different DSDs. S51-G3 and S51-G5

Figure 6-17 indicates C_D^n and C_{D0}^p for S51-G3 and S51-G5 with 54.96 μm and 47.26 μm MVD. As expected for C_{D0}^p for larger droplets, the darg variations are stronger. Because the larger droplets affected the ice profile shape where it caused more instability around the angle. The same manner was observed for C_D^n.

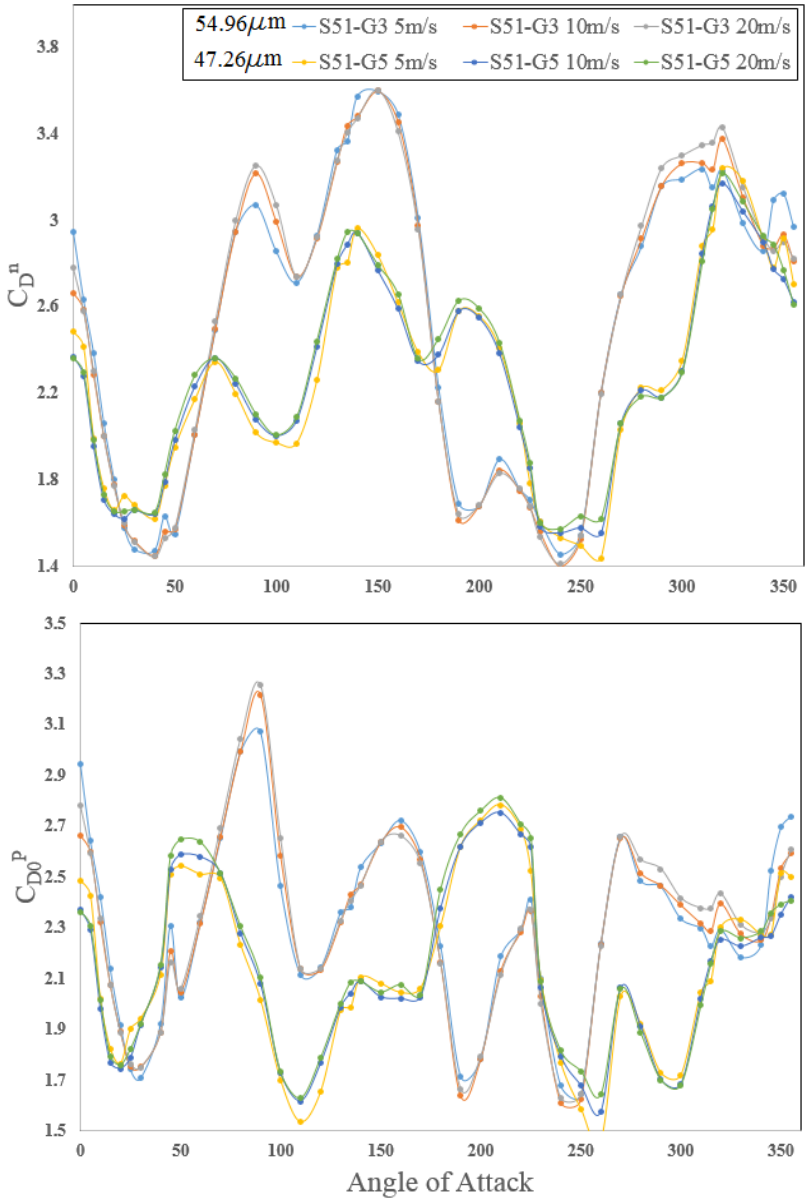

Figure 6-17: Droplet effects on C_D^n and C_{D0}^p

6-7-Effects of projected area

As it was shown in Figure 6-1, the aerodynamic coefficients based on ice projected area presented by C_D^P, C_L^P, C_M^P, the aerodynamic coefficients based on angle member projected area presented by C_{D0}^P, C_{L0}^P, C_{M0}^P and aerodynamic coefficient of bare angle member defined by C_{Dbare}^P and C_{Lbare}^P. As it is observed for all models except S51-G3 C_D^P is smaller than C_{Dbare}^P. It is explained by considering the effects of projected area. For the models with ice profiles, the projected area increased and the drag coefficient decreased. It seems that for bigger ice profiles. It has been shown that C_{D0}^P is greater because it was calculated based on angle member projected area, which is smaller than angle member with ice profiles and caused to increase on drag coefficient.

The obtained results for lift coefficient of all models; Figure 6-18 to Figure 6-21, show that the curves have same tendency based on different projected area. C_{L0}^P has the maximum variation between $-2.5 \leq C_{L0}^P \leq 2.5$ because of using angle member projected area in the calculation which is smaller than real projected area. It caused the lift coefficient increases for different angles of attack. Same results were obtained for the lift coefficient of bare angle member with a little difference; $-2 \leq C_{Lbare}^P \leq 2$. As it is shown the lift values of angle member with ice profiles based on ice projected area has the minimum values compare to other calculated coefficient.

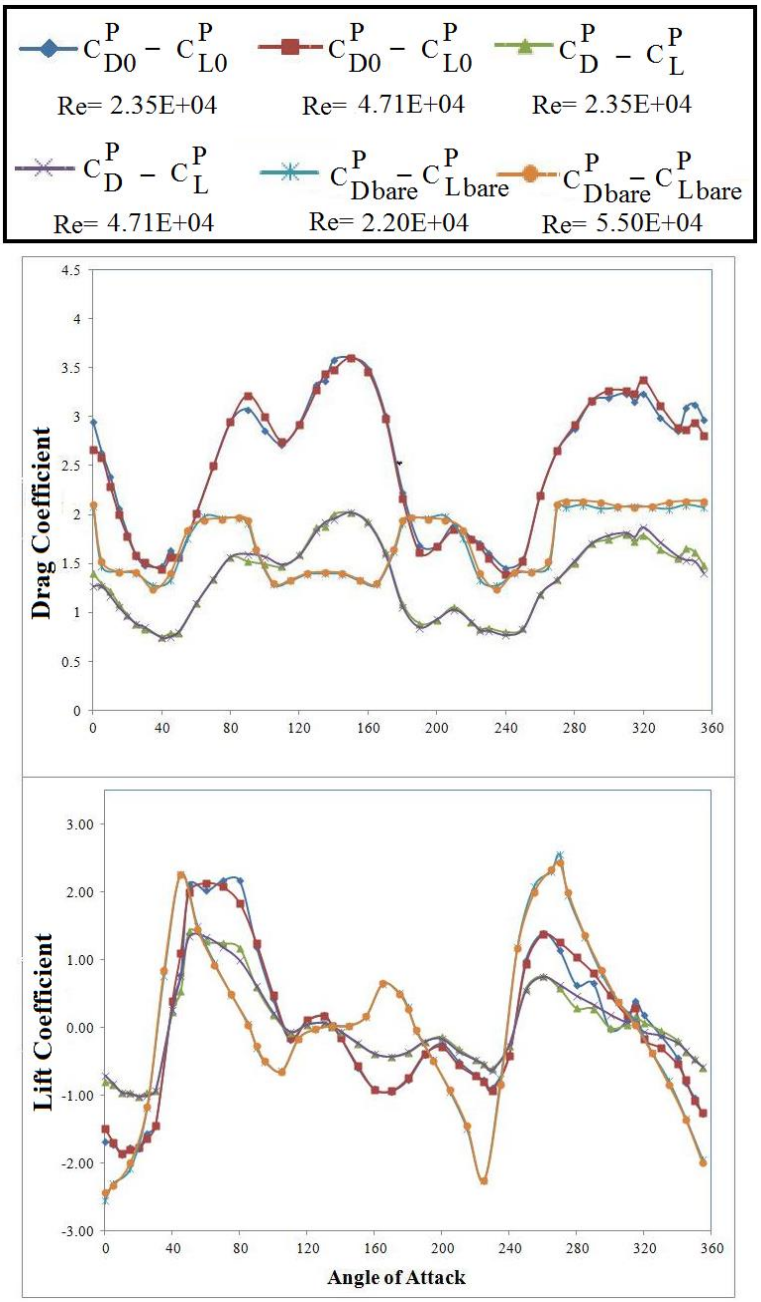

Figure 6-18: Aerodynamic coefficients of S51-G3 for two projected areas

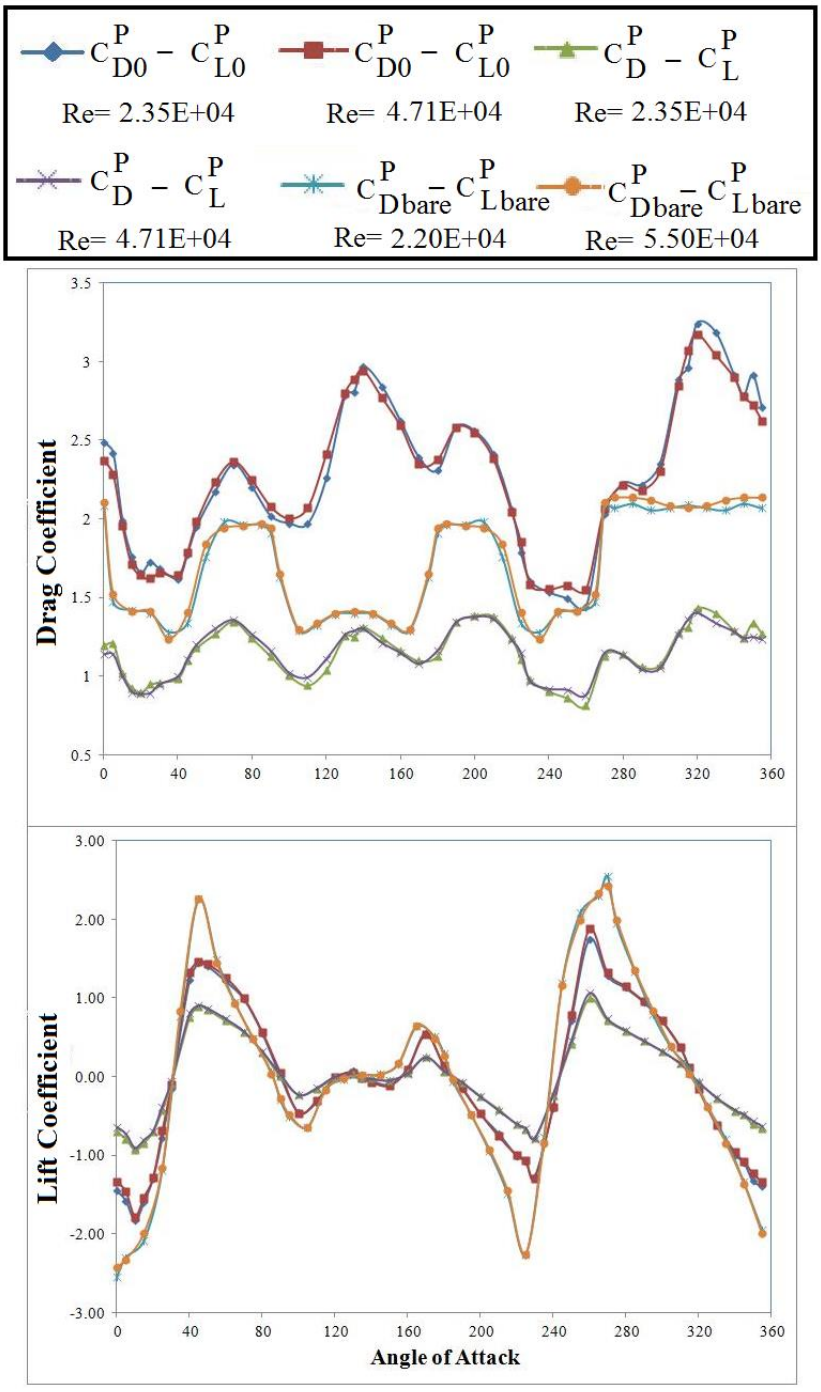

Figure 6-19: Aerodynamic coefficients of S51-G5 for two projected areas

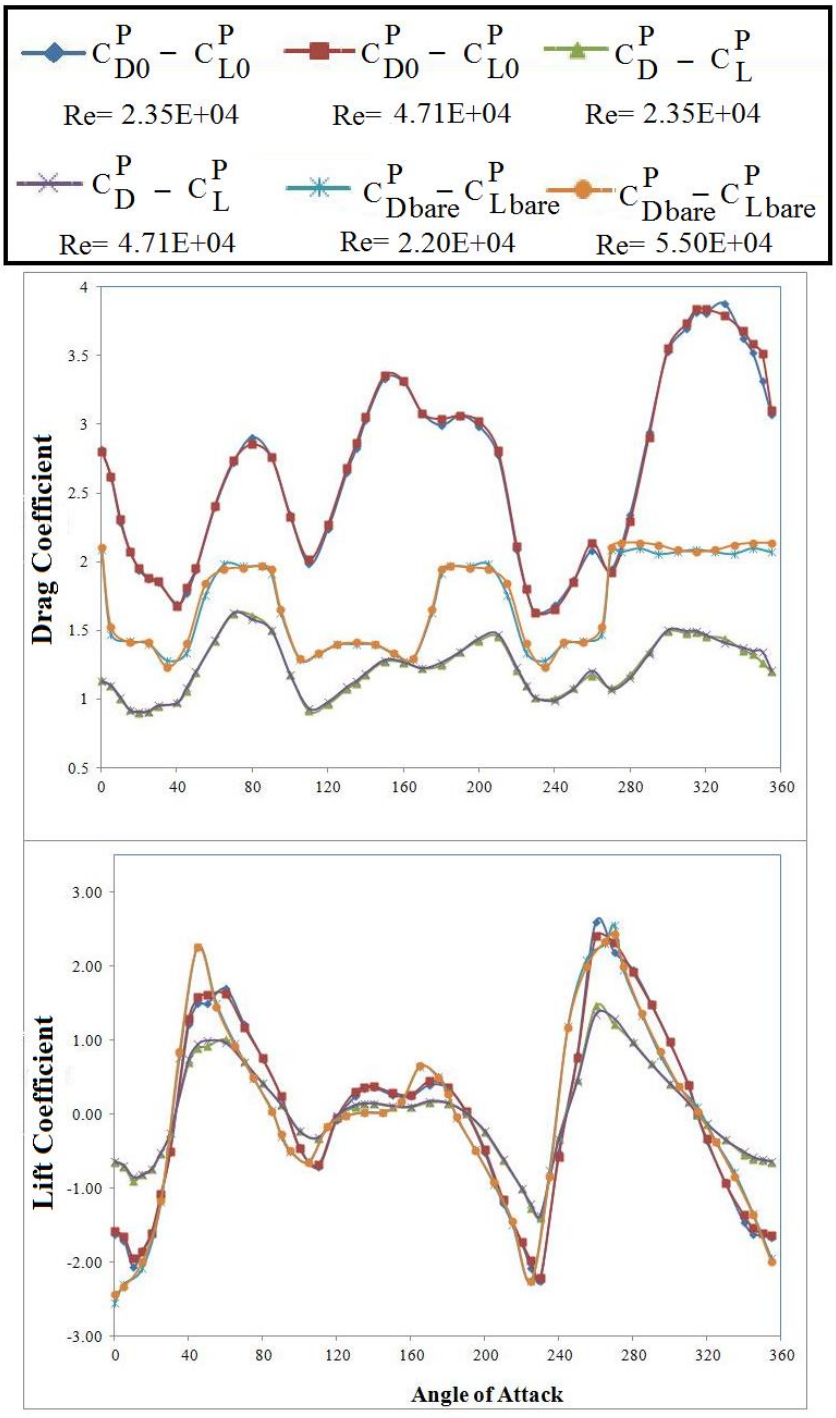

Figure 6-20: Aerodynamic coefficients of S51-G6 for two projected areas

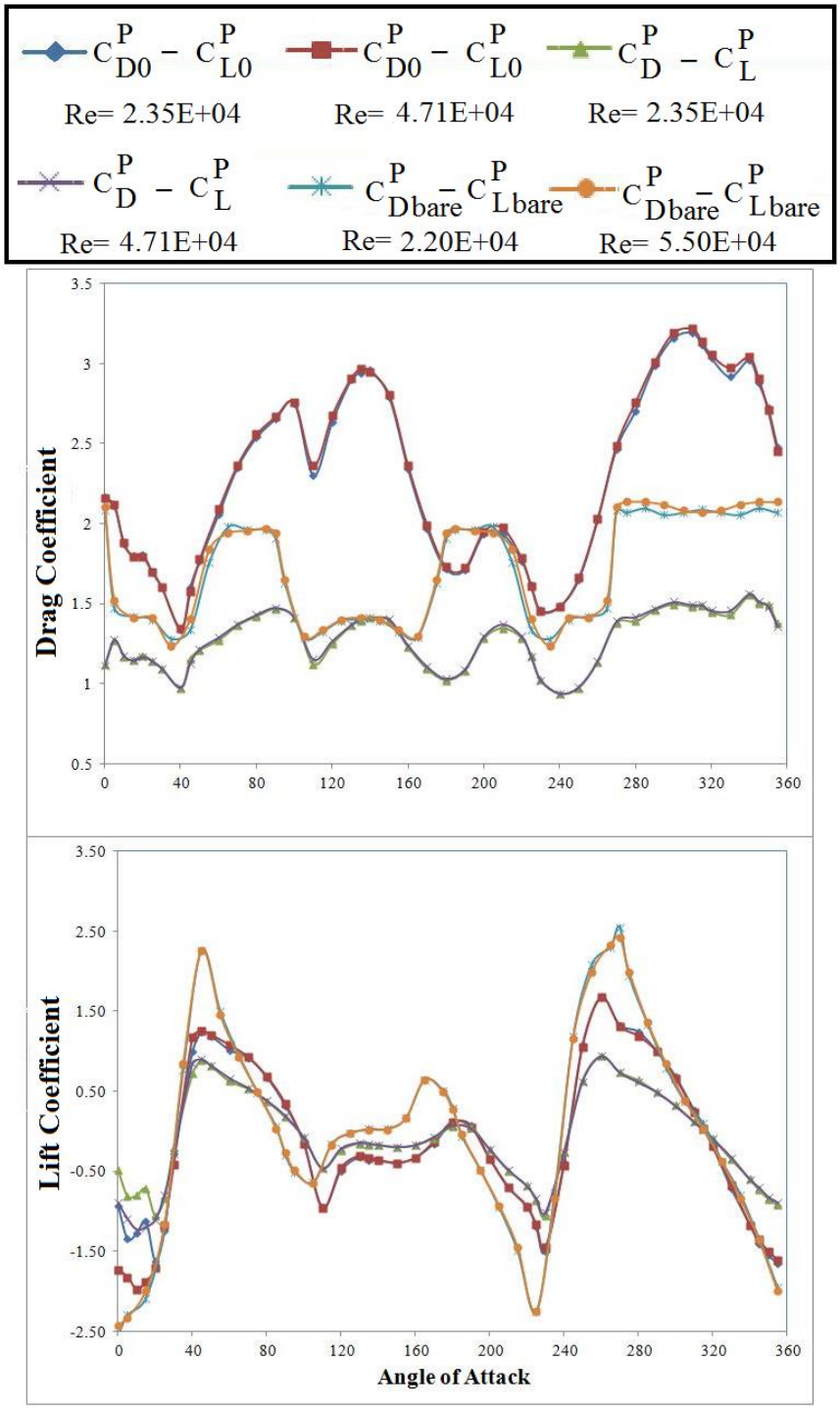

Figure 6-21: Aerodynamic coefficients of S51-G7 for two projected areas

6-8-Drag from standard

Table 6-1 shows calculated drag from ISO12494 and measured drag coefficients from tunnel experiments for α=0°. The drag calculation procedure explained in section 4-2-5. It is shown that the measured values for all profiles are less than the drag values from standard. The reason of this result is that the real projected area was used for the measured values, while for the standard, the projected area of the angle member without ice and the equivalent ice thickness were applied.

Table 6-1: Calculated drag coefficients based on ISO12494

Sample	Calculated C_D	Measured C_D for 5m/s	Measured C_D for 10m/s	Measured C_D for 20m/s
S25-G1	1.722	1.190	1.171	1.173
S25G2	1.691	1.174	1.141	1.104
S51-G3	1.672	1.401	1.267	1.322
S51-G4	1.627	1.074	1.036	1.033
S51-G5	1.688	1.195	1.140	1.137
S51-G6	1.726	1.150	1.134	1.130

An attempt was made to obtain a comparison between calculated drag from ISO12494 and measured drag for different angle of attacks. In order to calculate drag coefficient, the appropriate formula should be used. The drag force for α=0° is calculated based on:

$$F_{D0} = C_{D0} \times \frac{1}{2} \times \rho \times V_0^2 \times A_0 \quad (6\text{-}1)$$

Where C_{D0} is the drag coefficient for α=0°, V_0 is air velocity in m/s, A_0 is the projected area in m^2 for α=0° and ρ is air density in kg/m^3.

Based on the equation (6-1) and Figure 6-22 which is reproduced from standard ISO 12494, the drag force for different angle of attacks is calculated by:

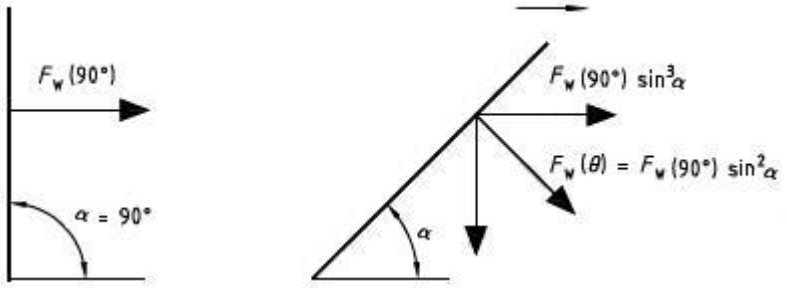

Figure 6-22: Drag force formulation for different angle of attacks. Adopted from ISO 12494

$$F_{Di} = C_{Di} \times \frac{1}{2} \times \rho \times V_i^2 \times A_i \quad (6\text{-}2)$$

where C_{Di} is drag coefficient, V_i is air velocity in m/s, A_i is the projected area in m^2 and ρ is air density in kg/m^3. From Figure 6-17:

$$F_{Di} = F_{D0} \times \sin^3(\alpha) \quad (6\text{-}3)$$

By substituting equation (6-1) and (6-2) into (6-3):

$$C_{Di}^{P} = \frac{C_{D0} \times Sin(\alpha)^3 \times A_0}{A_i} \qquad (6\text{-}4)$$

where C_{Di} is drag coefficient, C_{D0} is drag coefficient for $\alpha=0°$, A_i is the projected area in m^2 and A_0 is the projected area for $\alpha=0°$ in m^2.

In order to calculate drag coefficients of ice-covered angle bars regarding to ISO12494 the same procedure explained in section 5-3-2 was applied. Once these data were known, tabulated data from the same standard by applying equation 6-4 provided the drag coefficient of the ice-covered angle bar for different angle of attacks (Figure 6-22).

As it is shown in Figure 6-23, the drag values have small differences between $0°<\alpha<40°$ and $140°<\alpha<180°$ for different ice profile shapes while for tunnel drag measurements, Figure 6-11, it was observed that different ice profiles have completely different drag values.

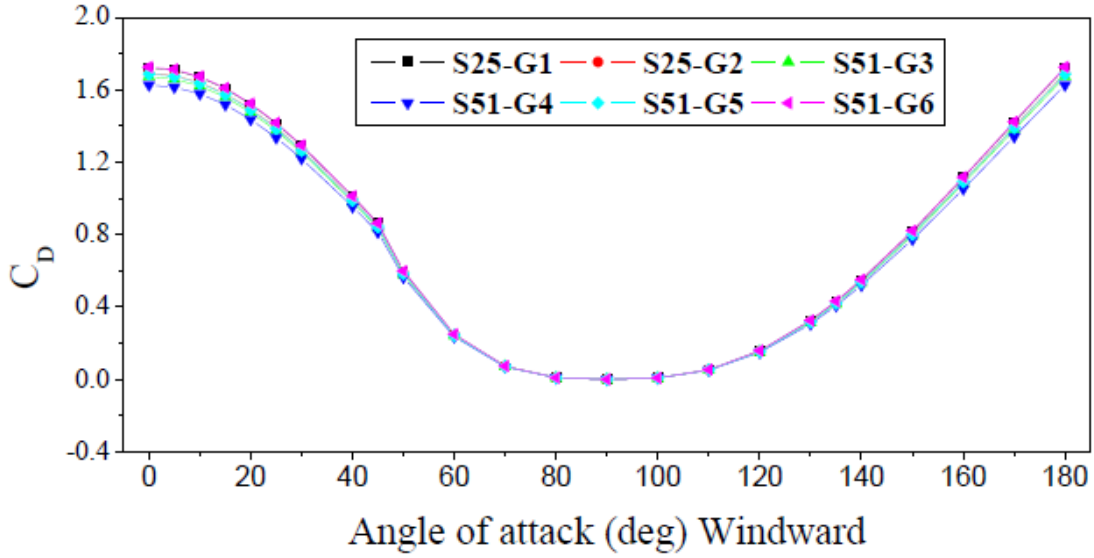

Figure 6-23: Drag coefficient from ISO12494 for a windward direction

Figure 6-24 shows normalized drag coefficient for both experimental and theoretical calculation. It seems that both curves have periodic shape where in some angle of attacks the experimental results has lower values compared to the theoretical results.

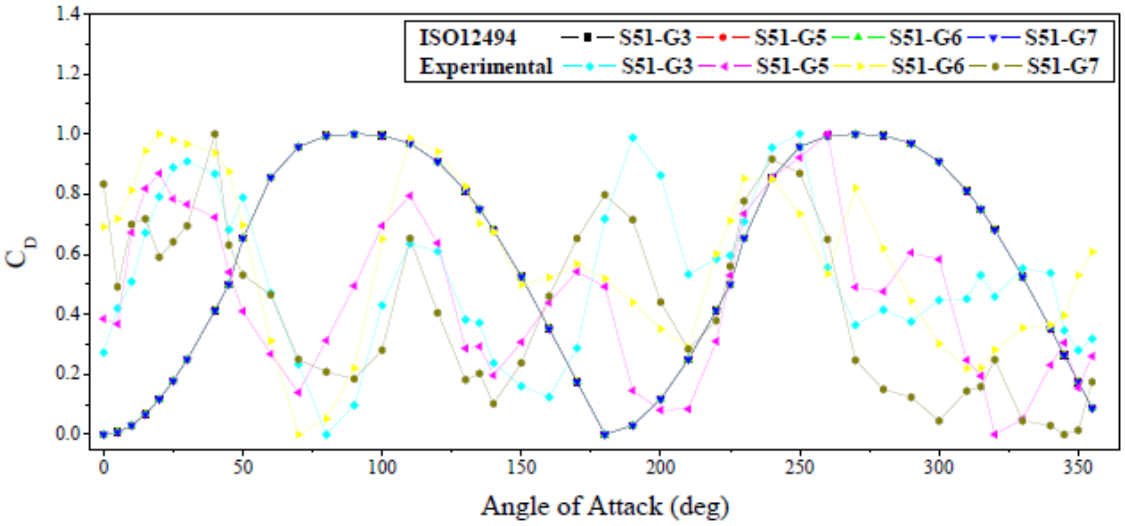

Figure 6-24: Normalized drag coefficient obtained from ISO12494 and experimental tests for S51-G3, G5, G6 and G7

Table 6-2 shows the calculated drag coefficient for different droplet diameters in the aerosol cloud. It seems that by decreasing MVD, the drag coefficient decreases. This result is confirmed by the measured drags from Figure 6-16 for two models with different MVDs.

Table 6-2: Calculated drag coefficient for different icing conditions presented by different MVDs

MVD (μm)	LWC (gr/m^3)	CD from ISO
84.4	5.8	1.68
54.96	2.9	1.67
47.26	3.3	1.63
39	2.8	1.61

6-9-Aerodynamic Forces

6-9-1- Drag Force per unit length

It has been shown in Figure 6-25 for lower velocity around 5 m/s with corresponding Re = 0.95E+04 to 4.34E+04, the drag force does not change extremely while for higher velocities around 10 m/s the drag force of the members with ice profile is smaller than bare angle member, Figure 6-26.

Figure 6-25 shows that the drag forces decreases for S51-G5 compare to S51-G7. It is explained by considering the ice profile dimension. As it is observed from Figure 6-12, S51-G5 has bigger ice profile compare to S51-G7. It is shown that for bare angle $13N \langle F_D \langle 15N$ while it decreases to $9N \langle F_D \langle 11N$ for the members with ice profile. (because there is no Reynolds effect for each profiles separately)

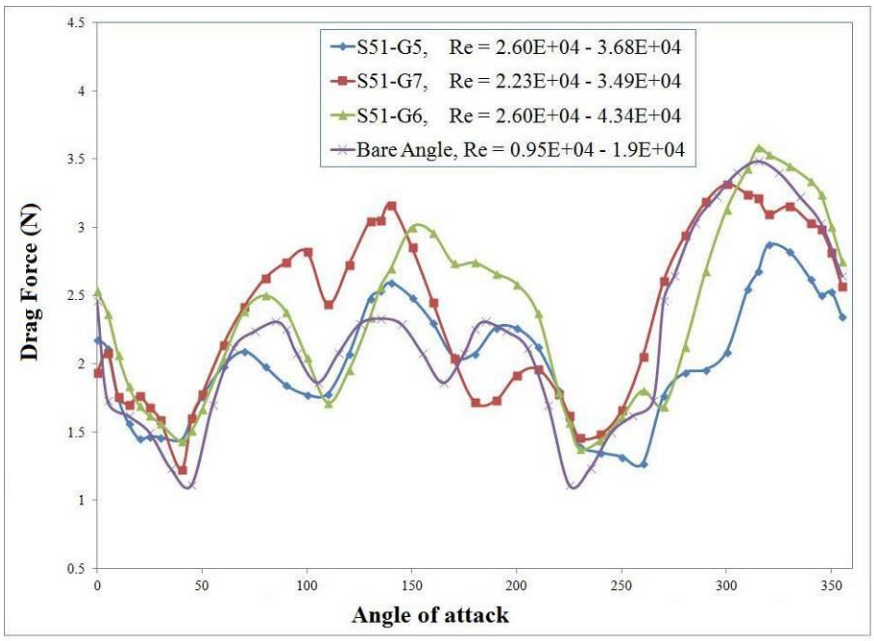

Figure 6-25: Drag force of different ice profiles compare to bare member for V ≈ 5 m/s

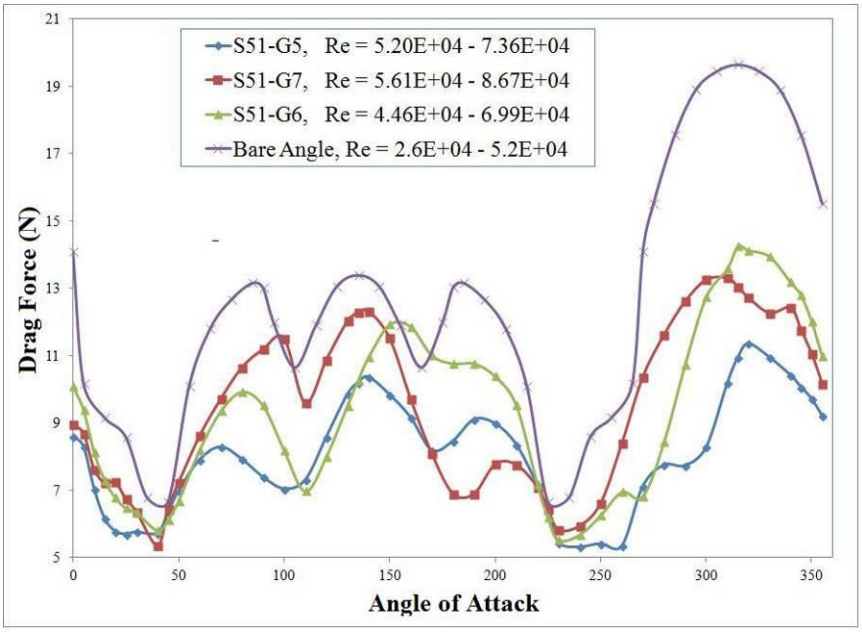

Figure 6-26: Drag force of different ice profile compare to bare member for V ≈ 10 m/s

6-9-2- Lift Force per unit length

It is observed from Figures 6-27 and 6-28, the lift force decrease compare to lift force of bare angle member while the curves keep the same tendency of the lift force for bare angle member.

Figure 6-27 shows that the $-2.5N \langle F_L \langle +2.5N$ for bare angle member when it reduces to $-1.5N \langle F_L \langle +1.5N$ for different angle of attack. It may be explained by considering the effects of ice profiles on lift force. The lift force variations are less than drag force variations for different angle of attack. It is explained by the ice profiles shapes, which cause variations on pressure field parallel to angle member while those effects are smaller for pressure field normal to it.

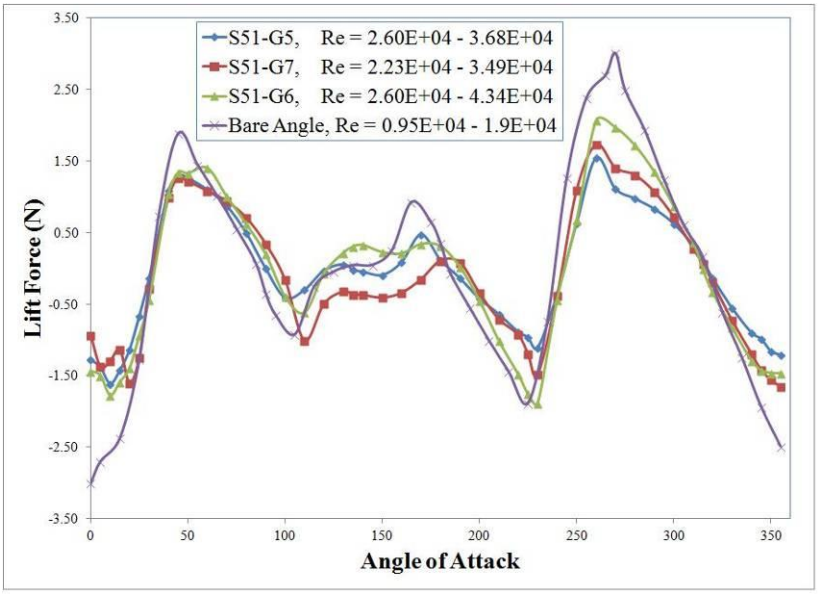

Figure 6-27: Lift force of different ice profile compare to bare member for V ≈ 5 m/s

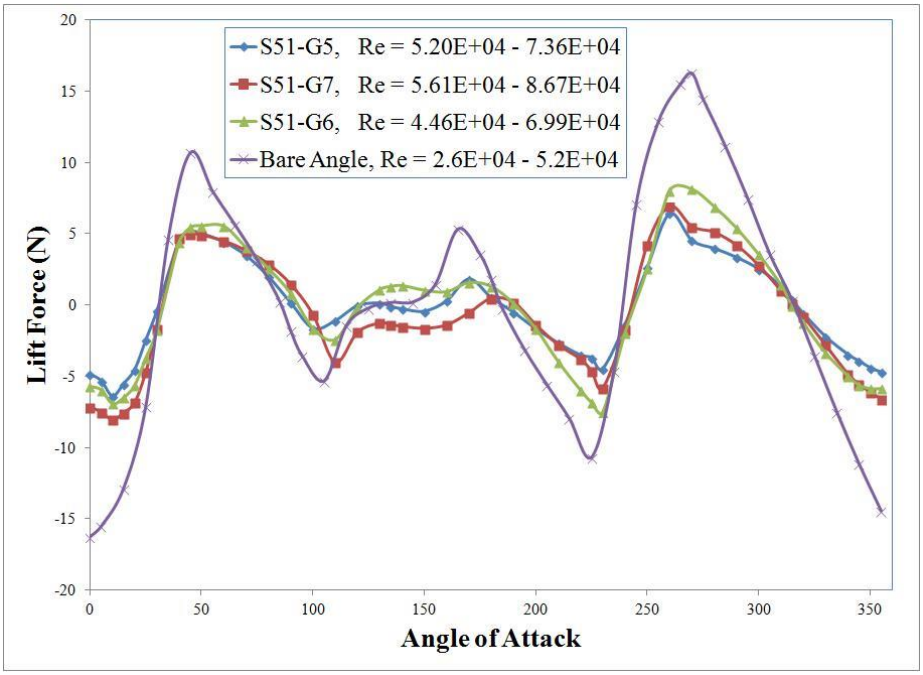

Figure 6-28: Lift force of different ice profile compare to bare member for V ≈ 10 m/s

Conclusion

It was found that there were no significant effects regarding the Reynolds number on drag, lift and moment coefficients. The same results were obtained for all ice samples based on different wind speeds.

The ice thickness effects for S25-G1 and S25-G2 showed that the drag coefficient decreased when ice thickness increased for different Reynolds numbers. For S51-G3 and S51-G4, increasing ice thickness decreased drag coefficient in the same icing conditions and for different Reynolds numbers.

It was observed that the drag variations for S51-G4 was greater than for S25-G2 with respect to an increasing ice thickness which means that higher projected areas cause lower drag coefficient without considering flow field variations.

The examination of the aerodynamic coefficients for different ice profiles compared to a bare one showed that the drag coefficient for the ice profiles was reduced compared to a bare profile.

A new parameter, *t*, was defined as ice thickness in the wind direction in order to explain drag variations. S51-G6 had minimum *t*, so the projected area was reduced and C_D increased while for S51-G5 *t* was maximum, so the projected area was increased and C_D decreased.

The effects of DSD in the cloud that angle member exposed to aerodynamic coefficients indicated that, for two different DSDs, there was a similar tendency of drag, lift and moment coefficients; however, the aerodynamic coefficients were reduced by decreasing DSDs. The same results were obtained for different air velocities.

Calculation of drag from ISO12494 for $\alpha=0°$ showed greater values of drag compared to measured drag coefficient from tunnel experiments. This discrepancy was explained by considering the real projected area for measured coefficients. Then, an attempt was made to obtain a comparison between calculated drag from ISO12494 and measured drag for different angle of attacks. As a result, the appropriate formula was derived.

The lift force variations were less than drag force variations for different angle of attack. It was explained by the ice profiles shapes, which caused variations on pressure field parallel to angle member while those effects were smaller for pressure field normal to it.

It was shown that for lower velocity around 5 m/s with corresponding Re = 0.95E+04 to 4.34E+04, the drag force had not extreme changes while for higher velocities around 10 m/s the drag force of the members with ice profile was smaller than bare angle member.

CHAPTER 7

AN INTRODUCTION OF USING PIV TECHNIQUE TO STUDY THE EFFECTS OF ICE SHAPE ON THE VORTEX SHEDDING OF A CYLINDER

CHAPTER 7

AN INTRODUCTION OF USING PIV TECHNIQUE TO STUDY THE EFFECTS OF ICE SHAPE ON THE VORTEX SHEDDING OF A CYLINDER

Introduction

As it mentioned before, the study of the variations of flow characteristics such as velocity field, turbulent intensity and vorticity with considering icing effects is significant to help better understanding of flow around bluff body. These characteristics are used to make detailed flow field measurements to quantify the evolution of unsteady flows around different models for different conditions

In this chapter, the focus is mainly on the use of Particle Image Velocimetry (PIV) to perform velocity field measurements on a simple shape (cylinder profile), bare and with ice

accretion. This investigation is important in order to study the effects of accreted ice on flow fields of bluff body and particularly to apply the measurement process to angle members. It is also significant for aerodynamic studies. The aim is to assess the PIV applicability to the understanding of such phenomena to provide useful information about aerodynamic characteristics of bluff bodies specially the variations of drag and lift coefficients.

7-1-Test models

Two cylinders having a length of 87cm and a diameter of 3.8cm were used. The blockage ratio and aspect ratio for the models were around 8.3% and 24%. The first model was a bare cylinder having a symmetric profile with a smooth surface (Figure 7-1a). The second cylinder had an ice accretion profile on its windward side (Figure 7-1b). The considered shape was obtained from measurements performed at CAIRWT.

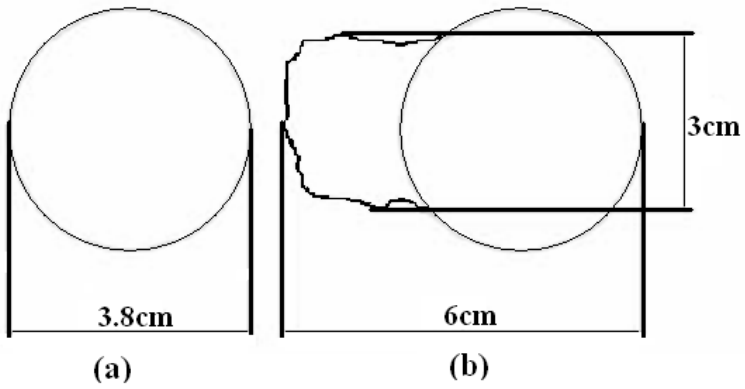

Figure 7-1: Accretion cylinders with a) bare profile, and b) profile with ice accretion shape

The ice profile was made of cement and a casting process was used to reproduce the ice profile on the surface of the cylinder. The profiles were covered with black, opaque paint, to minimize reflection during PIV measurements. For the PIV tests, the cylinders were mounted in the middle of the test section of the tunnel.

7-2-Test procedure

The first measurements on the bare cylinder were performed in the middle of the test section at zero angle of attack. PIV measurements were done for different Reynolds numbers (2×10^5-1.2×10^6). The region where the measurements were performed is indicated in Figure 7-2. For this region, Canon lens with lens aperture opening of f/1.4 was used.

The origin was at the center of the test section.

- The x-axis coincided with the tunnel longitudinal center line and it was oriented in the direction of the free-stream velocity.

- The y-axis was placed vertically and oriented upward.

The following test parameter values are reported in Table 7-1: distance between the laser sheet and CCD camera, laser pulse energy, time between two exposures and number of image pairs for each area.

A CCD camera defines as a digital camera with a sensor that converts light into electrical charges. The image sensor employed by most digital cameras is a Charge Coupled Device which is CCD camera.

Five calibration images were acquired for each image series in order to calculate the magnification factor, M, and the observation area position. After the displacement data were measured, they were converted to velocity using the known magnification factor and the exposure time.

For each experimental condition, the time series of the particle images were captured to calculate the continuous evolution of the velocity fields. The velocity fields were averaged to get the statistic parameters such as mean velocity and vorticity. Typical instantaneous velocity fields for each case were introduced to show the basic flow structure of the flow separation of the wind surface. This information will be useful to calculate the drag coefficient and drag variations.

These procedures and measurements were repeated for the cylinder with ice accretion shape models to calculate the velocity field and observe the effect of ice accretion on velocity field around the cylinder.

Table 7-1: Test parameters of PIV investigations

Trigger rate (Hz)	Time between pulses (μs)	Exposure time (μs)	No. of images	Distance between light sheet & CCD camera (m)	Laser pulse energy (mJ)
500	40	50.044	500	0.85	100-500

Table 7-2 shows the dynamic and thermodynamic parameters of the ice accretion process and Table 7-3 displays the CAIRWT adjusted parameters for the PIV measurements.

Table 7-2: Ice accretion parameters

Air velocity during ice accretion (m/s)	Water pressure (kPa)	Air pressure (kPa)	Air temperature during ice accretion (°C)	LWC (g/m^3)
10	400	400	-10	4.5

Table 7-3: Velocity measurement values

Air temperature during PIV measurements (°C)	Air velocity during PIV measurements (m/s)
18	5-10-20

7-3-Experimental Results

Figure 7-2 shows the instantaneous flow field on the model upper side with zero

angle of attack for both bare and ice accretion shape profiles. When the flow follows the bare profile contour, it is clearly visible that the velocity increases to a maximum (exactly before the red circle in Figure 7-2a) and then decreases as we move further around the cylinder. Therefore, based on the inviscid theory, a decrease in velocity corresponds to an increase in pressure. The fluid elements experience a net pressure force opposite to the flow direction. At some point, the momentum of the fluid is insufficient to move the elements further into the region of increasing pressure, and the flow starts to separate from the surface (the red circle in both figures 7-2a-b). This observation might also be explained by the change of direction required for the flow to follow the cylinder surface. When there is ice on the cylinder (Figure 7-2b), the adverse pressure increases for a shorter distance and the onset of separation occurs closer to the front of the cylinder.

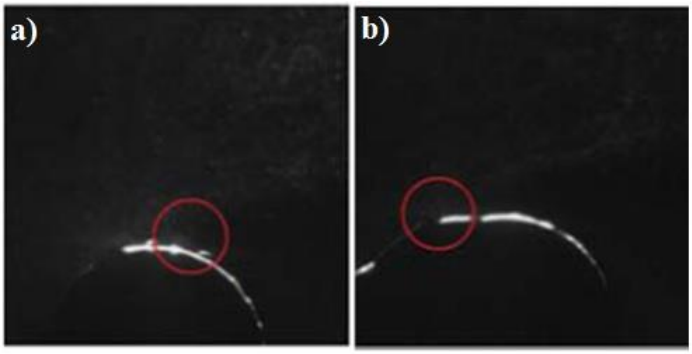

Figure 7-2: Flow field around a) a bare profile, and b) an ice accretion shape profile; air velocity: 10m/s

A von Karman vortex street is a repeated pattern of swirling vortices in the wake of a bluff body caused by the unsteady separation of the flow [63]. A specific Re number range

($47<Re<10^7$) must be considered [63] in order to shed vortices; the tests were conducted for Reynolds number range 2×10^5-1.2×10^6. Vortex shedding occurs in the wake of the bare profile (Figure 7-3) and large scale vortices are formed behind the model. Red contour shows positive vortices while blue contour shows negative vortices. The observations were made only on the upper part of the cylinder but it is expected from other experiments for the shedding to occur alternately on the upper and lower part of the cylinder. The shedding frequency may be calculated using the Strouhal relationship [43], with a Strouhal number of 0.185. The calculated shedding frequency was 48.68Hz which agrees well with the observed period of vortex shedding of about 0.02s.

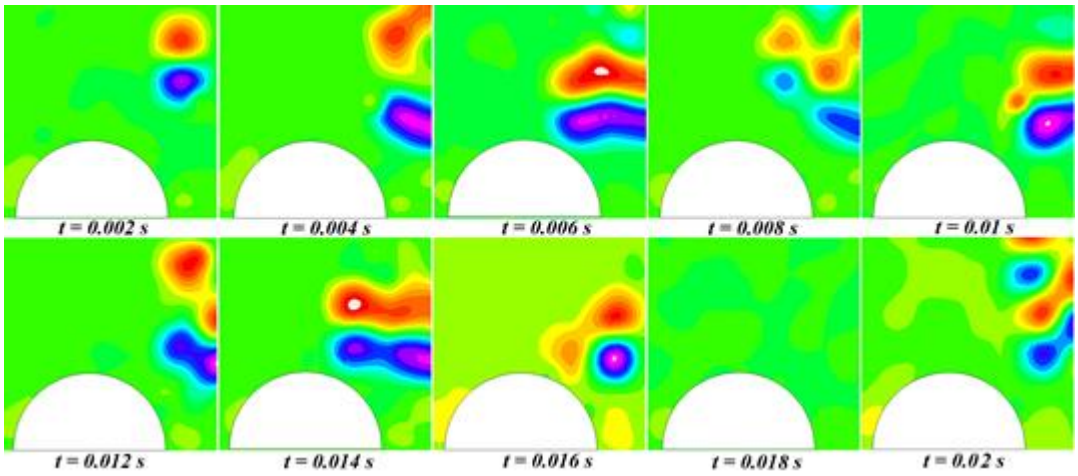

Figure 7-3: Vorticity contour for bare profile, air velocity: 10m/s

Figure 7-4 shows a complicated vortex shedding but because of the specific geometry of the ice, this shedding is unstable. Again, red contour shows positive vortices while blue

contour shows negative vortices. Vorticity is function of the velocity field which is specified mathematically as its curl [63]. The ice accretion profile causes serious variations in pressure distribution and velocity fields, so each variation in a velocity field affects vorticity.

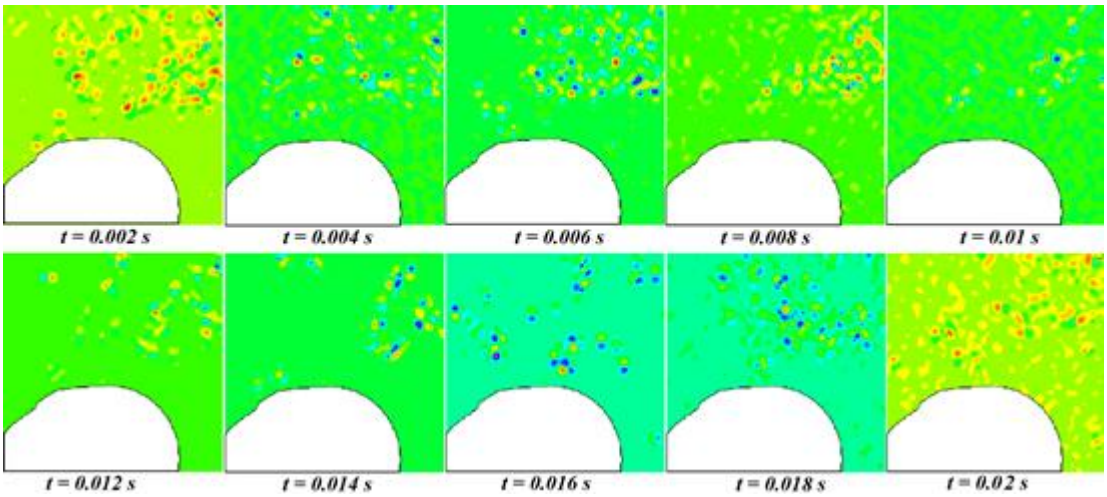

Figure 7-4: Vorticity contour for ice accretion profile, air velocity: 10m/s

Figure 7-5 and Figure 7-6 show the mean velocity field obtained by averaging 500 instantaneous velocity fields measured in the stream-wise center plane for an air velocity of 10m/s. There was a strong reverse flow starting at x/d = 1.4 in Figure 7-5 because of increasing pressure. The length of the recirculation region extended to x/d = 2.5. When the split beam was used, it shut the laser sheet on the cylinder from two sides (up and down), and other recirculation vortices were formed symmetrically, in respect to the wake center line (y = 0).

Figure 7-6, the recirculation area was shifted in front of the cylinder. This area started at x/d = 1.4 and increased at x/d = 2 when the cylinder center was at x/d = 2.5. Based on the recirculation region in Figures 7-5 and 7-6, the ice profile increased in this region and caused the reverse differential pressure to increase, which had a great impact on the aerodynamic coefficients.

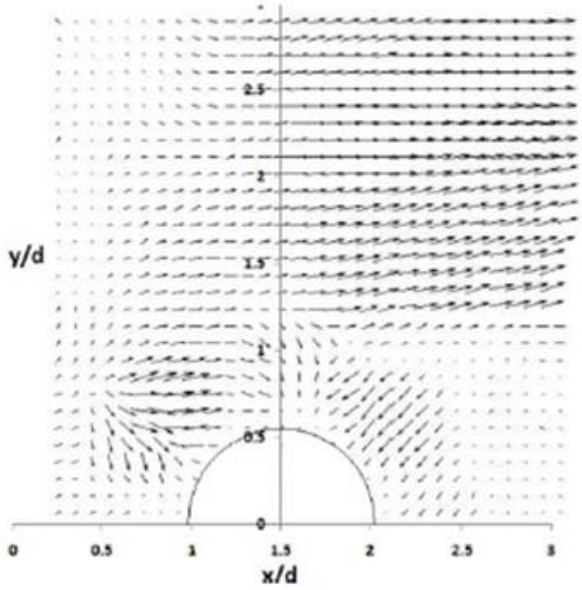

Figure 7-5: Average velocity field vectors for bare profile, air velocity: 10m/s

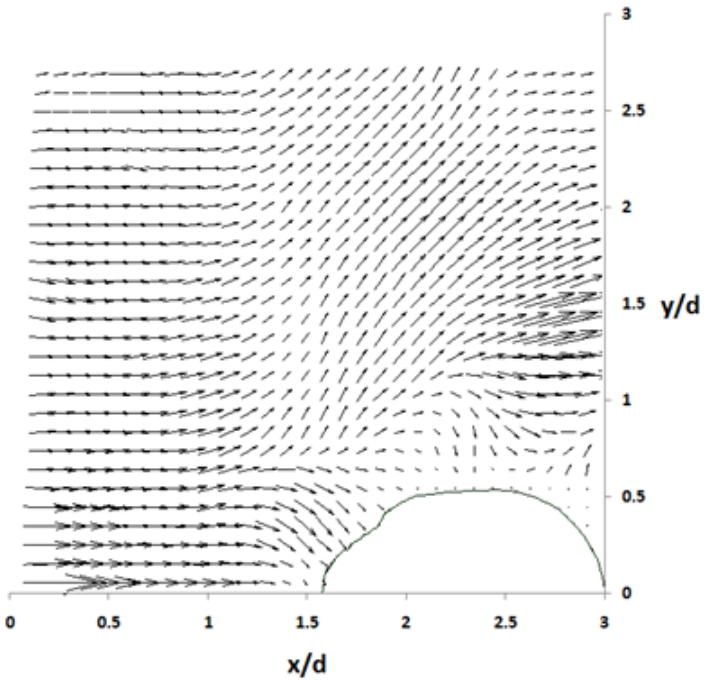

Figure 7-6: Average velocity field vectors for ice accretion profile, air velocity: 10m/s

Conclusion

An experimental study on a circular cylinder covered with ice was conducted using the PIV technique. Velocity measurements were performed on two different cylinder configurations; bare, and with ice accretion profile. The main objective was to assess the use of PIV as a new tool for the study of ice accretion phenomena and also to calculate velocity field and vorticity values in order to use the results as input parameters for calculating an aerodynamic coefficient. The PIV measurements gave detailed information on the flow field structure. Surveys of the cylinder upper side and wake, together with vorticity, rendered obvious the consequences of ice formation on the velocity field. Moreover, the separation, vertical structures and reversed flow regions were clearly

detected (Actually it was a second step to use an angle member and calculate drag coefficient but unfortunately the PIV machine was failed down more than 1 year ago and till now it is in UK for repairing).

CHAPTER 8

CONCLUSIONS AND RECOMMENDATIONS

CHAPTER 8

CONCLUSIONS AND RECOMMENDATIONS

8-1-Conclusions

The work described in this thesis concerns wind tunnel icing simulations based on information gained from nature. Ice shape and ice mass were obtained for different model orientations as well as wind azimuth and thermo-physical parameters. The drag variations were studied by producing experimental models based on DSDs and LWCs. The experiments were carried out in the CIGELE icing wind tunnel while the aerodynamic variations were investigated by creating experimental cement molded ice profile models to study the effects of wind velocity and wind direction on aerodynamic coefficients. The experiments were carried out in the Sherbrooke University aerodynamic wind tunnel.

It was shown that the droplets started to freeze from the stagnation line and continued on both sides of an angle member. For different angles of attack, the tightly packed glaze ice was observed while the ice morphology for different sideslip angles showed that when the sideslip angle increased, the tightly packed glaze ice changed to glaze ice feathers form.

It was shown that when the droplets are not large enough (less than about 80 μm) and the air velocity is high enough (greater than 10 m/s), then numerous large droplets were still present close to mid-height even at the streamwise position of x=0.5 m leading to the greatest MVD and LWC at mid-height. The LWC increases in the vertical direction toward the bottom for low air velocities and then, if the MVD of the cloud is large enough, also for higher air velocities. Results of ice accretion measurements on the angle bar reflect the observation that ice tends to accumulate mostly in positions where LWC is higher.

This study has shown that it is possible to model the effects of ice and wind loads on a simple angle member when the ice profiles completely reproduced by cement have the same ice surface texture. The aerodynamic models presented can serve as a basis to study various ice profiles of atmospheric glaze ice in terms of drag, lift and moment coefficients. Various bluff body geometries can be easily investigated using these models.

It is also shown that the aerodynamic coefficients for a bluff body such as an angle member with ice profiles is independent of Reynolds number. The average C_D^P is between 1.05 to 1.28 compare with an average drag coefficient of 2 for a bare angle member. From the literature the calculated drag for flat plate in the flow was 2 while it is 1.2 for the

circular cylinder when Re number is less than 10^5.

On the other hand C_D^n varies from 1.34 to 3.88 where C_D^{p0} variations is in the same order of C_D^n which is 1.55 to 3.22.

The calculated drag coefficient for different icing conditions was in the range of 1.61 to 1.68. The high difference between the calculated and measured drag was because of the uniformity assumption of ice thickness and applying effects of angle of attack in the formulation for the calculated drag which decrease the precision of calculations. Otherwise both the calculated and measured drag coefficients indicate that the drag decreased compared to a bare angle member. However, measured values showed that, the more ice thickness and projected area there are, the smaller the drag coefficient they have for a relevant model.

It was explained that the drag coefficient for truss elements is between 2.66 to 3.43 which is higher than the drag coefficient of bare angle member. It was expected to have higher drag values for truss elements because of existence of shielding effects.

The lift force variations were less than drag force variations for different angle of attack. It was explained by the ice profiles shapes, which caused variations on pressure field parallel to angle member while those effects were smaller for pressure field normal to it. On the other hand for drag coefficient, it was shown that for lower velocity around 5 m/s with corresponding Re = 0.95E+04 to 4.34E+04, the drag force had not extreme changes while

for higher velocities around 10 m/s the drag force of the members with ice profile was smaller than bare angle member.

8-2-Recommendations for future study

- Ice simulation on truss element models: The effects of angle member corners on an ice profile shape have been studied by taking into consideration the ice profiles photos for different angles and model orientations. Experimental studies of ice shape for telecommunication towers and some aerodynamic airfoils have also been carried out where in site measurements were considered in some researches. In this study, an experimental approach to model ice and wind effects as well as thermo-physical parameters of icing was introduced. Coupling this new experimental approach of ice simulation with the experimental approaches of the truss element models subjected to icing loads may provide a reliable corner effects for different situations.

- Considering shielding effects: In this study, to start with a simple model to demonstrate the new approach, we proposed only one simple model, mounted in both an icing wind tunnel and an aerodynamic wind tunnel. However, improvements of the experimental model accounted for the effects of other tower members or shielding effects which used to apply to two or more similar members during icing and aerodynamic measurements. Adding the influence of the other members is expected to give us a reliable approach in order to calculate aerodynamic coefficients on larger and complicated bluff bodies.

- Reduced-scale experiments of whole transmission towers: Reduced-scale experimental results indicate that the experimental model accurately calculates the aerodynamic coefficients of an iced angle member subjected to different wind velocities. However, it was found that the reduced-scale model possesses a high degree of sensitivity to the aerodynamic measurements, which is believed to be unimportant in a reduced-scale of the whole tower. Therefore, it is recommended to have a whole reduced-scale of tower for aerodynamic measurements in order to have a better understanding of drag and lift variations.

- Considering different icicle profiles: In this study, different glaze ice profiles considered for aerodynamic measurements showed much different values of drag, lift and moment coefficients. However, the aerodynamic results from finger icicle glaze ice showed that the icicles length and thickness affect real projected area and contrary these effects change the drag coefficient. Therefore, it is recommended to cast different cement moulded icicle profiles of an angle member with different icicle length and icicle thickness to study the variation of aerodynamic coefficients based on real projected areas.

APPENDIX A

CAIRWT LAYOUT

APPENDIX A: CAIRWT Layout

Test Section (a)

The most important segment of any icing wind tunnel is the part called the test section where the icing structure being analyzed is placed. The test section of the CAIRWT is around 3m long with a constant rectangular cross-section 46cm high and 92cm wide (Figure A-1). The test section length to hydraulic diameter ratio (defined in section B1) typically chosen is 2 or more [90]. Here, this ratio is around 5.

Figure A-1: Schematic view of the Test Section

The size of the test section as well as its constant cross-sectional area should serve to maintain constant most of the meteorological elements in this part of the tunnel. Normally, a small divergence in the wall of a test section ensuring that constant static pressure is

maintained on the right value. This is due to the fact that, for this subsonic unpressurized wind tunnel, the non-maintenance of this condition may produce changes in the dynamic characteristics within the range of accuracy of their measurement only. A far more significant point influencing local velocity inside the test section is the problem of blockage of flow by an icing body. The walls, roof and floor of the test section are made of Plexiglas, in order to avoid the potential for creating additional turbulence due to rough surfaces. The smooth surface of the Plexiglas, therefore, makes it possible to obtain high quality air flow with a decreased level of turbulence.

The transparency of the Plexiglas also bypasses the need for installing observation windows to be used for flow visualization or for taking photographs. The floor of the test section is fixed with silicone to a wooden base which is used as a substrate in order to reinforce the entire construction. On this surface, the Plexiglas has been installed in a way to prevent the water leakage when the heaters warm up. Those surfaces conduct water to drain at both ends of the test section. The Plexiglas walls are strengthened with aluminium rakes and the joints between the plates are made of silicone to ensure that the section is tightly sealed. The body under observation can be placed inside the test section by opening its roof. This roof made of Plexiglas moves up on one hinging device and also opens sideway. The top edges of the walls are encased in U-shaped rubber stripping which is used to provide a high level of adjacency between both covers and the tops of the walls. The entire test section is located inside a 3.5-m long, 4.5-m wide and 3-m high test chamber. This room may be used for preparation of the equipment to be used there, observation of the ice accretion process and various manipulations with the ice patterns already obtained.

Diffusers (b), (i)

The total length of diffusers is of at least three or four times that of the test section and the typical equivalent cone angle is in the range of 2-3.5° with smaller angles being more desirable. The area ratio is typically 2-3, again with smaller values being more desirable [99]. The CAIRWT has two diffusers with a cone angle around 3°. The sections with a downstream widening cross-section, or diffusers, are destined to recover the static pressure and to reduce the air speed before passing the segments containing the three main systems for maintaining the icing conditions inside the tunnel. The first diffuser extending from the downstream end of the test section to the first corner after the test section is intended to receive the *highly waked* air flow after it passes the icing object, and also to reduce flow velocity by expanding it. The second diffuser, called a return passage, has a length of 7.8 m and is located between the fan sections.

Corners Incorporating Turning Vanes (c), (f), (j), (l)

Four corner sections are designed so that the loss of velocity head is reduced by using turning vanes shaped like cambered airfoils with 1 m in length.

Legs (d)

The legs may continue the diffuser or may have a constant area. These segments with constant cross-sections are intended to cause re-laminarization and decrease the level of its free stream turbulence. The converging and preparatory sections, as well as the smaller

fitting section ahead of the fan location, belong to this group of segments.

Air Deflector (Chicanes) (e)

The air deflector is a temporary barrier, or serpentine curve, on a wind path, especially designed to reduce speed and turbulence. CAIRWT`s chicanes zigzag to collect water droplets, preventing them to accumulate on the ventilator of the fan.

Transition Area (g)

This area is a transition from a rectangular to a circular cross section, which takes the flow into the fan.

Fan (h)

It is the most common device for producing flow in subsonic wind tunnels. This fan is an axial flow fan type. Axial flow fans, or propellers, produce swirl in the flow and they induce some combinations of pre-rotated blades and straightening blades. The fan itself is the source of the power input while the blades absorb some energy in the process of carrying out the flow. The role of the fan and its straightener is to provide a rise in pressure of the flow passing through the section. The increase in pressure provided must be equal to the pressure losses throughout all the other sections of the tunnel in any given steady flow operating condition.

Heat Exchanger (k)

This segment is designed to obtain and maintain the required air temperature test without affecting the streamline or other fluid parameters. The complete process and other equipment that is related to heat exchange will be described in Section 2-3-2.

Heating Element (m)

There are two heating elements inside the tunnel located in front of the honeycomb. They have wide stainless steel fins with a diameter of around 0.95 cm. The total element dimensions with the fins are 127.5cm × 30cm and their power is around 7500 Watts. These elements are used after each experiment to melt the ice accumulated inside the tunnel. They are monitored from a control panel.

Flow Conditioners (Honeycomb) (n)

The objective of obtaining a spatially uniform steady stream of air throughout the volume of a wind tunnel test section has been pursued for nearly a century. Over that time, as already indicated, a general arrangement of elements was settled upon, but problems still remain and the result is not viewed as truly optimized yet. One area that continues to resist fully rational quantitative design treatment is the management and control of *turbulence* in the flow. Prandtl did some work in order to obtain stream uniformity more than 60 years ago. The approach then, as now, was to use *honeycombs* to force the flow to go essentially in the same direction, and screens to bring the various parts of the flow closer to constant

speed. A honeycomb is a guiding device through which the individual air filaments are rendered parallel [23].

The honeycomb of the CAIRWT is a CRIII-1/4-5052-0.0015N-3.4 model with 115cm in length and 175cm in height. There are 4 horizontal rods at every 35 cm which reinforce the honeycomb grid.

Spray Nozzles (o)

The water is injected into the tunnel via three air-assisted nozzles which are located in a horizontal spray bar as shown in Figure A-2. The spacing between nozzles is 20 cm and is adjustable by 3cm. Air-assisted nozzles provide the finest degree of atomization for a given capacity and pressure. Presently, two types of air-assisted nozzles are available in CIGELE laboratories which will be named Type A and Type B. Both are manufactured by Spray Systems Co. and incorporate the same 2050 stainless steel water cap, and different stainless steel air caps, 67147 (type A) and 67-6-20-70 (type B).

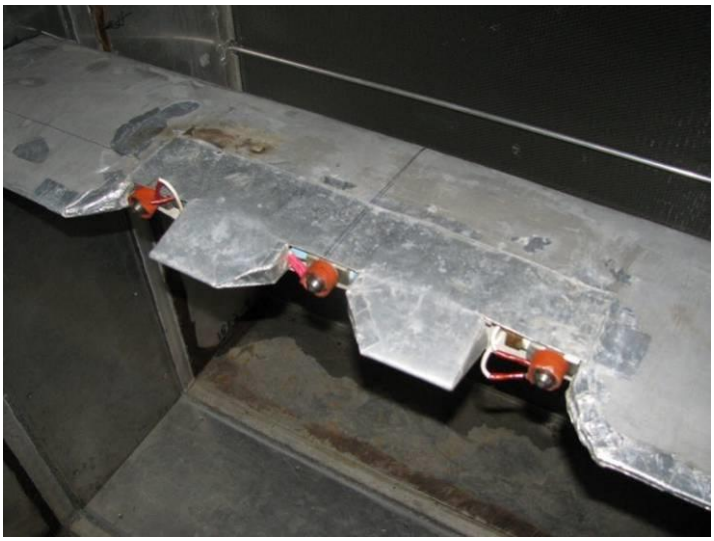

Figure A-2: CAIRWT`s Spray Bars with Heating Element

Settling Area (p)

These segments with downstream narrowing cross-sections are intended to cause an acceleration and contraction of the air flow, producing its re-laminarization and decreasing the level of its free stream turbulence.

Contraction Nozzle (q)

The contraction *cone* takes the flow from the settling area to the test section while increasing the average speed by a factor of up to 20 or more, although typical values are in the range of 6-10 and for CAIRWT, it is around 4. CAIRWT's contraction cone as is the case of other nozzles in different wind tunnels is in fact never conical in shape, in spite of the term sometimes being used to refer to this section of the wind tunnel.

APPENDIX B

CAIRWT CALIBRATION RESULTS

APPENDIX B: CAIRWT Calibration Results

Introduction

The airstream created in a wind tunnel is defined by the parameters listed in Chapter 3 together with their spatial and time distributions. The air flow calibration process in CAIRWT focuses on determining velocity profiles in different cross-sections and the variation of the airstream velocity in time, which is characterized by the level of turbulence. In two phase flows such as the air flow carrying water droplets in icing tunnels, the LWC, DSD and their uniformity in a cross-section should also be considered in order to characterize the spray. The variation of LWC in a cross-section may describe by uniformity maps. A single parameter, MVD, is often used instead of the entire DSD in order to describe droplet size in a cloud. Thus, CAIRWT calibration contains two parts: airflow calibration, which consists of air velocity and turbulence measurements in the spray bar section and in the test section, and spray calibration including LWC and DSD measurements in the test section.

Before starting this research, the CAIRWT was under construction with general modifications. It was necessary to recalibrate the tunnel before doing any ice simulation. In this chapter, first the regime of the flow is determined followed by the air flow calibration for three parts to be investigated: spray bar section, entrance of the test section and middle of the test section in order to obtain velocity and turbulence. The LWC uniformity map is

obtained for the middle of the test section. At the end of the chapter the LWC and DSD plots are obtained based on different air and water pressures.

B-1-Flow Regime in the test section

Firstly, the Reynolds number and tunnel boundary layers are estimated in the test section by using the formulation below. If the duct is noncircular like the test section of CAIRWT, the Reynolds number is calculated using a hydraulic radius R_h, defined by:

$$D_h = \frac{4A}{P} = \frac{4(Cross\,Sectional\,Area)}{Wetted\,Perimeter} \tag{B-1}$$

Chapter 3 provides the dimensions of the test section. This data and the application of equation (B-1) yield the hydraulic diameter:

$$\begin{vmatrix} w = 62cm \\ h = 46cm \end{vmatrix} \Rightarrow D_h = 61.33cm \tag{B-2}$$

Equation B-3 shows Reynolds number for different air velocities inside the test section. The transition zone between laminar and turbulent internal flows occurs between 2300 and 4000. According to Equation B-3 the Reynolds number changes between 0 to 1.2×10^6 and the flow is turbulent in the middle of the test section.

$$\mathrm{Re} = \frac{\rho V D_h}{\mu} \tag{B-3}$$

Then, the entrance length for turbulent flow is calculated from:

$$\frac{L_e}{D_h} \approx 4.4\,\mathrm{Re}^{\frac{1}{6}} \Rightarrow \begin{vmatrix} L_{e,V_{\min}} = 18.69m \\ L_{e,V_{\max}} = 27.88m \end{vmatrix} \qquad \text{(B-4)}$$

The length of CAIRWT test section is 3m, which is only 10-15% of the calculated entrance length. Therefore the flow in the test section is in the inviscid core with thin boundary layers in the entrance region. It means that the variation of velocity through streamwise direction and the turbulence level are very low in the test section. Uniformity of velocity is an important factor when modeling ice accumulation; and the air flow calibration will provide the level of uniformity.

B-2-Relationship of fan frequency and air velocity

Air velocity is controlled by adjusting fan frequency. Therefore, the first goal of calibration measurements is to derive the relationship between fan frequency and air velocity in the middle of the test section. Figure B-1 shows this linear relation and corresponding tabulated data respectively, which are applicable to set the tunnel velocity throughout the experiments.

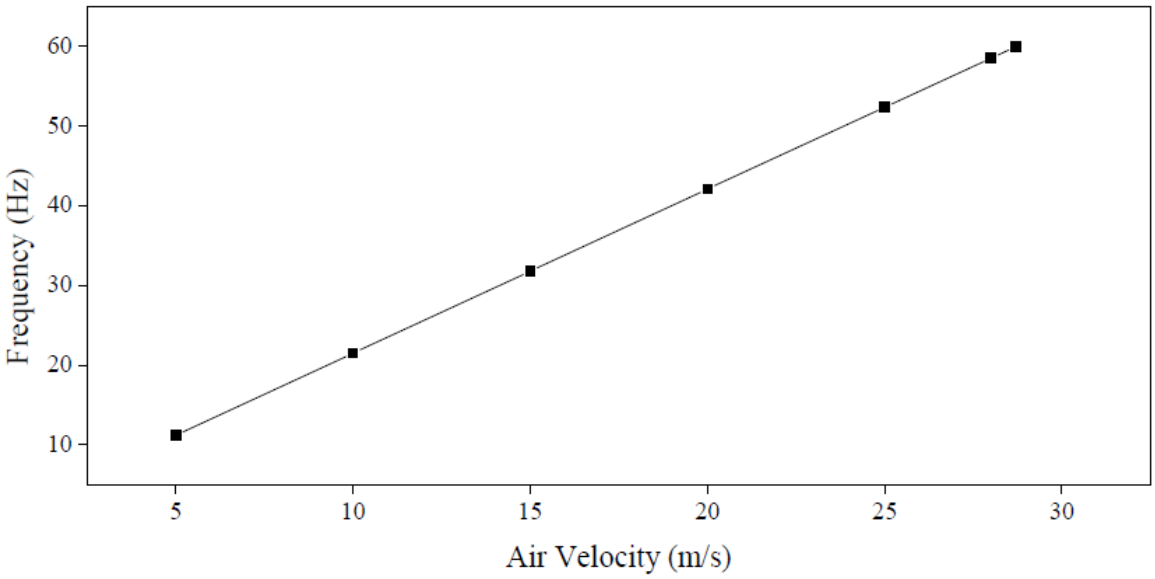

Figure B-1: Relationship between fan frequency and air velocity in the test section

B-3-Air flow calibration

The air flow calibration consists of air velocity and turbulence measurements in the tunnel. Transverse and vertical distribution of these parameters have been measured at the spray bar section (A in Figure B-2) as well as in the entrance (B) and middle (C) of test section by using a Pitot tube in a circuit with a precise differential pressure transducer and an NI data acquisition card.

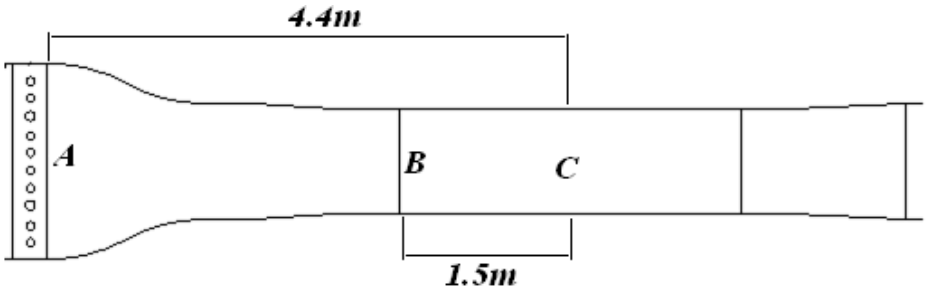

Figure B-2: Sections of air flow calibration

The calibration process was the same in all sections. The total and static pressures were transferred from the Pitot tube to the OMEGA instrument which converted them to current in the range of 4-20 mA. Each measurement took 30 s. The NI data acquisition card with additional circuit was used to transfer this current to the LABVIEW program in order to display it together with the voltage. These voltage values were applied to calculate velocities after the velocity-voltage relationship had been determined using Omega anemometer. The velocity data acquired during 30 s was then used to calculate mean velocities and turbulence levels as presented in Section 1-3. Measurements were performed with four different air velocities as measured in the test section: V_{a1} = 5 m/s, V_{a2} = 10 m/s, V_{a3} = 20 m/s and V_{a4} = 28 m/s. These velocities are almost 4 times greater than those measured in the spray bar section due to the contraction preceding the test section.

B-3-1-Air Flow Calibration in Spray Bars Section (A)

A simple setup was used to carry out calibration in the spray bar section. First, the spray bar was removed and the Pitot tube was inserted into a plastic arm which was moved

horizontally in the place of the spray bar or vertically in the middle of the section. For the measurements in the horizontal direction, the plastic arm carrying the Pitot tube was fixed from outside of tunnel wall; however, when the measurement position was far from the tunnel wall, and also in measurements in the vertical direction, the plastic arm was fixed from the inside. In both cases, a tripod was used to fix the Pitot tube and to avoid its vibration. It should be noted that the tripod was always placed far enough from the Pitot tube in order to reduce its effects on the air flow in the vicinity of the Pitot tube.

The setup is shown in Figure B-3. The measurements took place at an average of 12-cm-intervals vertically from bottom to top, avoiding the positions of the horizontal bars reinforcing the honeycomb, and at 20-cm-intervals horizontally from the right side of the spray bar section toward the other side. These intervals were reduced in the boundary layers near the tunnel walls.

Figure B-3 Setup for velocity measurements in (a) vertical and (b) horizontal directions in the spray bar section

Both Figures B-4 and B-5 present velocity and turbulence profiles horizontally and vertically in the spray bar section. The black lines indicate the positions of the tunnel walls, while the red lines indicate the position of the horizontal bars reinforcing the honeycomb. Figures B-4 and B-5 show the regions of uniform velocity. In these regions, the turbulence level is also reduced, which confirms the role of the honeycomb. Better uniformity may be observed horizontally because there are some fluctuations in vertical velocity at the positions of the horizontal bars in the honeycomb. Velocity drops and turbulence level increases in the boundary layer near the tunnel walls. More severe changes occur toward the top due to the proximity of the corner preceding the spray bar section. The corner causes flow separation here where local velocity vector may point upstream. This was not

verified by measurements; therefore, the curves are not completed until the tunnel wall.

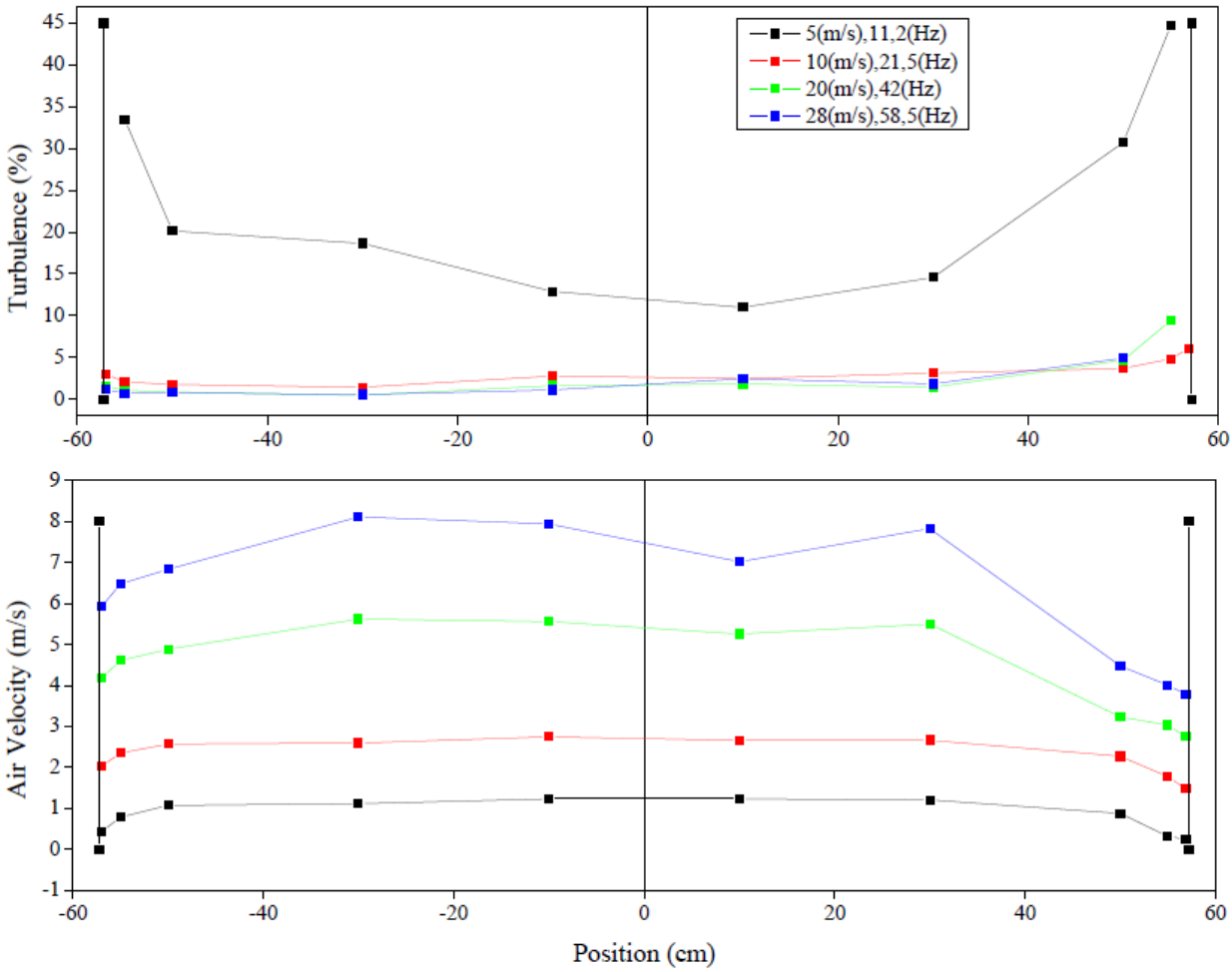

Figure B-4: Horizontal turbulence and velocity distribution in the spray bar section

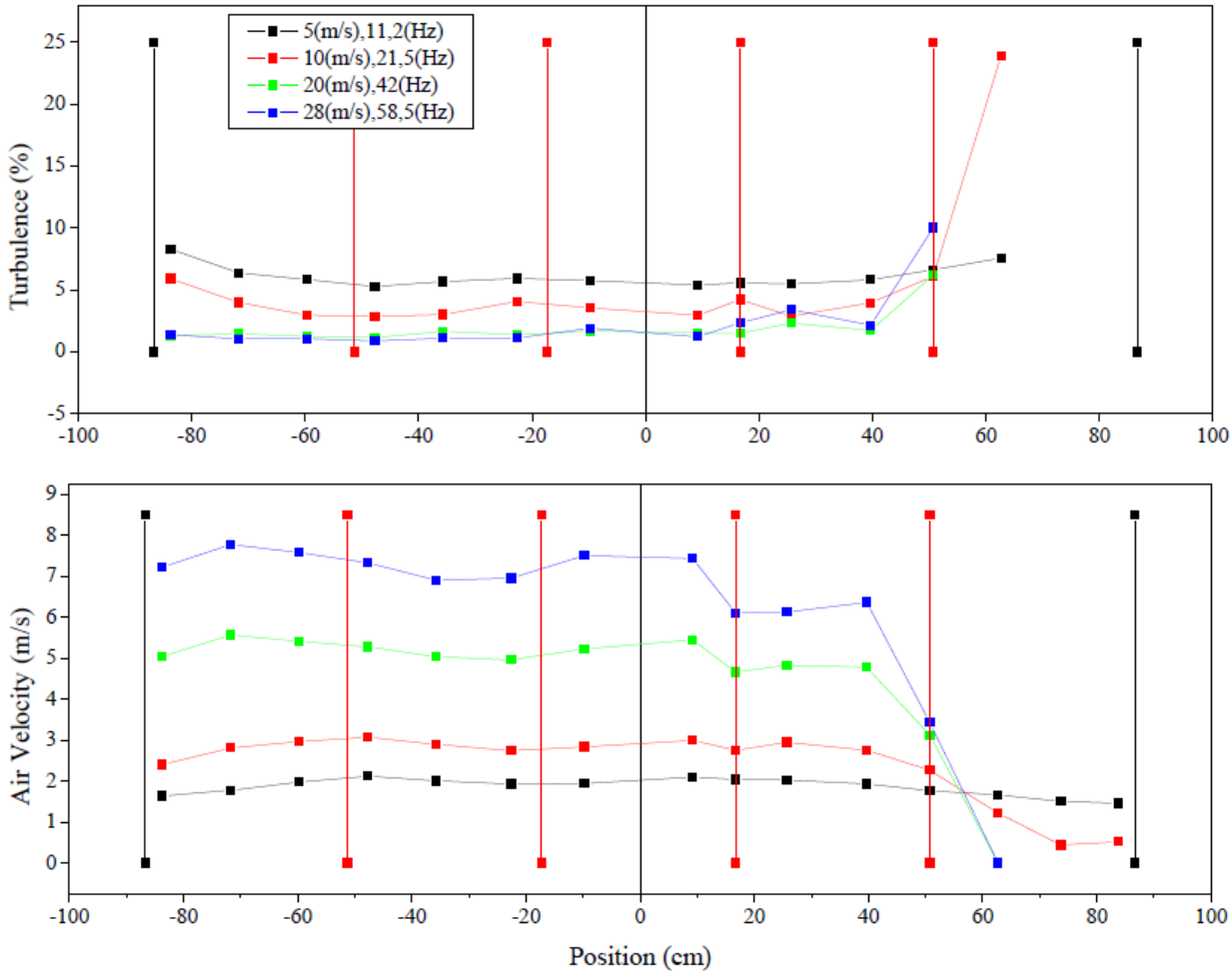

Figure B-5: Vertical turbulence and velocity distribution in the spray bar section

B-3-2-Air Flow Calibration at the entrance of Test Section (B)

Both Figures B-6 and B-7 show velocity and turbulence profiles horizontally and vertically in the entrance of the test section. After the flow passed the contraction section, uniformity is greatly improved; although the velocity is lower and the turbulence level is higher near the top of the tunnel than near the other walls. This result is the consequence of the corner as discussed in the previous section.

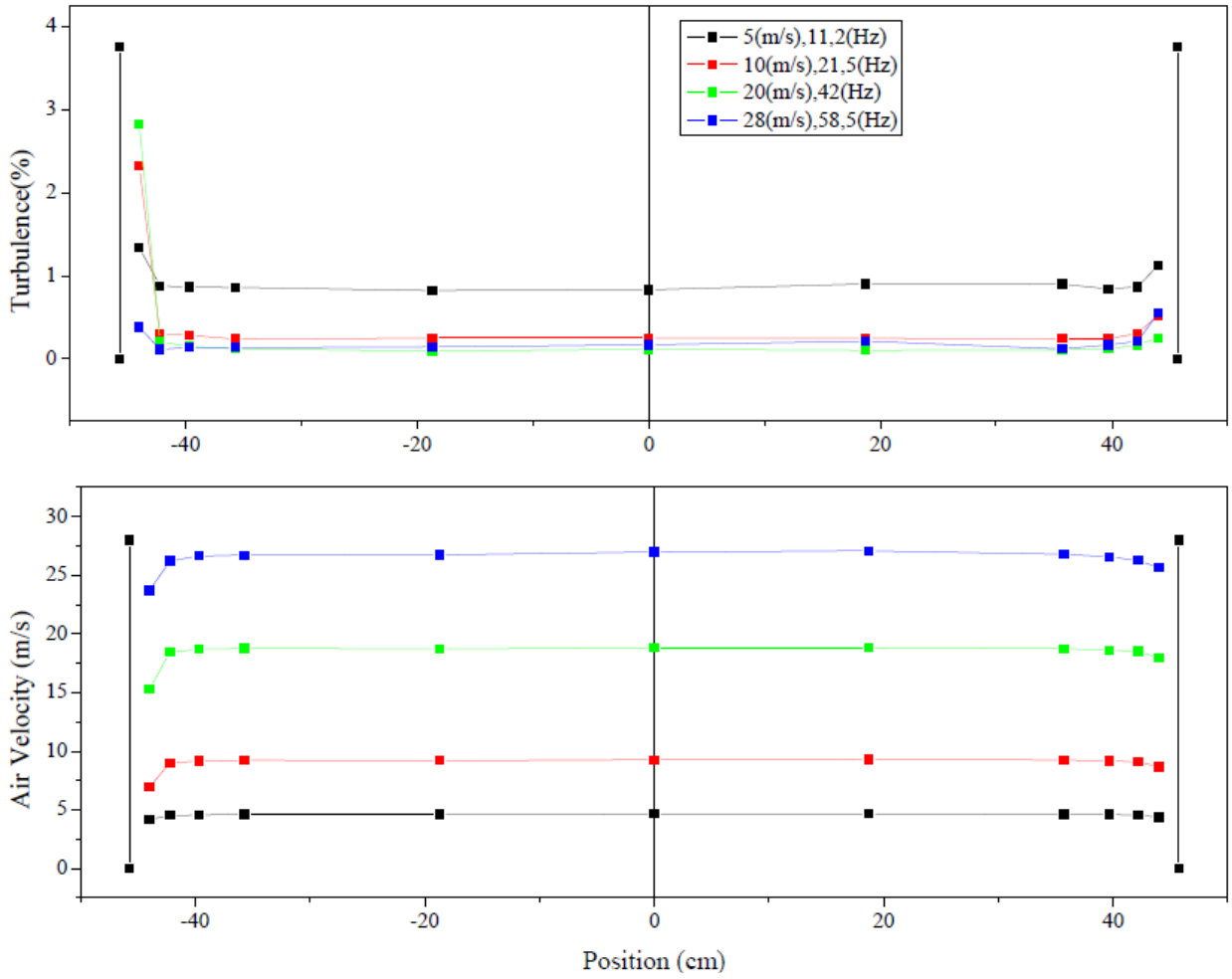

Figure B-6: Horizontal turbulence and velocity distribution at the middle of the entrance of the test section

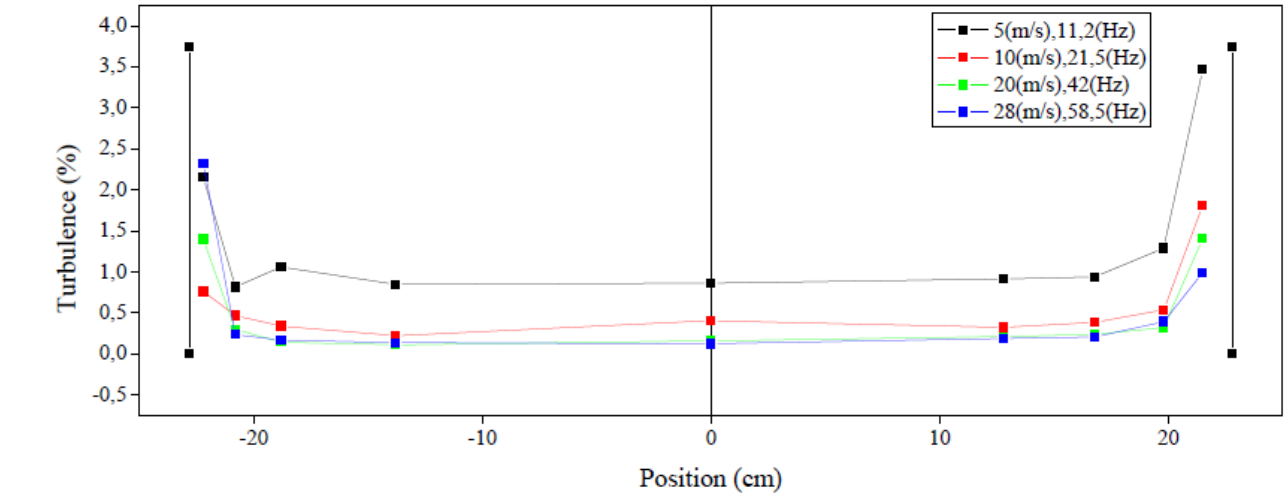

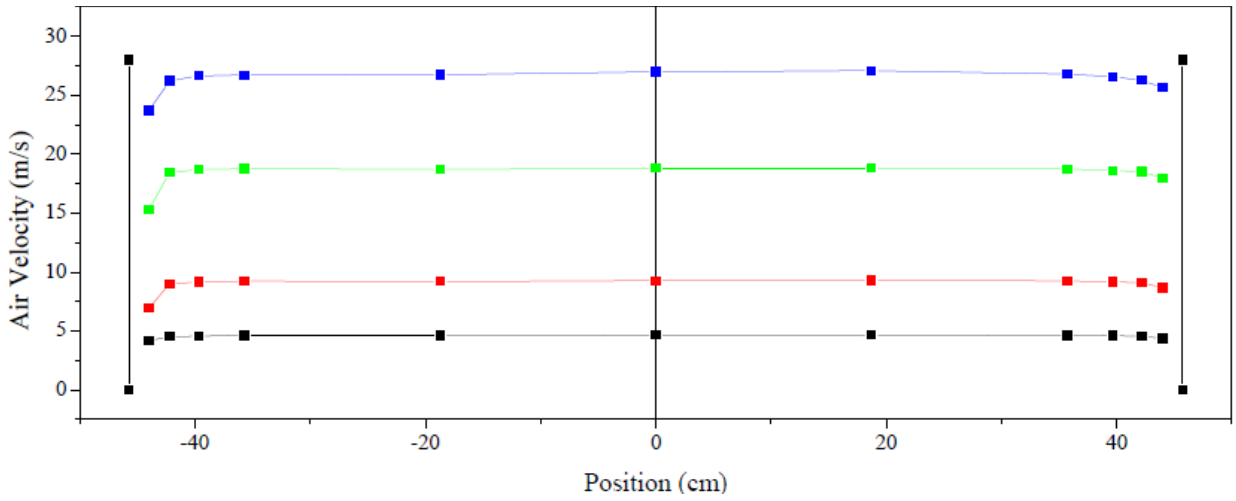

Figure B-7: Vertical turbulence and velocity distribution at the middle of the entrance of the test section

B-3-3-Air Flow Calibration in the Middle of the Test Section (C)

Calibration results in the middle of the test section are shown in Figures B-8 and B-9. Once the flow enters the test section, the boundary layers begin growing. Simultaneously, the air velocity in the inviscid core increases downstream in the entrance region. However,

as it was mentioned, this variation is very small, because the length of the test section is less than 15% of the length of the entrance region. The most important observation is the excellent uniformity of velocity profile and the low level of turbulence, although the increase of the boundary layers from the entrance of the test section is also considerable. The particular importance of these results lays in the fact that icing objects are usually placed in this section.

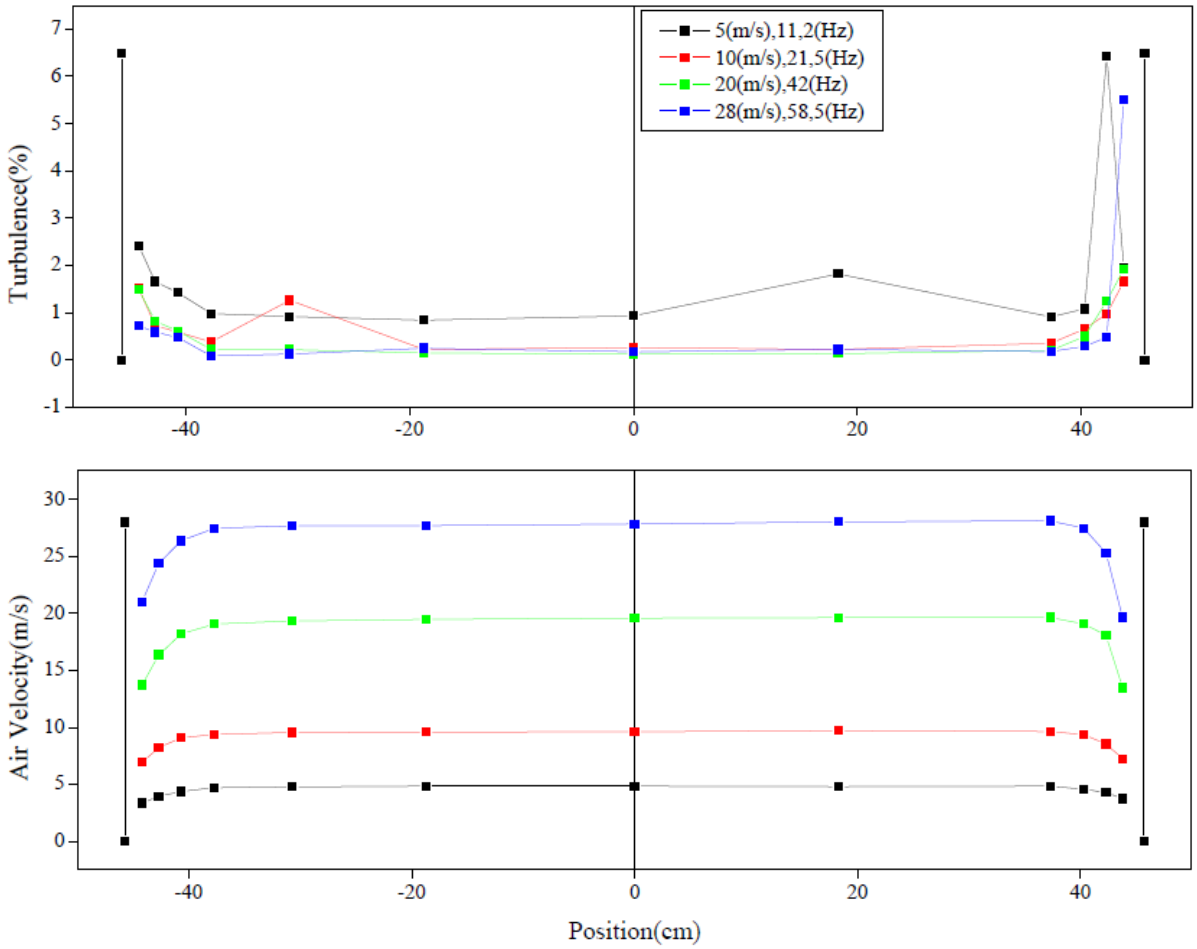

Figure B-8: Horizontal turbulence and velocity distribution in the middle of the test section

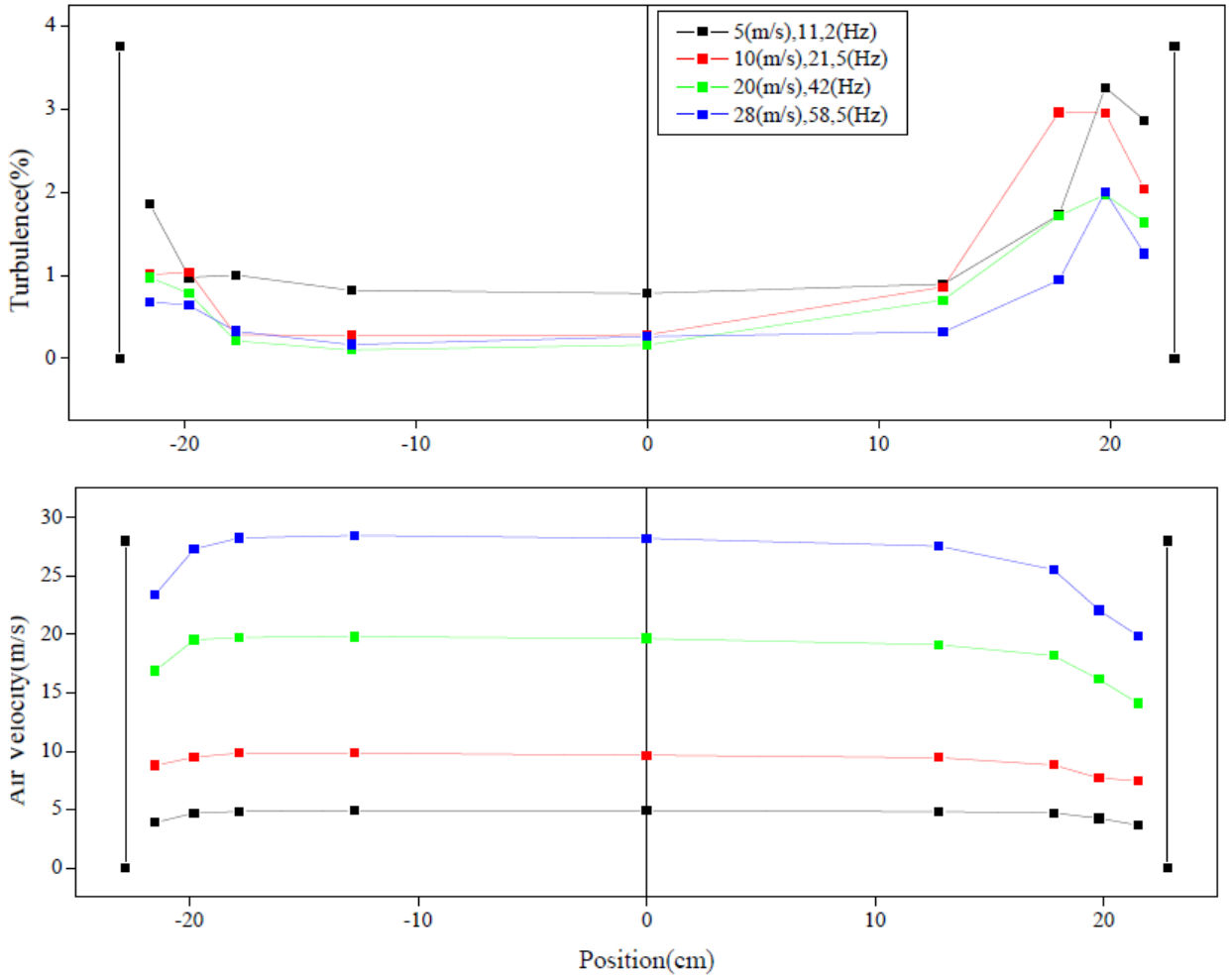

Figure B-9: Vertical turbulence and velocity distribution in the middle of the test section

B-4-Sprays Calibration

The spray was produced by three type A nozzles (see chapter 3) in the calibration process whose results are presented in the subsequent sections.

B-4-1-LWC Uniformity in the Middle of the Test Section

The LWC uniformity was measured by a technique which was applied in the NASA

Lewis Icing Research Tunnel [100]. This technique involves accreting ice on a 3.8-cm-diameter cylinder and measuring its circumference at different positions. The cylinder was mounted in 7 vertical positions with 5-cm-increments, and circumferences were measured with horizontal increments of 5 cm at each vertical position.

The shape of ice accreted on the cylinder is controlled by several parameters including LWC, DSD, air velocity and temperature, and duration of spray. The duration of spray was varied between 3 and 10 minutes and air temperature was set at -20°C. This temperature was determined so as to avoid shedding and dry ice accretion. The tests were carried out for two different velocities; V_{a1}=5 m/s and V_{a2}=28 m/s. Pressures in nozzle water and air lines were set at 300 kPa and 100 kPa, respectively, which provided a cloud with MVD above 60 μm (depending on air velocity), and at 300 kPa and 320 kPa, respectively, providing a cloud with MVD of around 40 μm (see Chapter 3 for details). The resulting clouds will be referred to as "cloud with large droplets" and "cloud with small droplets".

Circumference measurements were converted to relative LWC normalized to the measurement at the center of the test section using the equation below:

$$\frac{LWC(x,y)}{LWC_c} = \frac{C(x,y) - C_{cylinder}}{C_c - C_{cylinder}} \tag{B-5}$$

where C(x,y) is the circumference of the iced cylinder at each location, C_c is the iced circumference at the center location, and $C_{cylinder}$ is the un-iced circumference of the cylinder. Results are presented by the contour maps shown in Figures B-10 to B-13.

The two forces which are the most significant for determining particle trajectory are inertia and aerodynamic drag [101]. If inertia forces are small then drag will dominate and the droplets will follow the streamlines of air closely. This is the case for small droplets and for high velocities, when most of the droplets are concentrated close to the geometrical center of the section as shown in Figure B-12. For large droplets and low velocities, on the other hand, inertia will dominate and droplet trajectories will be deflected toward the bottom as it may be observed in Figure B-11. It may also be concluded from Figure B-10 to B-13 that the droplet cloud is more expanded in the section when the air velocity is lower. The transverse zone of uniformity for low velocities extends almost to the entire width of the test section. However, the vertical separation of droplets of different sizes is also considerable for low velocities. Clouds with uniform DSD may be obtained for high velocities. In this case, the DSD inside the cloud is more uniform for small droplets, but the expansion of the cloud is greater for large droplets.

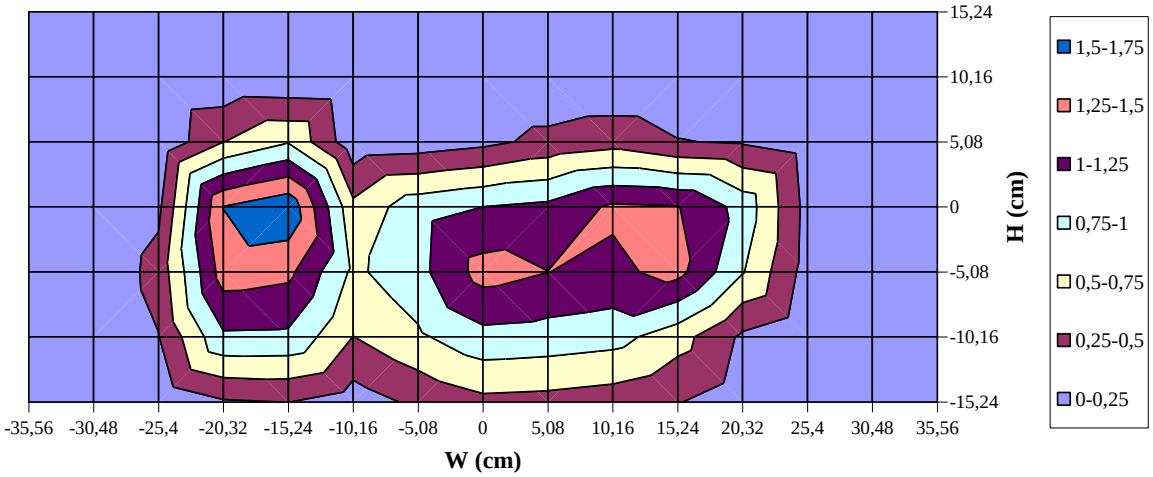

Figure B-10: LWC uniformity for large droplets and high velocity

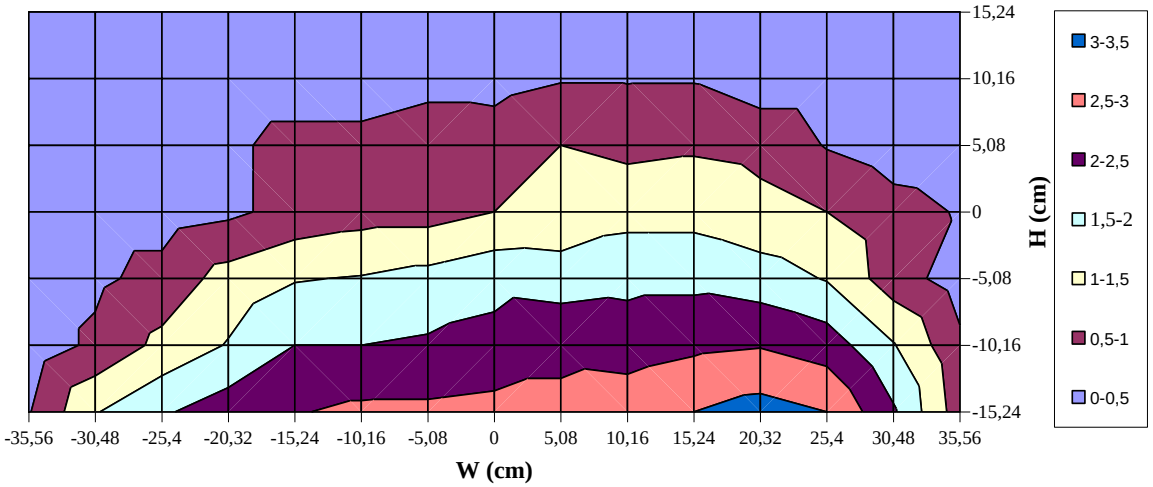

Figure B-11: LWC uniformity for large droplets and low velocity

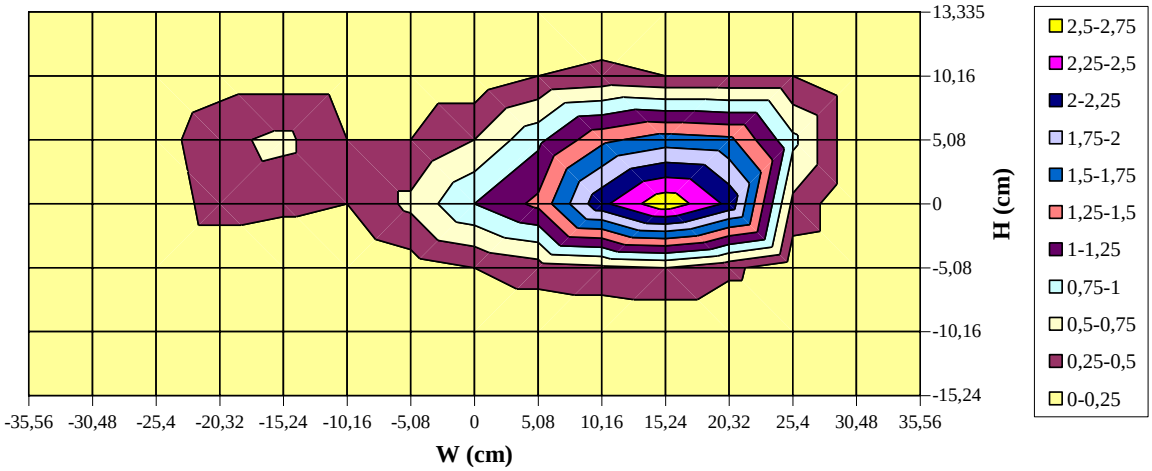

Figure B-12: LWC uniformity for small droplets and high velocity

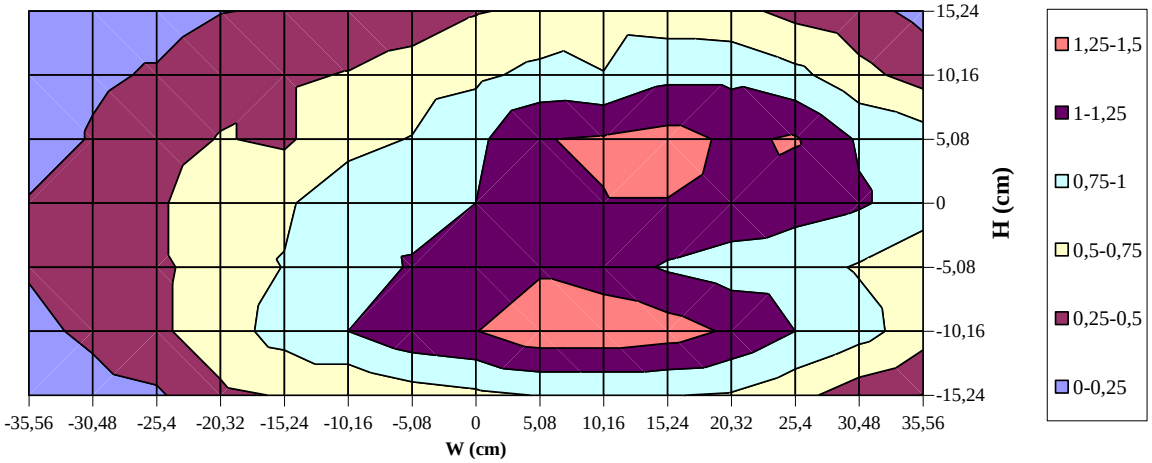

Figure B-13: LWC uniformity for small droplets and low velocity

B-4-2-LWC in the Middle of the Test Section

The integrated system for icing studies manufactured by DMT was used to measure LWC and DSD in the proximity of the geometrical center of the middle of the test section. In these series, the temperature was set at 15°C and the duration of each measurement was

30 s. The measurements were repeated for the four velocities which were also used in the air flow calibration. The droplet size was adjusted by the pressures in the nozzle water and air lines. The water pressure, P_w, was set at 100 kPa, 200 kPa, 300 kPa and 400 kPa, and the air pressure, P_a, was varied from a maximum when the flow was observed to a minimum which was 70 kPa. Figure B-14 shows the LWC as a function of differential pressure, $dP = P_w - P_a$, for different air velocities and nozzle water pressures.

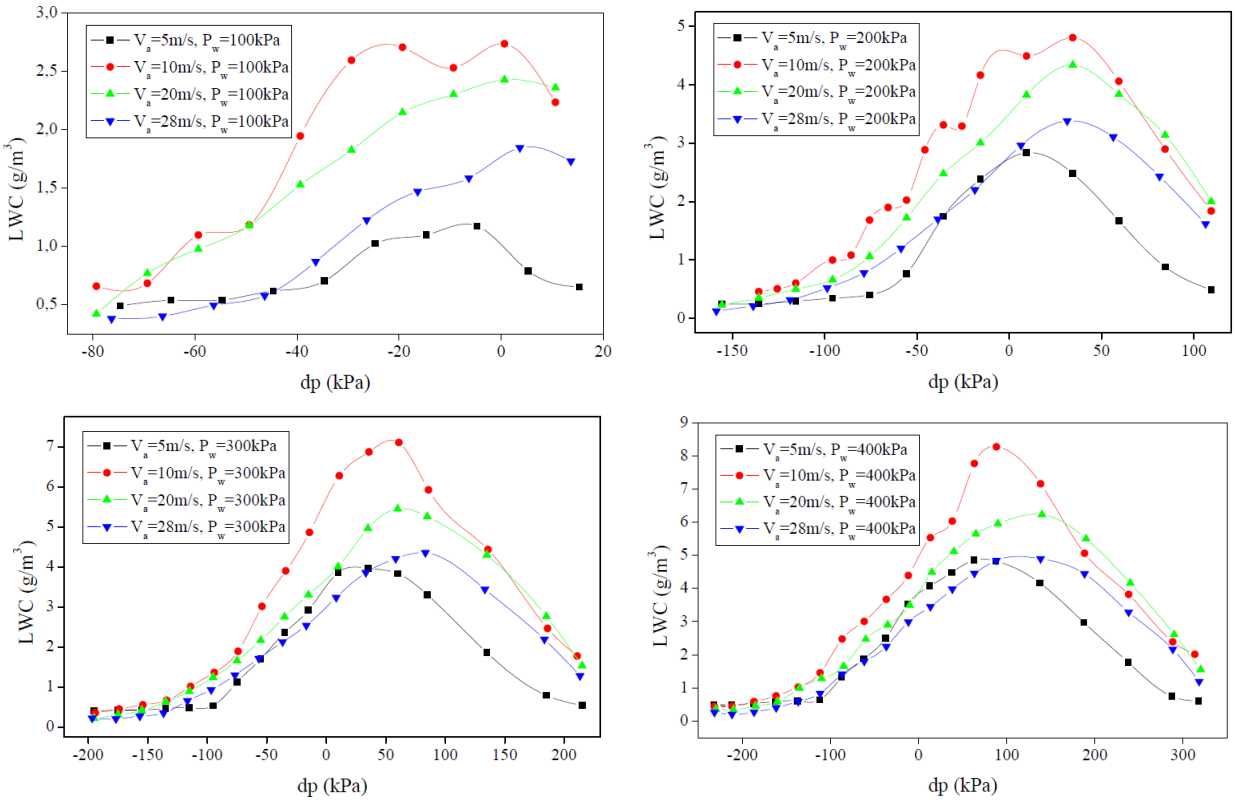

Figure B-14: LWC as a function of air velocity and nozzle pressures in the middle of the test section

Calibration results show that LWC increases slowly with the differential pressure up to about dp = –100 kPa when it reaches a value between 0.5 and 1.5 g/m^3. Then, a steep increase follows until the LWC reaches a maximum. This maximum occurs for a differential pressure between 0 and 100 kPa, and this value increases with water pressure. The maximum LWC increases with water pressure; whereas it increases with air velocity when it is low (below 10-15 m/s), and it then decreases. Thus, the lowest maximum (1.2 g/m^3) was measured for the lowest water pressure (100 kPa) and for the lowest air velocity (5 m/s). The highest maximum (8.3 g/m^3) was measured for the highest water pressure (400 kPa) and for air velocity of 10 m/s. The range of LWC that may be maintained by type A nozzles in the geometrical center of the middle of the test section is between 0.2 and 8 g/m^3.

B-4-3-DSD in the Middle of the Test Section

The LWC and DSD were measured simultaneously; thus, the procedure and the conditions of the DSD measurements were the same as those presented in Chapter 3. Figure B-15 shows the MVD as a function of differential pressure for different air velocities and nozzle water pressures.

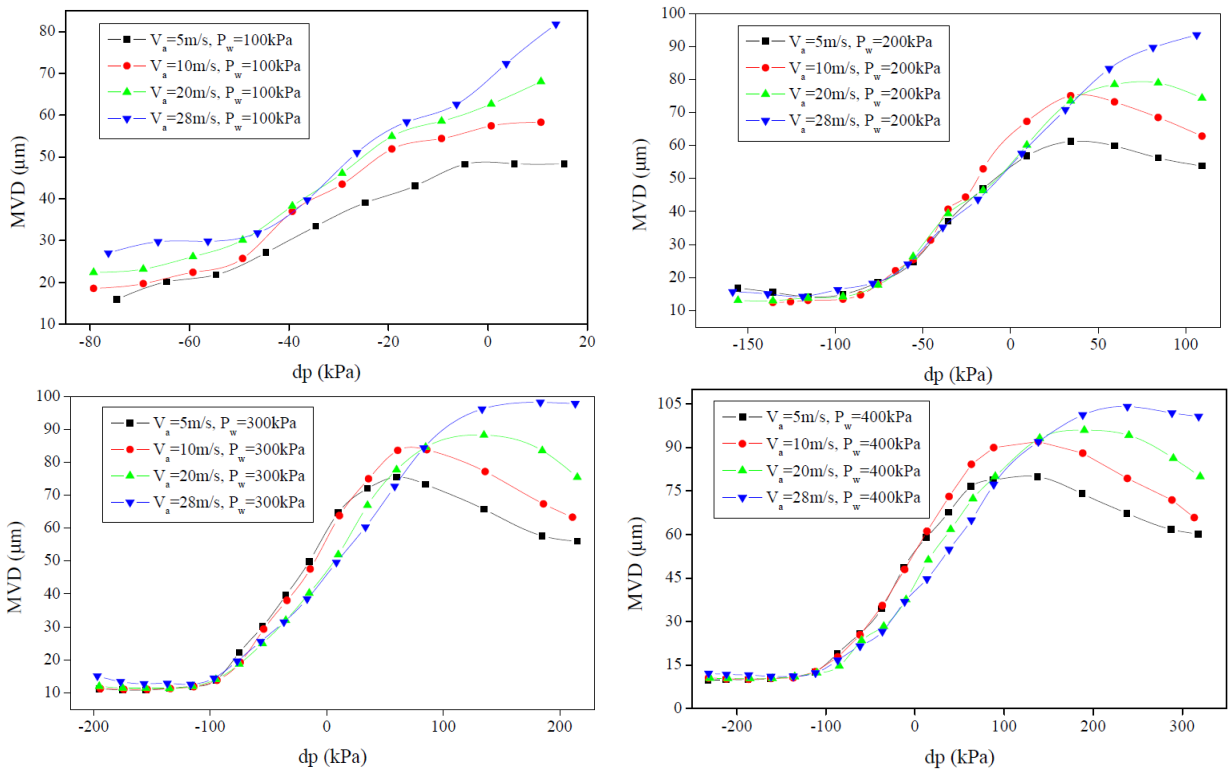

Figure B-15: MVD as a function of air velocity and nozzle pressures in the middle of the test section

The MVD is nearly constant for differential pressures below –100 kPa, and takes a value between 10 and 15 µm. Then, a steep increase follows in approximately the same region where the LWC also increases steeply. Thus, the maximum MVD appears for differential pressure between 0 and 100 kPa, and this value increases with water pressure. The maximum MVD increases with water pressure; and, contrary to the tendency of LWC, it increases with air velocity in the entire velocity range considered (5-28 m/s). The maximum MVD varies from 50 µm for the lowest velocity and water pressure to 100 µm for the highest air velocity and water pressure. The range of MVD that may be reached by type A nozzles in the geometrical center of the middle of the test section is between 10 and 100 µm.

APPENDIX C

TEST CONDITIONS AND RESULTS

RAW DATA

APPENDIX C: Test Conditions and Results Raw Data

Icing Simulation

Table C-1: Angle member dimensions for icing simulation

Specimen	Section	Material	**L**ength (mm)	Width-**b** (mm)	**T**hickness (mm)
A51x**L**9	L51x3.2	**A**luminum	920	50.8	3.175
A51x**L**4	L51x3.2	**A**luminum	460	50.8	3.175

Table C-2: Thermo physical parameters for different glaze ice accretions with icicles

Test Number	V_a (m/s)	T_a (°C)	P_a (kPa)	P_w (kPa)	LWC (g/m^3)	Time duration (min)	Ice definition
1	10	-5	320	200	1	45	Glaze with icicles
2	10	-5	100	200	1.8	30	Glaze with icicles
3	10	-5	300	300	3.3	15	Glaze with icicles

Table C-3: Thermo physical parameters for different glaze ice accretions

Test Number	V_a (m/s)	T_a (°C)	P_a (kPa)	P_w (kPa)	LWC (g/m^3)	Time duration (min)	Ice definition
1	20	-5	300	300	3.3	30	Glaze ice
2	10	-5	160	120	0.9	150	Glaze ice
3	10	-5	160	120	0.9	30	Glaze ice

Table C-4: Thermo physical parameters for different rime ice accretions

Test Number	V_a (m/s)	T_a (°C)	P_a (kPa)	P_w (kPa)	LWC (g/m^3)	Time duration (min)	Ice definition
1	10	-10	300	200	1	40	Rime ice
2	10	-10	300	250	1.85	15	Rime ice
3	5	-30	325	400	7.8	30	Rime ice
4	20	-15	160	120	0.9	60	Rime ice
5	10	-15	160	120	0.9	10	Rime ice

Table C-5 Thermo physical parameters of ice simulation

Specimen	V_a(m/s)	T_a(°C)	P_w(kPa)	P_a(kPa)	LWC(g/cm^3)	Time duration (min)
A51xL9-1	10	-5	120	160	0.9	30
A51xL9-2	25	-5	300	300	2.9	45
A51xL4	10	-5	120	160	0.9	30

Table C-6 Ice mass per unit length of horizontal angle member for different angles of attack and low LWC

LWC = 0.9 g/m^3				
No.	Angle of Attack	Ice Mass per Unit Length (gr/cm)		
		First Experiment	Second Experiment	Third Experiment
1	180	3.05	9.30	6.64
2	192	3.33	7.19	8.68
3	204	2.63	9.19	9.98
4	216	2.46	7.02	3.99
5	234	4.48	9.33	2.47
6	252	2.87	14.68	6.97
7	264	2.43	11.96	8.63
8	270	1.88	10.38	2.88
9	288	1.99	8.652	5.64
11	306	2.64	7.68	7.81
12	324	2.27	6.89	4.95
13	342	2.78	7.18	6.17
14	354	1.98	11.83	4.07
15	360	2.91	12.28	3.92

Table C-7 Ice mass per unit length of horizontal angle member for different angles of attack and high LWC

LWC = 2.9 g/m^3			
No.	Angle of Attack	Ice Mass per Unit Length (gr/cm)	
		First Experiment	Second Experiment
1	180	21.95	21.95
2	192	27.93	27.93
3	204	23.24	31.34
4	216	24.17	31.05
5	225	23.08	30.69
6	234	22.27	29.57
7	252	30.42	39.01
8	264	35.58	35.18
9	270	27.73	27.73
11	288	29.27	41.60
12	306	30.51	31.91
13	324	23.52	31.88
14	342	24.62	29.44
15	354	26.24	37.16
16	360	31.62	30.92

Table C-8 Ice mass per unit length of horizontal angle member for different sideslip angles and low LWC

LWC = 0.9 g/m^3				
No.	Sideslip Angle	Ice Mass per Unit Length (gr/cm)		
		First Experiment	Second Experiment	Third Experiment
1	0	2.91	12.28	3.92
2	6	2.69	5.72	10.10
3	14	4.11	3.49	4.66
4	18	3.39	6.16	3.58
5	25	7.57	3.87	4.14
6	32	3.95	3.17	2.74
7	45	2.30	1.75	3.02
8	53	5.11	3.43	2.24
9	65	1.61	2.28	2.13
11	77	1.62	1.07	1.33

Table C-9 Ice mass per unit length of horizontal angle member for different sideslip angles and high LWC

LWC = 2.9 g/m^3				
No.	Sideslip Angle	Ice Mass per Unit Length (gr/cm)		
		First Experiment	Second Experiment	Third Experiment
1	0	31.62	21.20	13.38
2	6	32.65	17.20	8.53
3	14	34.92	13.90	14.64
4	18	34.28	26.40	10.79
5	25	27.43	24.30	9.73
6	32	31.14	23.60	7.24
7	45	32.37	32.30	9.34
8	53	30.20	28.10	9.78
9	65	28.72	27.90	8.24

Table C-10 Ice mass per unit length of horizontal angle member for different rolling angles and low LWC

LWC = 0.9 g/m^3				
No.	Rolling Angle	Ice Mass per Unit Length (gr/cm)		
		First Experiment	Second Experiment	Third Experiment
1	6	1.99	1.62	1.67
2	12	2.28	1.99	1.59
3	18	4.36	4.55	3.67
4	24	5.14	4.77	4.53

Table C-11 Ice mass per unit length of horizontal angle member for different rolling angles and high LWC

LWC = 2.9 g/m^3				
No.	Rolling Angle	Ice Mass per Unit Length (gr/cm)		
		First Experiment	Second Experiment	Third Experiment
1	6	31.62	32.65	34.70
2	12	36.98	25.14	30.94
3	18	36.49	15.46	25.60
4	24	34.05	13.89	-

Table C-12 Ice mass per unit length of vertical angle member for different angle of attack and low LWC

LWC = 0.9 g/m^3				
No.	Angle of Attacks	Ice Mass per Unit Length (gr/cm)		
		First Experiment	Second Experiment	Third Experiment
1	135	3.43	3.04	2.76
2	171	2.34	2.29	2.20
3	207	2.30	2.78	2.69
4	219	3.00	3.25	2.71
5	243	2.64	3.55	2.97
6	261	2.57	2.51	2.79
7	297	2.37	3.24	3.01
8	297	1.95	2.12	2.97
9	303	2.31	2.76	2.53
10	309	1.84	2.06	2.86
11	315	2.62	2.35	2.33

Table C-13 Ice mass per unit length of vertical angle member for different sideslip angles and low LWC

LWC = 0.9 g/m^3				
No.	Angle of Attacks	Ice Mass per Unit Length (gr/cm)		
		First Experiment	Second Experiment	Third Experiment
1	0	2.15	2.35	2.33
2	6	2.26	3.10	2.61
3	22	2.86	2.64	2.65
4	45	3.30	3.63	3.71
5	67	2.98	3.87	3.39
6	90	3.78	2.64	2.73

Table C-14 Ice mass per unit length of vertical angle member for different rolling angles and low LWC

LWC = 0.9 g/m^3				
No.	Angle of Attacks	Ice Mass per Unit Length (gr/cm)		
		First Experiment	Second Experiment	Third Experiment
1	0	2.15	2.35	2.33
2	6	0.28	0.13	0.15
3	22	1.33	1.18	0.66
4	45	1.65	1.67	1.66
5	67	1.57	2.09	1.26
6	-6	0.05	0.04	0.039
7	-22	0.13	0.44	0.34
8	-45	1.26	1.146	0.62
9	-67	2.82	2.08	1.82
10	-6	0.05	0.04	0.039

Aerodynamic Experiments

Table C-15 Angle member specifications with related thermo physical parameters

Specimen	Section	Material	LWC (g/m^3)	Ice Type	Air velocity V_a(m/s)	Ice accretion time (min)	Air temperature T_a(°C)
S25-**G**1	L25x3.2	**S**teel	0.9	**G**laze	20	15	-5
S25-**G**2	L25x3.2	**S**teel	0.9	**G**laze	20	30	-5
S51-**G**3	L51x3.2	**S**teel	3.3	**G**laze	20	30	-5
S51-**G**4	L51x3.2	**S**teel	3.3	**G**laze	20	45	-5
S51-**G**5	L51x3.2	**S**teel	2.9	**G**laze	20	30	-5
S51-**G**6	L51x3.2	**S**teel	0.9	**G**laze	10	30	-5
S51-**G**7	L51x3.2	**S**teel	0.9	**G**laze	20	30	-5

Table C-16: Air velocity and angle of attack for aerodynamic models

Specimen	S25-G1	S25-G2	S51-G3	S51-G4	S51-G5	S51-G6	S51-G7
Air Velocity (m/s)	5-10-20	5-10-20	5-10-20	5-10-20	5-10-20	5-10-20	5-10-15
Angle of attack (°)	0<α<360	-20<α<20 160<α<200	0<α<360	-20<α<20 160<α<200	0<α<360	0<α<360	0<α<360

Table C-17 Models length with and without ice

Models	Length with ice (m)	Length without ice (m)	Length without ice (%)
S25-G1	1.6610	0.1454	8
S25-G2	1.6610	0.1454	8
S51-G3	1.4896	0.3104	17
S51-G4	1.4686	0.3394	19
S51-G5	1.2420	0.5644	31
S51-G6	1.2440	0.5624	31
S51-G7	1.4606	0.3434	19

Table C-18 to C-24 shows the aerodynamic coefficient correspond to the raw data which they have been corrected regarding to the angle length not covered with ice.

Table C-18 Log-Sheet data for sample S25-G1

Angle of Attack	Drag Coefficient			Lift Coefficient			Moment Coefficient		
	5 m/s	10 m/s	20 m/s	5 m/s	10 m/s	20 m/s	5 m/s	10 m/s	20 m/s
0	1.4255	1.3559	1.3068	0.5674	0.5397	0.5202	-0.1704	-0.1732	-0.1707
5	1.3688	1.3290	1.3285	0.5566	0.5404	0.5402	-0.2302	-0.2219	-0.2189
10	1.3353	1.3305	1.3137	0.5595	0.5574	0.5504	-0.2656	-0.2691	-0.2641
15	1.2907	1.2997	1.2958	0.5575	0.5614	0.5597	-0.3094	-0.3038	-0.3036
20	1.2316	1.2276	1.2385	0.5459	0.5441	0.5490	-0.3478	-0.3370	-0.3384
25	1.1620	1.1526	1.1714	0.5253	0.5211	0.5295	-0.3475	-0.3420	-0.3441
30	1.1046	1.0973	1.1173	0.5157	0.5123	0.5216	-0.3271	-0.3158	-0.3230
40	0.9296	0.9391	0.9744	0.4320	0.4364	0.4528	-0.1341	-0.1246	-0.1279
45	0.9366	0.9697	0.9817	0.4353	0.4507	0.4563	0.0594	0.0304	0.0234
50	1.0401	1.0243	1.0280	0.4912	0.4837	0.4855	0.1380	0.1638	0.1627

Angle of Attack	Drag Coefficient			Lift Coefficient			Moment Coefficient		
	5 m/s	10 m/s	20 m/s	5 m/s	10 m/s	20 m/s	5 m/s	10 m/s	20 m/s
60	1.1354	1.1424	1.1530	0.5272	0.5304	0.5353	0.2940	0.3186	0.3296
70	1.2645	1.2984	1.2882	0.5607	0.5757	0.5712	0.3645	0.3539	0.3487
80	1.3511	1.3545	1.3630	0.5743	0.5757	0.5793	0.3182	0.3155	0.3199
90	1.4263	1.4049	1.3951	0.6106	0.6015	0.5973	0.2593	0.2586	0.2589
100	1.3390	1.3124	1.3269	0.5287	0.5183	0.5240	0.1355	0.1356	0.1414
110	1.2280	1.2065	1.2261	0.4581	0.4501	0.4574	0.0384	0.0385	0.0392
120	1.1622	1.0989	1.1034	0.4218	0.3988	0.4005	-0.0400	-0.0201	-0.0159
130	1.2753	1.2563	1.2617	0.4584	0.4515	0.4535	-0.0181	-0.0178	-0.0135
135	1.3779	1.3548	1.3457	0.4913	0.4830	0.4798	-0.0385	-0.0343	-0.0318
140	1.4013	1.4001	1.4143	0.5021	0.5017	0.5068	-0.0599	-0.0580	-0.0549
150	1.4734	1.4755	1.4858	0.5475	0.5483	0.5521	-0.1229	-0.1182	-0.1129
160	1.3502	1.3528	1.3851	0.5113	0.5124	0.5246	-0.1664	-0.1592	-0.1576
170	1.2230	1.2159	1.2566	0.4772	0.4745	0.4903	-0.1967	-0.1910	-0.1913
180	1.0271	1.0426	1.0571	0.4040	0.4101	0.4158	-0.1577	-0.1644	-0.1643
190	0.9869	0.9733	0.9705	0.4070	0.4014	0.4002	-0.0289	-0.0291	-0.0283
200	1.0322	1.0378	1.0503	0.4580	0.4605	0.4661	0.1490	0.1428	0.1410
210	1.1848	1.1828	1.2010	0.5424	0.5415	0.5498	0.1614	0.1541	0.1474
220	1.2793	1.3122	1.3253	0.6010	0.6164	0.6226	0.1219	0.1106	0.1024
230	1.3125	1.3338	1.3370	0.6309	0.6411	0.6427	0.0398	0.0316	0.0249
240	1.1589	1.1459	1.1571	0.5492	0.5430	0.5483	-0.0312	-0.0449	-0.0523
250	0.8918	0.9133	0.9355	0.3980	0.4076	0.4175	-0.0200	-0.0207	-0.0231
260	1.0967	1.1225	1.1325	0.4774	0.4886	0.4930	-0.0179	-0.0097	-0.0084
270	1.2252	1.2195	1.2283	0.5042	0.5018	0.5054	0.0178	0.0297	0.0306
280	1.3445	1.3080	1.2994	0.5356	0.5210	0.5176	0.0441	0.0337	0.0364
290	1.2884	1.2986	1.2952	0.4859	0.4898	0.4885	0.0182	0.0104	0.0134
300	1.2815	1.2636	1.2672	0.4712	0.4646	0.4659	-0.0145	-0.0193	-0.0171
310	1.2019	1.2116	1.2360	0.4430	0.4466	0.4556	-0.0228	-0.0316	-0.0320
315	1.1344	1.1080	1.1399	0.4103	0.4007	0.4122	-0.0138	-0.0179	-0.0204
320	1.0976	1.0814	1.0838	0.3989	0.3930	0.3939	0.0048	-0.0016	-0.0032
330	1.1649	1.1195	1.1210	0.4340	0.4171	0.4177	0.0137	0.0138	0.0142
340	1.1895	1.1714	1.1728	0.4451	0.4384	0.4389	-0.0199	-0.0205	-0.0159
345	1.2176	1.2125	1.2073	0.4649	0.4630	0.4610	-0.0480	-0.0482	-0.0446
350	1.2764	1.2590	1.2550	0.4968	0.4900	0.4884	-0.0917	-0.0832	-0.0802
355	1.3115	1.2838	1.2890	0.5158	0.5048	0.5069	-0.1165	-0.1196	-0.1189

Table C-19 Log-Sheet data for sample S25-G2

Angle of Attack	Drag Coefficient			Lift Coefficient			Moment Coefficient		
	5 m/s	10 m/s	20 m/s	5 m/s	10 m/s	20 m/s	5 m/s	10 m/s	20 m/s
340	1.1735	1.1415	1.1041	-0.3742	-0.3894	-0.3856	0.0074	-0.0184	-0.0438
-20	1.0605	1.0886	1.0791	-0.4645	-0.4747	-0.4646	0.0128	-0.0149	-0.0503
-15	1.0282	1.0546	1.0476	-0.5016	-0.5236	-0.5172	0.0003	-0.0301	-0.0552
-10	0.9841	1.0090	1.0499	-0.5549	-0.5548	-0.5793	-0.0178	-0.0519	-0.0944
-5	1.1704	1.2155	1.2119	-0.7302	-0.7374	-0.7315	-0.1218	-0.1038	-0.1454
0	1.1093	1.1404	1.1445	-0.6904	-0.7048	-0.7002	-0.0064	-0.0407	-0.1105
5	1.0488	1.0742	1.0790	-0.6140	-0.6100	-0.6165	0.0695	0.0133	-0.0237
10	0.9080	0.9487	0.9527	-0.1026	-0.0865	-0.0862	0.1645	0.1285	0.1049
15	0.7717	0.7666	0.7633	-0.4086	-0.4791	-0.4956	0.2722	0.2723	0.2691
20	0.8170	0.8127	0.8185	0.3533	0.4035	0.4030	0.3881	0.3772	0.3749
160	0.7187	0.7228	0.7156	0.6023	0.6454	0.6532	0.4467	0.4030	0.4056
165	0.9366	0.9779	0.9844	1.0573	1.0493	1.0495	0.7255	0.7633	0.7988
170	0.8522	0.8711	0.8675	0.9881	0.9998	1.0025	0.6043	0.6453	0.6743
175	1.5256	1.5606	1.5616	0.0485	0.0564	0.0608	1.2278	1.2214	1.2070
180	1.1952	1.1974	1.2097	-0.0449	-0.0393	-0.0301	0.6944	0.7185	0.7051
185	1.5222	1.5311	1.5554	-0.1643	-0.1630	-0.1649	1.1326	1.1764	1.1802
190	1.3608	1.4022	1.4252	-0.2541	-0.1981	-0.1860	1.0488	1.1193	1.0973
195	1.6532	1.6312	1.6479	-0.0545	-0.0536	-0.0382	1.2057	1.2100	1.1866
200									

Table C-20 Log-Sheet data for sample S51-G3

Angle of Attack	Drag Coefficient			Lift Coefficient			Moment Coefficient		
	5 m/s	10 m/s	20 m/s	5 m/s	10 m/s	20 m/s	5 m/s	10 m/s	20 m/s
0	1.4011	1.2669	1.3221	-0.7974	-0.7113	-0.7435	-0.4000	-0.3791	-0.3968
5	1.2978	1.2744	1.2719	-0.8494	-0.8362	-0.8308	-0.3916	-0.3968	-0.4018
10	1.2359	1.1850	1.1935	-0.9692	-0.9635	-0.9688	-0.4261	-0.4234	-0.4348
15	1.1221	1.0884	1.0897	-0.9644	-0.9828	-0.9979	-0.4108	-0.4252	-0.4403
20	1.0378	1.0240	1.0214	-1.0272	-1.0250	-1.0283	-0.4244	-0.4321	-0.4440
25	0.9694	0.9754	0.9814	-0.9593	-1.0085	-1.0118	-0.3887	-0.4052	-0.4199
30	0.9555	0.9801	0.9781	-0.9387	-0.9366	-0.9254	-0.3079	-0.3195	-0.3287
40	0.9845	0.9676	0.9661	0.2325	0.2611	0.3051	0.3562	0.3465	0.3577
45	1.1145	1.0659	1.0440	0.5319	0.7538	0.9871	0.7130	0.7153	0.7486
50	1.0397	1.0518	1.0581	1.4191	1.3418	1.3182	0.8840	0.8815	0.8885

Angle of Attack	Drag Coefficient			Lift Coefficient			Moment Coefficient		
	5 m/s	10 m/s	20 m/s	5 m/s	10 m/s	20 m/s	5 m/s	10 m/s	20 m/s
60	1.2622	1.2616	1.2766	1.2673	1.3394	1.3666	0.9080	0.9066	0.9165
70	1.4285	1.4325	1.4516	1.2463	1.1901	1.1782	0.8275	0.8274	0.8348
80	1.5917	1.5923	1.6186	1.1707	0.9913	0.9755	0.7517	0.7620	0.7812
90	1.5239	1.5967	1.6146	0.5913	0.6169	0.6163	0.6042	0.6419	0.6355
100	1.2907	1.3540	1.3886	0.1867	0.2164	0.2168	0.4624	0.4653	0.4788
110	1.1476	1.1603	1.1598	-0.0780	-0.0651	-0.0743	0.3549	0.3512	0.3532
120	1.1647	1.1597	1.1631	0.0420	0.0413	0.0403	0.2468	0.2409	0.2354
130	1.3242	1.3019	1.3054	0.0717	0.0687	0.0707	0.1941	0.1965	0.1912
135	1.3316	1.3608	1.3477	0.0117	0.0106	0.0132	0.1808	0.1795	0.1651
140	1.4253	1.3882	1.3852	-0.0584	-0.0590	-0.0589	0.1714	0.1604	0.1530
150	1.4794	1.4804	1.4820	-0.2418	-0.2304	-0.2308	0.1342	0.1246	0.1218
160	1.5042	1.4894	1.4696	-0.3927	-0.3932	-0.3910	0.1129	0.1017	0.0945
170	1.3908	1.3761	1.3674	-0.4363	-0.4331	-0.4234	0.0656	0.0679	0.0566
180	1.0897	1.0577	1.0570	-0.3789	-0.3662	-0.3538	-0.0285	-0.0390	-0.0462
190	0.8999	0.8598	0.8734	-0.2153	-0.2080	-0.2013	-0.1717	-0.1788	-0.1938
200	0.9881	0.9899	0.9945	-0.1439	-0.1701	-0.1868	-0.3001	-0.3015	-0.3087
210	1.2187	1.1873	1.1783	-0.3222	-0.3558	-0.3818	-0.3345	-0.3282	-0.3499
220	1.1826	1.1789	1.1845	-0.4747	-0.4828	-0.4879	-0.3017	-0.2990	-0.3110
225	1.1750	1.1520	1.1541	-0.5331	-0.5509	-0.5664	-0.3086	-0.3117	-0.3196
230	1.0957	1.0606	1.0453	-0.6080	-0.6328	-0.6649	-0.2799	-0.2801	-0.2842
240	0.9234	0.8872	0.8956	-0.2664	-0.2699	-0.2935	-0.2396	-0.2318	-0.2394
250	0.8919	0.8811	0.8917	0.5745	0.5443	0.5451	-0.1038	-0.1065	-0.1093
260	1.2027	1.2009	1.1981	0.7608	0.7500	0.7664	-0.1346	-0.1287	-0.1249
270	1.3368	1.3342	1.3374	0.5762	0.6326	0.6426	-0.1335	-0.1284	-0.1223
280	1.3011	1.3170	1.3438	0.2833	0.4700	0.4891	-0.1039	-0.1063	-0.1036
290	1.3291	1.3314	1.3661	0.2758	0.3387	0.3454	-0.0862	-0.0962	-0.1016
300	1.2791	1.3085	1.3229	-0.0091	0.1902	0.1922	-0.0923	-0.1023	-0.1068
310	1.2757	1.2868	1.3198	0.0413	0.0751	0.0729	-0.1106	-0.1199	-0.1212
315	1.2206	1.2536	1.3023	0.1535	0.1109	0.0375	-0.1575	-0.1619	-0.1671
320	1.2704	1.3267	1.3477	0.0726	-0.0663	-0.0463	-0.1849	-0.1874	-0.1941
330	1.2045	1.2543	1.2733	-0.0451	-0.1222	-0.1200	-0.2178	-0.2268	-0.2307
340	1.2154	1.2259	1.2418	-0.1928	-0.2306	-0.2376	-0.2514	-0.2627	-0.2678
345	1.3492	1.2533	1.2482	-0.3530	-0.3387	-0.3498	-0.2993	-0.2904	-0.2874
350	1.3957	1.3118	1.2953	-0.4610	-0.4824	-0.4801	-0.3208	-0.3227	-0.3124
355	1.3689	1.2957	1.3025	-0.5888	-0.5816	-0.5953	-0.3380	-0.3392	-0.3318

Table C-21 Log-Sheet data for sample S51-G4

Angle of Attack	Drag Coefficient			Lift Coefficient			Moment Coefficient		
	5 m/s	10 m/s	20 m/s	5 m/s	10 m/s	20 m/s	5 m/s	10 m/s	20 m/s
-20	1.0739	1.0360	1.0333	-0.1043	-0.1105	-0.1135	-0.2250	-0.2154	-0.2133
-15	0.9873	0.9585	0.9612	-0.0841	-0.0950	-0.0941	-0.2072	-0.2027	-0.2081
-10	0.8980	0.8872	0.8938	-0.0869	-0.0954	-0.0948	-0.1885	-0.1937	-0.2039
-5	0.9957	0.8919	0.8941	-0.1345	-0.1226	-0.1237	-0.2229	-0.2069	-0.2127
0	0.9346	0.9176	0.9205	-0.1501	-0.1605	-0.1639	-0.2106	-0.2146	-0.2206
5	0.9831	0.9626	0.9706	-0.2193	-0.2250	-0.2277	-0.2138	-0.2113	-0.2164
10	0.9895	0.9731	0.9783	-0.2560	-0.3222	-0.3272	-0.2095	-0.2070	-0.2169
15	1.0020	0.9853	0.9854	-0.3346	-0.3502	-0.3623	-0.2002	-0.1982	-0.2019
20	1.0086	0.9918	0.9927	-0.4193	-0.4199	-0.4243	-0.1776	-0.1790	-0.1863
160	1.3487	1.3544	1.3542	-0.2414	-0.2524	-0.2496	0.1403	0.1383	0.1335
165	1.4403	1.4098	1.4198	-0.3479	-0.3361	-0.3334	0.1417	0.1311	0.1286
170	1.3207	1.3152	1.3176	-0.3449	-0.3495	-0.3430	0.1034	0.1006	0.0973
175	1.3279	1.3524	1.3660	-0.4114	-0.4184	-0.4074	0.0946	0.0953	0.0897
180	1.2180	1.1522	1.1544	-0.4261	-0.3858	-0.3766	0.0692	0.0567	0.0508
185	1.1499	1.0866	1.1578	-0.3887	-0.3672	-0.3772	0.0431	0.0257	0.0194
190	1.0054	1.0272	1.0268	-0.3620	-0.3566	-0.3539	-0.0099	-0.0138	-0.0194
195	0.8884	0.9392	0.9530	-0.3384	-0.3462	-0.3405	-0.0450	-0.0604	-0.0670
200	0.7394	0.7935	0.8076	-0.2405	-0.2622	-0.2731	-0.0798	-0.0977	-0.1082

Table C-22 Log-Sheet data for sample S51-G5

Angle of Attack	Drag Coefficient			Lift Coefficient			Moment Coefficient		
	5 m/s	10 m/s	20 m/s	5 m/s	10 m/s	20 m/s	5 m/s	10 m/s	20 m/s
0	1.1950	1.1397	1.1369	-0.6957	-0.6429	-0.6386	-0.2056	-0.2071	-0.2118
5	1.2057	1.1378	1.1460	-0.7891	-0.7310	-0.7346	-0.2044	-0.2048	-0.2146
10	1.0171	0.9980	1.0148	-0.9332	-0.9092	-0.9152	-0.2345	-0.2342	-0.2463
15	0.9266	0.8988	0.9114	-0.8418	-0.8074	-0.8292	-0.2047	-0.2086	-0.2193
20	0.8951	0.8863	0.8932	-0.6971	-0.6929	-0.6934	-0.1479	-0.1470	-0.1524
25	0.9478	0.8915	0.9086	-0.4257	-0.3803	-0.3711	-0.0315	-0.0276	-0.0268
30	0.9593	0.9465	0.9486	-0.0874	-0.0587	-0.0347	0.1061	0.1276	0.1344
40	0.9855	0.9992	1.0039	0.7504	0.8036	0.8455	0.4043	0.4241	0.4463
45	1.0988	1.1084	1.1325	0.8939	0.9081	0.9104	0.5901	0.5930	0.6041
50	1.1795	1.2001	1.2276	0.8514	0.8695	0.8775	0.5854	0.6035	0.6200

Angle of Attack	Drag Coefficient			Lift Coefficient			Moment Coefficient		
	5 m/s	10 m/s	20 m/s	5 m/s	10 m/s	20 m/s	5 m/s	10 m/s	20 m/s
60	1.2676	1.3030	1.3319	0.7077	0.7350	0.7598	0.5636	0.5839	0.6117
70	1.3470	1.3582	1.3567	0.5657	0.5733	0.5645	0.5499	0.5708	0.5803
80	1.2397	1.2649	1.2795	0.3130	0.3213	0.3203	0.4833	0.5155	0.5310
90	1.1271	1.1612	1.1758	0.0024	0.0273	0.0265	0.4586	0.4701	0.4777
100	1.0033	1.0203	1.0216	-0.2295	-0.2361	-0.2316	0.3318	0.3415	0.3429
110	0.9414	0.9920	0.9991	-0.1559	-0.1472	-0.1520	0.2603	0.2750	0.2788
120	1.0390	1.1096	1.1229	-0.0121	-0.0036	-0.0048	0.2307	0.2474	0.2510
130	1.2561	1.2640	1.2733	0.0314	0.0196	0.0203	0.2264	0.2337	0.2359
135	1.2521	1.2878	1.3141	-0.0074	-0.0117	-0.0101	0.1958	0.2018	0.2019
140	1.3117	1.3020	1.3011	-0.0205	-0.0316	-0.0362	0.1659	0.1726	0.1762
150	1.2433	1.2121	1.2236	-0.0439	-0.0519	-0.0565	0.1160	0.1196	0.1218
160	1.1618	1.1488	1.1794	0.0468	0.0400	0.0383	0.0431	0.0456	0.0481
170	1.0977	1.0793	1.0844	0.2558	0.2441	0.2536	-0.0216	-0.0591	-0.0737
180	1.1287	1.1639	1.2001	0.0656	0.0728	0.0846	-0.1383	-0.1633	-0.1804
190	1.3428	1.3432	1.3684	-0.0791	-0.0732	-0.0632	-0.2319	-0.2427	-0.2550
200	1.3833	1.3787	1.4024	-0.2557	-0.2556	-0.2498	-0.2604	-0.2915	-0.3101
210	1.3811	1.3660	1.3951	-0.4128	-0.4347	-0.4461	-0.3197	-0.3413	-0.3676
220	1.2415	1.2314	1.2509	-0.6065	-0.6052	-0.6159	-0.3459	-0.3662	-0.3933
225	1.1055	1.1472	1.1625	-0.6654	-0.6612	-0.6696	-0.3332	-0.3828	-0.4006
230	0.9785	0.9656	0.9774	-0.7744	-0.7901	-0.8014	-0.3503	-0.3825	-0.3972
240	0.9041	0.9177	0.9282	-0.2385	-0.2305	-0.2478	-0.3501	-0.3784	-0.3965
250	0.8624	0.9117	0.9427	0.4144	0.4493	0.4504	-0.1456	-0.1730	-0.2032
260	0.8141	0.8792	0.9175	0.9934	1.0630	1.1122	0.0751	0.0585	0.0274
270	1.1298	1.1474	1.1446	0.7140	0.7362	0.7605	-0.0104	-0.0273	-0.0244
280	1.1387	1.1331	1.1181	0.5779	0.5864	0.5987	0.0110	0.0001	-0.0045
290	1.0588	1.0430	1.0422	0.4530	0.4566	0.4719	0.0367	0.0133	0.0055
300	1.0722	1.0504	1.0474	0.3233	0.3244	0.3353	0.0009	-0.0147	-0.0218
310	1.2802	1.2645	1.2477	0.1647	0.1689	0.1743	-0.0468	-0.0557	-0.0607
315	1.3127	1.3613	1.3539	0.0488	0.0505	0.0615	-0.1001	-0.1026	-0.0963
320	1.4335	1.4035	1.4238	-0.0640	-0.0703	-0.0609	-0.1154	-0.1162	-0.1133
330	1.4016	1.3386	1.3585	-0.2723	-0.2701	-0.2642	-0.1404	-0.1423	-0.1556
340	1.2905	1.2839	1.2977	-0.4393	-0.4263	-0.4255	-0.1576	-0.1678	-0.1766
345	1.2442	1.2421	1.2920	-0.4874	-0.4842	-0.5030	-0.1557	-0.1650	-0.1820
350	1.3373	1.2505	1.2710	-0.6091	-0.5666	-0.5733	-0.1794	-0.1710	-0.1789
355	1.2724	1.2328	1.2258	-0.6544	-0.6314	-0.6250	-0.1819	-0.1828	-0.1896

Table C-23 Log-Sheet data for sample S51-G6

Angle of Attack	Drag Coefficient			Lift Coefficient			Moment Coefficient		
	5 m/s	10 m/s	20 m/s	5 m/s	10 m/s	20 m/s	5 m/s	10 m/s	20 m/s
0	1.1499	1.1340	1.1297	-0.6533	-0.6397	-0.6275	-0.1983	-0.1991	-0.2022
5	1.1275	1.0941	1.0969	-0.7147	-0.6926	-0.6866	-0.2099	-0.2121	-0.2162
10	1.0507	1.0025	1.0108	-0.9027	-0.8522	-0.8532	-0.2506	-0.2437	-0.2500
15	0.9447	0.9229	0.9168	-0.8167	-0.8216	-0.8326	-0.2413	-0.2372	-0.2442
20	0.8996	0.9017	0.9063	-0.7402	-0.7457	-0.7573	-0.1810	-0.1952	-0.2075
25	0.9159	0.9083	0.9099	-0.5299	-0.5214	-0.5244	-0.0908	-0.1001	-0.1079
30	0.9262	0.9466	0.9520	-0.2622	-0.2587	-0.2399	0.0534	0.0408	0.0380
40	0.9502	0.9761	0.9681	0.6968	0.7462	0.7980	0.3871	0.3885	0.3951
45	1.0010	1.0591	1.0819	0.8919	0.9427	0.9408	0.4982	0.5074	0.5150
50	1.1450	1.1912	1.1970	0.9168	0.9932	1.0126	0.5672	0.5900	0.5979
60	1.4568	1.4237	1.4302	1.0066	0.9625	0.9452	0.6920	0.6699	0.6756
70	1.7084	1.6186	1.6250	0.7206	0.6991	0.6933	0.7728	0.7507	0.7500
80	1.6657	1.6054	1.5770	0.4139	0.4154	0.4017	0.6840	0.6777	0.6830
90	1.5296	1.4993	1.4982	0.1269	0.1285	0.1112	0.6735	0.6670	0.6675
100	1.1823	1.1780	1.1736	-0.2271	-0.2347	-0.2666	0.4847	0.4849	0.4913
110	0.9111	0.9140	0.9298	-0.3289	-0.3157	-0.3278	0.3324	0.3361	0.3435
120	0.9470	0.9649	0.9783	-0.0335	-0.0192	-0.0149	0.2257	0.2392	0.2461
130	1.0411	1.0745	1.0875	0.0969	0.1241	0.1330	0.1777	0.1838	0.1865
135	1.1403	1.1132	1.1300	0.1351	0.1421	0.1489	0.1512	0.1397	0.1367
140	1.1635	1.1777	1.1868	0.1411	0.1473	0.1509	0.1104	0.1119	0.1104
150	1.3052	1.2730	1.2829	0.0992	0.1119	0.1124	0.0518	0.0517	0.0449
160	1.2857	1.2654	1.2700	0.0915	0.1002	0.1055	-0.0091	-0.0009	-0.0054
170	1.2494	1.2210	1.2219	0.1556	0.1757	0.1925	-0.0902	-0.0789	-0.0718
180	1.2888	1.2447	1.2640	0.1465	0.1516	0.1682	-0.1691	-0.1594	-0.1614
190	1.3529	1.3415	1.3431	0.0099	0.0142	0.0257	-0.2457	-0.2628	-0.2433
200	1.4246	1.4231	1.4405	-0.2466	-0.2272	-0.2185	-0.3235	-0.3191	-0.3421
210	1.4738	1.4515	1.4700	-0.6306	-0.6034	-0.6013	-0.4350	-0.4176	-0.4206
220	1.2222	1.2118	1.2288	-1.0141	-1.0047	-1.0055	-0.4876	-0.4777	-0.4860
225	1.1328	1.0984	1.1011	-1.2696	-1.2133	-1.2056	-0.6607	-0.6446	-0.6448
230	1.0194	1.0100	1.0063	-1.4006	-1.3725	-1.3491	-0.7219	-0.7267	-0.7186
240	1.0216	1.0048	0.9879	-0.3108	-0.3453	-0.3866	-0.5473	-0.5552	-0.5767
250	1.1146	1.0787	1.0710	0.4674	0.4408	0.4246	-0.2659	-0.2682	-0.2935
260	1.2762	1.1713	1.2036	1.4613	1.3526	1.3993	0.0844	0.0795	0.0833
270	1.0452	1.0822	1.0693	1.2211	1.2911	1.2894	0.2473	0.2461	0.2433
280	1.2076	1.1754	1.1505	0.9810	0.9654	0.9522	0.1577	0.1515	0.1509

Angle of Attack	Drag Coefficient			Lift Coefficient			Moment Coefficient		
	5 m/s	10 m/s	20 m/s	5 m/s	10 m/s	20 m/s	5 m/s	10 m/s	20 m/s
290	1.3487	1.3432	1.3262	0.6805	0.6771	0.6771	0.0925	0.0829	0.0830
300	1.4640	1.4905	1.5004	0.4084	0.4151	0.4245	0.0471	0.0412	0.0400
310	1.5307	1.4774	1.4931	0.1647	0.1546	0.1629	0.0174	0.0111	0.0080
315	1.5295	1.4867	1.4952	-0.0042	-0.0054	0.0008	-0.0111	-0.0096	-0.0197
320	1.4809	1.4549	1.4661	-0.1393	-0.1272	-0.1214	-0.0132	-0.0224	-0.0333
330	1.4214	1.4394	1.4083	-0.3407	-0.3465	-0.3285	-0.0565	-0.0655	-0.0721
340	1.4136	1.3530	1.3726	-0.5454	-0.5087	-0.5066	-0.1126	-0.1143	-0.1203
345	1.3877	1.3253	1.3483	-0.6112	-0.5806	-0.5789	-0.1309	-0.1338	-0.1403
350	1.2797	1.2664	1.3447	-0.6229	-0.6177	-0.6532	-0.1486	-0.1543	-0.1683
355	1.2171	1.1964	1.2093	-0.6490	-0.6387	-0.6405	-0.1678	-0.1690	-0.1776

Table C-24 Log-Sheet data for sample S51-G7

Angle of Attack	Drag Coefficient			Lift Coefficient			Moment Coefficient		
	5 m/s	10 m/s	15 m/s	5 m/s	10 m/s	15 m/s	5 m/s	10 m/s	15 m/s
0	0.9981	1.1215	1.1164	-0.4852	-0.8976	-0.8693	0.1493	0.0873	0.4663
5	1.2196	1.2701	1.2742	-0.8097	-1.0974	-1.1120	-0.4708	-0.0418	0.2209
10	1.0848	1.1704	1.1750	-0.7985	-1.2347	-1.2564	0.0901	0.1872	0.3312
15	1.0733	1.1455	1.1445	-0.7197	-1.2012	-1.2469	0.1778	0.2832	0.4333
20	1.1557	1.1776	1.1673	-1.0546	-1.1115	-1.1347	0.1980	0.3428	0.5662
25	1.1226	1.1401	1.1415	-0.8358	-0.7921	-0.7940	0.2079	0.4315	0.6488
30	1.0882	1.0936	1.0946	-0.1924	-0.2820	-0.2952	0.2166	0.4387	0.5834
40	0.8901	0.9712	0.9752	0.7192	0.8500	0.8463	0.1639	0.3160	0.4212
45	1.1294	1.1519	1.1296	0.8893	0.8973	0.8859	0.4430	0.4243	0.5016
50	1.1944	1.2099	1.2170	0.8142	0.8228	0.8310	0.2493	0.2875	0.3241
60	1.2369	1.2713	1.2901	0.6232	0.6634	0.6777	0.1705	0.2144	0.2568
70	1.3765	1.3647	1.3731	0.5314	0.5370	0.5391	0.1269	0.1612	0.1886
80	1.4032	1.4213	1.4318	0.3763	0.3829	0.3797	0.0510	0.1043	0.1370
90	1.4185	1.4683	1.4755	0.1754	0.1903	0.1897	0.1839	0.1370	0.1135
100	1.3564	1.4127	1.4145	-0.0779	-0.0832	-0.0892	0.1323	0.0941	0.0738
110	1.1153	1.1214	1.1519	-0.4624	-0.4696	-0.4793	0.1996	0.0979	0.0564
120	1.2762	1.2489	1.2679	-0.2335	-0.2185	-0.2208	0.1051	0.0591	0.0305
130	1.4202	1.3645	1.3692	-0.1525	-0.1439	-0.1410	0.0140	0.0036	0.0056
135	1.4070	1.3945	1.4060	-0.1715	-0.1564	-0.1550	0.2967	0.1864	0.1553

Angle of Attack	Drag Coefficient			Lift Coefficient			Moment Coefficient		
	5 m/s	10 m/s	15 m/s	5 m/s	10 m/s	15 m/s	5 m/s	10 m/s	15 m/s
140	1.4721	1.4153	1.4105	-0.1748	-0.1722	-0.1687	0.5628	0.2661	0.2035
150	1.3841	1.3956	1.4033	-0.2004	-0.1982	-0.1989	0.2797	0.2374	0.2329
160	1.2399	1.2277	1.2391	-0.1745	-0.1763	-0.1771	0.3432	0.2822	0.3003
170	1.1154	1.0927	1.1073	-0.0852	-0.0738	-0.0742	0.3495	0.2908	0.2977
180	1.0212	1.0219	1.0303	0.0613	0.0700	0.0764	0.4394	0.3215	0.2664
190	1.0750	1.0816	1.0897	0.0483	0.0302	0.0427	0.1005	0.0545	0.1314
200	1.2527	1.2837	1.2948	-0.2267	-0.2297	-0.2278	0.2448	0.1698	0.2813
210	1.3543	1.3463	1.3722	-0.4913	-0.4847	-0.4841	0.2357	0.2439	0.4322
220	1.2928	1.2855	1.2958	-0.6771	-0.6879	-0.6986	0.5597	0.3268	0.3837
225	1.1754	1.1727	1.1680	-0.8643	-0.8444	-0.8394	0.7360	0.3373	0.2536
230	1.0348	1.0230	1.0199	-1.0525	-1.0204	-1.0396	0.3673	0.2298	0.1709
240	0.9442	0.9376	0.9370	-0.2477	-0.2707	-0.2817	-0.0246	-0.0968	-0.1735
250	0.9751	0.9719	0.9778	0.6356	0.6222	0.6303	-0.1699	-0.2689	-0.3311
260	1.1171	1.1356	1.1404	0.9389	0.9385	0.9389	-0.3715	-0.4059	-0.4391
270	1.3784	1.3800	1.3907	0.7411	0.7331	0.7411	-0.1495	-0.1283	-0.1218
280	1.4412	1.3901	1.4172	0.6380	0.6109	0.6251	-0.0813	-0.0648	-0.0694
290	1.4580	1.4586	1.4686	0.4881	0.4859	0.4952	-0.0883	-0.0822	-0.0681
300	1.5090	1.4975	1.5114	0.3249	0.3145	0.3197	-0.0849	-0.1045	-0.0703
310	1.4448	1.4812	1.4924	0.1225	0.1121	0.1128	-0.0916	-0.0723	-0.0437
315	1.4353	1.4854	1.4936	0.0274	0.0150	0.0214	-0.0853	-0.0120	0.0064
320	1.3772	1.4496	1.4582	-0.0862	-0.0915	-0.0887	-0.0798	-0.0818	-0.0551
330	1.5089	1.4304	1.4573	-0.3488	-0.3283	-0.3288	-0.1814	-0.1337	-0.0448
340	1.5194	1.5520	1.5620	-0.5987	-0.6025	-0.5938	-0.1691	-0.1004	0.0887
345	1.5384	1.5021	1.5173	-0.7334	-0.7083	-0.7020	-0.1535	-0.0492	0.0946
350	1.5296	1.4931	1.4835	-0.8486	-0.8252	-0.8128	-0.1913	-0.0618	0.0986
355	1.4250	1.3775	1.3615	-0.9193	-0.8941	-0.8754	-0.1935	-0.0435	0.1458

Table C-25 shows the aerodynamic coefficient of bare angle member derived from [16].

Table C-25 Log-Sheet data for bare angle member [16]

Angle Member Profile	**2x2**				**1x1**			
Angle of Attack	C_d~5m/s	C_d~10m/s	C_l~5m/s	C_l~10m/s	C_d~5m/s	C_d~10m/s	C_l~5m/s	C_l~10m/s
0	2.085563	2.102898	-2.54827	-2.42961	1.710561	1.715377	-1.52697	-1.64566
5	1.470905	1.52286	-2.29745	-2.32815	1.312741	1.295493	-1.72846	-1.79271
15	1.420219	1.413726	-2.08415	-1.99016	1.45356	1.477201	-1.52116	-1.41525
25	1.40049	1.411979	-1.18886	-1.16591	1.482118	1.503182	-0.80509	-0.75246
35	1.278123	1.23576	0.764669	0.842662	1.179681	1.265866	0.331542	0.456361
45	1.335343	1.403078	2.256783	2.257412	1.526186	1.387773	1.960347	2.470087
55	1.756852	1.838351	1.493669	1.452023	1.882844	1.912977	1.040001	1.062
65	1.981019	1.943021	0.947996	0.926367	1.959318	1.965689	0.59265	0.599912
75	1.965196	1.956676	0.483744	0.487388	1.9323	1.967944	0.276988	0.280358
85	1.965772	1.971042	0.057668	0.037812	1.825965	1.894599	-0.32533	-0.19698
90	1.910199	1.941934	-0.29643	-0.27227	1.84106	1.856667	-0.06812	-0.11586
95	1.627507	1.650792	-0.50762	-0.48827	1.58444	1.585289	-0.39019	-0.34672
105	1.289216	1.297478	-0.63969	-0.64947	1.314487	1.347265	-0.48654	-0.40484
115	1.32639	1.335511	-0.16202	-0.1652	1.42936	1.435588	-0.1891	-0.15173
125	1.394702	1.399342	-0.02882	-0.02275	1.4293	1.452262	-0.20195	-0.14944
135	1.398463	1.412813	0.025545	0.018212	1.533677	1.522228	-0.04468	-0.03597
145	1.394702	1.399342	0.028823	0.022748	1.4293	1.452262	0.201945	0.14944
155	1.32639	1.335511	0.162021	0.165199	1.42936	1.435588	0.189096	0.151729
165	1.289216	1.297478	0.639691	0.649468	1.314487	1.347265	0.486539	0.404839
175	1.627507	1.650792	0.507622	0.488272	1.58444	1.585289	0.390193	0.346716
180	1.910199	1.941934	0.296427	0.272266	1.84106	1.856667	0.068123	0.115859
185	1.965772	1.971042	-0.05767	-0.03781	1.825965	1.894599	0.325332	0.196985
195	1.965196	1.956676	-0.48374	-0.48739	1.9323	1.967944	-0.27699	-0.28036
205	1.981019	1.943021	-0.948	-0.92637	1.959318	1.965689	-0.59265	-0.59991
215	1.756852	1.838351	-1.49367	-1.45202	1.882844	1.912977	-1.04	-1.062
225	1.335343	1.403078	-2.25678	-2.25741	1.526186	1.387773	-1.96035	-2.47009
235	1.278123	1.23576	-0.76467	-0.84266	1.179681	1.265866	-0.33154	-0.45636
245	1.40049	1.411979	1.188859	1.165912	1.482118	1.503182	0.805086	0.752458
255	1.420219	1.413726	2.08415	1.990156	1.45356	1.477201	1.521159	1.415252
265	1.470905	1.52286	2.297448	2.328148	1.312741	1.295493	1.728463	1.792712

Angle Member Profile	**2x2**				**1x1**			
Angle of Attack	C_d~5m/s	C_d~10m/s	C_l~5m/s	C_l~10m/s	C_d~5m/s	C_d~10m/s	C_l~5m/s	C_l~10m/s
270	2.085563	2.102898	2.548273	2.429606	1.710561	1.715377	1.526967	1.645656
275	2.069601	2.13688	1.947364	1.994727	2.12271	2.149121	1.795756	1.72088
285	2.097581	2.138062	1.339577	1.359146	2.076218	2.100932	1.192831	1.144365
295	2.056454	2.121774	0.790886	0.842066	2.013802	2.046552	0.793075	0.730906
305	2.070414	2.083978	0.370403	0.381738	2.044565	2.022413	0.345883	0.324324
315	2.08867	2.073118	0.095466	0.035213	2.075421	2.005361	0.039013	0.061426
325	2.070414	2.083978	-0.3704	-0.38174	2.044565	2.022413	-0.34588	-0.32432
335	2.056454	2.121774	-0.79089	-0.84207	2.013802	2.046552	-0.79308	-0.73091
345	2.097581	2.138062	-1.33958	-1.35915	2.076218	2.100932	-1.19283	-1.14437
355	2.069601	2.13688	-1.94736	-1.99473	2.12271	2.149121	-1.79576	-1.72088

References

[1] M. Farzaneh, “Ice Accretion on H.V. Conductors and Insulators and Related Phenomena,” *Philosophical Transactions*, vol. 358, pp. 1–35, 2000.

[2] A. Leblond and M. Farzaneh, “Guidelines for Meteorological Icing Models, Statistical Methods and Topographical Effects,” 2006.

[3] M. Farzaneh, *Atmospheric Icing of Power Networks*. Berlin: Springer, 2008.

[4] J. Druez, P. McComber, and J. Laflamme, “Field data on transmission line icing collected at the mount valin test site,” in *Arctic/Polar Technology ASME*, 1994, pp. 51–55.

[5] E. Sundin and L. Makkonen, “Ice Loads on a Lattice Tower Estimated by Weather Station Data,” *Applied Meteorology*, pp. 523–529, 1998.

[6] M. Vargas and J.-C. Tsao, “Observations on the growth of roughness elements into icing feathers,” in *45th AIAA Aerospace Sciences Meeting*, 2007, pp. 10889–10910.

[7] M. Vargas, J. A. Giriunas, and T. P. Ratvasky, “Ice Accretion Formations on a NACA 0012 Swept Wing Tip in Natural Icing Conditions,” 2002.

[8] X. Presteau, E. Montreuil, A. Chazottes, X. Vancassel, and P. Personne, “Experimental and numerical study of scallop ice on swept cylinder,” in *1st AIAA Atmospheric and Space Environments*, 2009, p. 4124.

[9] R. Z. Blackmore and E. P. Lozowski, “Spongy Icing Modeling, Spongy Icing Modeling: Progress and Prospects,” in *International Offshore and Polar Engineering*, 2003, pp. 429–434.

[10] N. Maeno, L. Makkonen, K. Nishimura, K. Kosugi, and T. Takahashi, “Growth rates of icicles,” *Journal of Glaciology*, vol. 40, no. 135, pp. 319–326, 1994.

[11] L. Makkonen, “A model of icicle growth,” *Journal of Glaciology*, vol. 34, no. 116, pp. 64–70, 1998.

[12] L. E. Kollar and M. Farzaneh, “Wind-tunnel investigation of icing of an inclined cylinder,” *International Journal of Heat and Mass Transfer*, vol. 53, no. 5–6, pp. 849–861, 2010.

[13] M. S. Virk, M. C. Homola, and P. J. Nicklasson, “Effect of Rime Ice Accretion on Aerodynamic Characteristics of Wind Turbine Blade Profiles,” *Wind Engineering*, vol. 34, no. 2, pp. 207–218, 2010.

[14] C. Cuerno-Rejado, G. Lopez-Martonez, J. L. Escudero-Arahuetes, and J. Lopez-Dõez, “Experimental aerodynamic characteristics of NACA 0012 airfoils with simulated glaze and rime ice,” in *International Mechanical Engineering*, 2001, p. 215.

[15] D. C. Bayar, “Drag coefficients of latticed towers,” *Journal of structural engineering*, vol. 112, no. 2, pp. 417–430, 1986.

[16] S. Prud’homme, F. Legeron, A. Laneville, and M. K. Tran, “Wind Forces on Single and Shielded Angle Members in Lattice Structures,” *Journal of Wind Engineering and Industrial Aerodynamics*, 2012.

[17] T. Han, “Computational analysis of three-dimensional turbulent flow around a Bluff Body in ground proximity,” *AIAA*, no. 9, p. 27, 1989.

[18] M. S. Ingber, “A vorticity method for determining drag on Bluff Bodies,” *Journal of Dynamics of Fluids*, vol. 2, no. 1, pp. 1–11, 2006.

[19] J. Hoffman, “Computational of Mean Drag for Bluff Boddy Problems Using Adaptive DNS/LES,” in *Courant Institute of Mathematical Sciences*, 1995, pp. 1–24.

[20] X. Chi, B. Zhu, T. .-P. Shih, H. E. Addy, and Y. K. Choo, “CFD analysis of the aerodynamic of a business-jet airfoil with leading-edge ice accretion,” in *42nd AIAA Aerospace sciences meeting and exhibit*, 2004, p. 560.

[21] M. B. Bragg and E. Loth, “Effects of large droplet ice accretion on airfoil and wing aerodynamics and control,” Washington, DC, 2000.

[22] S. Lee and M. B. Bragg, “Investigation of factors affecting iced-airfoil aerodynamics,” *Journal of Aircraft*, vol. 40, no. 3, pp. 499–508, 2003.

[23] J. B. Barlow, W. H. Rae JR., and A. Pope, *Low Speed Wind Tunnel Testing*. John Willey & Sons Inc., 1999.

[24] H. Banitalebi Dehkordi, L. Kollar, M. Farzaneh, P. Camirand, and C. Damours, “Introduction, Instrumentation and Calibration of CIGELE Atmospheric Icing Research Wind Tunnel (CAIRWT),” 2009.

[25] F. Gregorio, A. Ragni, M. Airoldi, and G. Romano, “PIV Investigation on Airfoil with Ice Accretions and Resulting Performance Degradation,” in *IEEE*, 2001, pp. 94–105.

[26] R. Huschke, *Glossary of meteorologyNo Title*. Boston, USA: American Meteorological Society, 1959.

[27] G. Poots, *Ice and snow accretion on structures*. Taunton, Somerset, England: Research Studies Press, 1996.

[28] CIGRE 291, “Guidelines for meteorological icing models, Statistical methods and topographical effects,” 2006.

[29] E. Eranti and G. Lee, *Cold Region Structural Engineering*. New York, 1986.

[30] K. Uenoa and M. Farzaneh, "Linear stability analysis of ice growth under super-cooled water film driven by a laminar airflow," *Physics of fluid*, vol. 23, no. 042103, 2011.

[31] P. Tattleman and I. I. Gringorten, "Estimated glaze ice and wind loads at the earth's surface for the contiguous," 1973.

[32] M. Roberge, "A study of wet snow shedding from an overhead cable," McGill University, 2006.

[33] Y. Sakamoto, "Snow accretion on overhead wires," *Philosophical Transactions*, vol. 358, pp. 2941–2970, 2000.

[34] C. Rawlins, "Research on vibration of overhead ground wires," *Power Delivery IEEE Transactions*, vol. 3, no. 2, pp. 769–775, 1998.

[35] M. Vargas, "Current experimental basis for modeling ice accretions on swept wings," *Journal of Aircraft*, vol. 44, no. 1, 2007.

[36] M. Papadakis, H. W. Yeong, S. C. Wong, M. Vargas, and M. Potapczuk, "Experimental investigation of ice accretion effects on swept wing," Springfield, Virginia, 2005.

[37] J. Druez, S. Louchez, and P. McComber, "Ice shedding from cables," *Cold Regions Science and Technology*, vol. 23, pp. 377–388, 1995.

[38] M. Baenziger, "Broken conductor loads on transmission line structures," University of Wisconsin, 1981.

[39] M. Matsuura, H. Matsumoto, Y. . Maeda, and Y. Oota, “The study of ice shedding phenomena on transmission lines,” in *1st International Symposium on Cable Dynamics*, 1995, pp. 181–188.

[40] ISO12494, *International Standards of Atmospheric Icing on Structures, ISO12494*. 2001.

[41] C. Gurung, H. . Yamaguchi, and T. Yukino, “Identification of large amplitude wind induced vibration of ice-accreted transmission lines based on field observed data,” *Engineering Structures*, vol. 24, pp. 179–188, 2002.

[42] J.-M. Toussaint, “Le galop des lignes électriques: Mesures en soufflerie et simulations,” Université de Liège, Belgium, 1998.

[43] EPRI 792, *Transmission line reference book: Wind-induced conductor motion*. Palo Alto, CA, USA: Electric Power Research Institute, 1979.

[44] R. Zdero and O. F. Turan, “The effect of surface strands, angle of attack, and ice accretion on the flow field around electrical power cables,” *Journal of wind engineering and industrial aerodynamics*, vol. 98, pp. 672–678, 2010.

[45] O. Nigol and P. G. Buchan, “Conductor galloping part I,” *IEEE Transactions on Power Apparatus and Systems*, vol. 100, no. 2, 1981.

[46] W. W. H. Yeung, “On the Relationships among Strouhal Number, Pressure Drag, and Separation Pressure for blocked bluff-body flow,” *Journal of Fluids Engineering*, vol. 132, 2010.

[47] B. Ahlborn, M. L. Seto, and B. R. Noack, “On drag, Strouhal number and vortex-street structure,” *Journal of Fluid Dynamics Research*, vol. 30, pp. 379–399, 2002.

[48] G. Buresti, “Bluff-body aerodynamics, International Advanced School on wind excited and aeroelastic vibrations,” Italy, 2000.

[49] G. K. Batchelor, *An Introduction to Fluid Dynamics*. Cambridge, U.K.: Cambridge University Press, 1967.

[50] M. S. Ingber and S. N. Kempka, “A Galerkin implementation of the generalized Helmholtz decomposition for vorticity formulations,” *Journal of computational physics,*, vol. 169, pp. 215–237, 2001.

[51] J. Hoffman, “Computation of mean drag for bluff body problems using adaptive DNS/LES,” 2005.

[52] R. I. Basu, “Aerodynamic forces on structures of circular cross section, Part I. Model-Scale data obtained under two-dimensional conditions in low-turbulence streams,” *wind engineering and industrial aerodynamics*, vol. 21, pp. 273–294, 1985.

[53] M. Matsumoto, H. Ishizaki, C. Matsuoka, Y. Daito, Y. Ichikawa, and S. A., “Aerodynamic effects of the angle of attack on rectangular prism,” *wind engineering and industrial aerodynamics*, vol. 77 & 78, pp. 531–542, 1998.

[54] F. T. Lynch and A. Khodadoust, “Effects of ice accretions on aircraft aerodynamics,” *Journal of Aerospace Sciences*, vol. 37, no. 8, pp. 669–767, 2001.

[55] M. K. Politovich, “Aircraft icing cause by large super-cooled droplets,” *Applied Meteorology*, vol. 28, pp. 856–868, 1989.

[56] A. Roshko and W. Fiszdon, “On the persistence of transition in the near wake,” in *On problems of aerodynamics and continuum mechanics*, 1969.

[57] H. W. Liepmann, “The rise and fall of ideas in turbulence,” *American Journal of Science*, vol. 67, pp. 221–294, 1979.

[58] Y. I. Jang and S. J. Lee, “PIV analysis of near-wake behind a sphere at a sub-critical Reynolds number,” *Experimental Fluid*, vol. 44, pp. 905–914, 2008.

[59] P. W. Bearman, “Near wake flows behind two and three dimensional bluff bodies,” *Wind Engineering and Industrial Aerodynamics*, vol. 69–71, pp. 33–54, 1997.

[60] A. Roshko, “On the Drag and Shedding Frequency of Two-Dimensional Bluff Bodies,” 1954.

[61] K. Marakkos and J. T. Turner, “Vortex generation in the cross – flow around a cylinder attached to an end – all,” *Optics & Laser Technology*, vol. 38, no. 4–6, pp. 277–285, 2006.

[62] H.-C. Lim and S. J. Lee, “PIV measurements of near wake behind a U-grooved cylinder,” *Fluids and Structures*, vol. 18, pp. 119–130, 2003.

[63] T. Von Karman, *Aerodynamics*. McGraw Hill, 1963.

[64] G. Buresti, “Vortex shedding from bluff bodies,” in *In Wind Effects on Buildings and Structures*, 1998, pp. 61–95.

[65] M. Li, “Aerodynamic loading of stationary and oscillating cable,” McMaster University, 1993.

[66] G. Schewe, “On the force fluctuations acting on a circular cylinder in cross flow from sub-critical up to trans-critical Reynolds numbers,” *Fluid Mechanic*, vol. 133, pp. 265–285, 1983.

[67] C. Pickering and N. Halliwell, “LSP and PIV: photographic film noise,” *Applied optics*, vol. 23, pp. 2961–2969, 1984.

[68] R. Adrian, “Scattering particle characteristics and their effect on pulsed laser measurements of fluid flow: speckle velocimetry vs. particle image velocimetry,” *Applied optics*, vol. 23, no. 11, pp. 1690–1691, 1984.

[69] H. Oualli, S. Hanchi, A. Bouabdellah, R. Askovic, and M. Gad-El-Hak, “Interaction between the near wake and the cross – section variation of a circular cylinder in uniform flow,” *Experiments in Fluids*, vol. 44, no. 5, pp. 807–818, 2008.

[70] D. Shiel and A. Leonard, “Investigation of a drag reduction on a circular cylinder in rotary oscillation,” *Fluid Mechanic*, vol. 431, pp. 297–322, 2001.

[71] J.-C. Lin, J. Towfighi, and D. Rockwell, “Instantaneous structure of the near-wake of a circular cylinder: on the effect of Reynolds number,” *Fluids and Structures*, vol. 9, pp. 409–418, 1995.

[72] N. Fujisawa, S. Tanahashi, and K. Srinivas, “Evaluation of pressure field and fluid forces on a circular cylinder with and without rotational oscillation using velocity data from PIV measurement,” *Measurement Science and Technology*, vol. 16, no. 4, pp. 989–996, 2005.

[73] M. Gad-El-Hak, “Flow control,” *Applied Mechanics Reviews*, vol. 42, pp. 261–293, 1989.

[74] F. De Gregorio, A. Ragni, M. Airoldi, and G. P. Romano, “PIV investigation on airfoil with ice accretions and resulting performance degradation,” in *International Congress on Instrumentation in Aerospace Simulation Facilities*, 2001, pp. 94–105.

[75] E. C. Maskell, “A theory of the blockage effects on bluff bodies and stalled wings in a closed wind tunnel,” 1963.

[76] C. F. Cowdrey, “The application of Maskell’s theory of wind-tunnel blockage to very large solid models,” Teddington, UK, 1968.

[77] D. M. Sykes, “Blockage corrections for large bluff bodies in wind tunnels,” *Advances in road vehicle aerodynamics*, pp. 311–321, 1973.

[78] H. B. Awbi, “The investigation of wind tunnel wall interference on bluff-body models,” Trent Polytechnic, 1974.

[79] H. Utsunomiya, F. Nagao, Y. Ueno, and M. Noda, “Basic study of blockage effects on bluff bodies,” *Wind Engineering and Industrial Aerodynamics*, vol. 49, pp. 247–256, 1993.

[80] M. Noda, H. Utsunomiya, and F. Nagao, “Basic study on blockage effects in turbulent boundary layer flows, Journal of Wind Engineering and Industrial Aerodynamics,” vol. 54/55, pp. 645–656, 1995.

[81] K. Takeda and M. Kato, “Wind tunnel blockage effects on drag coefficient and wind induced vibration,” *Wind Engineering and Industrial Aerodynamics*, vol. 41–44, pp. 897–904, 1992.

[82] A. Laneville and J. Y. Trepanier, “Blockage effects in smooth and turbulent flows: The case of two dimensional rectangular cylinders,” *Wind Engineering and Industrial Aerodynamics*, vol. 22, pp. 169–176, 1986.

[83] S. G. Cober, G. A. Isaac, and J. W. Strapp, “Charactrization of Aircraft Icing Environemnts That Include Supercooled Large Drops,” *Journal of Applied meteorol*, vol. 40, pp. 1984–2002, 2001.

[84] R. K. Jeck, “Representative Values of Icing Related Variables Aloft in freezing Rain and Freezing Drizzle, DOT/FAA/AR-TN95/119,” Atlantic city, 1996.

[85] R. K. Jeck, “Icing-Design Envelopes (14 CFR Parts 25 and 29, Appendix C) Converted to a Distance-Based Format, DOT/FAA/AR-00/30,” Atlantic city, 2002.

[86] S. A. Frisch, B. E. Martner, I. Djalalova, and M. R. Poellot, “Comparison of radar/radiometer retrievals of stratus cloud liquid-water content profiles with in situ measurements by aircraft,” *Journal of Geophysical Research*, vol. 105, no. D12, p. 15361, Jun. 2000.

[87] Air Force Geophysics Laboratory, *Handbook of Geophysics and space Environment*. United States Air Force, 1985.

[88] L. E. Kollar and M. Farzaneh, “Modeling the evolution of droplet size distribution in two-phase flows,” *International, Journal of Multiphase Flow*, vol. 33, no. 11, pp. 1255–1270, 2007.

[89] L. E. Kollar and M. Farzaneh, “Spray characteristics of artificial aerosol clouds in a low-speed icing wind tunnel,” *Journal of Atomization and Sprays*, vol. 19, no. 4, pp. 387–405, 2009.

[90] M. B. Bragg, “Experimental aerodynamic characteristics of an NACA 0012 airfoil with simulated glaze ice,” *Journal of Aircraft*, vol. 25, no. 9, pp. 849–854, 1988.

[91] M. Mousavi, “Experimental and Theoretical Verification of Two Icing Codes,” University of Quebec at Chicoutimi, 2003.

[92] P. M. Chaine, R. W. Verge, G. Castonguay, and J. Gariepy, “Wind and Ice Loading in Canada,” Toronto, 1974.

[93] DantecDynamics, “2D PIV and Interferometric Particle Imaging (IPI),” 2006.

[94] S. Prud’homme, “Développement d’un banc d’essai actif et passif à 3 ddl pour essais sectionnels en soufflerie.,” Université de Sherbrooke, 2010.

[95] E. P. Lozowski, J. R. Stallabrass, and P. F. Hearty, “The icing of an unheated, non-rotating cylinder, Part II: Icing wind tunnel experiments,” *Journal of Climate & Applied Meteorology*, vol. 22, no. 12, pp. 2063–2074, 1983.

[96] L. E. Kollar, M. Farzaneh, and A. R. Karev, “Modeling Droplet Size Distribution near a Nozzle Outlet in an Icing Wind Tunnel,” *Journal Atomization and Sprays*, vol. 16, no. 6, pp. 673–686, 2006.

[97] L. E. Kollar and M. Farzaneh, “Modeling and Experimental Study of Variation of Droplet Cloud Characteristics in a Low-Speed Horizontal Icing Wind Tunnel,” in in *Wind Tunnels: Aerodynamics, Models and Experiments*, Hauppauge, NY: Nova Science Publishers inc, 2011, pp. 93–127.

[98] S. F. Hoerner, *Practical information on aerodynamic drag and hydrodynamic resistance*, 3rd ed. Midland Park, N.J., 1965.

[99] S. B. Pope, *Turbulent Flows*. Cambridge University Press., 2000.

[100] R. F. Ide, “Liquid Water Content and Droplet Size Calibration of the NASA Lewis Icing Research Tunnel,” 1990.

[101] L. Makkonen, “Models for the growth of rime, glaze, icicles and wet snow on structures,” *Philosophical Transactions of the Royal Society*, vol. 358, no. 1776, pp. 2913–2939, 2000.